Hydrodynamic Diffuse Interface Models for Cell Morphology and Motility

DISSERTATION

zur Erlangung des akademischen Grades
Doctor rerum naturalium
(Dr. rer. nat.)

vorgelegt an der

Technischen Universität Dresden
Fakultät Mathematik und Naturwissenschaften
Fachrichtung Mathematik

von

Wieland Marth

geboren am 26. Mai 1986 in Lichtenstein

Tag der Einreichung: 24. März 2016
Tag der Verteidigung: 27. Mai 2016

1. Gutachter: Prof. Dr. rer. nat. habil. Axel Voigt
Technische Universität Dresden
2. Gutachter: Prof. Dr. James J. Feng
University of British Columbia

Abstract

In this thesis, we study mathematical models that describe the morphology of a generalized biological cell in equilibrium or under the influence of external forces. Within these models, the cell is considered as a thermodynamic system, where streaming effects in the cell bulk and the surrounding are coupled with a Helfrich-type model for the cell membrane. The governing evolution equations for the cell given in a continuum formulation are derived using an energy variation approach. Such two-phase flow problems that combine streaming effects with a free boundary problem that accounts for bending and surface tension can be described effectively by a diffuse interface approach. An advantage of the diffuse interface approach is that models for e.g. different biophysical processes can easily be combined. That makes this method suitable to describe complex phenomena such as cell motility and multi-cell dynamics. Within the first model for cell motility, we combine a biological network for GTPases with the hydrodynamic Helfrich-type model. This model allows to account for cell motility driven by membrane protrusion as a result of actin polymerization. Within the second model, we moreover extend the Helfrich-type model by an active gel theory to account for the actin filaments in the cell bulk. Caused by contractile stress within the actin-myosin solution, a spontaneous symmetry breaking event occurs that lead to cell motility. In this thesis, we further study the dynamics of multiple cells which is of wide interest since it reveals rich non-linear behavior. To apply the diffuse interface framework, we introduce several phase field variables to account for several cells that are coupled by a local interaction potential. In a first application, we study white blood cell margination, a biological phenomenon that results from the complex relation between collisions, different mechanical properties and lift forces of red blood cells and white blood cells within the vascular system. Here, it is shown that inertial effects, which can become of relevance in various parts of the cardiovascular system, lead to a decreasing tendency for margination with increasing Reynolds number. Finally, we combine the active polar gel theory and the multi-cell approach that is capable of studying collective migration of cells. This hydrodynamic approach predicts that collective migration emerges spontaneously forming coherently-moving clusters as a result of the mutual alignment of the velocity vectors during inelastic collisions. We further observe that hydrodynamics heavily influence those systems. However, a complete suppression of the onset of collective migration cannot be confirmed. Moreover, we give a brief insight how such highly coupled systems can be treated numerically using finite elements and how the numerical costs can be limited using operator splitting approaches and problem parallelization with OPENMP.

Kurzfassung

Diese Dissertation beschäftigt sich mit mathematischen Modellen zur Beschreibung von Gleichgewichts- und dynamischen Zuständen von verallgemeinerten biologischen Zellen. Die Zellen werden dabei als thermodynamisches System aufgefasst, bei dem Strömungseffekte innerhalb und außerhalb der Zelle zusammen mit einem Helfrich-Modell für Zellmembranen kombiniert werden. Schließlich werden durch einen Energie-Variations-Ansatz die Evolutionsgleichungen für die Zelle hergeleitet. Es ergeben sie dabei Mehrphasen-Systeme, die Strömungseffekte mit einem freien Randwertproblem, das zusätzlich physikalischen Einflüssen wie Biegung und Oberflächenspannung unterliegt, vereinen. Um solche Probleme effizient zu lösen, wird in dieser Arbeit die Diffuse-Interface-Methode verwendet. Ein Vorteil dieser Methode ist, dass es sehr einfach möglich ist, Modelle, die verschiedenste Prozesse beschreiben, miteinander zu vereinen. Dies erlaubt es, komplexe biologische Phänomene, wie zum Beispiel Zellmotilität oder auch die kollektive Bewegung von Zellen, zu beschreiben. In den Modellen für Zellmotilität wird ein biologisches Netzwerk-Modell für GTPasen oder auch ein Active-Polar-Gel-Modell, das die Aktinfilamente im Inneren der Zellen als Flüssigkristall auffasst, mit dem Multi-Phasen-Modell kombiniert. Beide Modelle erlauben es, komplexe Vorgänge bei der selbst hervorgerufenen Bewegung von Zellen, wie das Vorantreiben der Zellmembran durch Aktinpolymerisierung oder auch die Kontraktionsbewegung des Zellkörpers durch kontraktile Spannungen innerhalb des Zytoskelets der Zelle, zu verstehen. Weiterhin ist die kollektive Bewegung von vielen Zellen von großem Interesse, da sich hier viele nichtlineare Phänomene zeigen. Um das Diffuse-Interface-Modell für eine Zelle auf die Beschreibung mehrerer Zellen zu übertragen, werden mehrere Phasenfelder eingeführt, die die Zellen jeweils kennzeichnen. Schließlich werden die Zellen durch ein lokales Abstoßungspotential gekoppelt. Das Modell wird angewendet, um White blood cell margination, das die Annäherung von Leukozyten an die Blutgefäßwand bezeichnet, zu verstehen. Dieser Prozess wird dabei bestimmt durch den komplexen Zusammenhang zwischen Kollisionen, den jeweiligen mechanischen Eigenschaften der Zellen, sowie deren Auftriebskraft innerhalb der Adern. Die Simulationen zeigen, dass diese Annäherung sich in bestimmten Gebieten des kardiovaskulären Systems stark vermindert, in denen die Blutströmung das

Stokes-Regime verlässt. Schließlich wird das Active-Polar-Gel-Modell mit dem Modell für die kollektive Bewegung vom Zellen kombiniert. Dies macht es möglich, die kollektive Bewegung der Zellen und den Einfluss von Hydrodynamik auf diese Bewegung zu untersuchen. Es zeigt sich dabei, dass der Zustand der kollektiven gerichteten Bewegung sich spontan aus der Neuausrichtung der jeweiligen Zellen durch inelastische Kollisionen ergibt. Obwohl die Hydrodynamik einen großen Einfluss auf solche Systeme hat, deuten die Simulationen nicht daraufhin, dass Hydrodynamik die kollektive Bewegung vollständig unterdrückt. Weiterhin wird in dieser Arbeit gezeigt, wie die stark gekoppelten Systeme numerisch gelöst werden können mit Hilfe der Finiten-Elemente-Methode und wie die Effizienz der Methode gesteigert werden kann durch die Anwendung von Operator-Splitting-Techniken und Problemparallelisierung mittels OPENMP.

Acknowledgment

I gratefully acknowledge the funding of this work by the projects SFB Transregio 96 and SPP 1506. But besides that, there are a lot of people to whom I would like to express my sincere thanks. Without them this thesis would simply not have been possible. Among others, I owe my deepest gratitude to my supervisor Prof. Axel Voigt who introduced me in this area of research and who supported me throughout my work, to Dr. Sebastian Aland who introduced me to the physics of two-phase flow and diffuse interface models, to Dr. Simon Praetorius for his help in numerical questions and his work on AMDiS, to M.Eng. Siqi Ling who did a great job for the multi-mesh implementation of my code, to M.Sc. Francesco Alaimo for is useful answers to my question concerning physics and to Florian Stenger for his advices in post-processing and mesh generation. I also give a big thank-you to all other members of my institute and research group who stimulated interesting and fruitful discussions over the last few years. Furthermore, I thank the organizers of the research program ”Coupling Geometric PDEs with Physics for Cell Morphology, Motility and Pattern Formation”, especially Prof. Anotida Madzvamuse, for giving me the opportunity to attend this program, the Isaac Newton Institute for Mathematical Sciences in Cambridge/UK for their organization and accommodation and the Graduate Academy of TU Dresden for their funding. Moreover, I would like to thank all those people who helped me in proofreading this thesis. Last but not least, let me give thanks to my family for their support throughout my studies.

This thesis contains a lot of pictures. Many of them were created by me and some of them were already published in my papers. Moreover, right holders of external pictures are fully acknowledged. These pictures were either taken from wikipedia.org and have a free license or they were extracted from other publications which is allowed for educational use provided that the original source is cited.

Contents

List of Figures

List of Tables

CHAPTER 1

Introduction

Biological cells are the smallest unit of life and are for itself of utmost complexity. Understanding the basic processes within a cell helps to understand life. A basic instrument of understanding those processes are mathematical models that assist to bridge the gap between experiments and a fundamental understanding of several biological explanations. In recent years the simulation science supported by exponentially growing computer power made fundamental progress giving rise to the development of more and more complex models. Contributing to this evolution, in this thesis we study mathematical models for cell mechanics that describe equilibrium and dynamic properties of biological cells based on a hydrodynamic diffuse interface Helfrich-type model. In fact, cells are very complex structures mostly embedded in a fluid environment comprising several parts such as cytosol, cytoskeleton and different organelles that behave mechanically different. Depending on the spatial scale as well as on the time scale which can range anywhere from milliseconds (cell in micro channel), seconds (blood flow) to hours (migrating cell on a substrate) each biological component can become more or less dominant.

At long time scales elastic contributions from the bulk can be neglected since the cell can restore its shape and dissipate stress. Consequently, as a first approach the shape of the cell is determined by the bending properties of its membrane, regarded as lipid bilayer. This allows us to approximate cells as lipid vesicles that are fluid-filled sacs surrounded by a lipid membrane. Those vesicles, which serve as simple model, have been extensively studied in literature e.g. [46, 94, 227]. As a very first attempt to understand vesicles, Helfrich [121] mentioned that the basic component determining their shape is the bending strain of a two-dimensional lipid membrane Γ and came up with the idea that vesicles minimize the functional that is nowadays known as the Helfrich energy,

$$E_S(\Gamma) = \int_\Gamma b_n(H - H_0)^2 \,\mathrm{ds},$$

under the conditions of volume and surface area conservation and without topological transitions. Here, b_n is the bending rigidity, H the mean curvature and H_0 the spontaneous curvature. In the last years, the Helfrich model has been adopted to more complicated biological phenomena because many of these results have proven in good agreement with experiments. Although the model neglects contributions from the cell bulk, it covers the basic shapes of red blood cells (RBCs) in equilibrium.

The evolution of the cell and its membrane are considered as a free boundary problem where the dynamics are determined by a minimization process of an internal energy of a thermodynamic system that contains the cell interior and the surrounding media. The cell membrane here is presented as interface between both phases on which for a hydrodynamic system a jump condition holds that relates the fluid stress tensor to the variation of the Helfrich energy with respect to Γ. Accordingly, this includes the consideration of the Navier-Stokes equations for the fluid flow. If only the equilibrium state is of interest, we can neglect the fluid flow and we obtain non-hydrodynamic geometric evolution equations.

Different modeling strategies have been developed to numerically solve free boundary methods. These methods are basically classified into interface tracking and interface capturing methods. Interface tracking methods are for instance the immersed boundary method [120, 126, 135, 136], non-continuum particle-based mesoscale simulation methods [99, 100, 182, 195], boundary integral methods [98, 247, 248] and surface finite-elements methods [25, 84, 85]. However, these methods require an explicit tracking of the membrane and are based on a Lagrangian description with moveable grid points. Interface capturing methods, on the other hand, use an Eulerian description with a fixed mesh as the interface is implicitly defined by a level-set of an auxiliary function. Representatives are the level set method e.g. [64, 144, 145, 218] and the diffuse interface or phase field method e.g. [31, 67, 74, 129, 151] that we will apply in this thesis as it provides a simple means of handling moving boundaries.

Diffuse interface methods can be traced back to the study on gas-liquid interfaces by van der Walls in 1893. Using a similar formalism, Landau [146] developed a mean-field approach for phase transitions. An underlying free energy $\mathcal{E}(\phi)$ defines the physics of the system. Cahn and Hilliard [39] extended this theory and came up with a diffuse interface theory of phase transitions to describe phase separation of a binary alloy. We also refer to the reviews given in [17, 89, 234]. Within the diffuse interface approach, the interface Γ is smeared out with thickness ε and implicitly defined by the zero level-set of ϕ. The interior and exterior are labeled with different but constant values. Then, the diffuse Helfrich energy is given by

$$\mathcal{E}_H(\phi) = \frac{b_n}{2\varepsilon} \int_\Omega \left(\varepsilon\Delta\phi - \frac{1}{\varepsilon}(\phi^2 - 1)(\phi + \sqrt{2}H_0\varepsilon) \right)^2 \mathrm{d}\mathbf{x}. \tag{1.1}$$

The basic principle of the phase field calculus is that it converges to the geometric analogon as the diffuse interface goes to zero. The convergence can be shown by asymptotic analysis that is not trivial. However, diffuse interface methods have a robust physical basis since their evolution equations are derived from the physical principle of energy dissipation.

In Chapter 2, we give an introduction to underlying mathematical techniques and modeling approaches we use in this thesis. In Chapter 3, we show how the diffuse interface method can be applied to the hydrodynamic free boundary problem that considers the Helfrich bending energy. Performing an energy variation approach, we obtain the diffuse interface Navier-Stokes-Helfrich system [77] that serves as basis for our further studies within this thesis. Moreover, the diffuse interface method allows us to easily extend our model to additional models. This makes the method suitable to describe complex biological phenomena such as cell motility (Part I) and multi-cell dynamics (Part II).

Cell motility is a self-propelled motion emerged spontaneously or in response to external signals, where an internal force is mediated to its surrounding. Cell motility plays a crucial role within various biological processes. In wound healing processes, for instance, keratinocytes as part of the epidermis try to migrate into the destroyed parts and close the wound. Moreover, cancer cells spread out from their initial tumor and can create new metastases in the whole body. Certainly, an understanding of those processes is of basic interest, see [55, 103, 124, 189] for a review. In this thesis, we develop and study two models for cell motility that combine the mechanical Navier-Stokes-Helfrich model to further active processes. These processes are membrane protrusion due to actin polymerization and contractile stress due to actin-myosin reactions. Preceding to the mechanical mechanisms for cell motility is a polarization of the cell, where a front and a rear has to be defined as a result of a spatial stimulus.

In Chapter 5, we study a biochemical network for GTPases, where a Turing instability characterizes the polarity of the cell and determines the membrane protrusion coming from the actin polymerization. Usually such diffusion driven instabilities require large differences in the diffusion coefficients of the involved species. This might not be realistic in our case as diffusion coefficients for proteins are similar to each other. Here, we consider a biochemical network [209] with reaction-diffusion equations for membrane-bound and cytoplasmic GTPases, where, as a result of different association and disassociation rates between membrane and cytoplasm, a much more realistic Turing instability is formed [152]. The diffuse interface approach hereby allows us to account for the different dimensionalities of the biochemical network, which can easily be coupled to mechanical Navier-Stokes-Helfrich model. In Chapter 6, we append an active polar gel model [58, 101, 203] to our previous Navier-Stokes-Helfrich model [242]. Here, the direction of the actin filaments and accordingly the polarity of the cell is represented by a macroscopic orientation field. Both systems for cell motility become active and far from equilibrium as a result of a propelling mechanism that consumes energy and mediates a force to its surrounding. Within the first model we relate the concentration of active

GTPases to protrusion force acting on the surface membrane and within our second model we account for the contractile stress between actin filaments by a phenomenological contractile stress tensor [206] that can break the symmetry of the orientation field and cause an active motion of the cell. These models allow us to simulate the dynamics of cells and to reproduce the primary phenomenology

In many biological systems, however, cells appear with various other cells. As a result of their interaction, systems of multiple cells offer a rich non-linear behavior. For instance the Fåhræus–Lindqvist effect [96] describes that the complex microstructure of the blood, where the elasticity of the RBCs and their collision rate, which highly depends on the flow rate, affect the macroscopic viscosity. Moreover, actively driven cells can form stable clusters in absence of any attractive potential known as motility-induced phase separation [114]. To understand and describe such phenomena we extend the framework for a single cell to multiple cells, see Chapter 7. We therefore consider one phase field for a single cell and couple all cells via a local interaction potential. Within our thermodynamic consistent approach the most expensive part, i.e. computing the distance between cells, has been avoided as this information is already contained in the phase field description of the cells. In Chapter 8, we apply this model to describe white blood cell margination within the vascular system, a biological phenomenon occurring as a result the interplay between collisions and different mechanical properties of RBCs and white blood cells (WBCs), which can easily be treated with our approach. Reproducing previous results [99], we subsequently show that inertial effects, which can become of relevance in various parts of the cardiovascular system, suppress the tendency for margination.

Finally, in Chapter 9, we combine the active polar gel theory to our multi-phase approach to study the onset of collective motion in systems of self-propelled cells. We derive different models that are either non-hydrodynamic or hydrodynamic. We first study interactions between two cells that can be used as a benchmark problem to predict how bigger systems evolve. Moreover, we conduct several simulations to investigate the collective behavior of multiple cells and the ordering processes in an initially disordered crowd. We show that the for growing elasticity of the cell the collective motion is suppressed. Within the hydrodynamic model, the collision modeling is completely different but it allows us to account for multiple orientation fields. To our knowledge, or model is the first that combines the advantages of the diffuse interface method where we can account for various microscopic properties of the cell bulk and membrane in a hydrodynamic continuum formulation to the dynamics of multiple cells. It is thereby a promising model for the study of multi-cell dynamics in hydrodynamic suspensions. We further give a brief insight how such highly coupled systems can be treated numerically and how the numerical costs can be limited using operator splitting approaches, problem parallelization with OPENMP and multi-mesh strategies.

Some shown results have already been published in Marth and Voigt [174], Marth et al. [176, 177] and partially in Haußer et al. [118] and Ling et al. [156] and are submitted for publication, see Marth and Voigt [175].

Chapter 2

Mathematical preliminaries

In this thesis, we study mathematical models for cells and cell membranes. These models are given in a continuum formulation and consist of several partial differential equations (PDEs). The fundamental idea is to consider the cell evolution as a free boundary problem. There are developed different modeling and computational strategies to numerically solve free boundary methods. In this thesis, we consider the diffuse interface or phase field approach. This approach requires a basic understanding of mathematical techniques that are given in a brief review in this chapter. To be more precise, we give an overview of the basic notation used in this thesis, see Section 2.1 and Section 2.2. The geometric evolution equations are developed using a gradient flow approach based on the physical principle, the energy dissipation, see Section 2.3. A general introduction to phase field modeling is given in Section 2.4. An advantage of the diffuse interface models is that we can easily append additional equations such as continuity equations that account for the different dimensionality of bulk and surface. An introduction to these models and its diffuse interface description is shown in Section 2.6. In Section 2.5, we give some examples of surface energies. Moreover, in Section 2.7, we give an introduction to two-phase flows that describe the flow in two separated phases connected by an interface whose evolution is determined by surface energies. Depending on the choice of the underlying surface energy, we can describe different physical phenomena e.g. fluid drops or lipid membranes. Combining geometric evolution equations in a diffuse interface description with fluid flow that distinguishes between the inside and the outside of the surface yields the so-called diffuse two-phase flow derived in a general description in Section 2.8.

2.1. Domain and notation

In this section, we briefly introduce some basic notations that will be used in this thesis. We consider the spatial domain $\Omega \subset \mathbb{R}^s$ bounded by $\partial\Omega$. The time domain is an interval $I := [0, T] \subset \mathbb{R}$ with $T > 0$. Furthermore, Ω contains a smooth closed surface $\Gamma \subset \mathbb{R}^{s-1}$. See Fig. 2.1 for an illustration. Usually, Γ is time dependent. Therefore, we may also write $\Gamma := \Gamma(t)$, for $t \in I$. For our purposes, it is sufficient to set $s = 2, 3$. We denote the interior of Γ with $\Omega_1 := \Omega_1(t) \subset \Omega$. With respect to its interior, the surface is sometimes called Γ_1. The exterior is denoted by $\Omega_0 := \Omega_0(t) \subset \Omega$. Ω_0 and Ω_1 are open and bounded. We claim $\Omega_1 \cap \Omega_0 = \emptyset$ and it holds $\Omega = \Omega_1 \cup \Gamma \cup \Omega_0$. The length, area or volume of a domain $\Omega \subset \mathbb{R}^s$, for $s = 1, 2, 3$ is denoted by $|\Omega|$. Here, we will always call $|\Omega_1|$ the volume of $\Omega_1 \subset \mathbb{R}^{2,3}$ and $|\Gamma|$ the area of $\Gamma \subset \mathbb{R}^{1,2}$.

In connection to the topic of the thesis, we will later call Ω_1 the cell interior or bulk, Ω_0 the extra-cellular matrix or surrounding fluid, Γ the cell membrane and $\bar{\Omega}_1 := \Omega_1 \cup \Gamma$ the whole cell.

We denote a scalar by $a \in \mathbb{R}$ and a vector $\mathbf{b} := (b_1, \dots, b_s)^\top \in \mathbb{R}^s$ with $s = 2, 3$. It is clear that $\mathbf{b}^\top = (b_1, \dots, b_s)$. All functions $f := f(t, \mathbf{x}) : I \times \Omega \to \mathbb{R}$ as well as $\mathbf{f} := \mathbf{f}(t, \mathbf{x}) := (f_1(t, \mathbf{x}), \dots, f_s(t, \mathbf{x}))^\top : I \times \Omega \to \mathbb{R}^s$ are usually space and time dependent. The gradient of f in $\mathbf{x} \in \Omega$ is defined through

$$\nabla f = (\frac{\partial f}{\partial x_1}, \dots, \frac{\partial f}{\partial x_s})^\top \in \mathbb{R}^s$$

and for $\mathbf{f}$ we have the Jacobian matrix $\nabla \mathbf{f} = \left(\frac{\partial f_i}{\partial x_j}\right)_{i,j} \in \mathbb{R}^{s \times s}$, which is quadratic since $\Omega \subset \mathbb{R}^s$,$i, j = 1, \dots, s$. The directional derivative of f is $\nabla f \cdot \mathbf{b} =: (\frac{\partial f}{\partial b_1}, \dots, \frac{\partial f}{\partial b_s})^\top \in \mathbb{R}^s$, for $\mathbf{b} \in \mathbb{R}^s$, where $\cdot$ denotes the inner product, defined below. The divergence is defined through

$$\nabla \cdot \mathbf{f} = \sum_{i=1}^{s} \frac{\partial f_i}{\partial x_i} \in \mathbb{R}$$

and for a matrix $\mathbf{A} = (a_{ij})_{i,j} \in \mathbb{R}^{n \times n}$ we have $\nabla \cdot \mathbf{A} = (\sum_{i=1}^{s} \frac{\partial a_{i1}}{\partial x_i}, \dots, \sum_{i=1}^{s} \frac{\partial a_{is}}{\partial x_i})^\top \in \mathbb{R}^s$. The Laplacian of f is

$$\Delta f = \nabla \cdot \nabla f = \sum_{i=1}^{s} \frac{\partial^2 f}{\partial x_i^2} \in \mathbb{R}$$

and can be defined element-wise for $\mathbf{\Delta f} = \nabla \cdot \nabla \mathbf{f} = (\sum_{i=1}^{s} \frac{\partial^2 f_1}{\partial x_i^2}, \dots, \sum_{i=1}^{s} \frac{\partial^2 f_s}{\partial x_i^2})^\top \in \mathbb{R}^s$. In this thesis $\nabla\nabla f$ also appears which identifies the Hessian matrix i.e. $\nabla\nabla f = \left(\frac{\partial^2 f}{\partial x_i \partial x_j}\right)_{i,j} \in \mathbb{R}^{s \times s}$. The inner product is understood for $b, c \in \mathbb{R}^s$ as $b \cdot c := \sum_{i=1}^{n} b_i c_i \in \mathbb{R}$ and can also be denoted by $b^\top c$. We thus consider the norm of a vector to be the Frobenius norm $|a| := \sqrt{a \cdot a} \in \mathbb{R}$ if not stated otherwise. The outer product or tensor product is $b \otimes c := (b_i c_j)_{i,j} \in \mathbb{R}^{s \times s}$ and can also be denoted by $bc^\top$. We further consider

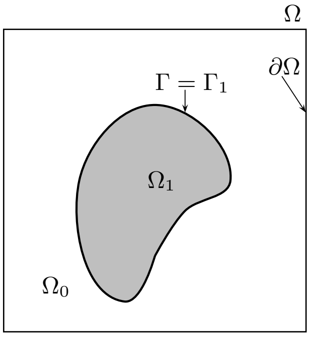

Figure 2.1. – Illustration of the two-dimensional mathematical domain Ω

the Frobenius inner product defined for $B, C \in \mathbb{R}^{s\times s}$ with $B : C := \sum_{i=1}^{n}\sum_{j=1}^{n} b_{ij}c_{ij} \in \mathbb{R}$.

2.2. Surface analysis and integral theorems

$\Gamma(t)$ is a free moving boundary embedded in Ω with prescribed velocity $\mathbf{v} = V\mathbf{n} + \mathbf{T}$. Here, the differentiable function $\mathbf{n}(\mathbf{x})$ denotes the surface normal of Γ in $\mathbf{x} \in \Gamma$ pointing from Ω_1, $V = \mathbf{v}\mathbf{n}$ is the normal velocity and $\mathbf{T}$ is the tangential velocity. We further assume that $\partial\Gamma(t)$ is empty. Two appropriate parameters to characterize the shape of Γ are the mean curvature given as

$$H(\mathbf{x}) = \frac{1}{s-1}\sum_{i=1}^{s-1} k_i(\mathbf{x}),$$

with k_i the principle curvatures and the Gaussian curvature given as

$$K(\mathbf{x}) = \prod_{i=1}^{s-1} k_i(\mathbf{x}).$$

In addition, the mean curvature is given by $H(\mathbf{x}) = 1/(s-1)\nabla \cdot \mathbf{n}(\mathbf{x})$. We furthermore introduce the surface delta function $\delta_\Gamma(\mathbf{x})$ defined in its support Γ such that we have $\int_\Omega \delta_\Gamma(\mathbf{x}) f(\mathbf{x})\,\mathrm{d}\mathbf{x} = \int_\Gamma f(\mathbf{x})\,\mathrm{ds}$ for a sufficient smooth test function f. We can also define differential operators on Γ. Given a differentiable function f in the neighborhood of Γ, the surface gradient reads

$$\nabla_\Gamma f = \mathbf{P}_\Gamma \nabla f,$$

where $\mathbf{P}_\Gamma = \mathbf{I} - \mathbf{n} \otimes \mathbf{n}$ is the projection operator, with $\mathbf{I}$ the identity matrix. It is clear that $\mathbf{P}_\Gamma \mathbf{n} = \mathbf{0}$ holds. Since $\mathbf{P}$ is a matrix, we might also write $\nabla_\Gamma f = \mathbf{P}_\Gamma \cdot \nabla f$, denoting a matrix-vector multiplication. The surface divergence is given through

$$\nabla_\Gamma \cdot \mathbf{v} = \mathbf{P}_\Gamma : \nabla \mathbf{v}.$$

Since $\nabla_\Gamma f$ is in the tangential plane of Γ, we have $\nabla_\Gamma f \cdot \mathbf{n} = 0$. The Laplace-Beltrami operator on Γ is defined as the surface divergence of the surface gradient i.e.

$$\Delta_\Gamma f = \nabla_\Gamma \cdot \nabla_\Gamma f = \nabla \cdot (\mathbf{P}_\Gamma \nabla f).$$

Now, we refer some useful integral theorems. So we consider the scalar functions u, v and the vector valued function $\mathbf{f} = (f_1, \dots, f_2)$. We recall the divergence theorem or Gauß's theorem

$$\int_{\Omega_1} \nabla \cdot \mathbf{f} = \int_\Gamma \mathbf{f} \cdot \mathbf{n} \,\mathrm{d}s,$$

from which the formulas for integration by parts or Green's formulas clearly follow with $\mathbf{w}v := \mathbf{f}$

$$\int_{\Omega_1} \mathbf{w} \cdot \nabla v \,\mathrm{d}\mathbf{x} = \int_\Gamma \mathbf{w} \cdot \mathbf{n} v \,\mathrm{d}s - \int_{\Omega_1} (\nabla \cdot \mathbf{w}) v \,\mathrm{d}\mathbf{x}$$

and with $\nabla u := \mathbf{w}$

$$\int_{\Omega_1} \nabla u \cdot \nabla v \,\mathrm{d}\mathbf{x} = \int_\Gamma \nabla u \cdot \mathbf{n} v \,\mathrm{d}s - \int_{\Omega_1} (\Delta u) v \,\mathrm{d}\mathbf{x}.$$

This can also be done on the surface Γ that gives

$$\int_\Gamma \nabla_\Gamma u \cdot \nabla_\Gamma v \,\mathrm{d}s = \int_{\partial\Gamma} \nabla_\Gamma u \cdot \mathbf{n}_{\partial\Gamma} v \,\mathrm{d}s - \int_\Gamma (\Delta_\Gamma u) v \,\mathrm{d}s.$$

2.3. Variational derivative and gradient flow

We consider a biological cell as a thermodynamic system. The governing evolution equations for the cell are derived using an energy variation approach following the second law of thermodynamics. Then, the evolution of the cell is understood as an energy minimizing process. In this section, we give a short introduction to these physical concepts. A broader introduction is given in De Groot and Mazur [59]. It is clear that the determination of extrema requires dealing with derivatives. Since the underlying space of those energy functionals is infinite dimensional, we need more general approach, the variational derivatives. For a deeper insight, we refer to the work of Cowan [54].

2.3.1. Variational derivative

H will denote a Hilbert space with $\|\cdot\|_H$, the inner produkt $\langle \cdot\,, \cdot \rangle_H$ and the dual pair $[\,\cdot\,, \cdot\,]_{H^* \times H}$. Given $\phi \in H$ and a functional $E\colon H \to \mathbb{R}$, i.e. $E \in H^*$. Then, the derivative of E is given by

$$\lim_{\xi \to 0} \frac{1}{\xi} \left(E(\phi + \xi h) - E(\phi) \right) = \left[E'(\phi), h \right]_{H^* \times H}, \qquad \forall h \in H.$$

If this limit exists, we may also write

$$\frac{\mathrm{d}}{\mathrm{d}\xi}E(\phi+\xi h)\bigg|_{\xi=0} = \left[E'(\phi),h\right]_{H^*\times H}, \qquad \forall h\in H.$$

By using the representation theorem of Riesz, we are able to express the derivative $E'(\phi)\in H^*$ by a function $\mathrm{grad}E\in H$ such that

$$\left[E'(\phi),h\right] = \langle \mathrm{grad}E, h\rangle_H, \qquad \forall h\in H,$$

then $\mathrm{grad}E$ is denoted as variational derivative. Furthermore, we introduce $\frac{\delta E}{\delta\phi}$ denoting the result that can be derived from

$$\frac{\mathrm{d}}{\mathrm{d}\xi}E(\phi+\xi h)\bigg|_{\xi=0} = \int_\Omega \frac{\delta E}{\delta\phi} h\,\mathrm{d}\mathbf{x}.$$

Note that the choice of H determines the shape of $\mathrm{grad}E$. Let $\Omega\subset\mathbb{R}^s$. In case of $L^2(\Omega)$ with $\mathrm{grad}E, h\in L^2(\Omega)$, we have

$$\langle \mathrm{grad}E, h\rangle_{L^2} = \int_\Omega \mathrm{grad}E h\,\mathrm{d}\mathbf{x} = \int_\Omega \frac{\delta E}{\delta\phi}h\,\mathrm{d}\mathbf{x},$$

where $\frac{\delta E}{\delta\phi} := \mathrm{grad}E$ denotes the variational derivative in L^2 with respect to ϕ. Considering the space $H^{-1}(\Omega)$, $\mathrm{grad}E, h^*\in H^{-1}(\Omega)$ and its inner product given by

$$\langle \mathrm{grad}E, h^*\rangle_{H^{-1}} = \int_\Omega -\Delta^{-1}\mathrm{grad}E h^*\,\mathrm{d}\mathbf{x} = \int_\Omega \frac{\delta E}{\delta\phi}h^*\,\mathrm{d}\mathbf{x},$$

where $-\Delta\frac{\delta E}{\delta\phi} := \mathrm{grad}E$ denotes the variational derivative in H^{-1} with respect to ϕ.

In this thesis, the functional E is regarded as energy of a thermodynamic system with a thermodynamic quantity $\phi(t)$ being time dependent. To determine the variational derivative, we can also derive E with respect to time. Accordingly, we have

$$\begin{aligned}\frac{\mathrm{d}}{\mathrm{dt}}E(\phi(t)) &= \lim_{\varepsilon\to 0}\frac{1}{\varepsilon}\left(E(\phi(t+\varepsilon)) - E(\phi(t))\right)\\ &= \lim_{\varepsilon\to 0}\frac{1}{\varepsilon}\Big(E(\phi(t)+\varepsilon\phi'(t)+\mathcal{O}(\varepsilon^2)) - E(\phi(t)\Big)\\ &= \lim_{\varepsilon\to 0}\frac{1}{\varepsilon}\left(E(\phi(t)+\varepsilon\phi'(t)) - E(\phi(t))\right)\\ &= \langle \mathrm{grad}E, \phi'(t)\rangle_H.\end{aligned}$$

In the following, we will see the importance of the concepts of variational derivatives in the theory of variations, where the significance of using the spaces L^2 or H^{-1} can be applied to the physics of a non-conserved and conserved thermodynamic quantity.

2.3.2. Energy dissipation and gradient flow

We consider a thermodynamic system out of equilibrium in Ω and suppose the system is adiabatic, i.e there is no heat flux or flux of the energy across $\partial\Omega$. According to the second law of thermodynamics, the entropy production or rate of dissipation Π within this system is non-decreasing, hence, we have

$$\Pi \geq 0.$$

The equal sign holds if the system is reversible and the greater-than sign holds if the system irreversible. Since we can write the time derivative of the overall energy of a thermodynamic quantity $\phi(t)$ [59] as

$$\frac{\mathrm{d}}{\mathrm{dt}} E(\phi(t)) = -\Pi,$$

it clearly follows that

$$\frac{\mathrm{d}}{\mathrm{dt}} E(\phi(t)) = \langle \mathrm{grad} E, \phi'(t) \rangle_H \leq 0, \tag{2.1}$$

where we implicitly assume the temperature to be constant. Moreover, the gradient flow is given by

$$\phi'(t) = -\gamma \mathrm{grad} E, \tag{2.2}$$

for $t > 0$ and $\phi(0) = \phi^0 \in H$. With $\mathrm{grad}E$ being the variational derivative in L^2 we have

$$\phi'(t) = -\gamma \frac{\delta E}{\delta \phi}, \tag{2.3}$$

which we call L^2-gradient flow, and with $\mathrm{grad}E$ being the variational derivative in H^{-1} we have

$$\phi'(t) = \gamma \Delta \frac{\delta E}{\delta \phi}, \tag{2.4}$$

which we call H^{-1}-gradient flow. From a physical point of view, $\mathrm{grad}E$ is the force pushing the system toward its equilibrium, which is the state with the minimal energy where $\mathrm{grad}E = 0$. Furthermore, the flux $\phi'(t)$ is represented as a linear relation to $\mathrm{grad}E$, which is consistent to the linear response theory of Onsager [197] for systems close to equilibrium. The parameter $\gamma > 0$ is a phenomenological coefficient that is not known a priori. Inserting eq. (2.2) in eq. (2.1) gives

$$\frac{\mathrm{d}}{\mathrm{dt}} E(\phi(t)) = \langle \mathrm{grad} E, \phi'(t) \rangle_H = -\gamma \langle \mathrm{grad} E, \mathrm{grad} E \rangle_H \leq 0$$

and shows that the gradient flow is consistent to the second law of thermodynamics. In fact, choosing the negative variational derivative that points in the direction of the deepest descent of the energy is an efficient way for minimization procedures. Moreover, the H^{-1}-gradient flow is volume preserving, i.e

$$\frac{\mathrm{d}}{\mathrm{dt}} \int_\Omega \phi \, \mathrm{d}\mathbf{x} = 0. \tag{2.5}$$

We can easily verify this if we multiply eq. (2.4) with a constant test function $\psi = 1$ and integrate over the domain Ω:

$$\int_\Omega \psi \partial_t \phi dx = \gamma \int_\Omega \psi \Delta \frac{\delta E}{\delta \phi} \, \mathrm{d}\mathbf{x}.$$

Partial integration and applying homogeneous Neumann boundary conditions for the variation gives

$$\int_\Omega \psi \partial_t \phi dx = -\gamma \int_\Omega \nabla \psi \cdot \nabla \frac{\delta E}{\delta \phi} \, \mathrm{d}\mathbf{x},$$

and for constant ψ we have eq. (2.5).

Now, we consider a system with several thermodynamic quantities $\phi_1, \ldots, \phi_n$. Accordingly, the time derivative of the energy is given by

$$\frac{\mathrm{d}}{\mathrm{dt}} E(\phi_1(t), \ldots, \phi_n(t)) = \sum_{i=1}^{n} \int_\Omega \frac{\delta E}{\delta \phi_i} \phi_i'(t) \, \mathrm{d}\mathbf{x}, \tag{2.6}$$

where we applied the L^2-gradient flow. The linear response theory allows us to express the fluxes by a linear combination of all thermodynamics forces $\frac{\delta E}{\delta \phi_j}$. This can be understood as generalized gradient flow given by

$$\phi_i'(t) = -\sum_{j=1}^{n} \alpha_{ij} \frac{\delta E}{\delta \phi_j}, \tag{2.7}$$

in the L^2 sense. Here α_{ij}, $i, j = 1, \ldots, n$ denote the Onsager coefficients that are phenomenological coefficients, which are not known a priori but can be determined from a knowledge of the microscopic properties of the system. All non-diagonal elements describe the coupling between each thermodynamic quantity, which can either be dissipative or reactive. Inserting the fluxes eq. (2.7) into the time derivative eq. (2.6) gives

$$\frac{\mathrm{d}}{\mathrm{dt}} E(\phi_1(t), \ldots, \phi_n(t)) = -\sum_{i=1}^{n} \sum_{j=1}^{n} \alpha_{ij} \int_\Omega \frac{\delta E}{\delta \phi_i} \frac{\delta E}{\delta \phi_j} \, \mathrm{d}\mathbf{x}. \tag{2.8}$$

It was shown by Onsager that α_{ij} underlie the following relations for $i \neq j$:

$$\alpha_{ij}^r = -\alpha_{ji}^r, \qquad \text{if the coupling is reactive,} \tag{2.9}$$

$$\alpha_{ij}^d = \alpha_{ji}^d, \qquad \text{if the coupling is dissipative,} \tag{2.10}$$

where a reactive coupling as well as a dissipative coupling are again identified if $\phi_i'(t)$

and $\frac{\delta E}{\delta \phi_j}$ have the same and the opposite time reversal signature, respectively, see [59] for further explanations. Rewriting the time derivative gives

$$\begin{aligned}\frac{\mathrm{d}}{\mathrm{dt}}E(\phi_1(t),\dots,\phi_n(t)) &= -\sum_{i=1}^{n}\sum_{j=1}^{n}\alpha_{ij}^{r}\int_\Omega \frac{\delta E}{\delta\phi_i}\frac{\delta E}{\delta\phi_j}\,\mathrm{d}\mathbf{x} - \sum_{k=1}^{n}\sum_{l=1}^{n}\alpha_{kl}^{d}\int_\Omega \frac{\delta E}{\delta\phi_k}\frac{\delta E}{\delta\phi_l}\,\mathrm{d}\mathbf{x}\\ &= -\sum_{i=2}^{n}\sum_{j=1}^{i-1}(\alpha_{ij}^{r}+\alpha_{jr}^{r})\int_\Omega \frac{\delta E}{\delta\phi_i}\frac{\delta E}{\delta\phi_j}\,\mathrm{d}\mathbf{x} - \sum_{k=1}^{n}\sum_{l=1}^{n}\alpha_{kl}^{d}\int_\Omega \frac{\delta E}{\delta\phi_k}\frac{\delta E}{\delta\phi_l}\,\mathrm{d}\mathbf{x},\end{aligned}$$

using eq. (2.9) yields

$$\frac{\mathrm{d}}{\mathrm{dt}}E(\phi_1(t),\dots,\phi_n(t)) = -\sum_{k=1}^{n}\sum_{l=1}^{n}\alpha_{kl}^{d}\int_\Omega \frac{\delta E}{\delta\phi_k}\frac{\delta E}{\delta\phi_l}\,\mathrm{d}\mathbf{x} \le 0, \tag{2.11}$$

which imposes that the Onsager matrix α^d has to be positive semi-definite. These results show that only the dissipative coupling are responsible for the energy decay. In contrast, the reactive couplings transfer the energy from one quantity into another one.

A simple example shows how we derive partial differential equation using a gradient flow. We consider a thermodynamic quantity, say the temperature T, with its given energy functional

$$E(T(t)) = \frac{1}{2}\int_\Omega |\nabla T|^2\,\mathrm{d}\mathbf{x},$$

which tries to minimize the transition of T within the system. Applying a L^2-gradient flow to E we have

$$\frac{\delta E}{\delta T} = -\Delta T$$

and the evolution equation reads, finally,

$$\partial_t T = \gamma\Delta T \qquad \text{in } \Omega,$$

with initial conditions $T(t=0)=T_0$ and zero flux boundary conditions. This PDE is known as the heat equation and is usually derived using the constraints of mass conservation and applying Fick's law. Thus, γ is denoted as the thermal diffusivity.

2.4. Phase field modeling

In this thesis, we consider various free boundary problems that are solved with a diffuse interface method, also known as phase field method. So far, there have been developed various numerical methods to solve free boundary problems. Examples are level set methods, front tracking methods, volume-of-fluid methods and immersed boundary methods. The idea of diffuse interface methods is that the surface is approximated by a

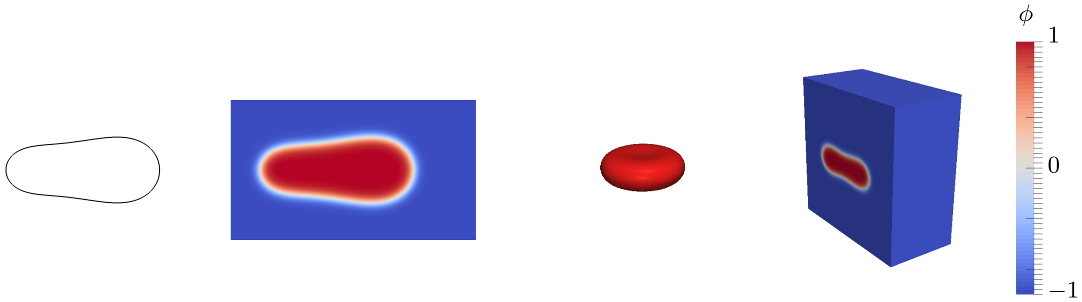

Figure 2.2. – diffuse interface approximation of a 1D (left) and a 2D surface (right)

smooth phase field function $\phi := \phi(t, \mathbf{x}) : I \times \Omega \to \mathbb{R}$ defined as

$$\phi(t, \mathbf{x}) := \tanh\left(\frac{r(t, \mathbf{x})}{\sqrt{2}\varepsilon}\right), \tag{2.12}$$

where $r(t, \mathbf{x}) : I \times \Omega \to \mathbb{R}$ is a signed-distance function assigning each $\mathbf{x} \in \Omega$ its shortest distance to Γ. We pick r such that $\Omega_1 := \{\mathbf{x} : \phi(t, \mathbf{x}) \approx 1\}$ and $\Omega_0 := \{\mathbf{x} : \phi(t, \mathbf{x}) \approx -1\}$. Because ϕ is continuous, we have to smooth out the transition of ϕ between these subdomains characterized by the interface width parameter ε. For small ε the transition becomes sharper and for bigger ε the interface is more smoothed out. Thus, Γ is implicitly defined by the zero level-set of ϕ i.e. $\Gamma(t) := \{\mathbf{x} : \phi(t, \mathbf{x}) = 0\}$. Fig. 2.2 shows how $\Gamma \subset \mathbb{R}$ (left) and $\Gamma \subset \mathbb{R}^2$ (right) is approximated by ϕ. As a result of the diffuse interface method, the problem is reformulated in a higher dimension. Furthermore, the interfacial width ε has to be chosen sufficiently small so that the consistency between the computed results based on the diffuse interface models and that based on the sharp interface descriptions can be numerically confirmed. However, diffuse interface models have many advantages. For instance, as we have seen in the further section, we can define our order parameter ϕ as a thermodynamic variable and can construct numerical methods that are a priori thermodynamically consistent. We furthermore can easily deal with topological changes and guarantee mass conservation. Moreover, it is straightforward to couple additional equations and we are able to solve those equations with a standard finite element toolbox. Within the diffuse interface description, we are able to recover some basic features of the surface:

$$\begin{aligned}
\mathbf{n} &= -\frac{\nabla\phi}{|\nabla\phi|} && \text{(normal vector)},\\
H &= \nabla \cdot \left(-\frac{\nabla\phi}{|\nabla\phi|}\right) && \text{(mean curvature)},\\
V &= \frac{\partial_t\phi}{|\nabla\phi|} && \text{(normal velocity)}.
\end{aligned}$$

We can further reformulate the characteristic function χ_{Ω_1} for Ω_1 defined as

$$\chi_{\Omega_1} \begin{cases} 1 & \text{in } \Omega_1, \\ 0 & \text{otherwise}, \end{cases} \tag{2.13}$$

within the diffuse interface context:

$$\tilde{\phi} = \frac{1}{2}(\phi + 1). \tag{2.14}$$

In addition, the surface delta function δ_Γ can be approximated by

$$\delta_\phi := \frac{\varepsilon}{2}|\nabla\phi|^2 + \frac{1}{4\varepsilon}(\phi^2 - 1)^2 \to s_\delta \delta_\Gamma, \tag{2.15}$$

$$\delta_\phi := \varepsilon|\nabla\phi|^2 \to s_\delta \delta_\Gamma, \tag{2.16}$$

$$\delta_\phi := \frac{1}{\varepsilon}(\phi^2 - 1)^2 \to 2 s_\delta \delta_\Gamma, \tag{2.17}$$

with a scaling parameter $s_\delta = \frac{2\sqrt{2}}{3}$. Hence, the length/area of Γ can be calculated by $\int_\Gamma \mathrm{d}s \approx \int_\Omega s_\delta \delta_\phi \, \mathrm{d}\mathbf{x}$. The projection operator $\mathbf{P}_\Gamma$ can also be translated and written as

$$\mathbf{P}_\phi = \mathbf{I} - \frac{\nabla\phi}{|\nabla\phi|} \otimes \frac{\nabla\phi}{|\nabla\phi|}. \tag{2.18}$$

For the evolution of ϕ, we presume, if not stated otherwise, the following Dirichlet boundary condition

$$\phi(t, \mathbf{x}) = -1 \qquad \text{on } I \times \partial\Omega, \tag{2.19}$$

which neglects any contact of Γ with $\partial\Omega$.

2.5. Surface energies

From a mathematical point of view, surface energies are functionals $E : \Gamma \to \mathbb{R}$. They can serve as basis for geometric evolution equations that describe the evolution of a surface minimizing this particular energy. Several physical phenomena follow those rules: a water droplet minimizes its surface area and a biomembrane minimizes its Willmore or Helfrich energy.

2.5.1. Surface area and tension energy

We first consider the surface area (energy)

$$E(\Gamma) = \int_\Gamma \mathrm{d}s, \tag{2.20}$$

and its variation given by

$$\frac{\delta E}{\delta \Gamma} \cdot \mathbf{n} = H, \tag{2.21}$$

is called mean curvature flow. The minimum, or critical point of E, is reached if the mean curvature flow vanishes i.e.$\frac{\delta E}{\delta \Gamma} \cdot \mathbf{n} = 0$. For the corresponding phase field calculus [67] the Cahn-Hilliard energy introduced by Cahn and Hilliard [39] is

$$\mathcal{E}_{CH}(\phi) = \int_\Omega \frac{\varepsilon}{2}|\nabla \phi|^2 + \frac{1}{\varepsilon} W(\phi)\, \mathrm{d}\mathbf{x}, \tag{2.22}$$

with $W(\phi)$ a double well potential defined as

$$W(\phi) = \frac{1}{4}(\phi^2 - 1)^2.$$

In this particular shape, $W(\phi)$ adopts its minimum $W(\phi) = 0$ for $\phi = -1$ and $\phi = 1$. The double well penalizes any mixing of the two phases and holds the phase field in the values -1 and 1 while the first term accounts for the fact that gradients in the phase field are energetically unfavorable. It has been shown that $\mathcal{E}_{CH}(\phi) \to \frac{2\sqrt{2}}{3} E(\Gamma)$ as $\varepsilon \to 0$ in the sense of Γ-convergence [38, 95, 188]. Its variation

$$\frac{\delta \mathcal{E}_{CH}}{\delta \phi} = -\varepsilon \Delta \phi + \frac{1}{\varepsilon} W'(\phi), \tag{2.23}$$

with $W'(\phi) = (\phi^2 - 1)\phi$ is then called diffuse mean curvature flow and converges as $\frac{\delta \mathcal{E}_{CH}}{\delta \phi} \to \sqrt{2}\frac{\delta E}{\delta \Gamma}\mathbf{n}$ for $\phi = 0$ as $\varepsilon \to 0$, see [215]. Adopting the L^2-gradient flow to the Cahn-Hilliard energy eq. (2.20) gives

$$\partial_t \phi = -\gamma(-\varepsilon \Delta \phi + \frac{1}{\varepsilon} W'(\phi)) \qquad \text{in } I \times \Omega, \tag{2.24}$$

which is called Allen-Cahn equation that describes order–disorder kinetics or so-called Model-A dynamics of a non-conserved variable. These dynamics are slightly different to the H^{-1}-gradient flow

$$\partial_t \phi = \nabla \cdot \left(\gamma \nabla(-\varepsilon \Delta \phi + \frac{1}{\varepsilon} W'(\phi)) \right) \qquad \text{in } I \times \Omega, \tag{2.25}$$

which is known as Cahn-Hilliard equation that can be used to describe the kinetics of spinodal decomposition and it is also called Model-B dynamics of a conserved variable. Since ϕ is conserved, the evolution of the phase field has changed. In case of a constant mobility, it has been proved that the evolution of $\phi = 0$ converges to the Mullins-Sekerka model, which is also called the Hele-Shaw model with surface tension [13, 201]. For a phase field depended mobility $\gamma(\phi) = 1 - \phi^2$ Cahn et al. [40] showed by formal asymptotics that the zero level set of the phase field follows the law of the surface diffusion flow i.e.

$$V = \Delta_\Gamma H.$$

The Cahn-Hilliard equation is a fourth order equation. Sometimes it might be favored, due to computational reasons, to extend the second order Allen-Cahn equation by a Lagrange multiplier λ_{volume} to preserve to volume:

$$\partial_t \phi = -\gamma(-\varepsilon\Delta\phi + \frac{1}{\varepsilon}W'(\phi) + \lambda_{volume}) \qquad \text{in } I \times \Omega, \tag{2.26}$$

which is the so called non-local Ginzburg–Landau equation. For the derivation of λ_{volume} we integrate eq. (2.26) over Ω

$$\int_\Omega \partial_t \phi \,\mathrm{d}\mathbf{x} = -\gamma(-\varepsilon \int_\Omega \Delta\phi \,\mathrm{d}\mathbf{x} + \frac{1}{\varepsilon}\int_\Omega W'(\phi)\,\mathrm{d}\mathbf{x} + |\Omega|\lambda_{volume}).$$

The first term on the left-hand side vanishes due to our assumption. Moreover, we can show that the first term on the right-hand side also vanishes and we arrive at

$$\lambda_{volume} = -\frac{1}{|\Omega|}\frac{1}{\varepsilon}\int_\Omega W'(\phi)\,\mathrm{d}\mathbf{x}. \tag{2.27}$$

In physical applications, the surface area energy can be used to describe the dynamics of a surface under the influence of a surface tension σ. The surface tension energy, thus, reads

$$E_{ST}(\Gamma) = \int_\Gamma \sigma \,\mathrm{ds} \tag{2.28}$$

and within the diffuse interface context

$$\mathcal{E}_{ST}(\phi) := \sigma\mathcal{E}_{CH}(\phi) = \int_\Omega \sigma\left(\frac{\varepsilon}{2}|\nabla\phi|^2 + \frac{1}{\varepsilon}W(\phi)\right)\,\mathrm{d}\mathbf{x}. \tag{2.29}$$

2.5.2. Willmore energy

The Willmore energy [260] is given by

$$E(\Gamma) = \int_\Gamma H^2 \,\mathrm{ds}, \tag{2.30}$$

with H denoting the mean curvature defined as $H = \frac{1}{2}(k_1 + k_2)$, where k_1 and k_2 denote the principle curvatures. As a fundamental topic in differential geometry, the theory of minimal surfaces, the Willmore energy and its the variational problem is of basic interest. Surfaces minimizing the Willmore energy such that

$$\frac{\delta E}{\delta \Gamma} \cdot \mathbf{n} = 0 \tag{2.31}$$

holds, are called critical points of the Willmore energy or Willmore surfaces. As proved by Willmore, round spheres have the least possible Willmore energy of all compact surfaces in $\mathbb{R}^3$ with $E(\Gamma) = 4\pi$. For surfaces with genus one, the Willmore surface is a torus with $E(\Gamma) = 2\pi^2$. The Willmore flow can be specified by

$$\frac{\delta E}{\delta \Gamma} \cdot \mathbf{n} = \Delta_\Gamma H + 2H(H^2 - K),$$

with the Gaussian curvature $K = k_1 k_2$. As already mentioned, the round sphere is a critical surface because we can show

$$\frac{\delta E}{\delta \Gamma} \cdot \mathbf{n} = \Delta_\Gamma H + 2H(H^2 - K) = \frac{2}{r}\left(\left(\frac{1}{r}\right)^2 - \frac{1}{r^2}\right) = 0.$$

The evolution of Γ can differ depending on the dimension. A circle in 2D cannot fulfill eq. (2.31):

$$\frac{\delta E}{\delta \Gamma} \cdot \mathbf{n} = \frac{2}{r}\left(\left(\frac{1}{r}\right)^2 - \frac{1}{r}\right) \neq 0.$$

The Willmore energy can be reformulated within the phase field calculus as

$$\mathcal{E}(\phi) = \frac{1}{2\varepsilon}\int_\Omega \left(\varepsilon\Delta\phi - \frac{1}{\varepsilon}W'(\phi)\right)^2 \mathrm{d}\mathbf{x},$$

which has been derived by Du et al. [72] and was comprehensively discussed in the author's further publications. It has been shown in [74, 255] by asymptotic analysis that $\mathcal{E}(\phi) \to \frac{4\sqrt{2}}{3}E(\Gamma)$ if $\varepsilon \to 0$. Its variation is given by

$$\begin{aligned}\frac{\delta \mathcal{E}}{\delta \phi} &= -\Delta\mu + \frac{1}{\varepsilon^2}W''(\phi)\mu,\\ \mu &= -\varepsilon\Delta\phi + \frac{1}{\varepsilon}W'(\phi),\end{aligned}$$

with $W'(\phi) = (\phi^2 - 1)\phi$ and $W''(\phi) = 3\phi^2 - 1$ and analog to eq. (2.24) and eq. (2.25), we can construct the evolution equations for a non-conserved or conserved Willmore flow, respectively.

2.6. Continuity equations on moving domains

In the further section, we discuss continuity equations for a microscopic quantity and its concentration $c(t, \mathbf{x})$. The quantity c is advected by a velocity field, and accordingly time derivative describing the change of c along the velocity field or stream line reads

$$\frac{\mathrm{D}}{\mathrm{Dt}}c(t, (x_1(t), x_2(t), x_3(t))^\top) = \frac{\partial c}{\partial t} + \frac{\partial c}{\partial x_1}\frac{\partial x_1}{\partial t} + \frac{\partial c}{\partial x_2}\frac{\partial x_2}{\partial t} + \frac{\partial c}{\partial x_3}\frac{\partial x_3}{\partial t} = \frac{\partial c}{\partial t} + \mathbf{v} \cdot \nabla c,$$

with $v_i = \frac{\partial x_i}{\partial t}$, $i = 1, 2, 3$ is called material derivative.

2.6.1. Bulk equation

We consider the domain $\Omega_1(t)$ to be time-dependent. Then, the mass conservation equation for the bulk concentration C reads

$$\frac{\mathrm{D}C}{\mathrm{Dt}} + C\nabla \cdot \mathbf{v} = D_C \Delta C \qquad \text{in } I \times \Omega_1, \tag{2.32}$$

$$\nabla C \cdot \mathbf{n} = j \qquad \text{on } I \times \Gamma, \tag{2.33}$$

with initial condition $C(t, \mathbf{x}) = C^0(\mathbf{x})$ for $t = 0$ and $\mathbf{x} \in \Omega_1$, D_C a bulk diffusion coefficient and j a flux. eq. (2.32) can be rewritten to

$$\partial_t C + \nabla \cdot (\mathbf{v}C) = D_C \Delta C \qquad \text{in } I \times \Omega_1, \tag{2.34}$$

and extended to Ω by using the characteristic function χ_{Ω_1} from eq. (2.13) and applying it to eq. (2.32) gives

$$\partial_t(\chi_{\Omega_1} C) + \nabla \cdot (\chi_{\Omega_1} \mathbf{v} C) = D_C \nabla \cdot (\chi_{\Omega_1} \nabla C) + \delta_\Gamma j \qquad \text{in } I \times \Omega \tag{2.35}$$

in a sharp interface formulation, where we also extended C to Ω. Within the diffuse interface context, we approximate χ_{Ω_1} by $\tilde{\phi}$, eq. (2.14). Li et al. [153] have shown by matched asymptotic analysis that the reformulated eq. (2.35) converges to eq. (2.34) as the interface thickness, represented by ε, goes to zero. Additional boundary conditions on Γ are treated by adding a lower order term to eq. (2.35), see [153]. Accordingly, we have

$$\partial_t(\tilde{\phi} C) + \nabla \cdot (\tilde{\phi} \mathbf{v} C) = D_C \nabla \cdot (\tilde{\phi} \nabla C) + |\nabla \tilde{\phi}| j \qquad \text{in } I \times \Omega, \tag{2.36}$$

where $|\nabla \tilde{\phi}| \approx \delta_\Gamma$.

2.6.2. Surface equation

PDEs on surfaces are off broad interest offering a large variety of applications in science. The fundamental principle of mass conservation can also be formulated on a surface that can additionally change in time. We refer to the work of Cermelli et al. [50] for a brief introduction to this topic. However, the numerical treatment of those problems are challenging and still in focus of current research. Here, we give an overview of a mass conservation equation and a description for a suitable numerical treatment. We consider the time-dependent surface $\Gamma(t)$ and a concentration c fulfilling the mass conservation equation

$$\frac{\mathrm{D}c}{\mathrm{Dt}} + c\nabla_\Gamma \cdot \mathbf{v} = d_c \Delta_\Gamma c \qquad \text{on } I \times \Gamma, \tag{2.37}$$

with d_c a surface diffusion coefficient and an appropriate initial condition $c(t, \mathbf{x}) = c^0(\mathbf{x})$ for $t = 0$ and $\mathbf{x} \in \Gamma$. Decomposing the advective term in its normal and tangential part, with $\mathbf{I} = \mathbf{P}_\Gamma + \mathbf{n} \otimes \mathbf{n}$ gives

$$\begin{aligned}\mathbf{v} \cdot (\mathbf{I} \cdot \nabla c) &= \mathbf{v} \cdot (\mathbf{P}_\Gamma + \mathbf{n} \otimes \mathbf{n}) \nabla c \\ &= \mathbf{v} \cdot \mathbf{P}_\Gamma \nabla c + \mathbf{v} \cdot \mathbf{n} \otimes \mathbf{n} \cdot \nabla c \\ &= \mathbf{v} \cdot \nabla_\Gamma c + \mathbf{v} \cdot \mathbf{n} \, \nabla c \cdot \mathbf{n},\end{aligned}$$

where we split up the gradient in its tangential and normal part. Inserting in eq. (2.37) gives

$$\partial_t c + \nabla_\Gamma \cdot (\mathbf{v} c) + V \nabla c \cdot \mathbf{n} = d_c \Delta_\Gamma c \qquad \text{on } I \times \Gamma,$$

with $\mathbf{v} = V\mathbf{n} + \mathbf{T}$, where V is the normal velocity and $\mathbf{T}$ is the tangential velocity. A useful assumption is to extend c away from Γ to be constant in normal direction i.e $\nabla c \cdot \mathbf{n} = 0$. Accordingly, we arrive at

$$\partial_t c + \nabla_\Gamma \cdot (\mathbf{v} c) = d_c \Delta_\Gamma c \qquad \text{on } I \times \Gamma, \tag{2.38}$$

which we can numerically treat by using the diffuse domain approach. A numerical approach with surface finite elements is specified in [78, 81] and a diffuse interface method for an evolving surface Γ, using a fixed Eulerian mesh, is proposed in [79, 80, 83, 86]. We focus on the latter approach, extend c to Ω, apply the surface delta function δ_Γ and obtain the extension of (2.38) to the whole domain:

$$\partial_t(\delta_\Gamma c) + \nabla \cdot (\delta_\Gamma \mathbf{v} c) = d_c \nabla \cdot (\delta_\Gamma \nabla c) \qquad \text{in } I \times \Omega. \tag{2.39}$$

In the diffuse interface context we might use $\delta_\Gamma \approx |\nabla \phi|$. Rätz and Voigt [210] showed that eq. (2.39) converges to eq. (2.38) as $\varepsilon \to 0$ for a stationary surface. This was extended to a moving surface in [238]. Other publications applying this method are e.g. [9, 209, 211, 238].

2.6.3. Bulk-surface-coupling

Combining a mass conservation equation on the surface and within the bulk by a flux boundary condition yields a coupled bulk surface system given by

$$\partial_t C + \nabla \cdot (\mathbf{v} C) = D_C \Delta C \qquad \text{in } I \times \Omega_1, \tag{2.40}$$

$$D_C \nabla C \cdot \mathbf{n} = -j \qquad \text{on } I \times \Gamma, \tag{2.41}$$

$$\partial_t c + \nabla_\Gamma \cdot (\mathbf{v} c) = d_c \Delta_\Gamma c + j \qquad \text{on } I \times \Gamma, \tag{2.42}$$

which satisfies the conservation of both concentrations

$$\frac{\mathrm{D}}{\mathrm{Dt}}\left(\int_{\Omega_1} C \,\mathrm{d}\mathbf{x} + \int_{\Gamma} c \,\mathrm{ds}\right) = 0. \tag{2.43}$$

This can be shown by multiplying eq. (2.40) with an appropriate test function ψ, integrating over Ω_1 and setting $\mathbf{v} = \mathbf{0}$ for simplicity. Hence, we have

$$\int_{\Omega_1} \partial_t C \psi \,\mathrm{d}\mathbf{x} = D_C \int_{\Omega_1} \Delta C \psi \,\mathrm{d}\mathbf{x}.$$

Now, partial integration gives

$$\int_{\Omega_1} \partial_t C \psi \,\mathrm{d}\mathbf{x} = -D_C \int_{\Omega_1} \nabla c \cdot \nabla \psi \,\mathrm{d}\mathbf{x} + D_C \int_{\Gamma} \nabla C \cdot \mathbf{n} \psi \,\mathrm{ds}$$

and an insertion of the boundary condition eq. (2.41) and picking $\psi = 1$ lead to

$$\int_{\Omega_1} \partial_t C \,\mathrm{d}\mathbf{x} = -\int_{\Gamma} j \,\mathrm{ds}.$$

If we treat the surface eq. (2.40) similarly, we have $\int_\Gamma \partial_t c \,\mathrm{ds} = \int_\Gamma j \,\mathrm{ds}$, which is clear as we restricted any inflow and outflow to j and diffusion and advection within Γ and Ω_1 does not change the mass. Putting the last two equations together, we arrive at

$$\int_{\Omega_1} \partial_t C \,\mathrm{d}\mathbf{x} + \int_{\Gamma} \partial_t c \,\mathrm{ds} = 0,$$

shifting the time derivative, we arrive at eq. (2.43).

In physical or biological applications, the flux j depends on both concentrations describing adsorption to and desorption from Γ, then we have

$$j = r_a C - r_d c,$$

with parameters r_a and r_d denoting adsorption and desorption, respectively and C being the bulk concentration adjacent to Γ. In specific applications e.g. soluble surfactants, the concentration on Γ may become saturated with c_∞ the maximal concentration and the adsorption has to vanish:

$$j = r_a C (c_\infty - c) - r_d c. \tag{2.44}$$

To numerically solve this system, we reformulate it within the diffuse interface context as

$$\partial_t(\tilde{\phi} C) + \nabla \cdot (\tilde{\phi} \mathbf{v} C) = D_C \nabla \cdot (\tilde{\phi} \nabla C) + |\nabla \tilde{\phi}| j \qquad \text{in } I \times \Omega, \tag{2.45}$$

$$\partial_t(|\nabla \phi| c) + \nabla_\Gamma \cdot (|\nabla \phi| \mathbf{v} c) = d_c \nabla \cdot (|\nabla \phi| \nabla c) + |\nabla \phi| j \qquad \text{in } I \times \Omega, \tag{2.46}$$

and it was shown by Teigen et al. [238] that the diffuse interface approach matches the sharp interface approach as $\varepsilon \to 0$.

2.7. Two-Phase flow

The flow field of an isothermal, Newtonian and incompressible fluid can be described by the Navier-Stokes equation. We consider two immiscible phases denoted by Ω_i, with $i = 0, 1$ with densities ρ_i and viscosities η_i. In each phase, the conservation of momentum and mass holds yielding in two separate Navier-Stokes equations, for $i = 0, 1$ we have

$$\rho_i(\partial_t \mathbf{v} + (\mathbf{v} \cdot \nabla)\mathbf{v}) = \nabla \cdot \mathbf{S}_i + \mathbf{F}_i \qquad \text{in } I \times \Omega_i, \tag{2.47}$$

$$\nabla \cdot \mathbf{v} = 0 \qquad \text{in } \Omega_i, \tag{2.48}$$

where $\mathbf{F}_i$ denotes a body force or force density, e.g. $\mathbf{F}_i = (0, \rho_i g)^\top$ and

$$\mathbf{S}_i = -p\mathbf{I} + \eta_i \mathbf{D} \tag{2.49}$$

is the stress tensor, which is symmetric and describes the change of the fluid elements with respect to normal stresses and shear stresses, respectively. Here, p denotes the pressure and $\mathbf{D} = \frac{1}{2}(\nabla\mathbf{v} + \nabla\mathbf{v}^\top)$ is also known as the strain rate tensor. The interface $\Gamma(t)$ separating the different phase is determined by several interfacial conditions. As the two phase are viscous and no phase transitions occur, we have

$$[\mathbf{v}]_\Gamma = 0, \tag{2.50}$$

which means that the velocity is continuous across $\Gamma(t)$. The jump condition can be expressed by $[f]_\Gamma = f_0 - f_1$ or more formal $[f]_\Gamma = [f]_\Gamma(\mathbf{x}) = \lim_{h \to +0} f(\mathbf{x} - h\mathbf{n}_1(\mathbf{x})) - f(\mathbf{x} + h\mathbf{n}_1(\mathbf{x}))$ for all $\mathbf{x}$ on Γ, with $\mathbf{n}_1$ being the normal vector pointing out of Ω_1. Furthermore, we have to take into account the physical behavior of the interface denoted by its interfacial energy. Then, we arrive at

$$[\mathbf{S} \cdot \mathbf{n}]_\Gamma = \frac{\delta E}{\delta \Gamma}. \tag{2.51}$$

If we choose the surface tension energy eq. (2.28), we arrive at

$$[\mathbf{S} \cdot \mathbf{n}]_\Gamma = \sigma H \mathbf{n}, \tag{2.52}$$

which is the jump condition for a simple fluid interface. Picking the Willmore energy scaled with the bending rigidity b_n, we have

$$[\mathbf{S} \cdot \mathbf{n}]_\Gamma = \frac{b_n}{2}(-\Delta_\Gamma H - 2H(H^2 - K)). \tag{2.53}$$

We will later see how this jump condition can be modified by additional Lagrange multipliers for surface area conservation taking the physics of a biomembrane into account. A stretchable membrane can be described by a linear combination of the mean curvature and Willmore flow. For the sake of completeness, we introduce the kinetic energy of a fluid defined as

$$E_{kin}(\mathbf{v}) = \frac{\rho}{2} \int_{\Omega} |\mathbf{v}|^2 \,\mathrm{ds}, \tag{2.54}$$

with $\rho_0 = \rho_1 = const.$

2.8. General diffuse interface approach of a two-phase flow

Hohenberg and Halperin [123] published several models for critical phenomena close to phase changes. The model H, in their nomenclature, describes binary-fluid mixtures i.e. two-phase flows where they combined a Navier-Stokes equation for the fluid flow and a Cahn-Hilliard equation for the phase separation of two conserved phases. Model E, on the other hand, combines fluid flow with an Allen-Cahn equation to describe the dynamics of non-conserved variable. In this section, we generalize both models where the underlying interfacial energy is not specified in order to cover a wide range of physical phenomena. This energy is given in a diffuse interface approach where the interfacial layer has a certain thickness $\sim \varepsilon$. To derive the governing equations, we use an energy variation approach. At first, we consider a thermodynamic system with constant temperature whose overall energy

$$\mathcal{E}(\mathbf{v}, \phi) = \mathcal{E}_{kin}(\mathbf{v}) + \mathcal{E}_S(\phi)$$

is composed by $\mathcal{E}_{kin}$, the kinetic energy of the fluid and $\mathcal{E}_S$, a non specified surface energy depending on ϕ. The order parameter ϕ, on the other hand, can be considered as a non-dimensional concentration of a species within a phase or just as diffuse interface approximation of the surface. According to the seconds law of thermodynamics, see Section 2.3.2, we claim

$$\frac{\mathrm{d}\mathcal{E}}{\mathrm{dt}} = \int_{\Omega} \rho\mathbf{v} \cdot \partial_t \mathbf{v} + \frac{\delta \mathcal{E}_S}{\delta \phi} \partial_t \phi \,\mathrm{d}\mathbf{x} \overset{!}{\leq} 0, \tag{2.55}$$

where we choose $\rho = const.$ The conservation of mass and momentum for the velocity field $\mathbf{v}$ is

$$\rho \partial_t \mathbf{v} = -\rho(\mathbf{v} \cdot \nabla)\mathbf{v} - \nabla p + \nabla \cdot (\eta(\phi)\mathbf{D}) + \mathbf{F} \qquad \text{in } I \times \Omega, \tag{2.56}$$

$$\nabla \cdot \mathbf{v} = 0 \qquad \text{in } \Omega, \tag{2.57}$$

where we now describe the viscosity $\eta(\phi) = \eta_1 \frac{\phi+1}{2} + \eta_0 \frac{\phi-1}{2}$ as an interpolation between the two phases. Furthermore, the conservation of mass for the phase field is

$$\partial_t \phi = -\mathbf{v} \cdot \nabla \phi - \nabla \cdot \mathbf{J} \qquad \text{in } I \times \Omega, \tag{2.58}$$

where $\mathbf{F}$ is a body force and $\mathbf{J}$ is a flux that are both yet unspecified. Now, we plug in eq. (2.56) and eq. (2.58) into the energy derivative eq. (2.55) and determine the unknowns such that the overall free energy decreases:

$$\frac{\mathrm{d}\mathcal{E}}{\mathrm{dt}} = \int_\Omega \mathbf{v} \cdot (-\rho(\mathbf{v} \cdot \nabla)\mathbf{v} - \nabla p + \nabla \cdot (\eta(\phi)\mathbf{D}) + \mathbf{F}) + \frac{\delta \mathcal{E}_S}{\delta \phi}(-\mathbf{v} \cdot \nabla\phi - \nabla \cdot \mathbf{J}) \, \mathrm{d}\mathbf{x}.$$

Using the vector identity

$$(\mathbf{v} \cdot \nabla)\mathbf{v} = \frac{1}{2}\nabla|\mathbf{v}|^2 - \mathbf{v} \times (\nabla \times \mathbf{v}),$$

multiplying with $\mathbf{v}$ and taking into account that $\mathbf{v} \times (\nabla \times \mathbf{v})$ is perpendicular to $\mathbf{v}$ gives

$$\mathbf{v} \cdot (\mathbf{v} \cdot \nabla)\mathbf{v} = \frac{1}{2}\mathbf{v} \cdot \nabla|\mathbf{v}|^2. \tag{2.59}$$

Inserting in eq. (2.55) yields

$$\begin{aligned}\frac{\mathrm{d}\mathcal{E}}{\mathrm{dt}} = \int_\Omega &\mathbf{v} \cdot \left(-\frac{\rho}{2}\nabla|\mathbf{v}|^2 - \nabla p\right) + \mathbf{v} \cdot \nabla \cdot (\eta(\phi)\mathbf{D}) - \frac{\delta \mathcal{E}_S}{\delta \phi}\nabla \cdot \mathbf{J} \\ &+ \mathbf{v} \cdot \left(\mathbf{F} - \frac{\delta \mathcal{E}_S}{\delta \phi}\nabla\phi\right) \mathrm{d}\mathbf{x}.\end{aligned}$$

Now, partial integration, using the incompressibility eq. (2.57) and choosing the body force

$$\mathbf{F} = \frac{\delta \mathcal{E}_S}{\delta \phi}\nabla\phi$$

and the flux given by

$$\nabla \cdot \mathbf{J} = \gamma\frac{\delta \mathcal{E}_S}{\delta \phi},$$

with $\gamma > 0$ the mobility coefficient yield

$$\frac{\mathrm{d}\mathcal{E}}{\mathrm{dt}} = \int_\Omega -\nabla\mathbf{v} : \eta(\phi)\mathbf{D} - \gamma\frac{\delta \mathcal{E}_S}{\delta \phi}^2 \mathrm{d}\mathbf{x},$$

Taking into account that

$$\begin{aligned}\nabla\mathbf{v} : \mathbf{D} &= \mathbf{D} : \frac{\nabla\mathbf{v}}{2} + \mathbf{D} : \frac{\nabla\mathbf{v}}{2} \\ &= \mathbf{D} : \frac{\nabla\mathbf{v}}{2} + \mathbf{D}^\top : \frac{\nabla\mathbf{v}^\top}{2} \\ &= \mathbf{D} : \frac{\nabla\mathbf{v}}{2} + \mathbf{D} : \frac{\nabla\mathbf{v}^\top}{2} \\ &= \mathbf{D} : \mathbf{D},\end{aligned} \tag{2.60}$$

where we used the symmetry of the strain rate tensor $\mathbf{D}$, we end up with

$$\frac{\mathrm{d}\mathcal{E}}{\mathrm{dt}} = \int_\Omega -\eta(\phi)\mathbf{D} : \mathbf{D} - \gamma\frac{\delta\mathcal{E}_S}{\delta\phi}^2 \,\mathrm{d}\mathbf{x} \leq 0, \tag{2.61}$$

which is the energy law of the thermodynamic system. The viscous friction of the fluid and the variation of the surface energy are responsible for the energy dissipation, as $\eta(\phi) > 0$ and $\gamma > 0$. In fact, the unknowns are determined and we arrive at the general diffuse interface approach for a two-phase flow of the non-conserved variable (general model E):

$$\begin{aligned} \rho(\partial_t\mathbf{v} + (\mathbf{v}\cdot\nabla)\mathbf{v}) + \nabla p &= \nabla\cdot(\eta(\phi)\mathbf{D}) + \frac{\delta\mathcal{E}_S}{\delta\phi}\nabla\phi && \text{in } I\times\Omega,\\ \nabla\cdot\mathbf{v} &= 0 && \text{in } \Omega,\\ \partial_t\phi + \mathbf{v}\cdot\nabla\phi &= -\gamma\frac{\delta\mathcal{E}_S}{\delta\phi} && \text{in } I\times\Omega, \end{aligned}$$

with unspecified surface energy $\mathcal{E}_S$. The physical properties of the interface are now represented by the body force term added to the Navier-Stokes equation, which is only nonzero along the interface. The phase field equation advects the interface and uses a regularization term on the right-hand side, which is why we choose $\gamma > 0$ as small as possible. A pure advection equation with $\gamma = 0$ would still fulfill the energy dissipation law, eq. (2.55), however, it was numerically problematic. This system is also used for the dynamics of a conserved phase field, e.g. [76], by applying a Lagrange multiplier or a penalty term for the volume conservation. An advantage is that the phase field equation is two orders smaller than that of a conserved variable (see below), which can prevent numerical complexities. A conserved phase field evolution caused by an H^{-1}-gradient flow considers a flux given as $\mathbf{J} = -\gamma\nabla\frac{\delta\mathcal{E}_S}{\delta\phi}$. Accordingly, the energy dissipation law reads as

$$\frac{\mathrm{d}\mathcal{E}}{\mathrm{dt}} = \int_\Omega -\eta(\phi)\mathbf{D} : \mathbf{D} - \gamma\left|\nabla\frac{\delta\mathcal{E}_S}{\delta\phi}\right|^2 \mathrm{d}\mathbf{x} \leq 0. \tag{2.62}$$

Finally, the system for a general diffuse interface approach for a two-phase flow of a conserved variable (general model H) becomes

$$\begin{aligned} \rho(\partial_t\mathbf{v} + (\mathbf{v}\cdot\nabla)\mathbf{v}) + \nabla p &= \nabla\cdot(\eta(\phi)\mathbf{D}) + \frac{\delta\mathcal{E}_S}{\delta\phi}\nabla\phi && \text{in } I\times\Omega,\\ \nabla\cdot\mathbf{v} &= 0 && \text{in } \Omega,\\ \partial_t\phi + \mathbf{v}\cdot\nabla\phi &= \nabla\cdot\left(\gamma\nabla\frac{\delta\mathcal{E}_S}{\delta\phi}\right) && \text{in } I\times\Omega. \end{aligned}$$

Both systems require initial conditions $\phi(t,\mathbf{x}) = \phi^0(\mathbf{x})$, the initial shape of the two phases as well as $\mathbf{v}(t,\mathbf{x}) = \mathbf{v}^0(\mathbf{x})$ for $t > 0$, $\mathbf{x} \in \Omega$ and additional boundary conditions for ϕ, $\mathbf{v}$ and $\frac{\delta\mathcal{E}_S}{\delta\phi}$.

There has been done a lot of work considering a simple fluid interface applying the surface tension energy eq. (2.29), see [2, 17, 36, 127, 155, 157, 232, 264]. The governing equations are given by

$$\begin{aligned}
\rho(\partial_t \mathbf{v} + (\mathbf{v} \cdot \nabla)\mathbf{v}) + \nabla p &= \nabla \cdot (\eta(\phi)\mathbf{D}) + \frac{\delta \mathcal{E}_S}{\delta \phi}\nabla\phi && \text{in } I \times \Omega,\\
\nabla \cdot \mathbf{v} &= 0 && \text{in } \Omega,\\
\partial_t \phi + \mathbf{v} \cdot \nabla\phi &= \nabla \cdot \left(\gamma(\phi)\nabla\frac{\delta \mathcal{E}_S}{\delta \phi}\right) && \text{in } I \times \Omega,\\
\frac{\delta \mathcal{E}_S}{\delta \phi} &= \frac{3\sigma}{2\sqrt{2}}\left(-\varepsilon\Delta\phi + \frac{1}{\varepsilon}W'(\phi)\right) && \text{in } \Omega,
\end{aligned}$$

with a phase field dependent mobility $\gamma(\phi) = \bar{\gamma}W(\phi)$, $\bar{\gamma} = const.$ and appropriate initial conditions for $\mathbf{v}$ and ϕ and boundary conditions for $t > 0$ and $\mathbf{x} \in \Omega$:

$$\begin{aligned}
\mathbf{v}(t,\mathbf{x}) &= g(t,\mathbf{x}) && \text{(no slip)},\\
\nabla\frac{\delta \mathcal{E}_S}{\delta \phi} \cdot \mathbf{n} &= 0 && \text{(no flux)},\\
\nabla\phi \cdot \mathbf{n} &= \frac{1}{\varepsilon\sqrt{2}}\cos\theta(1-\phi^2) && \text{(contact angle)}.
\end{aligned}$$

That this system is a suitable model to treat two-phase flows has been shown in several benchmark computations [6, 10, 11]. It has been extended to different densities [3, 161] and applied to a diffuse domain approach [7]. These systems have a wide field of application. For instance, the dynamics of the interface has been changed by adding surfactants [239] or colloid particles [8, 9]. For sake of completeness, a thermodynamic consistent model for different densities is now specified below:

$$\begin{aligned}
\rho(\phi)(\partial_t \mathbf{v} + (\mathbf{v} \cdot \nabla)\mathbf{v}) + \nabla p &= \nabla \cdot (\eta(\phi)\mathbf{D}) + \frac{\mathrm{d}\rho}{\mathrm{d}\phi}\gamma(\phi)\nabla\frac{\delta \mathcal{E}_S}{\delta \phi} \cdot \nabla\mathbf{v}\\
&\quad - \frac{\sigma}{\varepsilon}\frac{3}{2\sqrt{2}}\nabla \cdot (\nabla\phi \otimes \nabla\phi) && \text{in } I \times \Omega,\\
\nabla \cdot \mathbf{v} &= 0 && \text{in } \Omega,\\
\partial_t \phi + \mathbf{v} \cdot \nabla\phi &= \nabla \cdot \left(\gamma(\phi)\nabla\frac{\delta \mathcal{E}_S}{\delta \phi}\right) && \text{in } I \times \Omega,\\
\frac{\delta \mathcal{E}_S}{\delta \phi} &= \frac{3\sigma}{2\sqrt{2}}\left(-\varepsilon\Delta\phi + \frac{1}{\varepsilon}W'(\phi)\right) && \text{in } \Omega.
\end{aligned}$$

As already mentioned, we can choose the surface energy depending on the physical problem. If we apply the Helfrich energy eq. (3.4) we can describe the evolution of a closed lipid membrane in an aqueous solution. The corresponding diffuse Navier-Stokes-Helfrich model is developed in Section 3.4.2. We can further influence the physics of the interface by additional Lagrange multipliers or penalty terms to enforce global surface area conservation, see eq. (3.37) or local surface area conservation, see eq. (3.66) or by an additional force term to describe active motion, see eq. (5.7).

Chapter 3

Diffuse interface models for cell morphology based on the Helfrich energy

In order to develop mathematical models that help us to describe and understand biological cells, we need to identify the main features of cells to be captured in our models. Therefore, we first outline the basic components of a cell, its physical interpretation and we further illustrate a general principle to derive mathematical models, see Section 3.1. Depending on the length and time scale as well as the nature of the cell different components of the cell determine its evolution. As a first step within this thesis, we consider the cell membrane to play a fundamental role. This is basically described by the so-called Helfrich energy [121] accounting for the bending physics of the membrane, introduced and discussed in Section 3.2. We consider the whole cell and its surroundings to be a thermodynamic system. The evolution of the cell can then be understood as a minimization procedure of a given energy that, as shown in Section 2.3.2, leads to a free boundary problem. In order to treat such a free boundary problem, we use a diffuse interface approach to develop the governing equations, see Section 2.4 and Section 2.5. For our models we further consider two cases: a non-hydrodynamic evolution where fluid environment is supposed to play a minor role, see Section 3.4.1 and a hydrodynamic two-phase flow model considering the influence of fluid flow in the outside and inside of the cell that is derived in Section 3.4.2. This so-called hydrodynamic diffuse interface Navier-Stokes-Helfrich model serves as our basic approach to describe biological phenomena such as cell motility and collective flow of cells. To account for different properties of the cell, the model is reformulated regarding an inextensibility condition (local surface conservation), Section 3.4.3 and surface tension, Section 3.5. It is further the starting point for the development of the active polar gel model derived in Chapter 6 and for the multi-phase approach for collective motion, see Chapter 7.

3.1. Classification and hydrodynamic approaches for cells

An eukaryotic cell is a highly complex structure consisting of several parts that behave mechanically different. In this section, we give a classification of the constituents of the cell and their physical properties. We further show how we can account for these properties within a continuum formulation of a two-phase flow approach that distinguishes between the cell bulk and the surrounding medium.

The cell bulk mainly comprises the cytoplasm and organelles. The cytoplasm, which typically accounts for 50% of the cell volume, is made up of two components: the cytosol and the cytoskeleton. The cytosol is a fluid structure and encloses organelles such as the nucleus or mitochondria. It further supports the organelles with different molecules that are dissolved in the cytosol. The cytoskeleton, on the other hand, determines the shape of the cell and is also responsible for cell motility [29]. It consists of actin filaments, microtubules and intermediate filaments. For an eukaryotic cell it is common to ignore the nucleus [246, 263] and to represent the interior as viscoelastic bulk material by applying e.g. the Oldroyd-B model [33, 187, 265, 269]. Another approach focuses on streaming effects within the cytosol and considers the cell bulk as a purely viscous fluid with an effective viscosity [105, 229]. In order to account for a more complex behavior of the cell bulk that goes beyond purely viscous or viscoelastic approaches, an active polar gel theory has been used to describe the physics of the actin cytoskeleton [131, 242, 259]. Other models, especially for cell motility, apply a two-phase flow only to the cell bulk and account for the two main components of the cytoplasm: the cytosol and cytoskeleton, see [15, 61] and [51] for a review.

The second phase is the exterior of the cell that is either an extracellular matrix, which is a tissue connecting and supporting the cells (in case of cell motility), or a fluid (in case of red blood cells or vesicles). However, in our approach we always assume a Newtonian fluid.

The interface i.e. the cell membrane separates the interior of a cell from its exterior. It is completely closed, impermeable and gives rise to bending forces described by a Helfrich energy [121], see Section 3.2. The cell membrane is a lipid bilayer and consists of two chains of small lipid proteins where the hydrophilic head points outwards and hydrophobic tail points inwards, see also Fig. 3.1c for an illustration. The cell membrane is an essential element in the development and evolution of cells and its functionality is not restricted to its structural role. It plays a crucial role during interactions of cells and the exchange of several proteins as well as for endocytosis and exocytosis. Moreover, actin filaments form the cell cortex, which is connected to the cell membrane. These filaments are elastic and responsible for membrane elasticity [30, 220]. They further lead to an effective surface tension of the membrane due to the contractility of the filaments

biological property	effective physical interpretation
impermeable membrane	volume conservation
lipid bilayer	bending stiffness
myosin in actin cortex	surface/cortical tension
actin cortex	membrane elasticity
cytoplasm in the bulk	Newtonian fluid
	active polar gel
	viscoelastic material

Table 3.1. – Effective physical interpretation of the components of a general eukaryotic cell

caused by myosin [88]. Therefore, it is also known as cortical tension in the literature. Tab. 3.1 gives a classification of the properties of a general eukaryotic cell and its effective physical interpretation.

However, not every cell has such a complex cell interior. Red blood cells, for instance, lose much of their organelles during their growth in order to obtain space for the binding of hemoglobin. A vesicle is an organelle whose interior completely consists of fluid, see Fig. 3.1c and [226] for a review. Vesicles have been widely used in the literature, see also Section 8, to describe red blood cells as the structure of a red blood cell is much simpler than that of an eukaryotic cell. Moreover, bulk and membrane elasticity can be neglected due to the high deformability of the cytoskeleton of RBCs. Because of the large stretch elasticity of the lipid bilayer, the surface of a vesicle is inextensible (i.e. locally conserved), see Section 3.4.3. Subsequently, Tab. 10.1 in conclusions, Chapter 10 shows the different physical properties that were considered within our models.

Depending on the spatial scale as well as on the time scale that can range anywhere from milliseconds (cell in micro channel) to hours (migrating cell on the substrate), each biological component can become more or less dominant. At long time scales elastic contributions can be neglected since the cell can restore its shape and dissipate stress. However, on short time scale they can become dominant. In our model for cell motility, Chapter 5.2, we therefore neglect membrane elasticity. Moreover, we treat the bulk as a viscous fluid considering streaming effects in the cytoplasm and it can likewise be understood as first order approximation of the viscoelastic properties. In conclusions, Chapter 10, we give a brief outlook to approaches including elastic contributions. In Chapter 6, we choose an approach to account for the elastic behavior of the bulk. Here, the bulk is assumed to be an active polar gel, where the actin filaments considered as small rod-like molecules, so-called liquid crystals, are represented by a continuum formulation of a polarization field. These gels represent an intermediate state of the bulk which exhibits a degree of order that is between that of ordinary liquids and solids and can furthermore exert a distortion stress during their translation. This allows us to describe the active nature of actin-myosin solutions by an additional contractile stress tensor.

To derive mathematical models, we consider the cell as thermodynamic system that

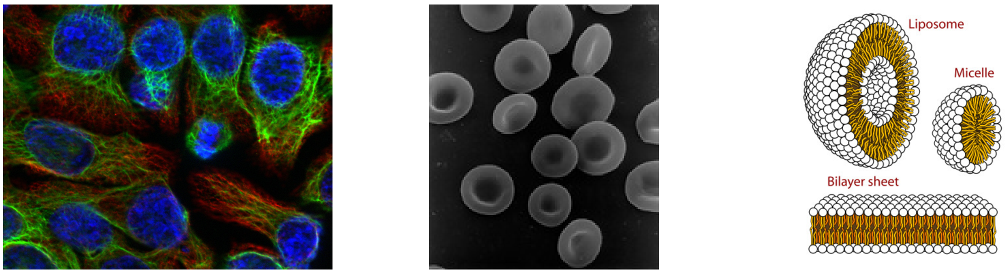

(a) (b) (c)

Figure 3.1. – Different Types of cells - (a) Cytoskeleton and nucleus (blue) of eukaryotic cells (keratinocytes). Shown are the actin filaments (red) and microtubles (green) (Picture self-taken from microscopy) (b) Red blood cells (c) Illustration of a vesicle (liposome) and further structures formed by a lipid bilayer. ((a) self-taken, (b) and (c) licensed under Public Domain via Commons, retrieved from `https://www.wikipedia.org`)

minimizes its energy and dissipates this energy in another state measured by the entropy. It has been shown that a cell membrane minimizes the Helfrich bending energy in order to develop an optimal shape. We extend this energy by additional Lagrange multipliers or penalty terms to conserve surface and volume of the cell, or if the surface conservation is not intended by a surface tension leading to an overall surface energy $E_S(\Gamma)$. Then, neglecting the hydrodynamics, the evolution of the cell can be described by the surface velocity $\mathbf{v}$ and is thus given by

$$\mathbf{v} = -\tilde{\gamma}\frac{\delta E_S}{\delta \Gamma}, \tag{3.1}$$

with $\tilde{\gamma} > 0$, which is consistent with the second law of thermodynamics since the overall energy is decaying in time:

$$\frac{\mathrm{d}E}{\mathrm{dt}} = \int_\Gamma \frac{\delta E}{\delta \Gamma} \cdot \mathbf{v}\,\mathrm{ds} = -\tilde{\gamma}\int_\Gamma \mathbf{v} \cdot \mathbf{v}\,\mathrm{ds} \leq 0.$$

This evolution can be translated to the diffuse interface approach where Γ is now implicitly defined by the zero level set of ϕ, see Section 2.4. Denoting $\mathcal{E}_S$ the diffuse interface formulation of the surface energy, the evolution now reads for $\gamma > 0$

$$\partial_t \phi = -\gamma\frac{\delta \mathcal{E}_S}{\delta \phi}, \tag{3.2}$$

which is the L^2-gradient flow, see eq. (2.3). Within these models the energy is only dissipated by the variation of the surface energy. Here, fluid flow is not considered, which is appropriate if only the stationary state is of interest. These models are therefore called non-hydrodynamic and given by a geometric evolution equation. If the dynamics of the fluid is taken into account, a kinematic force balance at the membrane Γ is posed between the membrane and the hydrodynamic forces

$$[\mathbf{S} \cdot \mathbf{n}]_\Gamma = \frac{\delta E_S}{\delta \Gamma}, \tag{3.3}$$

with the stress tensor $\mathbf{S}$ given in eq. (2.49). We now consider the surrounding medium as well as the cell bulk as viscous Newtonian fluid denoted by the domain $\Omega_0(t)$ and $\Omega_1(t)$, respectively. Then, the evolution given by eq. (3.3) with additional Navier-Stokes equations and interface advection is thermodynamically consistent. To prove this, we thus consider the overall energy

$$E = E_{kin} + E_S$$

and its evolution in time

$$\frac{\mathrm{d}E}{\mathrm{dt}} = \int_{\Omega_0} \rho \mathbf{v} \cdot \frac{\mathrm{D}\mathbf{v}}{\mathrm{Dt}} \,\mathrm{d}\mathbf{x} + \int_{\Omega_1} \rho \mathbf{v} \cdot \frac{\mathrm{D}\mathbf{v}}{\mathrm{Dt}} \,\mathrm{d}\mathbf{x} + \int_\Gamma \frac{\delta E_S}{\delta \Gamma} \cdot \mathbf{v},$$

with $\frac{\mathrm{D}\mathbf{v}}{\mathrm{Dt}}$ denoting the material derivative of $\mathbf{v}$. Using the Navier-Stokes equations $\rho \frac{\mathrm{D}\mathbf{v}}{\mathrm{Dt}} = \nabla \cdot \mathbf{S}_i$, we obtain

$$\begin{aligned}
\frac{\mathrm{d}E}{\mathrm{dt}} &= \int_{\Omega_0} \mathbf{v} \cdot \nabla \cdot \mathbf{S}_0 \,\mathrm{d}\mathbf{x} + \int_{\Omega_1} \mathbf{v} \cdot \nabla \cdot \mathbf{S}_1 \,\mathrm{d}\mathbf{x} + \int_\Gamma \frac{\delta E_S}{\delta \Gamma} \cdot \mathbf{v} \\
&= -\int_{\Omega_0 \cup \Omega_1} \nabla \mathbf{v} : \mathbf{S} \,\mathrm{d}\mathbf{x} + \int_\Gamma \mathbf{v} \cdot (\mathbf{n}_0 \cdot \mathbf{S}_0 + \mathbf{n}_1 \cdot \mathbf{S}_1) + \int_\Gamma \frac{\delta E_S}{\delta \Gamma} \cdot \mathbf{v} \\
&= -\int_{\Omega_0 \cup \Omega_1} \mathbf{D} : \mathbf{D} \,\mathrm{d}\mathbf{x} - \int_\Gamma \mathbf{v} \cdot [\mathbf{S} \cdot \mathbf{n}]_\Gamma + \int_\Gamma \frac{\delta E_S}{\delta \Gamma} \cdot \mathbf{v} \\
&= -\int_{\Omega_0 \cup \Omega_1} \mathbf{D} : \mathbf{D} \,\mathrm{d}\mathbf{x} \leq 0,
\end{aligned}$$

where we performed integration by parts, reformulated the jump condition with $\mathbf{n} := \mathbf{n}_1 = -\mathbf{n}_0$, inserted eq. (3.3), neglected the pressure within $\mathbf{S}_i = -p\mathbf{I} + \eta_i D$ using the incompressibility $\nabla \cdot \mathbf{v} = 0$, and after all applied eq. (2.60). Hence, the energy decreases due solely to viscous dissipation. Within our diffuse interface formulation the energy dissipation is additionally determined by the variation of the surface energy that is used due to the numerical stabilization of the advection of the phase field, see eq. (3.51) and (6.10).

3.2. Helfrich energy

3.2.1. Sharp interface formulation

The theoretical study of the elasticity of biomembranes was first performed by Canham [46], Helfrich [121] and Evans [94]. They tried to explain the specific discocyte shape of a RBC by focusing on the relevant elastic properties of the cell membrane. The main assumption of their approaches is to consider the cell membrane as a two-dimensional manifold embedded in $\mathbb{R}^3$, because the thickness of the cell membrane ($\approx 5\,\text{nm}$) [121] is much smaller than its length ($\sim \mu$m). In addition, they neglected any contribution from the bulk. Helfrich proposed that the cell membrane and its containing lipids undergo three type of strain: stretching, tilt and curvature. However, Helfrich mentioned that only the curvature is responsible for the shape change of the membrane, and accordingly the membrane minimizes the functional given by

$$E_H(\Gamma) = \int_\Gamma b_n(H - H_0)^2 + b_k K\,\mathrm{ds}, \tag{3.4}$$

which we call Helfrich energy, Canham-Helfrich energy or bending energy. To be more precise, Helfrich defined the energy as $E_S(\Gamma) = \int_\Gamma \frac{1}{2} b_n(\tilde{H} - \tilde{H}_0)^2 + b_k K\,\mathrm{ds}$ using the total curvature $\tilde{H} = k_1 + k_2$. We, however, follow the notation of [68, 75]. Here, b_n denotes the bending rigidity, b_k the Gaussian bending rigidity and H_0 the spontaneous curvature reflecting a possible asymmetry of the membrane justified by a different chemical environment on both sides of the lipid layers. It can also be a function of a protein concentration, see e.g. [249]. In this thesis, H_0 is assumed to be spatially homogeneous. For a review of models including spontaneous curvature, we refer to [118, 224, 227]. For our purposes, it is sufficient to suppose that cell membranes do not undergo any topological transitions. Due to the theorem of Gauß-Bonnet, which reads for the previous defined surface Γ as

$$\int_\Gamma K\,\mathrm{ds} = 4\pi(1 - g_e),$$

where g_e is the genus of the surface being e.g. zero for a sphere and one for a torus, the second term in eq. (3.4) is constant for all Γ and can accordingly be neglected. The Helfrich energy becomes

$$E_H(\Gamma) = \int_\Gamma b_n(H - H_0)^2\,\mathrm{ds}, \tag{3.5}$$

its variation is given by

$$\frac{\delta E_H}{\delta \Gamma} \cdot \mathbf{n} = b_n\left(\Delta_\Gamma H + 2H(H^2 - K) + 2KH_0 - 2HH_0^2\right)$$

and the critical point fulfills

$$\Delta_\Gamma H + 2H(H^2 - K) + 2KH_0 - 2HH_0^2 = 0.$$

Additionally, we consider an impermeable membrane, which means that the volume of the cell interior is conserved. It has been observed, that for vesicles the attachment and detachment of lipids on the membrane is hindered [121]. The membrane surface area can therefore be assumed to be constant that can be understood in two different ways: global surface area conservation where $\int_\Gamma \mathrm{ds} = const.$ allows us to stretch or compress surface elements locally and local surface area conservation or inextensibility constraint where local shape changes are forbidden. Here, we consider the lipids within the membrane as fluid moving along the surface with velocity $\mathbf{v}$ and fulfilling the incompressibility condition $\nabla_\Gamma \cdot \mathbf{v} = 0$. In the following, we consider the global surface conservation, but we will describe the treatment of the inextensibility condition later on, see Section 3.4.3.

Finally, we denote the Helfrich minimization problem: find $\Gamma^* \in L$, with $L := \{\Gamma \subset \mathbb{R}^3 : \Gamma \text{ smooth and closed}\}$ with

$$\Gamma^* := \min_{\Gamma \in L} b_n \int_\Gamma (H - H_0)^2 \,\mathrm{ds}, \tag{3.6}$$

subject to the constraints

$$|\Omega_1| := vol(\Gamma) = const. \tag{3.7}$$

$$|\Gamma| := \int_\Gamma \mathrm{ds} = const. \tag{3.8}$$

In summary, the Helfrich energy is an appropriate model to study the shape of cells whose surface is mainly determined by the impermeability, surface area conservation and bending properties of the membrane. It has been successfully used to study the equilibrium shape of cells and comparisons with experiments showed that a minimal surface of this energy reproduces the discocyte shape of a RBC. Although it neglects any elastic or viscous contribution from the cell bulk, it recovers the shape of a red blood cell admissibly, see Fig. 3.2.

For that reason, a lot of studies are based on the minimization of the Helfrich energy. Starting with single-component vesicles [223, 227] over the years more and more complex and fundamental components of cell membranes have been taken into account. These include lipids, proteins and cholesterol and their interplay on the morphology, structure and dynamics of membranes [14, 164, 256]. The coupling of the dynamics with the surrounding fluid has been applied to understand the complex motions and shape changes of RBCs within a flow field, e.g. tank-treading and tumbling motion [102]. Within a low Reynolds number regime, the Stokes limit is valid and various numerical approaches have also been considered in this limit to analyze the tank-treading and tumbling motion [26, 31, 32, 111, 135, 137, 233, 247, 267]. However, in regimes with Reynolds number of order unity or higher the Stokes limit is at least questionable. Modeling approaches that consider also inertial effects have recently been introduced by [12, 144, 219]. Models that consider multicomponent vesicles can be found in [118, 162, 164, 233]. In addition, the Helfrich energy has been applied to study open vesicles [217], protrusion and contraction forces within the cell bulk to describe cell motility [228, 229] and the flow single or multiple red blood cells e.g. [99, 100, 105, 125, 177, 182, 262].

Mathematical techniques and numerical methods developed for the Helfrich problem with or without fluid flow are parametric approaches [22–25, 60, 82, 216], level-set methods [64, 66, 144, 218], immersed boundary methods [120, 126, 135, 136], boundary integral methods [98, 247, 248], a particle-based simulation methods [99, 100, 125, 182, 195, 262] and the diffuse interface method, which we will focus on in the following sec-

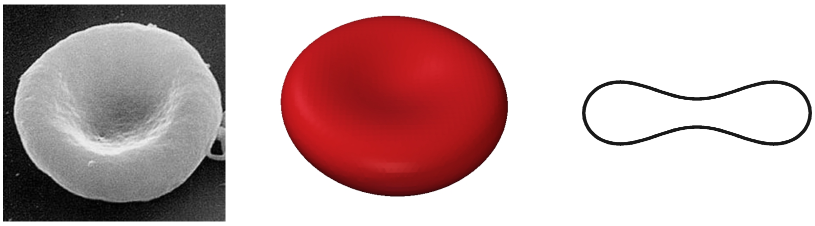

Figure 3.2. – Scanning electron micrograph of human red blood cells (left)(Picture licensed under Public Domain via Commons, retrieved from `https://www.wikipedia.org`) and stationary solution of an ellipsoid minimizing the Helfrich energy with volume and surface area conservation (middle) and cut through the surface (right). The Helfrich energy is an appropriate model to describe the equilibrium shape of RBCs.

tions. Finally, a comparison between a level-set and phase field methods is given in [167] and between level-set and parametric methods in [28].

3.2.2. Diffuse interface approximation

In this section, we review a diffuse interface approach for the minimization of the Helfrich energy. As shown in Section 2.4, we implicitly describe the surface Γ by the phase field function ϕ eq. (2.12). Using a gradient flow approach, we are able to derive the evolution equations for the surface Γ. Resulting equations are solved with adaptive finite elements. In this thesis our models follow the diffuse interface approximation of the Helfrich energy and the involved theory that was introduced by Du et al. in [72] and subsequent papers. Further theoretical and numerical investigations can be found in his recent publications. Moreover, reviews of existing diffuse interface models for the minimization of the Helfrich energy can be found in [67, 151].

The diffuse interface Helfrich energy is given by

$$\mathcal{E}_H(\phi) = \frac{b_n}{2\varepsilon}\int_\Omega \left(\varepsilon\Delta\phi - \frac{1}{\varepsilon}W_0'(\phi)\right)^2 \mathrm{d}\mathbf{x}, \tag{3.9}$$

where $W_0'(\phi) = (\phi^2-1)(\phi+\sqrt{2}H_0\varepsilon)$ stands for the modified double-well potential and was first indroduced by Du et al. [73], where they extended their previous studies of a diffuse interface approximation for the Willmore energy [72, 74]. In [73] and more rigorously in [255], the authors showed that $\mathcal{E}_H(\phi) \to \frac{4\sqrt{2}}{3}E_H(\Gamma)$ (eq. (3.5)) as $\varepsilon \to 0$. We additionally take into account the constraints arising from volume conservation, see eq. (3.7) and surface area conservation, see eq. (3.8) that can be translated into the phase field calculus as

$$\mathcal{V}(\phi) = \int_\Omega \phi\,\mathrm{d}\mathbf{x} = \mathcal{V}_0 = const. \qquad \text{since} \qquad \mathcal{V}(\phi) \to |\Omega_1| - |\Omega_0|, \tag{3.10}$$

$$\mathcal{E}_{CH}(\phi) = \int_\Omega \frac{\varepsilon}{2}|\nabla\phi|^2 + \frac{1}{\varepsilon}W(\phi)\,\mathrm{d}\mathbf{x} = \mathcal{A}_0 = const. \qquad \text{since} \qquad \mathcal{E}_{CH}(\phi) \to \frac{2\sqrt{2}}{3}|\Gamma|, \tag{3.11}$$

with desired states $\mathcal{V}_0 = \int_\Omega \phi(t=0,\mathbf{x})\,\mathrm{d}\mathbf{x}$ and $\mathcal{A}_0 = \mathcal{E}_{CH}(\phi(t=0,\mathbf{x}))$ corresponding to the initial or desired volume and surface area, respectively. Finally, we specify the diffuse Helfrich minimization problem:
Find $\phi^* \in L_\phi$, with $L_\phi := \{\phi \in H^2(\Omega) : \phi(t,\mathbf{x}) = 1,\ \nabla\phi(t,\mathbf{x}) \cdot \mathbf{n} = 0,\ t > 0,\ \mathbf{x} \in \partial\Omega\}$, with

$$\phi^* = \min_{\phi \in L_\phi} \mathcal{E}_S(\phi),$$

under the constraints

$$\mathcal{V}(\phi) = \mathcal{V}_0, \qquad \mathcal{E}_{CH}(\phi) = \mathcal{A}_0.$$

3.3. Nondimensionalization

Before we introduce the governing equations for the diffuse interface models, we consider a non-dimensional formulation of the proposed equations and energies. Accordingly, we choose the characteristic values for space $\mathbf{x} = L\hat{\mathbf{x}}$, velocity $\mathbf{v} = V\hat{\mathbf{v}}$ and energy $E = \eta V L^2 \hat{E}$, with characteristic length L, characteristic velocity V and fluid viscosity η. This yields a time scale $t = \frac{L}{U}\hat{t}$ and a pressure $p = \frac{\eta V}{L}\hat{p}$. Thus, the kinetic energy of a fluid eq. (2.54) becomes

$$\hat{\mathcal{E}}_{kin}(\hat{\mathbf{v}}) = \mathrm{Re} \int_{\hat{\Omega}} \frac{1}{2} |\hat{\mathbf{v}}|^2 \,\mathrm{d}\hat{\mathbf{x}} \tag{3.12}$$

in non-dimensional form. Moreover, the diffuse surface tension energy is given by

$$\hat{\mathcal{E}}_{ST}(\phi) = \frac{1}{\mathrm{Ca}} \int_{\hat{\Omega}} \frac{\hat{\varepsilon}}{2} |\hat{\nabla}\phi|^2 + \frac{1}{\hat{\varepsilon}} W(\phi) \,\mathrm{d}\hat{\mathbf{x}}, \tag{3.13}$$

and the non-dimensional Helfrich energy is

$$\hat{\mathcal{E}}_H(\phi) = \frac{1}{\mathrm{Be}} \int_{\hat{\Omega}} \frac{1}{2\hat{\varepsilon}} \left(\hat{\varepsilon}\hat{\Delta}\phi - \frac{1}{\hat{\varepsilon}} W_0'(\phi) \right)^2 \mathrm{d}\hat{\mathbf{x}}, \tag{3.14}$$

with $W_0'(\phi) = (\phi^2 - 1)(\phi + \sqrt{2}\hat{H}_0\varepsilon)$, where $\hat{H}_0$ is the non-dimensional spontaneous curvature. We have introduced tree dimensionless quantities:

- the Reynolds number Re$= \frac{\rho V L}{\eta}$, which is the ratio of inertial forces to viscous forces,
- the capillary number Ca$= \frac{2\sqrt{2}}{3}\frac{\eta V}{\sigma}$, which is the ratio of viscous forces to surface tension or capillary forces,
- and the bending capillary number Be$= \frac{4\sqrt{2}}{3}\frac{\eta V L^2}{b_n}$, which is the ratio of viscous forces to bending or Helfrich forces similarly defined in [32, 218].

The factors $\frac{2\sqrt{2}}{3}$ and $\frac{4\sqrt{2}}{3}$ take the scaling between diffuse and sharp interface energy into account. Please note, that we have to rescale the non-dimensional sharp interface energies with these factors:

$$\hat{E}_{ST}(\Gamma) = \frac{2\sqrt{2}}{3}\frac{1}{\mathrm{Ca}}\int_{\Gamma} \mathrm{ds} \tag{3.15}$$

and

$$\hat{E}_{H}(\Gamma) = \frac{4\sqrt{2}}{3}\frac{1}{\mathrm{Be}}\int_{\Gamma} (H - H_0)^2 \, \mathrm{ds}. \tag{3.16}$$

Next, we rewrite the two phase flow problem, eq. (2.47)-(2.48) in non-dimensional form. As reference values for density and viscosity, we pick ρ_0 and η_0 from the surrounding phase Ω_0, respectively. Hence, we have

$$\frac{V^2}{L}\rho_i(\partial_{\hat{t}}\hat{\mathbf{v}} + (\hat{\mathbf{v}} \cdot \hat{\nabla})\hat{\mathbf{v}}) + \frac{1}{L}\hat{\nabla}p = \frac{V}{L^2}\hat{\nabla} \cdot \left(\eta_i(\hat{\nabla}\hat{\mathbf{v}} + \hat{\nabla}\hat{\mathbf{v}}^{\top})\right) + \mathbf{F},$$

where p and $\mathbf{F}$ are still dimensional. A division by η_0 and $\frac{V}{L^2}$ and extension of the inertia term with ρ_0 gives

$$\frac{\rho_0 V L}{\eta_0}\frac{\rho_i}{\rho_0}(\partial_{\hat{t}}\hat{\mathbf{v}} + (\hat{\mathbf{v}} \cdot \hat{\nabla})\hat{\mathbf{v}}) + \frac{L}{V\eta_0}\hat{\nabla}p = \hat{\nabla} \cdot \left(\frac{\eta_i}{\eta_0}\hat{\mathbf{D}}\right) + \frac{L^2}{V\eta_0}\mathbf{F}.$$

Defining the Reynolds number with $\mathrm{Re} = \frac{\rho_0 V L}{\eta_0}$ and scaling the pressure with $p = \frac{\eta_0 V}{L}\hat{p}$, we arrive at

$$\mathrm{Re}\frac{\rho_i}{\rho_0}(\partial_{\hat{t}}\hat{\mathbf{v}} + (\hat{\mathbf{v}} \cdot \hat{\nabla})\hat{\mathbf{v}}) + \hat{\nabla}\hat{p} = \hat{\nabla} \cdot \left(\frac{\eta_i}{\eta_0}\hat{\mathbf{D}}\right) + \mathrm{St}\hat{\mathbf{F}} \tag{3.17}$$

with the Stokes number St$= \frac{L^2}{V\eta_0}$ representing the ratio of body forces to viscous forces. Another representation of eq. (3.17) is

$$\mathrm{Re}\frac{\rho_i}{\rho_0}\frac{\mathrm{D}\hat{\mathbf{v}}}{\mathrm{Dt}} = \hat{\nabla} \cdot \hat{\mathbf{S}}_{\mathbf{i}} + \mathrm{St}\hat{\mathbf{F}}, \tag{3.18}$$

with

$$\hat{\mathbf{S}}_i = -\hat{p}\mathbf{I} + \frac{\eta_i}{\eta_0}\hat{\mathbf{D}} \tag{3.19}$$

the non-dimensional stress tensor. Moreover, if we divide eq. (3.17) or eq. (3.18) by Re, we arrive at further dimensionless quantities, which can also by found in the literature:

- the Weber number We=Re $\cdot$ Ca,
- the Reynolds bending number Rb=Re $\cdot$ Be,
- the Froude number Fr$= \frac{\mathrm{St}}{\mathrm{Re}}$.

Remark 3.1 We classify the flow into two basic regimes with Re $\gg 1$ where inertial forces dominate and with Re $\ll 1$ that is called Stokes regime where inertia can be neglected and viscous forces dominate. The following example illustrates why cells in fluid flow live in a Stokes regime: considering equal viscosity $\eta = 10^{-3}$ Pa s and density $\rho = 10^3$ kg/m^3, the characteristic velocity and length for a bacterium E. coli are $V = 30 \cdot 10^{-6}$ m/s and $L = 2 \cdot 10^{-6}$ m, accordingly we have $\mathrm{Re} = 6 \cdot 10^{-5}$, whereas a human swimmer with $V = 1$ m/s and $L = 2$ yields $\mathrm{Re} = 2 \cdot 10^6$. As a consequence, eq. (3.17) becomes an Euler equation for $\mathrm{Re} \gg 1$ and for $\mathrm{Re} \ll 1$ we obtain the Stokes equation

$$\hat{\nabla}\hat{p} = \hat{\nabla} \cdot \left(\frac{\eta_i}{\eta_0}\hat{\mathbf{D}}\right) + \mathrm{St}\hat{\mathbf{F}}_i, \tag{3.20}$$

with $\hat{\nabla} \cdot \hat{\mathbf{v}} = 0$. These regimes are essential for the choice of the numerical technique to solve these equations and of course for the physics of the flow itself. Especially, for actively driven particles or so-called swimmers the linearity of the Stokes equation would not lead to an active motion if the swimming mechanism is symmetric. On the other hand, the same mechanism would lead to a motion in regimes where inertia is dominating. This phenomenon is known as Scallop theorem in the literature. Furthermore, we will see in Chapter 8 that the Reynolds number influences the lift force of a white blood cell and is therefore crucial for the occurrence of white blood cell margination. For a wide introduction into dimensional analysis, we refer to Papanastasiou et al. [199] and for flow in the Stokes regime see Happel and Brenner [117].

If not stated otherwise we only consider non-dimensional variables and energies therefore we drop the hats.

3.4. Evolution equations for diffuse Helfrich energy with surface conservation

In this section, we derive evolution equations for the surface membrane Γ that minimize the diffuse Helfrich energy. As already discussed, we classify all models either to be non-hydrodynamic eq. (3.1), see Section 3.4.1 or to be hydrodynamic eq. (3.3) and eq. (2.47)-(2.48), see Section 3.4.2. To derive the non-hydrodynamic model, we apply a gradient flow approach to the diffuse Helfrich energy and account for further volume and surface area constraints by adding Lagrange multipliers or penalty terms. Resulting geometric evolution equations are given in Section 3.4.1. Simulations of non-hydrodynamic models that can be used to describe an equilibrium shape of vesicles have been performed in [72, 73, 75]. More analytic studies that discuss existence and convergence can be found in [71, 74]. A numerical analysis that considers the finite element method is given in [69, 70]. Topological considerations including the calculation of the Euler number are investigated in [75, 92]. Other diffuse interface models can be found in [42–45, 149].

The hydrodynamic model -derived in Section 3.4.2- requires additional incompressible Navier-Stokes equations for the fluid flow. The physical property of the membrane, which is presented as interface between two fluid phases, is represented by an additional stress or body force term within the momentum equation. Thus, the phase field equation simplifies to a simple advection equation that is driven by the updated velocity field. Since the numerical treatment of an advection equation is unfavorable, we extend the phase field equation by small relaxation term, represented by the energy variation. There are similar approaches that are based on the model H derived in Hohenberg and Halperin [123], where the interfacial stress comes from the surface tension in order to describe a simple two-phase flow [36, 127, 155, 157, 264]. In Section 2.8, we have derived a thermodynamically consistent model for general two-phase flow. Since the underlying energy is now familiar, we are able to determine the particular Helfrich stress performing a similar procedure that considers the material derivative of the thermodynamic variables.

In this thesis, we follow the work of Du et al. [76], where the authors developed and analyzed a hydrodynamic model for vesicles. It has been applied in [12, 68, 77, 150, 174, 176, 177, 217]. Another hydrodynamic diffuse interface model has also been used in [31, 32, 129] with a different phase field formulation and without an explicit formulation of the diffuse Helfrich energy. More recently, in [97] a very general approach was given, that covers both diffuse interface formulations. A further approach can be found in [150].

3.4.1. Non-hydrodynamic model

Without fluid flow the minimization of the Helfrich problem is a geometric evolution equation, whose dynamics are given in eq. (3.2). We first review the evolution equations in absence of any constraints. Using the L^2-gradient flow eq. (2.3) we have on $I \times \Omega$

$$\partial_t \phi = -\gamma \frac{\delta \mathcal{E}_H}{\delta \phi}, \tag{3.21}$$

$$\frac{\delta \mathcal{E}_H}{\delta \phi} = \Delta \mu - \frac{1}{\varepsilon^2} W_0''(\phi) \mu, \tag{3.22}$$

$$\mu = \varepsilon \Delta \phi - \frac{1}{\varepsilon} W_0'(\phi), \tag{3.23}$$

with $W_0''(\phi) = 3\phi^2 + 2\phi\sqrt{2}H_0\varepsilon - 1$. Here, we split up the 4th order equation for ϕ as a system of 2nd order equations. Furthermore, it holds

$$\left(\frac{\delta \mathcal{E}_H}{\delta \phi} = 0 \right) \to \left(\Delta_\Gamma H + 2H(H^2 - K) + 2KH_0 - 2HH_0^2 = 0 \right),$$

i.e. the critical point of the diffuse interface approach asymptotically converges to the critical point of the sharp interface formulation as $\varepsilon \to 0$ [255]. We further introduce the variation of the Cahn-Hilliard energy denoted by

$$\kappa := \frac{\delta \mathcal{E}_{CH}}{\delta \phi} = -\varepsilon \Delta \phi + \frac{1}{\varepsilon} W'(\phi), \tag{3.24}$$

being a diffuse interface approximation of the mean curvature H with $\kappa \to \sqrt{2} H \delta_\Gamma$ if $\varepsilon \to 0$. In order to account for volume and surface area conservation during the minimization process, we either add Lagrange multipliers or penalty terms to the evolution equations. Moreover, it can be useful to adapt an H^{-1}-gradient flow eq. (2.4) to save the volume conservation. The resulting models are specified in the following.

Lagrange-Multipliers

First, we extend the diffuse Helfrich energy eq. (3.14) by two Lagrange multipliers accounting for the volume and surface area conservation

$$\mathcal{E}_S(\phi) = \mathcal{E}_H(\phi) + \frac{1}{\mathrm{Be}} \left(\lambda_{volume} \left(\mathcal{V}(\phi) - \mathcal{V}_0\right) + \lambda_{area} \left(\mathcal{E}_{CH}(\phi) - \mathcal{A}_0\right)\right) \tag{3.25}$$

and adapt a L^2-gradient flow

$$\partial_t \phi = -\gamma \frac{\delta \mathcal{E}_S}{\delta \phi}, \tag{3.26}$$

where the variation with respect to ϕ is given by

$$\frac{\delta \mathcal{E}_S}{\delta \phi} = \frac{1}{\mathrm{Be}} \left(\Delta\mu - \frac{1}{\varepsilon^2} W_0''(\phi)\mu + \lambda_{volume} + \lambda_{area}\kappa \right). \tag{3.27}$$

Then

$$\lambda_{volume}|\Omega| + \lambda_{area} \int_\Omega \kappa \, \mathrm{d}\mathbf{x} = -\int_\Omega \Delta\mu - \frac{1}{\varepsilon^2} W_0''(\phi)\mu \, \mathrm{d}\mathbf{x}, \tag{3.28}$$

$$\lambda_{volume} \int_\Omega \kappa \, \mathrm{d}\mathbf{x} + \lambda_{area} \int_\Omega \kappa^2 \, \mathrm{d}\mathbf{x} = -\int_\Omega \kappa(\Delta\mu - \frac{1}{\varepsilon^2} W_0''(\phi)\mu), \, \mathrm{d}\mathbf{x} \tag{3.29}$$

where eq. (3.28) can easily be derived from the evolution eq. (3.26), where we integrate over Ω and apply the volume conservation $\frac{\mathrm{d}}{\mathrm{dt}} \int_\Omega \phi \, \mathrm{d}\mathbf{x} = \int_\Omega \partial_t \phi = 0$. For eq. (3.29), we consider the surface area conservation, which is $\frac{\mathrm{d}}{\mathrm{dt}} \mathcal{E}_{CH} = \int_\Omega \kappa \partial_t \phi \, \mathrm{d}\mathbf{x} = 0$. Now, we multiply the evolution eq. (3.26) by κ, given in eq. (3.24), and integrate over Ω.

The resulting system of integro-partial differential equations is a challenging problem. An explicit treatment, where we first solve the linearized system of PDEs and afterward solve the linear system of the Lagrange multipliers, slightly violates the constraints [75].

Penalty terms

Another widely used and easily adoptable approach to fulfill the constraints are penalty terms. Now, we extend the diffuse Helfrich energy eq. (3.14) by two additional terms:

$$\begin{aligned} \mathcal{E}_S(\phi) &= \mathcal{E}_H(\phi) + \frac{p_1}{2\mathrm{Be}} (\mathcal{V}(\phi) - \mathcal{V}_0)^2 + \frac{p_2}{2\mathrm{Be}} (\mathcal{E}_{CH}(\phi) - \mathcal{A}_0)^2 \, \mathrm{d}\mathbf{x} \\ &= \frac{1}{\mathrm{Be}} \frac{1}{2\varepsilon} \int_\Omega \left(\varepsilon\Delta\phi - \frac{1}{\varepsilon} W_0'(\phi) \right)^2 + \frac{p_1}{2\mathrm{Be}} (\mathcal{V}(\phi) - \mathcal{V}_0)^2 \\ &\quad + \frac{p_2}{2\mathrm{Be}} (\mathcal{E}_{CH}(\phi) - \mathcal{A}_0)^2 \, \mathrm{d}\mathbf{x}, \end{aligned} \tag{3.30}$$

which adopt their minimum during the minimization process. The penalty parameters $p_1, p_2 > 0$ have to be chosen carefully. The corresponding evolution equations in $I \times \Omega$ are

$$\partial_t \phi = -\gamma \frac{\delta \mathcal{E}_S}{\delta \phi}, \tag{3.31}$$

$$\frac{\delta \mathcal{E}_S}{\delta \phi} = \frac{1}{\mathrm{Be}} \left(\Delta \mu - \frac{1}{\varepsilon^2} W_0''(\phi)\mu + p_1(\mathcal{V}(\phi) - \mathcal{V}_0) + p_2(\mathcal{E}_{CH}(\phi) - \mathcal{A}_0)\kappa \right). \tag{3.32}$$

Dealing with two different penalty terms can be problematic under certain circumstances. We can save at least the volume conservation constraint by applying a H^{-1}-gradient flow. As result of that, the evolution can differ but the equilibrium shape is similar. However, the system becomes of 6th order which might be numerically unfavourable. Accordingly, we consider the diffuse Helfrich energy that is only extended with the surface area penalty term

$$\mathcal{E}_S(\phi) = \frac{1}{\mathrm{Be}} \frac{1}{2\varepsilon} \int_\Omega \left(\varepsilon \Delta \phi - \frac{1}{\varepsilon} W_0'(\phi) \right)^2 + \frac{p_2}{2\mathrm{Be}} (\mathcal{E}_{CH}(\phi) - \mathcal{A}_0)^2 \, \mathrm{d}\mathbf{x}. \tag{3.33}$$

and we derive

$$\partial_t \phi = \gamma \Delta \frac{\delta \mathcal{E}_S}{\delta \phi}, \tag{3.34}$$

$$\frac{\delta \mathcal{E}_S}{\delta \phi} = \frac{1}{\mathrm{Be}} \left(\Delta \mu - \frac{1}{\varepsilon^2} W_0''(\phi)\mu + p_2(\mathcal{E}_{CH}(\phi) - \mathcal{A}_0)\kappa \right). \tag{3.35}$$

Such an approach was already considered without flow interactions in [44] and for hydrodynamic models in [156, 176, 177].

For all non-hydrodynamic models we assume the initial conditions given by

$$\phi(t, \mathbf{x}) = \phi^0(\mathbf{x}), \qquad \text{for } t = 0, \mathbf{x} \in \Omega$$

and the boundary conditions as

$$\phi(t, \mathbf{x}) = -1, \ \nabla \mu \cdot \mathbf{n} = 0, \qquad \text{for } t > 0, \mathbf{x} \in \partial\Omega$$

and additionally for the 6th order system

$$\nabla \frac{\delta \mathcal{E}_S}{\delta \phi} \cdot \mathbf{n} = 0, \qquad \text{for } t > 0, \mathbf{x} \in \partial\Omega.$$

Please note, for the system given by eq. (3.31) and (3.32) well-posedness can be established [52, 53] in case of homogeneous Neumann boundary conditions for ϕ. The authors further proved existence and uniqueness of the solution ϕ using the gradient flow structure and a time-discrete minimization structure. The numerical treatment can be found in [69–71, 75, 173, 174, 176, 177] and -as part of our numerical models- in the following sections.

Alternatively, a combination of Lagrange multipliers and penalty terms [75] can also be applied. The approach overcomes the error accumulation during the explicit treatment of the Lagrange multipliers. Moreover, it limits the error caused by a penalty formulation. Here, however, we focus on the treatment with penalty terms due to its simplicity.

3.4.2. Hydrodynamic Navier-Stokes-Helfrich model

Within a hydrodynamic approach we consider a two-phase flow for a Newtonian fluid eq. (2.47)-(2.48) with distinct viscosities η_0 in the surrounding fluid and η_1 in the cell interior. We further assume $\rho_0 = \rho_1$, for simplicity. Accordingly, the flow can be described by the kinetic energy of the fluid $\mathcal{E}_{kin} = \int_\Omega \frac{\mathrm{Re}}{2}|\mathbf{v}|^2 \,\mathrm{d}\mathbf{x}$. Across the interfaces the following jump conditions hold:

$$[\mathbf{v}]_\Gamma = 0 \qquad \text{zero velocity jump,} \tag{3.36}$$

$$[\mathbf{S}\cdot\mathbf{n}]_\Gamma = \frac{\delta E_S}{\delta\Gamma} \qquad \text{energy variation with global area constraint} \tag{3.37}$$

with the variation of the surface energy $\frac{\delta E_S}{\delta\Gamma} = \frac{\delta E_H}{\delta\Gamma} + \frac{p_2}{\mathrm{Be}}\left(\mathcal{E}_{CH}(\phi) - \mathcal{A}_0\right) H\mathbf{n}$ accounting for bending and surface area conservation. In order to derive a thermodynamically consistent diffuse interface approach, we consider the overall energy given in a diffuse interface formulation as

$$\begin{aligned}\mathcal{E}(\mathbf{v},\phi) &= \mathcal{E}_{kin}(\mathbf{v}) + \mathcal{E}_S(\phi) && (3.38)\\ &= \int_\Omega \frac{\mathrm{Re}}{2}|\mathbf{v}|^2 + \frac{1}{\mathrm{Be}}\frac{1}{2\varepsilon}\left(\varepsilon\Delta\phi - \frac{1}{\varepsilon}W_0'(\phi)\right)^2 + \frac{p_2}{2\mathrm{Be}}\left(\mathcal{E}_{CH}(\phi) - \mathcal{A}_0\right)^2 \,\mathrm{d}\mathbf{x}, && (3.39)\end{aligned}$$

where $\mathcal{E}_S(\phi)$ is taken from eq. (3.33). Now, we have to ensure that the overall free energy decays in time. Therefore, we calculate its time derivative

$$\begin{aligned}\frac{\mathrm{d}\mathcal{E}}{\mathrm{dt}} = \int_\Omega &\mathrm{Re}\,\mathbf{v}\cdot\frac{\mathrm{D}\mathbf{v}}{\mathrm{Dt}} + \frac{1}{\mathrm{Be}}\mu\left(\frac{\mathrm{D}\Delta\phi}{\mathrm{Dt}} - \frac{1}{\varepsilon^2}W_0''(\phi)\frac{\mathrm{D}\phi}{\mathrm{Dt}}\right)\\ &+ \frac{p_2}{\mathrm{Be}}\left(\mathcal{E}_{CH}(\phi) - \mathcal{A}_0\right)\left(\varepsilon\nabla\phi\frac{\mathrm{D}\nabla\phi}{\mathrm{Dt}} + \frac{1}{\varepsilon}W'(\phi)\frac{\mathrm{D}\phi}{\mathrm{Dt}}\right)\mathrm{d}\mathbf{x},\end{aligned} \tag{3.40}$$

where we now consider the material derivative of ϕ and $\mathbf{v}$ being defined by

$$\frac{\mathrm{D}\phi}{\mathrm{Dt}} = \partial_t\phi + \mathbf{v}\cdot\nabla\phi, \tag{3.41}$$

$$\frac{\mathrm{D}\mathbf{v}}{\mathrm{Dt}} = \partial_t\mathbf{v} + (\mathbf{v}\cdot\nabla)\mathbf{v}. \tag{3.42}$$

Hence, the conservation of momentum and mass for $\mathbf{v}$ as well as the conservation of mass for ϕ read

$$\mathrm{Re}\frac{\mathrm{D}\mathbf{v}}{\mathrm{Dt}} = -\nabla p + \nabla \cdot (\eta(\phi)\mathbf{D}) + \nabla \cdot \mathbf{S}_H + \nabla \cdot \mathbf{S}_{pen}, \tag{3.43}$$

$$\nabla \cdot \mathbf{v} = 0, \tag{3.44}$$

$$\frac{\mathrm{D}\phi}{\mathrm{Dt}} = -\nabla \cdot \mathbf{J}, \tag{3.45}$$

respectively. Here, the unknowns $\mathbf{J}$ as well as $\mathbf{S}_H$ and $\mathbf{S}_{pen}$ denote the flux of ϕ and the stresses resulting from the Helfrich energy and the penalty term, respectively. We now determine these unknowns such that the overall energy decreases. In eq. (3.40) we observe the following term and rewrite it

$$\begin{aligned}\frac{\mathrm{D}\Delta\phi}{\mathrm{Dt}} &= \Delta\partial_t\phi + \mathbf{v} \cdot \nabla\Delta\phi \\ &= \Delta\left(\frac{\mathrm{D}\phi}{\mathrm{Dt}} - \mathbf{v} \cdot \nabla\phi\right) + \mathbf{v} \cdot \nabla\Delta\phi \\ &= \Delta\frac{\mathrm{D}\phi}{\mathrm{Dt}} - \Delta\mathbf{v} \cdot \nabla\phi - 2\nabla\mathbf{v} : \nabla\nabla\phi,\end{aligned} \tag{3.46}$$

where we use eq. (3.41). In the same manner we rewrite

$$\begin{aligned}\frac{\mathrm{D}\nabla\phi}{\mathrm{Dt}} &= \nabla\partial_t\phi + \mathbf{v} \cdot \nabla\nabla\phi \\ &= \nabla\left(\frac{\mathrm{D}\phi}{\mathrm{Dt}} - \mathbf{v} \cdot \nabla\phi\right) + \mathbf{v} \cdot \nabla\nabla\phi \\ &= \nabla\frac{\mathrm{D}\phi}{\mathrm{Dt}} - \nabla\mathbf{v} \cdot \nabla\phi,\end{aligned} \tag{3.47}$$

where we used eq. (3.42). Inserting eq. (3.46) and eq. (3.47) into the time derivative of the energy eq. (3.40) gives

$$\begin{aligned}\frac{\mathrm{d}\mathcal{E}}{\mathrm{dt}} = &\int_\Omega \mathrm{Re}\,\mathbf{v} \cdot \frac{\mathrm{D}\mathbf{v}}{\mathrm{Dt}} + \frac{1}{\mathrm{Be}}\mu\left(\Delta\frac{\mathrm{D}\phi}{\mathrm{Dt}} - \frac{1}{\varepsilon^2}W_0''(\phi)\frac{\mathrm{D}\phi}{\mathrm{Dt}} - \Delta\mathbf{v} \cdot \nabla\phi - 2\nabla\mathbf{v} : \nabla\nabla\phi\right) \\ &+ \frac{p_2}{\mathrm{Be}}(\mathcal{E}_{CH}(\phi) - \mathcal{A}_0)\left((-\varepsilon\Delta\phi + \frac{1}{\varepsilon}W'(\phi))\frac{\mathrm{D}\phi}{\mathrm{Dt}} - \varepsilon\nabla\phi \cdot (\nabla\mathbf{v} \cdot \nabla\phi)\right)\mathrm{d}\mathbf{x} \\ = &\int_\Omega \mathrm{Re}\,\mathbf{v} \cdot \frac{\mathrm{D}\mathbf{v}}{\mathrm{Dt}} + \frac{\delta\mathcal{E}}{\delta\phi}\frac{\mathrm{D}\phi}{\mathrm{Dt}} - \frac{1}{\mathrm{Be}}\mu\Delta\mathbf{v} \cdot \nabla\phi - \frac{2}{\mathrm{Be}}\mu\nabla\mathbf{v} : \nabla\nabla\phi \\ &- \frac{p_2}{\mathrm{Be}}(\mathcal{E}_{CH}(\phi) - \mathcal{A}_0)\varepsilon\nabla\phi \cdot (\nabla\mathbf{v} \cdot \nabla\phi)\,\mathrm{d}\mathbf{x}.\end{aligned}$$

We now plug in the time evolution eq. (3.41) and eq. (3.42) and we arrive at

$$\begin{aligned}
\frac{\mathrm{d}\mathcal{E}}{\mathrm{dt}} &= \int_\Omega \mathbf{v} \cdot (-\nabla p + \nabla \cdot (\eta(\phi)\mathbf{D}) + \nabla \cdot \mathbf{S}_H + \nabla \cdot \mathbf{S}_{pen}) + \frac{\delta\mathcal{E}}{\delta\phi}(-\nabla \cdot \mathbf{J}) \\
&\quad + \frac{1}{\mathrm{Be}}\nabla\mathbf{v} : \nabla(\mu\nabla\phi) + \frac{2}{\mathrm{Be}}\mathbf{v} \cdot \nabla \cdot (\mu\nabla\nabla\phi) \\
&\quad - \frac{p_2}{\mathrm{Be}}(\mathcal{E}_{CH}(\phi) - \mathcal{A}_0)\varepsilon\nabla\mathbf{v} : (\nabla\phi \otimes \nabla\phi)\,\mathrm{d}\mathbf{x} \\
&= \int_\Omega \mathbf{v} \cdot \nabla \cdot (\eta(\phi)\mathbf{D}) + \mathbf{v} \cdot (\nabla \cdot \mathbf{S}_H + \nabla \cdot \mathbf{S}_{pen}) + \frac{\delta\mathcal{E}}{\delta\phi}(-\nabla \cdot \mathbf{J}) \\
&\quad - \frac{1}{\mathrm{Be}}\mathbf{v} \cdot (\nabla \cdot (\nabla\phi \otimes \nabla\mu) + \nabla \cdot (\mu\nabla\nabla\phi)) \\
&\quad + \frac{p_2}{\mathrm{Be}}(\mathcal{E}_{CH}(\phi) - \mathcal{A}_0)\varepsilon\mathbf{v} \cdot \nabla \cdot (\nabla\phi \otimes \nabla\phi)\,\mathrm{d}\mathbf{x},
\end{aligned}$$

where we use partial integration and incompressibility as well as the definition for μ (eq. (3.23)). Setting

$$\mathbf{J} = -\gamma\nabla\frac{\delta\mathcal{E}}{\delta\phi}, \tag{3.48}$$

$$\mathbf{S}_H = \frac{1}{\mathrm{Be}}(\nabla\phi \otimes \nabla\mu - \mu\nabla\nabla\phi), \tag{3.49}$$

$$\mathbf{S}_{pen} = -\frac{p_2}{\mathrm{Be}}(\mathcal{E}_{CH}(\phi) - \mathcal{A}_0)\varepsilon\nabla\phi \otimes \nabla\phi, \tag{3.50}$$

neglecting advection and pressure terms coming from the momentum equation after applying eq. (2.59), using eq. (2.60) and partial integration, leads to the following energy law

$$\frac{\mathrm{d}\mathcal{E}}{\mathrm{dt}} = \int_\Omega -\eta(\phi)\mathbf{D} : \mathbf{D} - \gamma\left|\nabla\frac{\delta\mathcal{E}}{\delta\phi}\right|^2 \leq 0, \tag{3.51}$$

which was already proposed in eq. (2.62) for a conserved order parameter ϕ. Putting everything together, we arrive at the following momentum equation containing the Helfrich and surface conservation stress:

$$\begin{aligned}
\mathrm{Re}(\partial_t\mathbf{v} + (\mathbf{v} \cdot \nabla)\mathbf{v}) + \nabla p = \nabla \cdot (\eta(\phi)\mathbf{D}) + \frac{1}{\mathrm{Be}}\nabla \cdot (\nabla\phi \otimes \nabla\mu - \mu\nabla\nabla\phi) \\
- \frac{p_2}{\mathrm{Be}}(\mathcal{E}_{CH}(\phi) - \mathcal{A}_0)\varepsilon\nabla \cdot (\nabla\phi \otimes \nabla\phi)\,,
\end{aligned} \tag{3.52}$$

with μ defined below and an advection equation for ϕ given in eq. (3.45). We have seen that we are able to derive thermodynamically consistent systems in two ways. During the derivation of the overall energy with respect to time we can understand occurring time derivatives of the thermodynamic quantities as material or partial derivative. Considering the material derivative gives us the particular stress resulting from a specific interfacial energy. Certainly, this is advantageous for theoretical considerations. For numerical purposes, however, it is not necessary since we have to solve the divergence of the stress tensor and the Hessian of ϕ. Accordingly, it is favorable is to account for partial time derivatives that yield the treatment of the variation of the interfacial energy in the momentum equation. In the following Remark, we will see that these two arising forces can be converted in each other.

Remark 3.2 It holds $\nabla \cdot (\mathbf{S}_H + \mathbf{S}_{pen}) = \frac{\delta \mathcal{E}_S}{\delta \phi} \nabla \phi$ with surface energy $\mathcal{E}_S$ defined in eq. (3.33).

To show this, we calculate the divergence of the stress tensors $\mathbf{S}_H$ and $\mathbf{S}_{pen}$:

$$\nabla \cdot \mathbf{S}_H = \frac{1}{\mathrm{Be}}(\Delta\mu\nabla\phi - \mu\Delta\nabla\phi), \tag{3.53}$$

$$\nabla \cdot \mathbf{S}_{pen} = -\frac{p_2}{\mathrm{Be}}(\mathcal{E}_{CH}(\phi) - \mathcal{A}_0)\left(\frac{\varepsilon}{2}\nabla|\nabla\phi|^2 + \varepsilon\Delta\phi\nabla\phi\right). \tag{3.54}$$

Additionally, we consider the energy densities of eq. (3.33)

$$e = e_H + e_{pen} = \frac{1}{\mathrm{Be}}\frac{1}{2\varepsilon}\left(\varepsilon\Delta\phi - \frac{1}{\varepsilon}W_0'(\phi)\right)^2 + \frac{p_2}{2}\left(\mathcal{E}_{CH}(\phi) - A_0\right)^2.$$

Determining the gradient of e and rearranging gives

$$\frac{1}{\mathrm{Be}}\mu\Delta\nabla\phi = \nabla e_H + \frac{1}{\mathrm{Be}}\frac{1}{\varepsilon^2}W_0''(\phi)\mu\nabla\phi, \tag{3.55}$$

$$\frac{p_2}{\mathrm{Be}}\left(\mathcal{E}_{CH}(\phi) - \mathcal{A}_0\right)\frac{\varepsilon}{2}\nabla|\nabla\phi|^2 = \nabla e_{pen} - \frac{1}{\varepsilon}W'(\phi)\nabla\phi. \tag{3.56}$$

Inserting eq. (3.55) into eq. (3.53) and eq. (3.56) into eq. (3.54) we have

$$\nabla \cdot \mathbf{S}_H = -\nabla e_H + \frac{1}{\mathrm{Be}}\mu\nabla\phi, \tag{3.57}$$

$$\nabla \cdot \mathbf{S}_{pen} = -\nabla e_{pen} + \frac{p_2}{\mathrm{Be}}\left(\mathcal{E}_{CH}(\phi) - \mathcal{A}_0\right)\kappa\nabla\phi. \tag{3.58}$$

Inserting into the momentum equation (3.43) gives

$$\mathrm{Re}(\partial_t\mathbf{v} + (\mathbf{v}\cdot\nabla)\mathbf{v}) + \nabla p = \nabla \cdot (\eta(\phi)\mathbf{D}) - \nabla e_H - \nabla e_{pen} + \frac{\delta\mathcal{E}_S}{\delta\phi}\nabla\phi$$

and redefining the pressure as $p = p_{old} + e_H + e_{pen}$, we finally arrive at the following diffuse interface Navier-Stokes-Willmore model with surface conservation in $I \times \Omega$:

$$\mathrm{Re}(\partial_t \mathbf{v} + (\mathbf{v} \cdot \nabla)\mathbf{v}) + \nabla p = \nabla \cdot (\eta(\phi)\mathbf{D}) + \frac{\delta \mathcal{E}_S}{\delta \phi}\nabla\phi, \tag{3.59}$$

$$\nabla \cdot \mathbf{v} = 0, \tag{3.60}$$

$$\partial_t \phi + \mathbf{v} \cdot \nabla \phi = \gamma \Delta \frac{\delta \mathcal{E}_S}{\delta \phi}, \tag{3.61}$$

$$\frac{\delta \mathcal{E}_S}{\delta \phi} = \frac{1}{\mathrm{Be}}\left(\Delta\mu - \frac{1}{\varepsilon^2}W_0''(\phi)\mu + p_2(\mathcal{E}_{CH}(\phi) - \mathcal{A}_0)\kappa\right), \tag{3.62}$$

$$\mu = \varepsilon\Delta\phi - \frac{1}{\varepsilon}W_0'(\phi), \tag{3.63}$$

$$\kappa = -\varepsilon\Delta\phi + \frac{1}{\varepsilon}W'(\phi). \tag{3.64}$$

The initial conditions are

$$\phi(t,\mathbf{x}) = \phi^0(\mathbf{x}),\ \mathbf{v}(t,\mathbf{x}) = \mathbf{v}^0(\mathbf{x}), \qquad \text{for } t = 0, \mathbf{x} \in \Omega$$

and the boundary conditions read as

$$\phi(t,\mathbf{x}) = -1,\ \nabla\mu \cdot \mathbf{n} = 0,\ \nabla\frac{\delta \mathcal{E}_S}{\delta \phi} \cdot \mathbf{n} = 0,\ \mathbf{v}(t,\mathbf{x}) = \mathbf{0}, \qquad \text{for } t > 0, \mathbf{x} \in \partial\Omega.$$

For the given system eq. (3.59) - (3.64), where eq. (3.61) is replaced by a L^2-gradient flow, i.e. $\partial_t\phi + \mathbf{v} \cdot \nabla\phi = -\gamma\frac{\delta\mathcal{E}_S}{\delta\phi}$ with an additional penalty term for volume conservation Du et al. [76] could prove the existence of global weak solutions and the uniqueness under extra regularity. Local time existence and uniqueness of strong solutions are shown in Liu et al. [158]. The introduced H^{-1}-gradient flow approach is not commonly used in the literature as it yields a system of 6th order. However, it provides a more stable system. For instance, we save the treatment of an additional penalty and the calculated chemical potential is much more smoother. Simulations have shown that this allows larger time steps. Nevertheless, the evolution is not completely different to a L^2-gradient flow as the term is only used for the stabilization of the phase field and its physical relevance is restricted by small γ.

3.4.3. Hydrodynamic model for inextensibility

Due to its physiological conditions, the lipid bilayer can be considered as fluid-like membrane, where the lipids can move freely and diffuse like a fluid whose motion is restricted to the surface. However, when it comes to stretching, the binding forces between each lipid are high and forbid any extension of the membrane. The membrane is therefore inextensible or in the fluid context incompressible along the surface Γ, accordingly, we have

$$\nabla_\Gamma \cdot \mathbf{v} = \mathbf{P}_\Gamma : \nabla\mathbf{v} = 0. \qquad \text{on } \Gamma \tag{3.65}$$

It is clear, that every membrane fulfilling this condition conserves its global surface area. The numerical treatment of the inextensibility condition is a serious problem and leads a further nonlinear coupling that implies the calculation of a Lagrange multiplier λ_{local} being both time and space dependent. The numerical treatment of the inextensibility constraint has been considered within a level-set approach [64, 144, 218, 219], immersed boundary methods [120, 126, 135, 136], boundary integral methods [98, 247, 248], a particle-based mesoscale simulation method [99, 100, 182, 195], parametric finite-elemtens methods [25] and the phase field method [31, 32, 129]. A comparison between phase field and level-set method is given in [167]. Here, we review the thermodynamically consistent phase field model proposed by Aland et al. [12], which has successfully been applied to our models, see Chapter 7 and Chapter 8. The basic idea of this approach is first to construct a tension force

$$\mathbf{F}_{inext} = \nabla \cdot (\delta_\Gamma \mathbf{P}_\Gamma \lambda_{local}),$$

where we introduce a local Lagrange parameter $\lambda_{local} = \lambda_{local}(t, \mathbf{x})$ that fulfills the following jump condition across the interface

$$[\mathbf{S} \cdot \mathbf{n}]_\Gamma = \frac{\delta E}{\delta \Gamma} + \lambda_{local} H \mathbf{n} + \nabla_\Gamma \lambda_{local}. \tag{3.66}$$

By solving $\nabla \cdot (\delta_\Gamma \mathbf{P}_\Gamma \lambda_{local}) = \delta_\Gamma(\lambda_{local} H \mathbf{n} + \nabla_\Gamma \lambda_{local})$, we see that $\mathbf{F}_{inext}$ is the extension of the jump condition, eq. (3.66), to Ω. This term can also be found in [31, 32, 129, 218] as basis of their approaches. Finally, we insert $\mathbf{F}_{inext}$ in a diffuse interface formulation to the right-hand side of the momentum equation (3.59) and arrive at

$$\mathrm{Re}(\partial_t \mathbf{v} + (\mathbf{v} \cdot \nabla)\mathbf{v}) + \nabla p = \nabla \cdot (\eta(\phi)\mathbf{D}) + \frac{\delta \mathcal{E}_S}{\delta \phi} \nabla \phi + \nabla \cdot (\delta_\phi \mathbf{P}_\phi \lambda_{local}), \tag{3.67}$$

in $I \times \Omega$. Furthermore, the inextensibility equation (3.65) is extended to the domain Ω:

$$\xi \varepsilon^2 \nabla \cdot (\phi^2 \nabla \lambda_{local}) + \delta_\phi \mathbf{P}_\phi : \nabla \mathbf{v} = 0, \tag{3.68}$$

where $\xi > 0$ is a parameter, independent of ε, determining the accuracy of the method. Small ξ tend to increase the region along the interface where the inextensibility is enforced, whereas higher ξ lead to larger errors in the method. According to the authors $\xi = 1$ is an appropriate choice. We pick $\delta_\phi = |\nabla \phi|/2$ and the projection operator $\mathbf{P}_\phi = \mathbf{I} - \frac{\nabla \phi \otimes \nabla \phi}{|\nabla \phi|^2}$. In [12] it has been shown, performing an asymptotic analysis, that the diffuse interface approach converges to the sharp interface constraint as $\varepsilon \to 0$, more precisely we obtain $\Delta \lambda_{local} = 0$ away from Γ and $\nabla_\Gamma \cdot \mathbf{v} = 0$ near Γ.

The disadvantage of the proposed model is that eq. (3.68) may lead to an accumulation of errors over time, violating the local inextensibility constraint. Hence, the membrane becomes stretched and compressed, similarly to the global surface area conservation. Nevertheless, we have applied this model, because on small time scales the method is still convincing and provides the behavior of inextensible membranes. Additionally, we restrict the error accumulation by adopting the global surface area constraint, yielding the jump condition

$$[\mathbf{S} \cdot \mathbf{n}]_\Gamma = \frac{\delta E}{\delta \Gamma} + \lambda_{local} H \mathbf{n} + \nabla_\Gamma \lambda_{local} + \lambda_{global} H \mathbf{n} \tag{3.69}$$

In order to overcome these problems Aland et al. [12] improved their approach by introducing a concentration c, normalized to 1, that is advected by the flow and stabilized by diffusion. Hence, its evolution reads

$$\partial_t c + \mathbf{v} \cdot \nabla c + c\mathbf{P}_\Gamma : \nabla v = d_c \nabla \cdot (\mathbf{P}_\Gamma \nabla c) \qquad \text{in } \Omega, \tag{3.70}$$

where d_c is a small diffusion coefficient. A restriction of the evolution of c to the surface, a diffuse interface approach, see eq. (2.39), may also be used. The concentration identifies those parts of the membrane that becomes stretched ($c < 1$) and compressed ($c > 1$). Finally, they extend eq. (3.68) to

$$\xi \varepsilon^2 \nabla \cdot (\phi^2 \nabla \lambda_{local}) + \delta_\phi \mathbf{P}_\phi : \nabla \mathbf{v} = \xi_2 \frac{c-1}{c} \delta_\phi \quad \text{in } \Omega \tag{3.71}$$

by a penalty term. This approach is similar to that proposed by [32] and can be related to an elastic energy

$$\mathcal{E}_{el} = \int_\Gamma \frac{K}{2} (1-c)^2 \,\mathrm{ds}. \tag{3.72}$$

It has been shown in [12] that the second approach is more accurate but it is necessary to deal with an additional equation for c, whose diffusion parameter d_c has to be chosen carefully. Dealing with the evolution equation for c may also lead to further time and mesh restriction that can increase the computational costs.

Remark 3.3 We can show that the first approach fulfills thermodynamic consistency. To show this, we repeat the overall energy, eq. (2.55) with constant density $\rho = 1$:

$$\frac{\mathrm{d}\mathcal{E}}{\mathrm{dt}} = \mathrm{Re} \int_\Omega \mathbf{v} \cdot \partial_t \mathbf{v} + \frac{\delta \mathcal{E}_S}{\delta \phi} \partial_t \phi \tag{3.73}$$

Setting the flux as

$$\mathbf{J} = -\gamma \nabla \frac{\delta \mathcal{E}_S}{\delta \phi} \tag{3.74}$$

and body force as

$$\mathbf{F} = \frac{\delta \mathcal{E}}{\delta \phi} \nabla \phi + \nabla \cdot (\delta_\phi \mathbf{P}_\phi \lambda_{local}), \tag{3.75}$$

inserting eq. (2.56) and eq. (2.58) into eq. (3.73), perfoming the same steps as in Section 2.8, inserting eq. (3.68) and partial integration yield the energy law

$$\frac{\mathrm{d}\mathcal{E}}{\mathrm{dt}} = \int -\mathbf{D} : \eta(\phi)\mathbf{D} - \gamma \left| \nabla \frac{\delta \mathcal{E}_S}{\delta \phi} \right|^2 - \xi \varepsilon^2 \phi^2 |\nabla \lambda_{local}|^2 \, \mathrm{d}\mathbf{x} \leq 0. \tag{3.76}$$

3.5. Hydrodynamic Navier-Stokes-Helfrich model with surface tension

Experiments have shown that especially crawling cells do not conserve their surface area [133]. As already mentioned in Section 3.1, myosin motors within the actin cell cortex lead to contraction of the cortex. As the cortex is highly connected to the cell membrane we observe a curvature minimizing effect [88] that can be understood as an effective surface tension. Thus, we extend the Helfrich energy with the surface tension energy eq. (2.29) [228] that reads

$$E_S(\Gamma) = E_H(\Gamma) + E_{ST}(\Gamma) = \frac{4\sqrt{2}}{3} \frac{1}{\mathrm{Be}} \int_\Gamma (H - H_0)^2 \, \mathrm{ds} + \frac{2\sqrt{2}}{3} \frac{1}{\mathrm{Ca}} \int_\Gamma \mathrm{ds} \tag{3.77}$$

in a non-dimensional sharp interface formulation. Within the diffuse interface formulation the surface energy becomes

$$\mathcal{E}_S(\phi) = \int_\Omega \frac{1}{\mathrm{Be}} \frac{1}{2\varepsilon} \left(\varepsilon \Delta \phi - \frac{1}{\varepsilon} W_0'(\phi) \right)^2 + \frac{1}{\mathrm{Ca}} \left(\frac{\varepsilon}{2} |\nabla \phi|^2 + \frac{1}{\varepsilon} W(\phi) \right) \mathrm{d}\mathbf{x}. \tag{3.78}$$

If ε tends to zero $\mathcal{E}_S(\phi) \to E_S(\Gamma)$, which has shown for the first part e.g. in [27] and for the second part in [188]. The Γ-convergence of the whole energy for $\varepsilon \to 0$ was shown in [212]. We also refer to the literature mentioned in previous sections. Similar to Section 3.4.2 the diffuse interface Navier-Stokes-Helfrich model with surface tension can be derived from the inner energy of the system that is given by

$$\mathcal{E}(\mathbf{v}, \phi) = \mathcal{E}_{kin}(\phi) + \mathcal{E}_S(\phi).$$

Performing the steps of the energy variation approach the resulting momentum equation reads

$$\begin{aligned} \mathrm{Re}(\partial_t \mathbf{v} + (\mathbf{v} \cdot \nabla)\mathbf{v}) + \nabla p = \nabla \cdot (\eta(\phi)\mathbf{D}) + \frac{1}{\mathrm{Be}} \nabla \cdot (\nabla \phi \otimes \nabla \mu - \mu \nabla \nabla \phi) \\ - \frac{1}{\mathrm{Ca}} \varepsilon \nabla \cdot (\nabla \phi \otimes \nabla \phi), \end{aligned} \tag{3.79}$$

where $\mathbf{S}_{pen}$ is replaced by the surface tension stress

$$\mathbf{S}_{ST} = -\frac{1}{\mathrm{Ca}} \varepsilon \nabla \phi \otimes \nabla \phi. \tag{3.80}$$

From the definition of the surface energy eq. (3.78), we can reformulate the momentum equation using Remark 3.2 which together with the incompressibility condition yield

$$\mathrm{Re}(\partial_t \mathbf{v} + (\mathbf{v} \cdot \nabla)\mathbf{v}) + \nabla p = \nabla \cdot (\eta(\phi)\mathbf{D}) + \frac{\delta \mathcal{E}_S}{\delta \phi} \nabla \phi, \tag{3.81}$$

$$\nabla \cdot \mathbf{v} = 0, \tag{3.82}$$

If we adopt a L^2-gradient flow for the evolution of ϕ we get

$$\partial_t \phi + \mathbf{v} \cdot \nabla \phi = -\gamma \frac{\delta \mathcal{E}_S}{\delta \phi}, \tag{3.83}$$

$$\frac{\delta \mathcal{E}_S}{\delta \phi} = \frac{1}{\mathrm{Be}} \left(\Delta \mu - \frac{1}{\varepsilon^2} W_0''(\phi)\mu \right) + \frac{1}{\mathrm{Ca}} \kappa + \lambda_{volume}, \tag{3.84}$$

$$\lambda_{volume} = \frac{1}{|\Omega|} \int_\Omega \frac{1}{\mathrm{Be}} \left(-\Delta \mu + \frac{1}{\varepsilon^2} W_0''(\phi)\mu \right) - \frac{1}{\mathrm{Ca}} \kappa \, \mathrm{d}\mathbf{x}, \tag{3.85}$$

we where we achieve volume conservation using a Lagrange multiplier, with μ and κ defined above in eq. (3.63) and eq. (3.64). Applying an H^{-1}-gradient flow, we obtain

$$\partial_t \phi + \mathbf{v} \cdot \nabla \phi = \gamma \Delta \frac{\delta \mathcal{E}_S}{\delta \phi}, \tag{3.86}$$

$$\frac{\delta \mathcal{E}_S}{\delta \phi} = \frac{1}{\mathrm{Be}} \left(\Delta \mu - \frac{1}{\varepsilon^2} W_0''(\phi)\mu \right) + \frac{1}{\mathrm{Ca}} \kappa, \tag{3.87}$$

which together with eq. (3.81) and eq. (3.82) constitute the conserved diffuse interface Navier-Stokes-Helfrich model with surface tension. Here, all equations are defined on $I \times \Omega$. In fact, neglecting the Helfrich stress, we have the stress resulting from a normal fluid-fluid interface, see Section 2.8. The initial and boundary conditions are obtained from Section 3.4.1.

Part I.

Hydrodynamic diffuse interface models for cell motility

CHAPTER 4

Introduction to Cell Motility

In various applications of living things cell motility plays a crucial role. As part of the immune system neutrophils respond to bacterial invasion and follow their signals. In wound healing processes keratinocytes as part of the epidermis try to migrate into the destroyed parts and close the wound. Furthermore, cancer cells spread out from their initial tumor and can create new metastases in the whole body. See Fig. 4.1 for some examples. Understanding these processes in many biological and biomedical processes helps to improve current medical therapies. Because of their complexity and the involved small length scales, a full understanding of the mechanisms behind cell motility is still missing. Certainly, the movement can be very different and span several physical scales. For instance the motion of a neutrophil can be compared to that of a sports car while the movement of a keratinocyte is more like a caterpillar. Although not mathematical, Abercrombie [4] proposed a model for cell motility (Fig. 4.2) that paved the way for all following models. Since the early attempts [15, 61, 62] to understand cell motility, mathematical models have been playing an important role and a large community has evolved. To get a broad overview we refer to [55, 103, 124, 189] for a review.

Different generic mechanisms have been proposed to describe motility in different situations. Many eukaryotic cells for example move using a crawling motion that can be relatively stable steady-state or constantly deforming. Responsible for this are processes of protrusion and retraction that are both driven by the turnover and reorganization of the actin cytoskeleton consisting of small rod-like protein bundles, the actin filaments. Two abilities of actin filaments are exploited by the cell in order to move: the ability to push by polymerization and the ability to contract by interacting with myosin. Together with the creation of new and the release of old adhesion sites, forces are mediated to the substrate that push the cell forward, see also Fig. 4.2. To be more precise, actin filaments

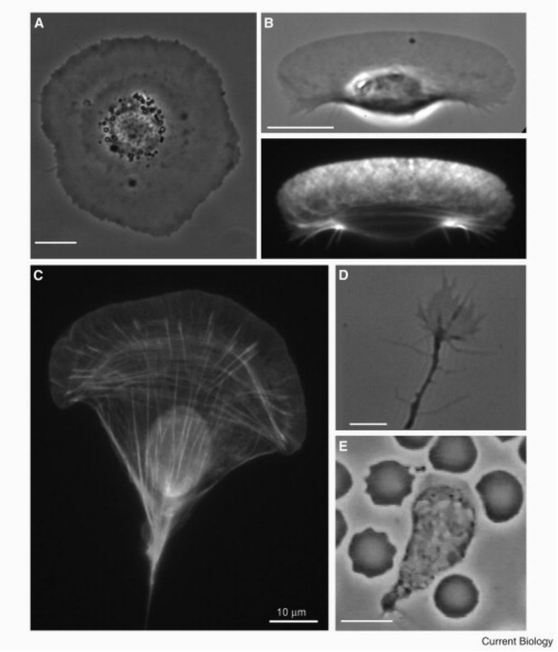

Figure 4.1. – Diverse shapes of motile cells obtained from microscopy. (a) stationary keratocyte (b) motile keratocyte (c) moving fibroblast (d) growth cone of a rat neuron (e) human neutrophil surrounded by red blood cells (Picture retrieved from [189])

polymerize at their front and drive the extension of sheet-like and rod-like protrusions of the cell membrane, while depolymerization takes place at the rear of the filaments. The underlying treadmilling process at the cell front if combined with local adhesion of the cell on a substrate leads to macroscopic motion. The treadmilling process and the associated crawling motion have been studied from a microscopic point of view, see e.g. [63, 190]. Continuum models, which allow for spatial and temporal resolution, have been considered for such a crawling motility mechanism in [87, 194, 214, 228, 229, 270, 272].

Preceding to the mechanical mechanisms for cell motility is a polarization of the cell, where a front and a rear has to be defined as a result of a spatial stimulus. Polarization is understood as a redistribution of several proteins, e.g. Rho family GTPases, and can be described by complex reaction kinetics within a signaling network [87, 174, 228, 246]. All these approaches use a reaction-diffusion system along the cell membrane and/or within the bulk to effectively account for actin polymerization and retraction and combine it with a mechanical or hydrodynamic model for cell dynamics. This allows us to describe the morphology and evolution of eukaryotic cells and link it to realistic signaling networks, e.g. as considered in [208, 209]. A mathematical model describing those phenomena is developed in Chapter 5. Since polymerization yields a reorganization of the actin cytoskeleton, other approaches describe polarity with an active gel theory where the direction of the filaments and consequently the polarity is represented by a macroscopic orientation field [176, 242, 270–272].

The active gel theory can be applied to other motility mechanisms that are less

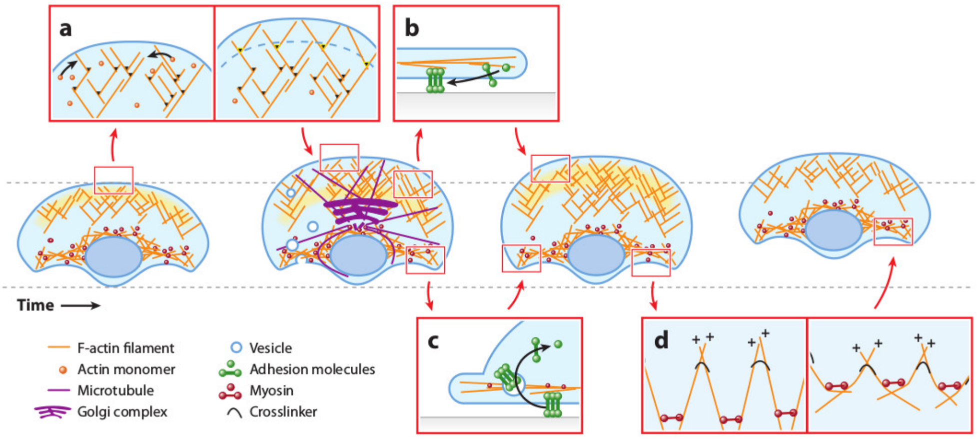

Figure 4.2. – Cartoon for cell motility. (a) Actin filaments polymerize at the cell front and push against the cell membrane. (b) New adhesion sites are created to the substrate at the front. (c) Release of old adhesion sites at the cell rear. (d) Contractile stress pushes the whole cell body forward. (d) Forces are mediated through the adhesion sites to the substrate. (Picture retrieved from [55])

explored but necessary in situations in which local adhesion is less evident [112, 119, 131, 202, 259]. In Chapter 6 we consider the motility mechanism arising by contractile stress due to the interaction of myosin and the actin filaments. Microscopically, myosin motor complexes use the energy from ATP hydrolysis to grab on neighboring actin filaments and exert stress. This process is also known for eukaryotic cells where it shapes the rear of the cell but it can also lead to motility itself. Here, the exerted stress is contractile and leads to a microscopic quadrupole flow around the myosin-actin complexes. A hydrodynamic active polar gel theory can be used to model these phenomena on a continuum level, see [131, 139–141, 203].

Cellular shapes change dynamically in striking ways as a result of mechanical interactions and complex reactions within the cell interior and on the cellular membrane. Many studies neglect the influence of the cell membrane to the shape of motile cells, but in [181] it has been argued that the actin filaments play a crucial role in the generation and remodeling of high membrane curvature regions. Moreover, depending on the observed time scales and cell types the physics of the membrane lipid bilayer cannot be neglected, see also Section 3.1.

Accordingly, we apply the Helfrich energy [121] where we consider the elastic properties of the membrane accounting for bending and surface tension. Within such an approach the membrane is considered as an elastic sheet and its evolution is driven by energy minimization. The surface tension is motivated since experiments have shown that especially crawling cells do not conserve their surface area [133]. As already mentioned in Section 3.1, myosin motors within the actin cell cortex lead to a contraction of the cortex. As the cortex is highly connected to the cell membrane, we observe a curvature minimizing effect [88] that can effectively be described by surface tension. Previous attempts in this direction have e.g. been considered in [87, 169, 170, 228, 229, 246, 272].

Within our approach, we consider a two-dimensional description of the cell since the height of the cell is small compared to its length. The underlying mathematical model is given in Section 3.5, where the bulk and the surrounding of the cell are regarded as Newtonian fluids. In fact, a crawling cell is strongly affected by the physics of its cytoskeleton within the bulk [29, 131, 251]. The first model accounts for viscous stress in the cell interior where we can adjust the viscosity ratio between bulk and extracellular matrix. Additionally, the second model considers the bulk as a solution of actin filaments described by active polar gel approach. Both models are far from equilibrium as a spontaneously occurring symmetry breaking event causes cell motility: a Turing-type instability within a biochemical network in the first model, Chapter 5 and a generic splay instability within an orientation field in the second model, Chapter 6.

Chapter 5

A model for membrane protrusion using a signaling network for GTPases

The processes of protrusion and retraction during cell movement are driven by the turnover and reorganization of the actin cytoskeleton. Within a reaction-diffusion model that combines processes along the cell membrane with processes within the cytoplasm, a Turing type instability is used to form the necessary polarity. This polarity distinguishes between cell front and rear and initiates the formation of different organizational arrays within the cytoplasm leading to protrusion and retraction. We use a simplified biochemical network model for the activation of GTPase which accounts for the different dimensionality of the cell membrane and the bulk. Moreover, it is combined it with a classical Helfrich-type model to account for bending and stiffness effects of the cell membrane. In addition, streaming within the cytoplasm and the extracellular matrix is taken into account. Combining these phenomena allows us to simulate the dynamics of cells and to reproduce the primary phenomenology.

This chapter is organized as follows: in Section 5.1 we introduce a minimal biochemical network model for the activation of GTPase to initiate the crawling motion. We further extend the diffuse interface Navier-Stokes-Helfrich model with surface tension by an active force that links the mechanical and biochemical model, as shown in Section 5.2. In Section 5.3, we also briefly describe the numerical approach to solve the coupled system and we furthermore perform convergence tests to numerically validate our method. Simulation results are discussed in Section 5.4, which include the formation of lamellipodia and filopodia-like structures, the response of the cell according to a chemoattractant

in the extracellular matrix and various parameter studies on the influence of bending rigidity and surface tension. Conclusions are drawn in Section 5.5, which also includes a discussion of generalizations of the model, extensions towards specific cell types and the combination with an additional orientation field describing the direction of the actin filaments, which is studied in Chapter 6.
The basic concepts, such as modeling, numerical methods and results discussed in this chapter are already published in Marth [173].

5.1. Cell polarity as a result of a Turing type instability

Proteins associated with actin are generally classified as actin binding-, actin associated- or actin modulating-proteins. Members of the Rho family of small GTPases have been shown to operate in distinct pathways signaling the formation of different organizational arrays of the actin filaments in the actin cytoskeleton. Rac and Cdc42 signal the formation of lamellipodia and filopodia, respectively, and Rho signals the formation of actin stress fibre bundles for the cell retraction. We thus need a detailed signaling network of small GTPases with the ability to distinguish between cell front and rear, which can be achieved through polarization. Various models have been proposed, see [130] for a review and comparison of mathematical models for single eukaryotic cells. One of the most detailed models is based on a Turing-type instability [115]. Such models are useful to consider, as the Turing instability can lead to spontaneous polarization. However, such a diffusion driven instability typically requires large differences in the diffusion coefficient of the involved species. This might not be realistic in our case as diffusion coefficients for proteins are similar to each other. However, diffusion along the cell membrane and within the cytoplasm can be different. Moreover, association and disassociation between the cell membrane and the cytoplasm might differ for various proteins. Taking these processes into account might form more realistic Turing mechanism [152]. Models that distinguish between cytoplasm and cell membrane have already been proposed for the investigation of cell polarity. In [16] a model of positive feedback is considered in which a single species of diffusible, membrane-bound signaling molecules can self-recruit from a cytoplasmic pool in the bulk. In this model, the polarization frequency has an inverse dependence on the number of signaling molecules. The frequency of polarization decreases as the number of molecules becomes large, which suggests that positive feedback can work alone or with additional mechanisms to create robust cell polarity. The results of [258] on the regulation of GTPase Cdc42 suggest that cell polarity is established through coupling of transport and signaling pathways and maintained actively by balance of flux between the cytoplasm and the membrane. A similar cytoskeleton-dependent mechanism that could account for the intrinsic ability of cells to polarize in response to Cdc42 activation was proposed in [257] and [170]. The mechanism involves a positive feedback loop between Cdc42-dependent actin polymerization and the delivery of Cdc42 to the plasma membrane. The detailed model that we introduce in the following section for signaling networks of the GTPase cycle accounting for the coupling of membrane bound and cytoplasmic processes has been shown to lead to a Turing instability in [207–209].

5.2. Mathematical model

5.2.1. Biochemical model for GTPases

The biochemical model for GTPases considers diffusion in the cell bulk and a reaction-diffusion system along the membrane combined with a flux boundary condition. The different dimensionality of the membrane and the bulk, as we have introduced in Section 2.6.3, is taken into account within the reaction-diffusion processes. Moreover, the model distinguishes between membrane-bound active and inactive state of the GTPases for which the concentrations are denoted by c_1 and c_2, respectively, and complexes of a cytoplasmic GTPase, denoted by C, see Fig. 5.1 for a schematic description.

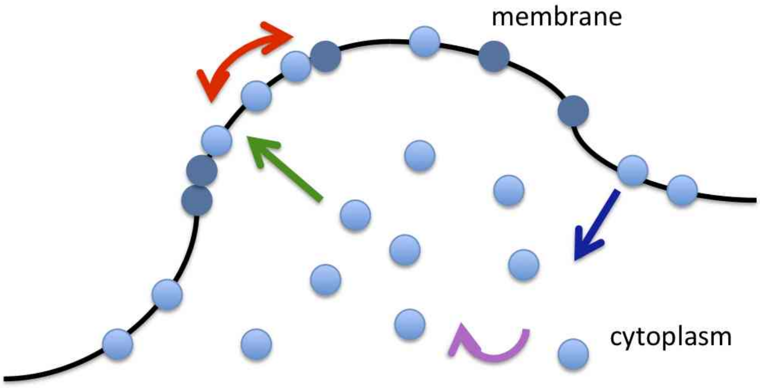

Figure 5.1. – Schematics of GTPase cycle. Colored arrows indicate various molecular transport mechanisms: red - diffusion along the membrane, purple - diffusion within the cytoplasm, green - association with the membrane, blue - disassociation from the membrane.

The model accounts for activation of GTPase by exchange of GDP by GTP, and inactivation by hydrolysis and dephosphorylation of GTP to GDP that are catalyzed by GEF and GAP protein, respectively. The resulting model reads in dimensionless form

$$\partial_t C + \nabla \cdot (C\mathbf{v}) = D_C \Delta C \qquad \text{in } I \times \Omega_1, \tag{5.1}$$

$$\partial_t c_1 + \nabla_\Gamma \cdot (\mathbf{v}c_1) = d_{c_1} \Delta_\Gamma c_1 + \bar{\gamma} h(c_1, c_2) \qquad \text{on } I \times \Gamma, \tag{5.2}$$

$$\partial_t c_2 + \nabla_\Gamma \cdot (\mathbf{v}c_2) = d_{c_2} \Delta_\Gamma c_2 - \bar{\gamma} h(c_1, c_2) + \bar{\gamma} q(c_1, c_2, C) \qquad \text{on } I \times \Gamma, \tag{5.3}$$

with the flux boundary condition

$$-D_C \nabla C \cdot \mathbf{n} = \bar{\gamma} q(c_1, c_2, C) \qquad \text{on } I \times \Gamma, \tag{5.4}$$

coupling the equations along the membrane and within the cytoplasm. The first equation is valid in the cytoplasm denoted by Ω_1 and the last two equations are defined on the cell membrane Γ. Since the cell moves in time with velocity $\mathbf{v}$, we also have to account

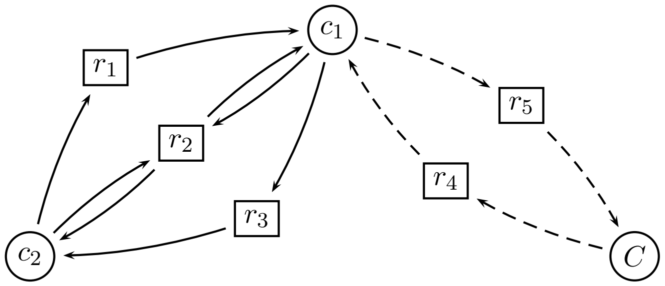

Figure 5.2. – Reaction network. The bipartite graph has two types of nodes, molecular species c_1, c_2 and C, and the reactions between them, denoted by r_i, $i = 1, \ldots, 5$, the index corresponds to the index of the kinetic coefficients. Directed edges of the graph represent the flow of the reaction fluxes. Solid edges indicated processes on the membrane and dashed edges processes within the cytoplasm, including association and disassociation.

for advection within the reaction-diffusion system. All quantities are assumed to be defined off the membrane. We assume a constant extension in normal direction $\mathbf{n}$, which is defined to point outwards. Similar reaction-diffusion models have been considered e.g. in [239] for related surfactant models on a deformable surface. The reaction kinetics in the equations are denoted by

$$h(c_1, c_2) = a_1 c_2 + a_2 \frac{c_1}{b_1 + c_1} c_2 - a_3 \frac{c_1}{b_2 + c_1}, \tag{5.5}$$

and the association and disassociation are modeled by

$$q(c_1, c_2, C) = a_4 C (1 - c_1 - c_2)_+ - a_5 c_2, \tag{5.6}$$

which follows from a Langmuir law as we have seen in eq. (2.44) following [238]. It models the membrane association as a reaction between the cytoplasmic GTPase complex and a free site on the membrane. $(.)_+$ thereby denotes the positive part of $(.)$ and takes into account that association of inactive GTPases occurs until the membrane is saturated. The system is given in dimensionless form with diffusion coefficients D_C, d_{c_1} and d_{c_2} in the cytoplasm and along the membrane, respectively. a_i are kinetic coefficients, b_i kinetic parameters, $\bar{\gamma}$ a dimensionless scaling factor. Fig. 5.2 shows the corresponding reaction network as a bipartite graph, distinguishing processes along the membrane and within the cytoplasm.

In [208] the velocity terms in the equations are neglected and the system is further reduced by assuming C to be spatially constant as a result of a larger diffusivity in the cytoplasm as along the membrane. Moreover, a linear stability analysis for the reduced system was shown to lead to a Turing instability for appropriate parameters. More recently, a Turing instability has also been found for the biologically more interesting regime in which $d_{c_1} = d_{c_2}$, see [207, 209]. Now, only different diffusivities within the cytoplasm and along the cell membrane as well as different association/disassociation coefficients are required to form Turing patterns. We will consider these parameters also for the evolving situation.

5.2.2. Coupling the mechanical and biochemical model

We combine the biological network with the hydrodynamic diffuse interface Navier-Stokes-Helfrich model with surface tension eq. (3.81)-(3.85). Here, we account for streaming effects within the cytoplasm. The Helfrich model considers a non-conserved L^2-gradient flow of the surface energy. In order to ensure the impermeability of the cell membrane, the model includes the calculation of a Lagrange multiplier. Consequently, the dynamics of the cell are modeled as a combined process of energy minimization for kinetic, bending and surface tension energy. A migrating cell is a thermodynamic system far from equilibrium where an active force constantly consumes energy to exert work to propel the cell. Accordingly, the jump condition becomes

$$[\mathbf{S} \cdot \mathbf{n}]_\Gamma = \frac{\delta E}{\delta \Gamma} + \frac{1}{\mathrm{Fa}} c_1 \mathbf{n}, \tag{5.7}$$

accounting for bending and surface tension and the active component associated with actin polymerization associated with the active state of the membrane bound GTPase c_1. The resulting protrusion force from the last contribution acts in normal direction [213] and its strength is related to c_1 [229, 229, 246] and scaled by the dimensionless quantity

$$\mathrm{Fa} = \frac{\eta_0 V}{\alpha L}, \tag{5.8}$$

called the active surface force number. Within our diffuse interface approach, the active force term reads $-\frac{1}{\mathrm{ReFa}} c_1 \nabla \phi$ and is added to the right-hand side of the momentum equation eq. (3.81). For simplicity, we neglect any retraction force. In the current model, we also do not consider adhesion explicitly. Possible extensions of the model in these directions are discussed in the Section 5.5.

5.2.3. Governing equations

We extend the reaction-diffusion system eq. (5.1)-(5.1) to the whole domain Ω by applying a diffuse interface approach, see Section 2.6.3 and eq. (2.45)-(2.46) in particular. So far, all quantities defined within the bulk, within the extracellular matrix and along the membrane are extended to the larger domain Ω and the governing equations are reformulated using the phase field variable. This allows us to circumvent the numerical subtleties in solving differential equations on evolving surfaces or within evolving domains. The dynamics of the cell is now governed by equations that couple the velocity field to the actual physical degrees of freedom along the membrane, in the bulk and the extracellular matrix. Finally, we may write down the highly coupled system that involves many nonlinearities and can be separated into three parts defined in $I \times \Omega$:

First, the Navier-Stokes equations read as

$$\mathrm{Re}\left(\partial_t \mathbf{v} + (\mathbf{v} \cdot \nabla)\mathbf{v}\right) + \nabla p = \nabla \cdot (\eta(\phi)\mathbf{D}) + \frac{\delta \mathcal{E}_S}{\delta \phi}\nabla \phi, \tag{5.9}$$

$$\nabla \cdot \mathbf{v} = 0, \tag{5.10}$$

determining the flow field. The second part determines the evolution of the interface given by a regularized advection equation for the phase field:

$$\partial_t \phi + \mathbf{v} \cdot \nabla \phi = -\gamma \frac{\delta \mathcal{E}_S}{\delta \phi}, \tag{5.11}$$

$$\frac{\delta \mathcal{E}_S}{\delta \phi} = \frac{1}{\mathrm{Be}}\left(\Delta \mu - \frac{1}{\varepsilon^2} W_0''(\phi)\mu\right) + \frac{1}{\mathrm{Ca}}\kappa + \lambda_{area}, \tag{5.12}$$

$$\mu = \varepsilon \Delta \phi - \frac{1}{\varepsilon} W_0'(\phi), \tag{5.13}$$

$$\kappa = -\varepsilon \Delta \phi + \frac{1}{\varepsilon} W'(\phi), \tag{5.14}$$

where $\gamma > 0$ is set as small as possible. In this case, we ensure volume conservation applying a Lagrange parameter given by

$$\lambda_{area} = \frac{1}{|\Omega|}\int_\Omega \frac{1}{\mathrm{Be}}\left(-\Delta \mu + \frac{1}{\varepsilon^2} W_0''(\phi)\mu\right) - \frac{1}{\mathrm{Ca}}\kappa \, \mathrm{d}\mathbf{x}. \tag{5.15}$$

Within the third part, we now determine the GTPase concentration in the updated domain

$$\partial_t(\tilde{\phi} C) + \nabla \cdot (\tilde{\phi}\mathbf{v}C) = D_C \nabla \cdot \left(\tilde{\phi}\nabla C\right) - \bar{\gamma}|0.5\nabla \phi| q(c_1, c_2, C), \tag{5.16}$$

$$\partial_t(|\nabla \phi| c_1) + \nabla \cdot (|\nabla \phi|\mathbf{v}c_1) = d_{c_1} \nabla \cdot (|\nabla \phi|\nabla c_1) + \bar{\gamma}|\nabla \phi| h(c_1, c_2), \tag{5.17}$$

$$\partial_t(|\nabla \phi| c_2) + \nabla \cdot (|\nabla \phi|\mathbf{v}c_2) = d_{c_2} \nabla \cdot (|\nabla \phi|\nabla c_2) - \bar{\gamma}|\nabla \phi| h(c_1, c_2), \tag{5.18}$$

with $\tilde{\phi} = \frac{1}{2}(1 + \phi)$ a rescaled phase-field function, which serves as an approximation of the characteristic function of $\Omega_1(t)$, $\tilde{\phi} \approx 1$ in the cytoplasm and $\tilde{\phi} \approx 0$ in the extracellular matrix.

The primary unknowns are velocity $\mathbf{v}$, pressure p, phase-field variable ϕ, and the concentrations c_1, c_2 and C. All other quantities are introduced to reformulate the higher order equation for ϕ into a system of second order equations, and λ_1 and $\tilde{\phi}$ are the Lagrange parameter, introduced to fulfill the volume constraint, and a rescaled phase-field function, respectively.

The coupled system obeys the following initial conditions

$$\mathbf{v}(t, \mathbf{x}) = \mathbf{v}^0(\mathbf{x}),\ \phi(t, \mathbf{x}) = \phi^0(\mathbf{x}),\ C(t, \mathbf{x}) = C^0(\mathbf{x}),\ c_1(t, \mathbf{x}) = c_1^0(\mathbf{x}),\ c_2(t, \mathbf{x}) = c_2^0(\mathbf{x}),$$

for $t = 0$ and $\mathbf{x} \in \Omega$, which are specified below, and the following Dirichlet boundary conditions

$$\mathbf{v}(t,\mathbf{x}) = \mathbf{0},\ \phi(t,\mathbf{x}) = -1,$$

and Neumann boundary conditions

$$\nabla\mu \cdot \mathbf{n} = \nabla\kappa \cdot \mathbf{n} = \nabla C \cdot \mathbf{n} = \nabla c_1 \cdot \mathbf{n} = \nabla c_2 \cdot \mathbf{n} = 0,$$

which hold for $t > 0$ and $\mathbf{x} \in \partial\Omega$. We use the same dimensionless quantities as before: the Reynolds number Re, the bending capillary number Be, which was similarly defined in [32, 218], the capillary number Ca and the active surface force number Fa that characterizes the strength of the cell protrusion.

Formal matched asymptotic analysis results showing the convergence to the sharp interface equations are not available. However, numerical convergence studies in [70, 74, 75] confirm the diffuse interface approximation without the protrusion force.

Furthermore, for the diffuse formulation of the reaction-diffusion system formal convergence to the sharp interface equations can be achieved following the general treatment in [153, 210, 238]. See also Section 2.6 for an overview.

5.2.4. Parameters

The parameters in our model follow either from experimental measurements or other simulation approaches. In order to relate the dimensionless numbers to measured values, we introduce a characteristic length $L = 5 \cdot 10^{-6}\,\mathrm{m}$, a typical cell radius and a characteristic velocity $V = 0.14 \cdot 10^{-6}\,\mathrm{m/s}$, a typical velocity of a moving cell, see e.g. [228, 229] and the references therein. We further consider the density of the cytoplasm $\rho = 10^3\,\mathrm{kg/m^3}$, which corresponds to that of water. As already mentioned, for simplicity, we consider a constant value for the viscosity in the cytoplasm and the extracellular matrix, which is estimated to be $\eta = 10\,\mathrm{Pa\,s}$. For the Reynolds number, we thus obtain $\mathrm{Re} = 7 \cdot 10^{-11}$, which is much smaller than the considered values in [32, 217, 218], where $\mathrm{Re} = 10^{-3}$ is used. To allow for comparison with these studies, we also use $\mathrm{Re} = 10^{-3}$ in our simulations. Hence, in both cases, inertia can be neglected. However, we still consider these terms for sake of completeness.

The bending capillary number Be and the capillary number Ca are determined by $b_N = 10^{-17}\,\mathrm{J}$ and $\sigma = 5 \cdot 10^{-6}\,\mathrm{N/m}$, respectively, which are measured for Dictyostelium cells in [231] and used in [228] we obtain $\mathrm{Be} = 6.6$ and $\mathrm{Ca} = 0.264$. For simplicity, we neglect the spontaneous curvature and set $H_0 = 0$ in all computations. Finally, the active surface force number Fa characterizes the cell protrusion. The corresponding parameter is denoted by α, which has the dimension $\mathrm{N/m^2}$ and measures the strength of the protrusion. As this is an effective term there are no experimental data available for α. We define the strength of the protrusion force to be in the same order as the elasticity force due to bending. With $\alpha = 5.6\,\mathrm{N/m^2}$, we obtain $\mathrm{Fa} = 0.05$ and together with the other parameters the considered characteristic velocity V.

The diffusion coefficients along the membrane are $7 \cdot 10^{-13}\,\mathrm{m^2/s}$ and within the cytoplasm $1.4 \cdot 10^{-11}\,\text{m}^2/\text{s}$, see [208] and the references therein. Realistic reaction parameters are not available. The parameters adapted here follow from a stability analysis of the system leading to a Turing instability, see [209]. All parameters used in the simulations are given in Tab. 5.1.

Symbol	Description	Value
L	typical cell radius	$5 \cdot 10^{-6}\,\text{m}$
V	typical velocity of crawling cell	$0.14 \cdot 10^{-6}\,\text{m/s}$
ρ	fluid density	$10^3\,\text{kg/m}^3$
η	dynamic viscosity of the fluid	$10\,\text{Pa s}$
b_N	bending rigidity	$10^{-18} - 10^{-17}\,\text{J}$
σ	surface tension	$10^{-6} - 10^{-5}\,\text{N/m}$
α	coefficient protrusion force	$0.39\,\text{N/m}^2$ and $5.6\,\text{N/m}^2$
ε	boundary layer parameter	0.03
γ	mobility	$\frac{\gamma}{\text{Be}} = 0.01$
D_C	diffusion coefficient of cytoplasm	20
d_{c_1}	diffusion coefficient along the membrane for c_1	1
d_{c_2}	diffusion coefficient along the membrane for c_2	1
a_1	kinetic coefficient	0
a_2	kinetic coefficient	160
a_3	kinetic coefficient	1
a_4	membrane attachment parameter	0.333
a_5	membrane detachment parameter	10
b_1	kinetic parameter	20
b_2	kinetic parameter	0.5
$\bar{\gamma}$	scaling parameter	400

Table 5.1. – Mechanical and chemical parameters. The values for b_N correspond to measurements for artificial vesicles, erythrocytes, neutrophils and dictyostelium [93, 231, 235, 268], respectively. The values for σ follow from [231]. The boundary layer parameter ε is a numerical parameter and determines the width of the diffuse interface. The regularization parameter γ is chosen to depend on Be, see [217]. All parameters of the reaction-diffusion system are given in dimensionless form. The diffusion coefficients are defined as follows $D_C = \tilde{D_C}/\tilde{d_{c_1}}$ and $d_{c_1} = \tilde{d_{c_1}}/\tilde{d_{c_1}} = 1$, $d_{c_2} = \tilde{d_{c_2}}/\tilde{d_{c_1}} = 1$, where the $\tilde{}$ notation denotes the dimensionful diffusion coefficients. Together with kinetic parameters a_i, b_i and $\bar{\gamma}$ obtained from [209], they lead to a Turing instability.

5.3. Numerical approach

The systems of partial differential equations are discretized using the adaptive finite element toolbox AMDiS [252, 254]. We use an adaptively refined triangular mesh with a high resolution along the cell membrane to guarantee at least five grid points across the diffuse interface. We further explore an operator splitting approach [19, 109] that allows us to solve the subproblems of the flow field, the phase-field evolution, the Lagrange multiplier and the reaction-diffusion problem separately in an iterative process. This coupling is of linear order in time [19] and yields small time steps. A P^2/P^1 Taylor-Hood element is used for the flow problem. All other quantities are discretized in space using P^2 elements. Here, we do not specify a fully discretized scheme, because the space discretization is straightforward. However, for a fully discrete finite element scheme of a related system, we refer to Section 6.3. In time, a semi-implicit discretization is used that together with an appropriate linearization of the involved non-linear terms leads to a set of linear systems in each time step for which the direct solver UMFPACK [57] is used. We split the time interval $I = [0,T]$ into equidistant time instants $0 = t_0 < t_1 < \dots$ and define the time steps $\tau := t^{n+1} - t^n$. We use $\tau = 10^{-3}$ for all computations. Of course, adaptive time steps may also be used. We define the discrete time derivative $d_t \cdot^{n+1} := (\cdot^{n+1} - \cdot^{n})/\tau$, where the upper index denotes the time step number.

The numerical approach for each subproblem is adapted from existing algorithms for the Navier-Stokes problem, the Helfrich model and reaction-diffusion models. In each time step we solve:

1. The flow problem for $\mathbf{v}^{n+1}$ and p^{n+1}:

$$\begin{aligned}\mathrm{Re}\left(d_t\mathbf{v}^{n+1} + (\mathbf{v}^n \cdot \nabla)\mathbf{v}^{n+1}\right) = -\nabla p^{n+1} + \Delta\mathbf{v}^{n+1} + \frac{\delta\mathcal{E}_S}{\delta\phi}^n \nabla\phi^n - \frac{1}{\mathrm{Fa}}c^n\nabla\phi^n,\\ \nabla \cdot \mathbf{v}^{n+1} = 0.\end{aligned}$$

2. The phase field evolution for ϕ^{n+1}:

$$\begin{aligned} d_t\phi^{n+1} &= -\mathbf{v}^{n+1} \cdot \nabla\phi^{n+1} - \gamma\frac{\delta\mathcal{E}_S}{\delta\phi}^{n+1},\\ \frac{\delta\mathcal{E}_S}{\delta\phi}^{n+1} &= \frac{1}{\mathrm{Be}}\left(\Delta\mu^{n+1} - \frac{1}{\varepsilon^2}W_0''(\phi^{n,n+1})\mu^{n,n+1}\right) + \frac{1}{\mathrm{Ca}}\left(-\varepsilon\Delta\phi^{n+1} + \frac{1}{\varepsilon}W'(\phi^{n,n+1})\right)\\ &\quad + \lambda_{area}^n,\\ \mu^{n+1} &= \varepsilon\Delta\phi^{n+1} - \frac{1}{\varepsilon}W_0'(\phi^{n,n+1}).\end{aligned}$$

We further linearize the non-linear terms by a Taylor expansion of order one:

$$\begin{aligned}W_0''(\phi^{n,n+1})\mu^{n,n+1} = (3(\phi^n)^2 - 1)\mu^n + \begin{pmatrix}6\phi^n\mu^n\\ 3(\phi^n)^2 - 1\end{pmatrix}\begin{pmatrix}\phi^{n+1} - \phi^n\\ \mu^{n+1} - \mu^n\end{pmatrix},\\ W'(\phi^{n,n+1}) = ((\phi^n)^2 - 1)\phi^n + (3(\phi^n)^2 - 1)(\phi^{n+1} - \phi^n),\end{aligned}$$

and $W_0'(\phi)^{n,n+1}$ similarly.

3. The Lagrange multiplier λ_{area}^{n+1}:

$$\begin{aligned}\lambda_{area}^{n+1} = \frac{1}{|\Omega|}\int_\Omega & \frac{1}{\mathrm{Be}}\left(-\Delta\mu^{n+1} + \frac{1}{\varepsilon^2}W_0''(\phi^{n+1})\mu^{n+1}\right) \\ & - \frac{1}{\mathrm{Ca}}\left(-\varepsilon\Delta\phi^{n+1} + \frac{1}{\varepsilon}W'(\phi^{n,n+1})\right)\,\mathrm{d}\mathbf{x} \\ & + \frac{1}{2\tau}(\mathcal{V}(\phi^{n+1}) - \mathcal{V}_0).\end{aligned}$$

   This approach uses an additional penalty term, as proposed by [75] and given by eq. (3.83), because the explicit treatment violates the constraint, where $\mathcal{V}_0$ denotes the desired cell volume and $\mathcal{V}(\phi^{n+1}) = \int_\Omega \phi^{n+1}\,\mathrm{d}\mathbf{x}$ its actual state. The penalty parameter is related to the time step size τ.

4. The concentrations C^{n+1}, c_1^{n+1} and c_2^{n+1}:

$$\begin{aligned} d_t(\tilde{\phi}^{n+1}C^{n+1}) + \nabla\cdot(\tilde{\phi}^{n+1}\mathbf{v}^{n+1}C^{n+1}) &= D_C\nabla\cdot\left(\tilde{\phi}^{n+1}\nabla C^{n+1}\right) \\ &\quad - \bar{\gamma}|0.5\nabla\phi^{n+1}|q(c_1^{n+1}, c_2^{n+1}, C^{n+1}), \\ d_t(|\nabla\phi^{n+1}|c_1^{n+1}) + \nabla\cdot(|\nabla\phi^{n+1}|\mathbf{v}^{n+1}c_1^{n+1}) &= d_{c_1}\nabla\cdot(|\nabla\phi^{n+1}|\nabla c_1^{n+1}) \\ &\quad + \bar{\gamma}|\nabla\phi^{n+1}|h(c_1^{n+1}, c_2^{n+1}), \\ d_t(|\nabla\phi^{n+1}|c_2^{n+1}) + \nabla\cdot(|\nabla\phi^{n+1}|\mathbf{v}^{n+1}c_2^{n+1}) &= d_{c_2}\nabla\cdot(|\nabla\phi^{n+1}|\nabla c_2^{n+1}) \\ &\quad - \bar{\gamma}|\nabla\phi|^{n+1}|h(c_1^{n+1}, c_2^{n+1}) \\ &\quad + \bar{\gamma}|\nabla\phi|^{n+1}|q(c_1^{n+1}, c_2^{n+1}, C^{n+1}),\end{aligned}$$

   with $\tilde{\phi}^{n+1} = \frac{1}{2}(1+\phi^{n+1})$. We again further linearize the non-linear terms q and h according to the proposed approach in [208].

The numerical approach for each subproblem has already been validated elsewhere. We therefore consider here only convergence tests for the coupled problem. After reaching the desired pattern on the cellular membrane to distinguish between cell front and rear, which can be obtained by solving subproblem 4 on a stationary circular shape using the proposed parameters in [209], the whole system is solved. A deformation of the cell can be observed and a movement in the direction of the cell front. After an initialization state a stationary form and a constant velocity is reached. We measure the following quantities:

1. the x_1-coordinate of the center of mass, which is defined as

$$x_{cm} = \frac{\int_\Omega \tilde{\phi}x_1\,\mathrm{d}\mathbf{x}}{\int_\Omega \tilde{\phi}\,\mathrm{d}\mathbf{x}}, \tag{5.19}$$

   where $\mathbf{x} = (x_1, x_2)$,

2. the circularity of the cell, which is defined as the quotient of the perimeter of an

area-equivalent circle and the perimeter of the cell

$$c_{cell} = \frac{2(\int_\Omega \tilde{\phi}\pi \, \mathrm{d}\mathbf{x})^{1/2}}{\frac{3}{2\sqrt{2}}\mathcal{E}_{CH}}, \tag{5.20}$$

where $\mathcal{E}_{CH}$ serves as an approximation of the surface area, see e.g. eq. (3.11),

3. the velocity of the cell, which is defined as $v_{cm} = |\mathbf{v}(x_{cm}, x_2)|$,
4. and the Helfrich energy $\mathcal{E}_H = \frac{1}{2\varepsilon}\frac{1}{\mathrm{Be}}\int_\Omega \left(\varepsilon\Delta\phi - \frac{1}{\varepsilon}W_0'(\phi)\right)^2 \mathrm{d}\mathbf{x}$.

All defined quantities are time dependent. A relative error can be defined to measure their temporal evolution. We use the following error norm:

$$\|e\|_2 = ((\sum_I |q_{t,ref} - q_t|^2)/(\sum_I |q_{t,ref}|^2))^{1/2},$$

where q_t is the temporal evolution of quantity q. The solution on the finest grid serves as reference solution $q_{t,ref}$. Tab. 5.2 shows the relative error norms as well as the relative order of convergence (ROC) for the desired quantities if ε is reduced. Together with ε, we also refine the mesh size to guarantee the same number of grid points within the diffuse interface layer for all simulations and the time step to ensure the same relation between mesh size and time step. The time interval is $I = [0, 3.5]$, which corresponds to an end time of $T = 123$ s. Other parameters are obtained from Tab. 5.1, in particular $\mathrm{Be} = 6.6$, $\mathrm{Ca} = 0.264$ and $\mathrm{Fa} = 0.05$. We see at least first order convergence, the higher numbers in ROC for x_{cm}, v_{cm} and $\mathcal{E}_H$ are probably due to the fact that additionally for higher ε the interfacial profile of ϕ may be seriously distorted out of equilibrium so that the solution deviates far from the sharp-interface solution.

	center of mass x_{cm}		cell velocity v_{cm}		circularity c_{cell}		energy $\mathcal{E}_H$	
ε	$\|e\|_2$	ROC	$\|e\|_2$	ROC	$\|e\|_2$	ROC	$\|e\|_2$	ROC
0.060	0.0530		0.1895		0.0094		0.1177	
0.042	0.0168	3.3081	0.0630	3.1734	0.0075	0.6807	0.0771	1.2190
0.030	0.0044	3.8812	0.0272	2.4244	0.0045	1.4408	0.0334	2.4180
0.021	0.0004	6.7472	0.0094	2.9673	0.0024	1.7358	0.0127	2.7072

Table 5.2. – Relative error norms and convergence orders for critical parameters.

As a further consistency test, we consider conservation of mass and cell volume. The total mass is measured as $c = \int_\Omega (c_1 + c_2)|\tilde{\phi}| \, \mathrm{d}\mathbf{x} + \int_\Omega C\nabla\tilde{\phi} \, \mathrm{d}\mathbf{x}$ and the volume is estimated as $\mathcal{V} = \int_\Omega \tilde{\phi} \, \mathrm{d}\mathbf{x}$. Fig. 5.3 shows the evolution of both quantities over time for the same parameters as above, and demonstrates the required conservation.

5.4. Simulations and results

We consider the dependency of cell motility on various parameters: the bending stiffness b_N, the surface tension σ and the protrusion force parameter α. Modifying the

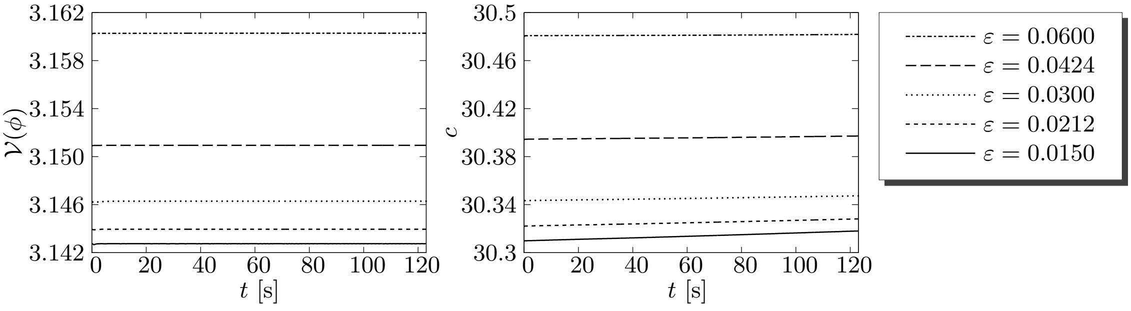

(a) volume conservation

(b) mass conservation

Figure 5.3. – Evolution of cell volume and mass of the GTPases for various parameters ε.

reaction-diffusion parameters also allows us to form either lamellipodia- or filopodia-like structures, which we demonstrate in an example. We further extend the model to consider chemotactic and compute the cell path according to a varying chemotaxis signal.

5.4.1. Mechanical dependency of motile cells

As initial condition, we consider a circular membrane of radius 1. To speed up the development of the Turing pattern, the simulation starts with a constant value $C = 9.25$ in $\Omega_1(0)$, $c_1 = 0.1758$ and $c_2 = 0.2186$ on the right-hand side of the cellular membrane and $c_1 = 0$ and $c_2 = 0$ on the left hand side. After a few iterations of the whole system, a stable Turing pattern with the desired polarity is formed. The resulting protrusion force leads to a movement to the right and a deformation of the cell shape forming a lamellipodia-like structure. Fig. 5.4 shows the time evolution of the phase field variable ϕ and the concentrations c_1, c_2 and C, respectively. The maximum of c_1 that signals the polymerization of the actin filament meshwork in our model is sharply localized at the cell front. The concentration profile of c_2 is less pronounced and the concentration of C within the cytoplasm shows only a small gradient towards the cell front. Both c_2 and C do not directly correspond to the cell movement in the considered model. We also show the velocity that reaches a maximum after the acceleration of the cell at the beginning before it is slowed down into a stationary profile leading to a stationary cell shape. During the stationary motion, two vortices over and beneath the cell occur. In this state, the shear stress and the stress corresponding to the Helfrich forces are in balance. The simulation is performed with $b_N = 10^{-17}$ J, $\sigma = 5 \cdot 10^{-6}$ N/m and $\alpha = 5.6$ N/m^2.

The stationary shape strongly depends on these parameters. To quantify the dependency, Fig. 5.5 shows the obtained stationary cell shapes for different bending stiffness b_N and different surface tension σ. For Fig. 5.5a, we vary the bending stiffness parameter and use a constant surface tension $\sigma = 2.5 \cdot 10^{-6}$ N/m. For Fig. 5.5b, we use different values for the surface tension and keep the bending stiffness $b_N = 10^{-17}$ J constant.

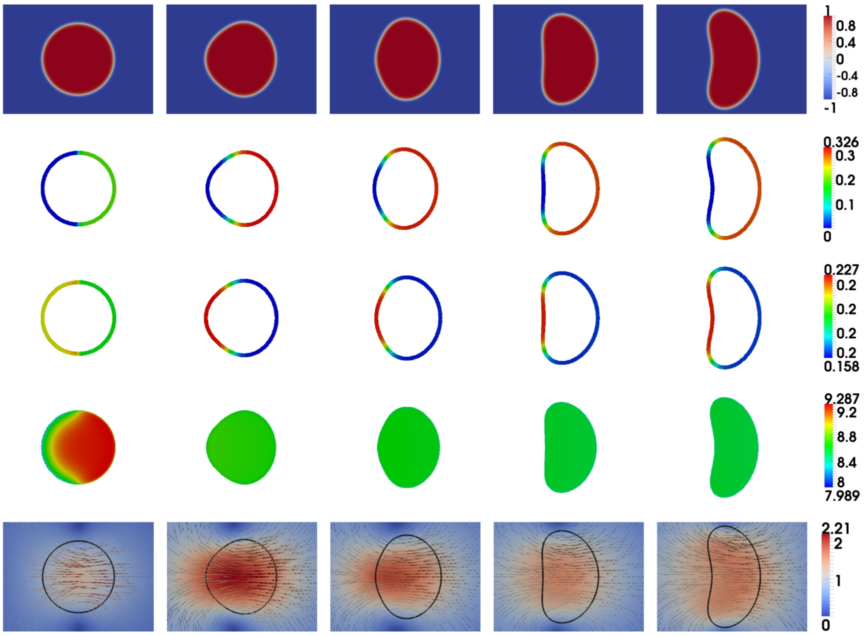

Figure 5.4. – Cell movement. First row - shape of the cell at different times evolving from left to right. Shown is the phase field variable ϕ. Second row - concentration of c_1 on cell membrane. Third row - concentration of c_2 on cell membrane. Forth row - concentration of C in the cytoplasm. Fifth row - magnitude and direction of $\mathbf{u}$. The maximum of $|\mathbf{u}|$ corresponds to $0.31 \cdot 10^{-6}$ m/s, which is in good agreement with the value reported in [229]. To visualize the concentrations along the cell membrane or in the cytoplasm the values of c_1 and c_2 and C are shown at the $[-0.9, 0.9]$ and $[0, 1]$ level sets of the phase field variable, respectively. The times t shown are 0.013, 0.3, 0.6, 1.2 and 8 which correspond to 4.64 s, 10.71 s, 21.43 s, 42.86 s and 250 s, from left to right.

$\alpha = 5.6$ N/m^2 is kept constant in all simulations.

As expected the cell remains more circular as stronger the bending stiffness and surface tension. More important, the results indicate that the influence of bending stiffness compared to surface tension is relatively small.

We now consider the influence of the protrusion force on the stationary cell shape. Fig. 5.5c shows the stationary cell shapes for different protrusion coefficients α. The other parameters are $b_N = 10^{-17}$ J and $\sigma = 5 \cdot 10^{-6}$ N/m. The dependency between protrusion and circularity as well as protrusion and velocity are shown in Fig. 5.6. These diagrams show that increasing α lead to more deformed (Fig. 5.6a) and faster cell (Fig. 5.6b). We further see that the difference between velocity peak and stationary velocity increases for increasing α. Additionally, the cell's stationary state is reached later. This is because the relaxation between Helfrich and surface tension on one side and protrusion on the other side also increases for higher protrusion and for smaller membrane stiffness, which is not shown here.

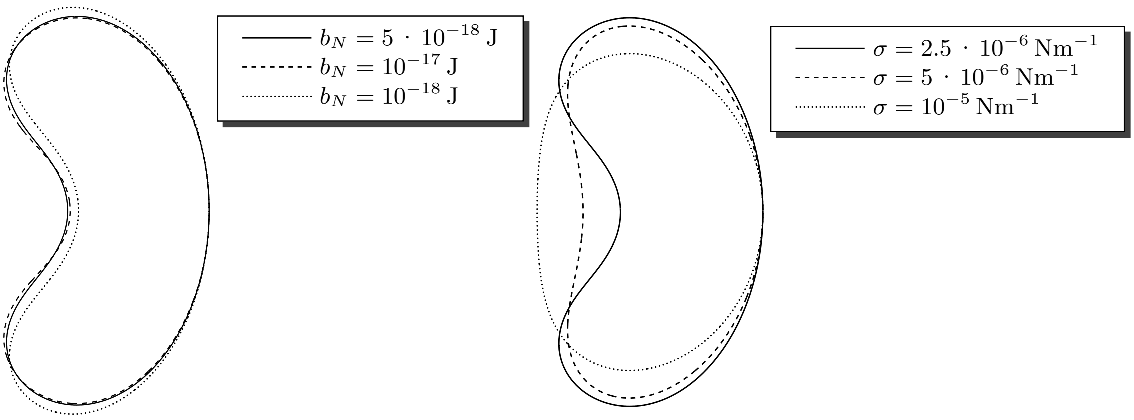

(a) $\sigma = 2.5 \cdot 10^{-6}\,\mathrm{N/m}$, $\alpha = 5.6\ \mathrm{N/m^2}$ **(b)** $b_N = 10^{-17}\ J$, $\alpha = 5.6\ \mathrm{N/m^2}$

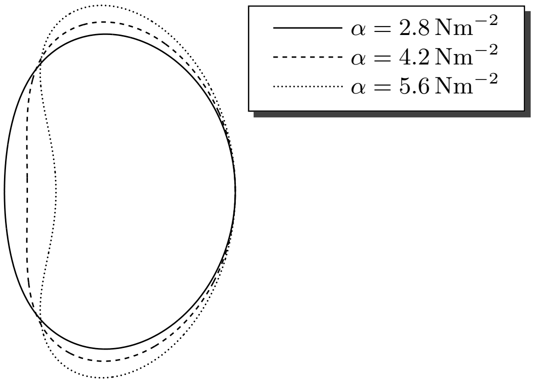

(c) $b_N = 10^{-17}$ J, $\sigma = 5 \cdot 10^{-6}$ N/m.

Figure 5.5. – Contour of the stationary cell shapes for varying bending, surface tension and protrusion values proposed in Tab. 5.1.

5.4.2. Formation of filipodia-like structures

In the previous example, the diffusion coefficients and kinetic parameters are chosen to form a Turing pattern that defines a polarity to distinguish between cell front and cell rear. Different parameters can lead to different patterns, but it has also been shown that the cell size influences these patterns [207]. We here focus on the parameters and demonstrate this by using again a circular initial shape of radius 1, a constant value of $C = 9.25$ in the cytoplasm and random initial conditions for c_1 and c_2 within $[0.1758 - 0.01, 0.1758 + 0.01]$ and $[0.2186 - 0.01, 0.2186 + 0.01]$, respectively. We here also modify the diffusion coefficient d_{c_2} along the membrane, which is set to be $d_{c_2} = 750$ and now differs from d_{c_1}. The second change in parameters concerns the active surface force number Fa, which now becomes $\mathrm{Fa} = 0.71$, corresponding to $\alpha = 0.39\,\mathrm{N/m^2}$. The elastic parameters of the membrane are set to be $b_N = 10^{-18}\,\mathrm{J}$ and $\sigma = 10^{-6}\,\mathrm{N/m}$. Fig. 5.7 shows the time evolution of the phase field variable, the concentrations of c_1 and c_2

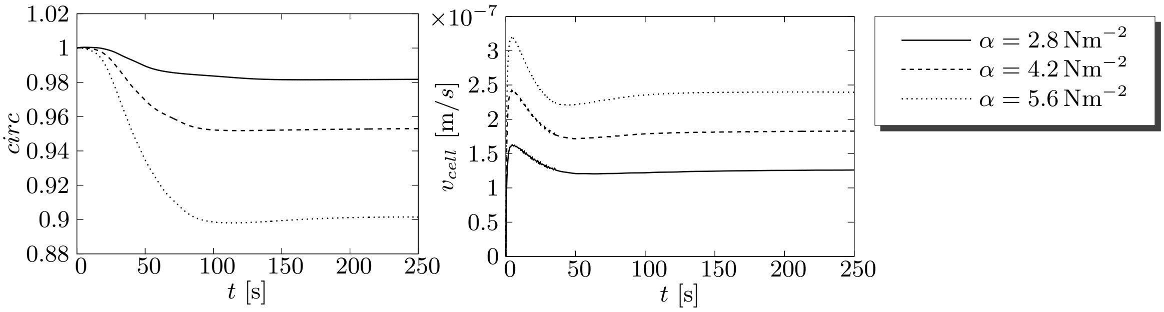

(a) circularity **(b)** velocity

Figure 5.6. – Variation of α leads to different cell shapes, the larger the protrusion force the stronger the deformation and the faster the cell movement for $b_N = 10^{-17}\,\mathrm{J}$, $\sigma = 5 \cdot 10^{-6}\,\mathrm{N/m}$.

along the membrane, the concentration of C within the cytoplasm as well as the velocity field. Due to the developing of various maxima in c_1, the cell only deforms but it does

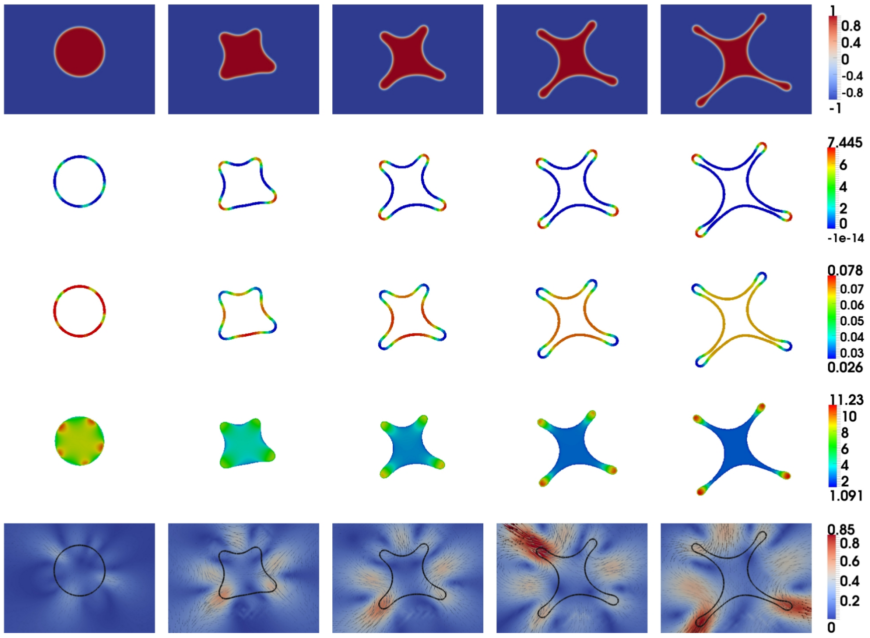

Figure 5.7. – Cell forming filopodia-like structures. First row - shape of the cell at different times evolving from left to right. Shown is the phase field variable ϕ. Second row - concentration of c_1 on cell membrane. Third row - concentration of c_2 on the cell membrane. Fourth row - concentration of C within the cytoplasm and last row - velocity field. The concentrations along the cell membrane and in the cytoplasm are shown at the $[-0.9, 0.9]$ and $[0, 1]$ level sets of the phase field variable, respectively. The times t corresponding to the columns are 0.1, 1, 2, 3 and 4 and are equal at 3.6 s, 35.7 s, 71.4 s, 107.1 s and 142.9 s, from left to right.

not move along one direction. In contrast to our previous simulations, we also achieve a pattern in C. A stationary shape is not reached within the simulation time. Please note that the correlation between the formation of filopodia and a more complex Turing pattern for the GTPase network model may be questionable. The presented results serve for an illustration of the influence of certain parameters to the cell's shape.

5.4.3. Reaction to spatial signals

It remains to be determined to what extent such an intrinsic polarization mechanism contributes under physiological conditions where cell polarization is controlled by spatial signals. In neutrophils, the actin cytoskeleton plays an important role in the amplification of the spatial signal provided by gradients of chemoattractants.

To demonstrate this effect, we modify eq. (5.17) by adding $\nabla_\Gamma \cdot (c_1 \nabla_\Gamma \tilde{c})$ to the left-hand side, with $\tilde{c}$ a given concentration of a chemoattractant in the extracellular matrix. A similar approach has been used in [87, 147]. The modified diffuse interface equation reads

$$\partial_t(|\nabla\phi|c_1) + \nabla \cdot (|\nabla\phi|\mathbf{v}c_1) + \nabla \cdot (|\nabla\phi|c_1\mathbf{P}_\phi\nabla\tilde{c}) = d_{c_1}\nabla \cdot (|\nabla\phi|\nabla c_1) + \bar{\gamma}|\nabla\phi|h(c_1,c_2), \tag{5.21}$$

where $\mathbf{P}_\phi = \mathbf{I} - \frac{\nabla\phi \cdot \nabla\phi}{|\nabla\phi|^2}$ denotes the projection operator. To illustrate the applicability of the approach, we use different modes of $\tilde{c}$ and its gradient:

1. $\nabla\tilde{c} = \xi(\cos\omega t, \sin\omega t)^T$, the chemoattractant rotates with the angular velocity ω,
2. $\nabla\tilde{c} = \xi(1, \sin\omega t)^T$, the chemoattractant changes its direction sinusoidally,
3. $\nabla\tilde{c} = \xi\mathcal{R}(\chi^{\lfloor\frac{n}{\vartheta}\rfloor+1}) \cdot \nabla\tilde{c}(\chi^{\lfloor\frac{n}{\vartheta}\rfloor})$, the chemoattractant randomly changes its direction by a specific angle ω. The random variable χ is determined every ϑ-th time step and has the possible values $\{-\omega, 0, \omega\}$. $\mathcal{R}$ denotes a rotation matrix and $\nabla\tilde{c}(\chi^{\lfloor\frac{n}{\vartheta}\rfloor})$ determines the old direction of the chemoattractant. Similar rules are proposed in [87].
4. $\nabla\tilde{c} = -\xi(\frac{\mathbf{x}-\mathbf{x}_0}{||\mathbf{x}-\mathbf{x}_0||_2})$, where the chemoattractant is space depended given by the distance between $\mathbf{x} = (x_1, x_2)^\top \in \Omega$ and $\mathbf{x}_0 = (x_{0_1}, x_{0_2})^\top \notin \Omega$, denoting the direction. This is used to qualitatively compare our simulation results with the work of Lautenschläger et al. [148] where a myeloid cell is following a signal coming out of a microtube.

The parameter ξ models the strength of the chemotactic signal, which is set to $\xi = 5$ in all simulations and thus dominates the reaction-diffusion system, leading to a pronounced maximum of c_1 in the direction of the strongest gradient of the chemoattractant. Fig. 5.8, corresponding to case 1, shows the resulting rotation of the cell together with the velocity field.

The maximum in c_1 always points in the direction of the highest gradient of the chemoattractant. We again observe the formation of a stationary shape here influenced

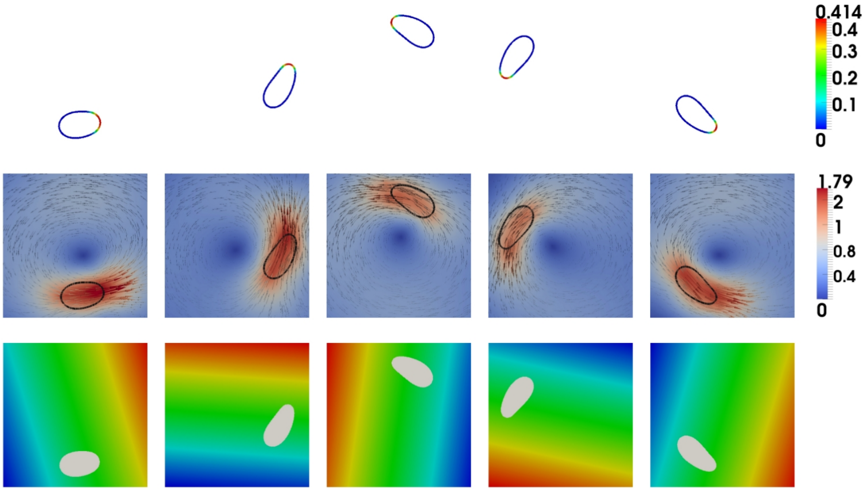

Figure 5.8. – Cell responds to a rotating spatial signal leading to a rotation, corresponding to case 1. The cell shape and velocity in the cytoplasm and in the extracellular matrix is shown for times t equal 21.4 s, 107.1 s, 214.3 s, 321.4 s and 428.6 s, from left to right.

by the spatial signal. Fig. 5.9, corresponding to case 2, shows the evolution of the cell from $t = 0$ s to $t = 428\,\mathrm{s}$ for $\omega = 0.014\,\mathrm{s}^{-1}$ (Fig. 5.9a) and $\omega = 0.056\,\mathrm{s}^{-1}$ (Fig. 5.9b). The third configuration, corresponding to case 3, is shown in Fig. 5.10 demonstrating a more chaotic movement, which becomes stronger for larger ω and smaller ϑ. Finally, Fig. 5.11 shows the qualitative results of our approach with a migrating myeloid, corresponding to case 4. The domain contains a microtube with $10\,\mu$m thickness and an ellipsoid cell is placed on the right side of the domain. The chemoattractant is constructed such that its maximum holds inside the tube. Given the cell its initial polarization, it immediately follows the signal into the tube. However, we also observe that the shape of the cell differs from the experimental results in [148] because we did not perform a rigorous data fit. Possible improvements are a higher viscosity of the cytoplasm or an adhesion potential between cell and channel wall. Other approaches such as elastic or viscoelastic approximations of the cell might also be meaningful.

(a) $\omega = 0.014\,\mathrm{s}^{-1}$ **(b)** $\omega = 0.056\,\mathrm{s}^{-1}$

Figure 5.9. – Cell responds to a sinusoidal spatial signal, corresponding to case 2.

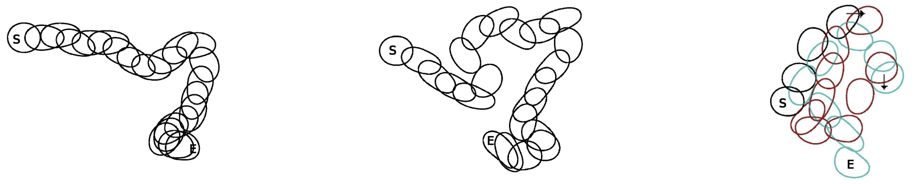

(a) $\omega = 30°$, $\vartheta = 400$ **(b)** $\omega = 60°$, $\vartheta = 400$ **(c)** $\omega = 60°$, $\vartheta = 100$

Figure 5.10. – Cell evolution corresponding to case 3. The staring point is labeled by S and the end point by E.

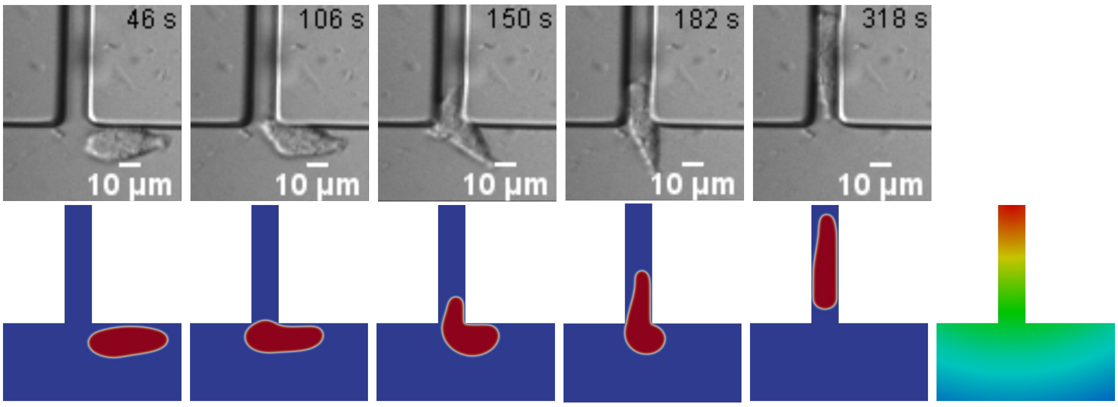

Figure 5.11. – Cell migration into a micro channel following a prescribed chemical signal (right), corresponding to case 4. Experimental results (pictures retrieved from [148]) are shown in the first row and the corresponding simulation results are shown in the second row.

5.5. Discussion

The movement of crawling cells is described using an effective model for the reorganization of the actin cytoskeleton, which is combined with a Helfrich model for the cell membrane and streaming within the cytoplasm and the extracellular matrix. The actin polymerization leading to cell protrusion is thereby initiated by a membrane-bound active state of the GTPase, as one component of a biochemical network model, taking into account the different dimensionality of the cytoplasm and the cell membrane. The model forms a Turing pattern in a parameter regime in which diffusion along the membrane can be equal for all components. The used network model is a minimal model with these characteristics and only takes into account the active and inactive state of the membrane-bound GTPase as well as complexes of cytoplasmic GTPase. However, the minimal model for the GTPases cycle already shows a large variety of different dynamical behavior, which range from sheet-like formation of lamellipodia and the evolution of stationary cell shapes, to fingering phenomena that are filopodia-like. The difference is achieved by changing the strength of the reaction and the diffusion parameters along the membrane.

The system of equations is formulated in a diffuse interface approach, which allows for an efficient numerical treatment. In particular, the reaction-diffusion model along the membrane and within the cytoplasm can be formulated as a coupled system in a fixed domain using the diffuse interface and diffuse domain approach. The same approach can be applied for more detailed biochemical network models, e.g. as proposed in [115]. The protrusion force can be generalized by taking into account various concentrations along the membrane and within the cytoplasm. In addition, a retracting force can be considered as well. If we denote concentrations along the membrane by c_i and within the cytoplasm by C_i, the general form for the non-dimensional momentum equation reads

$$\begin{aligned}\mathrm{Re}\,(\partial_t \mathbf{v} + (\mathbf{v}\cdot\nabla)\mathbf{v}) + \nabla p = \nabla\cdot(\eta(\phi)\mathbf{D}) + \frac{\delta\mathcal{E}_S}{\delta\phi}\nabla\phi - \sum_i \frac{1}{\mathrm{Fa}_i} c_i \nabla\phi \\ + \sum_i \frac{1}{\overline{\mathrm{Fa}}_i} C_i \mathbf{P}\end{aligned} \tag{5.22}$$

with $\mathrm{Fa}_i = \eta V/(\alpha_i L)$ the active surface force numbers and $\overline{\mathrm{Fa}}_i = \eta V/(\overline{\alpha}_i L)$ the active bulk force numbers. To describe protrusion and retraction we have $\alpha_i > 0$ and $\alpha_i < 0$, respectively. In [228, 229] only the last terms are considered, one for a protrusion and one for a retraction force. The importance of retraction for cell motility is e.g. considered in [90, 91] and needs to be taken into account for quantitative comparisons with specific cells. The last term in eq. (5.22) describes a force acting in the direction of the actin filaments, where $\mathbf{P}$ is a vector field indicating the averaged orientation field of the actin filament network, see Chapter 6. We can label this flow with a further cytoplasmic concentration C_i denoting the area of high activity or adhesion. Such macroscopic vector field $\mathbf{P}$ was of basic interest in [160, 270, 272] but without hydrodynamic effects. Tjhung et al. [242] developed a hydrodynamic model accounting for $\mathbf{P}$ but the active terms for the cell protrusion are directly inserted into the phase field:

$$\partial_t \phi + \nabla\cdot\Big(\mathbf{v} + \sum_i \frac{1}{\overline{\mathrm{Fa}}_i}\mathbf{P}\Big) = \gamma\Delta\phi^\natural.$$

An additional contribution being essential for cell motility is adhesion. Within the adhesion process, the actin network is connected to the substrate where a force is mediated that pushes the cell forward. In our previous model using a protrusive force to advect the cell, adhesion was not neglected, but in this sense, it was accounted for implicitly. A first step to consider adhesion is to introduce friction between the substrate and the cell by adding an effective friction term that is proportional to the local speed, similar to [228]:

$$\mathrm{Re}\,(\partial_t \mathbf{v} + (\mathbf{v}\cdot\nabla)\mathbf{v}) + \nabla p + \sum_i \frac{1}{\overline{\mathrm{Fa}}_i} C_i \tilde{\phi}\mathbf{v} = \nabla\cdot(\eta(\phi)\mathbf{D}) + \frac{\delta\mathcal{E}_S}{\delta\phi}\nabla\phi - \frac{1}{\mathrm{Fa}} c_1 \nabla\phi.$$

This effect on the cell motion is primarily to slow it down. Here, the adhesion can be considered either to be constant $C_i = 1$ or space depending. An active contribution of adhesion is e.g. considered [21, 160, 229, 270, 272]. We will now focus on an approach for adhesion considering a three dimensional cell. In [56] adhesion is modeled in the context of a Helfrich model using an effective contact potential W, as already proposed in [225]. W is thereby modeled as a function of the distance between the membrane and the substrate, e.g. in Lennard-Jones form $W(\overline{r}) = -\left((\beta_1/\overline{r})^{\beta}_{2} - (\beta_1/\overline{r})^{\beta_2/2}\right)$, with $\overline{r}$ the signed distance function to the substrate, β_1 and β_2 the thickness of the repulsive region and the rate of change of the adhesion potential, respectively. The generalized diffuse non-dimensional Helfrich energy reads

$$\begin{aligned}\mathcal{E}(\phi) = \frac{1}{2\varepsilon}\frac{1}{\mathrm{Be}}\int_\Omega\left(\varepsilon\Delta\phi - \frac{1}{\varepsilon}W_0'(\phi)\right)^2 \mathrm{d}\mathbf{x} + \frac{1}{\mathrm{Ca}}\int_\Omega\left(\frac{\varepsilon}{2}|\nabla\phi|^2 + \frac{1}{4\varepsilon}(\phi^2-1)^2\right)\mathrm{d}\mathbf{x}\\ + \frac{1}{\mathrm{Ad}}\int_\Omega W(\overline{r})\left(\frac{\varepsilon}{2}|\nabla\phi|^2 + \frac{1}{4\varepsilon}(\phi^2-1)^2\right)\mathrm{d}\mathbf{x},\end{aligned}$$

with the adhesion strength number $\mathrm{Ad} = 2\sqrt{2}/3\ \eta V/\delta$ and δ the strength of the adhesion interaction.

5.6. Conclusion

To summarize, the introduced model combines the main contributions to cell motility enabling to reproduce its primary phenomenology. The diffuse interface approach provides an easy to handle and efficient numerical approach to deal with the highly coupled system of equations. Although the model incorporates several simplifications, we are able to analyze the interplay between protrusion, membrane and fluid forces. We can recover the basic shapes and important aspects of motile cells. The approach can also be extended to incorporate additional phenomena. The simulation results are obtained not for a specific cell type, but within a realistic parameter range spanning a large class of cells and their environment. We therefore expect the model and the numerical approach to be useful also for quantitative simulations of specific cells.

Chapter 6

A model for contractile stress using active polar gels

We analyze a generic motility model with the motility mechanism arising by contractile stress due to the interaction of myosin and actin. A hydrodynamic active polar gel theory is used to model the bulk of a cell and is combined with a hydrodynamic Helfrich-type model to account for membrane properties. The overall model allows us to consider motility without the necessity for local adhesion.

This chapter has the following structure: after a brief motivation, we introduce the mathematical model in Section 6.2 that combines the previous diffuse interface Navier-Stokes-Helfrich model with bending and surface tension together with fluid flow. Moreover, an orientation field equation can be derived from an active polar gel theory that hereby considers the actin filaments as liquid crystals. We show that this model is thermodynamically consistent and extend it by an active contractile stress tensor leading to the model introduced in [242]. A numerical approach is given Section 6.3. Besides the reproduction of previous results, we undertake convergence studies for the highly nonlinear free boundary problem and show the robustness of the approach, see Section 6.4. In Section 6.5, we further compare the flow field of the motile cell with that of classical squirmer models and identify the motile cell as a puller or pusher depending on the strength of the myosin-actin interactions. In this chapter, we restrict our simulations to 2D. However, the described model can also be used for 3D cell motility, where the myosin-actin interactions are assumed to dominate and treadmilling only plays a minor role. The 3D simulations require an adequate preconditioner/solver for the system and its development is still current research.

The basic concepts, such as modeling, numerical methods and results in this chapter are already published in Marth et al. [176].

6.1. Contractile stress as a basic component of cell motility

As already discussed, cell motility can be decomposed into three basic steps: actin polymerization at the front, focal adhesion i.e. force mediation to the substrate, and contractile stress in the back. In recent experiments, Friedl and Wolf [107] found out that tumor cells migrate without any substrate. It has been argued that within these fluid environments a cortical flow, as a result of contractile stress between actin filaments is the dominant mechanism for motility [119, 131]. This mechanism creates an internal flow of actin that pushes the cell forward without the necessity for local adhesion and has been described by a hydrodynamic active polar gel theory. See [58, 101, 203] for a general review. Within the active polar gel approach, the bulk, or more specific the actin cytoskeleton consisting of actin filaments, is therefore considered as a liquid crystal i.e. microscopic small rod-like particles with a distinct polarization. Moreover, the cell interior represents an intermediate state which exhibits a degree of order that is between that of ordinary liquids and solids and can furthermore exert an elastic distortion stress during their translation in contrast to classical fluids. Actin filaments are strongly entangled and connected by cross-linking proteins, so-called myosin motors, that transform chemical energy from the ATP hydrolysis into mechanical energy and exert contractile stress [132]. In [242] the authors showed how such a phenomenological introduced contractile stress tensor [206] within a hydrodynamic system can spontaneously break the symmetry of the actin solution that leads to cell motility.

6.2. Mathematical model

The used model is an extension of the approach in [242] and provides a generic route to study individual processes leading to cell motility. It combines the Helfrich-Navier-Stokes Model with surface tension for a conserved order variable, i.e. eq. (3.81), eq. (3.82), eq. (3.86) and eq. (3.87), with an active polar gel theory that necessitates the treatment of an additional director or orientation field for the actin filaments. We show how such a thermodynamically consistent model can be derived. This model describes the evolution as a combined minimization process for kinetic, surface and Frank-like energy (defined below). Together with an active force accounting for the contractile stress, we can describe cell migration.

6.2.1. Energy

We consider the free energy of the system:

$$\mathcal{E}(\mathbf{P}, \phi, \mathbf{v}) = \mathcal{E}_{kin}(\mathbf{v}) + \mathcal{E}_S(\phi) + \mathcal{E}_P(\phi, \mathbf{P}), \tag{6.1}$$

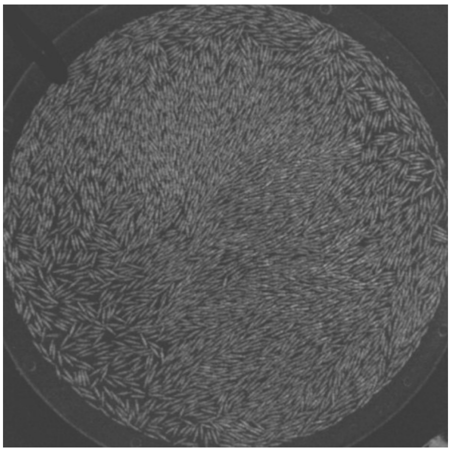

Figure 6.1. – Snapshot of vibrated copper-wire segments illustrating liquid crystals which in our approach serves as model for actin filaments within the bulk of the cell. (Picture retrieved from [206])

which consists of the kinetic energy E_{kin} inside and outside of the cell, characterized by the velocity $\mathbf{v}$. For the sake of simplicity, we consider equal density ρ and viscosity η for the cell bulk $\Omega_1(t)$ and the fluid outside $\Omega_0(t)$, which is considered as an isotropic Newtonian fluid. The cell membrane is implicitly defined by the zero level set of ϕ. In [242] the cell has been considered as a droplet considering a simple surface tension energy. In addition, we account for the Helfrich energy similar to Chapter 5 and consider the surface energy $\mathcal{E}_S$ given in eq. (3.78). $E_{\mathbf{P}}$ denotes the energy of the filament network and is given within a diffuse interface approximation [242] as

$$\mathcal{E}_P(\mathbf{P}, \phi) = \int_\Omega \frac{k}{2}(\nabla \mathbf{P})^2 + \frac{c_0}{4}|\mathbf{P}|^2(-2\phi + |\mathbf{P}|^2) + \beta_0 \mathbf{P} \cdot \nabla\phi \, \mathrm{d}\mathbf{x}, \tag{6.2}$$

where $\mathbf{P}$ is the mesoscopic average orientation of the actin filaments in the cell bulk $\Omega_1(t)$. eq. (6.2) is derived from a general distortion or Frank energy for liquid crystals that is given by

$$\mathcal{E}_F(\mathbf{P}) = \int_\Omega \frac{K_1}{2}(\nabla \cdot \mathbf{P})^2 + \frac{K_2}{2}(\mathbf{P} \cdot (\nabla \times \mathbf{P}))^2 + \frac{K_3}{2}(\mathbf{P} \times (\nabla \times \mathbf{P}))^2 \, \mathrm{d}\mathbf{x}. \tag{6.3}$$

The three terms in eq. (6.3) stand for the stiffness associated with splay, twist and bend deformations, respectively, see e.g. [58] for a broad introduction. Considering equal $K_1 = K_2 = K_3 =: k$ yields the first term in $\mathcal{E}_P$ with k a general elasticity parameter. Linking ϕ to the second term of eq. (6.2) allows us to restrict $\mathbf{P}$ to the cell interior: if $\phi < 0$ the minimum is obtained for $|\mathbf{P}| = 0$ and thus the term does not contribute to the energy, and for $\phi > 0$ the term forms a double-well with two minima with $|\mathbf{P}| = 1$ and the form specified by the parameter c_0. The last term in eq. (6.2) guarantees for $\beta_0 > 0$ that $\mathbf{P}$ points outwards in normal direction to the cell boundary. This is expected to be of relevance for polymerization and depolymerization of actin filaments and used

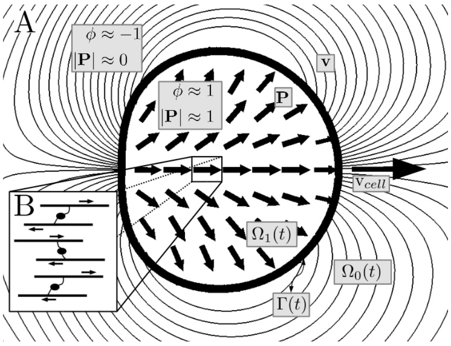

Figure 6.2. – (A) Schematic description for a moving cell. Shown is the splayed orientation field $\mathbf{P}$ in a motile steady state, with constant velocity v_{cell} as well as the streamlines of the velocity profile $\mathbf{v}$ and the phase field ϕ with the cell membrane $\Gamma(t)$ corresponding to the zero-level set of ϕ. (B) The orientation field serves as a model for the average aligned microscopic actin filaments which are connected by myosin motors.

in [160, 270, 272], but for the motility mode considered here a strong preference of the orientation of $\mathbf{P}$ at the cell boundary cannot be seen. They further applied β to obtain the same splayed orientation field for their non-hydrodynamic models, which we obtain by generic instability as a result of the interplay between the elasticity of the orientation field and the fluid flow. In [242] it is argued that small β_0 values can resemble the effect of a weak external field. We will therefore consider both cases $\beta_0 = 0$ and $0 < \beta_0 < 1$. Fig. 6.2 provides a schematic picture of the used variables.

Before we introduce the governing equations, we consider the orientation energy in a non-dimensional form. We use the same characteristic values introduced in Section 3.3. We further define the constants $c_1 = \frac{c_0 L^2}{k}$ and $\beta = \frac{\beta_0 L}{k}$ and in addition to the already introduced non-dimensional quantities Re, Be, Ca, we obtain the dimensionless polarization elasticity number

$$\mathrm{Pa} = \frac{\eta V L}{k}.$$

Accordingly, the orientation field energy in a non-dimensional form is written as

$$\mathcal{E}_P(\mathbf{P}, \phi) = \frac{1}{\mathrm{Pa}} \int_\Omega \frac{1}{2}(\nabla \mathbf{P})^2 + \frac{c_1}{4}|\mathbf{P}|^2(-2\phi + |\mathbf{P}|^2) + \beta \mathbf{P} \cdot \nabla \phi \, \mathrm{d}\mathbf{x}. \tag{6.4}$$

Together with the non-dimensional kinetic energy eq. (3.12) and the surface energy given in non-dimensional form in eq. (3.78), we can construct the system's overall energy.

6.2.2. Derivation of a thermodynamic model for active polar gels

In the following, we derive a thermodynamic model for active polar gels [264]. In our approach, the phase field serves as indicator of two different phases. Another approach considers ϕ as a density of a chemical species ATP [202, 203, 259]. The derivation is similar to Section 2.8 and extended by $\mathcal{E}_P(\mathbf{P},\phi)$. The free energy eq. (6.1) is written as

$$\begin{aligned}\mathcal{E}(\mathbf{v},\phi,\mathbf{P}) = \int_\Omega & \frac{\mathrm{Re}}{2}|\mathbf{v}|^2 + \frac{1}{\mathrm{Be}}\frac{1}{2\varepsilon}\left(\varepsilon\Delta\phi - \frac{1}{\varepsilon}W_0'(\phi)\right)^2 + \frac{1}{\mathrm{Ca}}\left(\frac{\varepsilon}{2}|\nabla\phi|^2 + \frac{1}{\varepsilon}W(\phi)\right) \\ & + \frac{1}{\mathrm{Pa}}\left(\frac{1}{2}(\nabla\mathbf{P})^2 + \frac{c_1}{4}|\mathbf{P}|^2(-2\phi + |\mathbf{P}|^2) + \beta\mathbf{P}\cdot\nabla\phi\right)\mathrm{d}\mathbf{x}.\end{aligned}$$

Its time derivative reads

$$\begin{aligned}\frac{\mathrm{d}\mathcal{E}}{\mathrm{dt}} = \int_\Omega & \mathrm{Re}\,\mathbf{v}\cdot\frac{\mathrm{D}\mathbf{v}}{\mathrm{Dt}} + \frac{1}{\mathrm{Be}}\mu\left(\frac{\mathrm{D}\Delta\phi}{\mathrm{Dt}} - \frac{1}{\varepsilon^2}W_0''(\phi)\frac{\mathrm{D}\phi}{\mathrm{Dt}}\right) + \frac{1}{\mathrm{Ca}}\left(\varepsilon\nabla\phi\frac{\mathrm{D}\nabla\phi}{\mathrm{Dt}} + \frac{1}{\varepsilon}W'(\phi)\frac{\mathrm{D}\phi}{\mathrm{Dt}}\right) \\ & + \frac{1}{\mathrm{Pa}}\left(\nabla\mathbf{P} : \frac{\mathrm{D}\nabla\mathbf{P}}{\mathrm{Dt}} + \left(c_1|\mathbf{P}^2|\mathbf{P} - c_1\mathbf{P}\phi + \beta\nabla\phi\right)\cdot\frac{\mathrm{D}\mathbf{P}}{\mathrm{Dt}}\right. \\ & \left. + \frac{c_1}{2}|\mathbf{P}|^2\frac{\mathrm{D}\phi}{\mathrm{Dt}} + \beta\mathbf{P}\cdot\frac{\mathrm{D}\nabla\phi}{\mathrm{Dt}}\right)\mathrm{d}\mathbf{x},\end{aligned}$$

where we consider the material derivative for $\mathbf{v}$, ϕ and $\mathbf{P}$ as given in eq. (3.42), eq. (3.41) and

$$\frac{\mathrm{D}\mathbf{P}}{\mathrm{Dt}} = \partial_t\mathbf{P} + (\mathbf{P}\cdot\nabla)\mathbf{P}. \tag{6.5}$$

Now, we consider the conservation of momentum and mass for $\mathbf{v}$ as well as the conservation of mass for ϕ that are given by

$$\mathrm{Re}\frac{\mathrm{D}\mathbf{v}}{\mathrm{Dt}} = \nabla\cdot\mathbf{S},, \tag{6.6}$$

$$\nabla\cdot\mathbf{v} = 0, \tag{6.7}$$

$$\frac{\mathrm{D}\phi}{\mathrm{Dt}} = -\nabla\cdot\mathbf{J}_\phi, \tag{6.8}$$

respectively, with the stress defined as $\mathbf{S} = -p\mathbf{I} + (\eta(\phi)\mathbf{D}) + \mathbf{S}_H + \mathbf{S}_{ST} + \mathbf{S}_\mathbf{P}$. Here, the unknowns $\mathbf{J}_\phi$, $\mathbf{S}_H$ and $\mathbf{S}_{ST}$ denote the flux of ϕ and the stresses resulting from the Helfrich energy and the surface tension energy, respectively. In addition, $\mathbf{S}_\mathbf{P}$ denotes the distortion stress coming from the orientation field that is also yet unspecified. We further consider an orientation field equation for $\mathbf{P}$ given as

$$\frac{\mathrm{D}\mathbf{P}}{\mathrm{Dt}} = -\mathbf{\Omega}\cdot\mathbf{P} + \xi\mathbf{D}\cdot\mathbf{P} - \nabla\cdot\mathbf{J}_P, \tag{6.9}$$

where, the left-hand side is the co-moving and co-rotational derivative, where the vorticity tensor defined as $\mathbf{\Omega} = \frac{1}{2}(\nabla\mathbf{v}^\top - \nabla\mathbf{v})$ takes rotational effects from the flow field into account and the deformation tensor $\mathbf{D} = \frac{1}{2}(\nabla\mathbf{v} + \nabla\mathbf{v}^\top)$ describes the flow alignment. Additionally, the flux $\mathbf{J}_P$ is unknown. Further explanations are given below. To summarize we have to determine the unknown stresses $\mathbf{S}_H$, $\mathbf{S}_\sigma$, $\mathbf{S}_P$ and the unknown fluxes $\mathbf{J}_\phi$ and $\mathbf{J}_P$ such that the overall energy is decreasing. To achieve this, we first rewrite

$\frac{\mathrm{D}\Delta\phi}{\mathrm{Dt}}$ and $\frac{\mathrm{D}\nabla\phi}{\mathrm{Dt}}$ as in eq. (3.46) and eq. (3.47) and in the same manner we rewrite

$$\frac{\mathrm{D}\nabla\mathbf{P}}{\mathrm{Dt}} = \nabla\frac{\mathrm{D}\mathbf{P}}{\mathrm{Dt}} - \nabla\mathbf{P} \cdot \nabla\mathbf{v}$$

and insert these results in the time derivative of the energy, which yields

$$\begin{aligned}\frac{\mathrm{d}\mathcal{E}}{\mathrm{dt}} = \int_\Omega &\mathrm{Re}\,\mathbf{v} \cdot \frac{\mathrm{D}\mathbf{v}}{\mathrm{Dt}} + \frac{1}{\mathrm{Be}}\mu\left(\Delta\frac{\mathrm{D}\phi}{\mathrm{Dt}} - \frac{1}{\varepsilon^2}W_0''(\phi)\frac{\mathrm{D}\phi}{\mathrm{Dt}} - \Delta\mathbf{v} \cdot \nabla\phi - 2\nabla\mathbf{v} : \nabla\nabla\phi\right) \\ &+ \frac{1}{\mathrm{Ca}}\left((-\varepsilon\Delta\phi + \frac{1}{\varepsilon}W'(\phi))\frac{\mathrm{D}\phi}{\mathrm{Dt}} - \varepsilon\nabla\phi \cdot (\nabla\mathbf{v} \cdot \nabla\phi)\right) \\ &+ \frac{1}{\mathrm{Pa}}\left(\nabla\mathbf{P} : \nabla\frac{\mathrm{D}\mathbf{P}}{\mathrm{Dt}} - \nabla\mathbf{P} : (\nabla\mathbf{P} \cdot \nabla\mathbf{v}) + (c_1|\mathbf{P}^2|\mathbf{P} - c_1\mathbf{P}\phi + \beta\nabla\phi) \cdot \frac{\mathrm{D}\mathbf{P}}{\mathrm{Dt}}\right) \\ &+ \frac{1}{\mathrm{Pa}}\left((\frac{c_1}{2}|\mathbf{P}|^2 - \beta\nabla \cdot \mathbf{P})\frac{\mathrm{D}\phi}{\mathrm{Dt}} - \beta\mathbf{P} \cdot (\nabla\mathbf{v} \cdot \nabla\phi)\right)\,\mathrm{d}\mathbf{x}.\end{aligned}$$

In addition, we define the non-dimensional chemical potentials as

$$\begin{aligned}\phi^\natural &:= \frac{\delta\mathcal{E}}{\delta\phi} = \frac{\delta\mathcal{E}_S}{\delta\phi} + \frac{\delta\mathcal{E}_P}{\delta\phi} \\ &= \frac{1}{\mathrm{Be}}\left(\Delta\mu - \frac{1}{\varepsilon^2}W_0''(\phi)\mu\right) + \frac{1}{\mathrm{Ca}}\left(-\varepsilon\Delta\phi + \frac{1}{\varepsilon}W'(\phi)\right) + \frac{1}{\mathrm{Pa}}\left(\frac{c_1}{2}|\mathbf{P}|^2 - \beta\nabla \cdot \mathbf{P}\right), \\ \mathbf{P}^\natural &:= \frac{\delta\mathcal{E}}{\delta\mathbf{P}} = \frac{1}{\mathrm{Pa}}\left(-\Delta\mathbf{P} + c_1|\mathbf{P}^2|\mathbf{P} - c_1\mathbf{P}\phi + \beta\nabla\phi\right),\end{aligned}$$

which helps us to rewrite

$$\begin{aligned}\frac{\mathrm{d}\mathcal{E}}{\mathrm{dt}} = \int_\Omega &\mathrm{Re}\,\mathbf{v} \cdot \frac{\mathrm{D}\mathbf{v}}{\mathrm{Dt}} + \phi^\sharp\frac{\mathrm{D}\phi}{\mathrm{Dt}} + \mathbf{P}^\sharp\frac{\mathrm{D}\mathbf{P}}{\mathrm{Dt}} - \frac{1}{\mathrm{Be}}\mu\Delta\mathbf{v} \cdot \nabla\phi - \frac{2}{\mathrm{Be}}\mu\nabla\mathbf{v} : \nabla\nabla\phi \\ &- \frac{1}{\mathrm{Ca}}\varepsilon\nabla\phi \cdot (\nabla\mathbf{v} \cdot \nabla\phi) - \frac{1}{\mathrm{Pa}}\left(\nabla\mathbf{v} : (\nabla\mathbf{P}^\top \cdot \nabla\mathbf{P}) + \beta\nabla\mathbf{v} \cdot (\mathbf{P} \otimes \nabla\phi)\right)\,\mathrm{d}\mathbf{x}.\end{aligned}$$

Plugging in the time evolutions for ϕ, $\mathbf{v}$ and $\mathbf{P}$, eq. (6.8), (6.6) and (6.9), respectively, we arrive at

$$\begin{aligned}\frac{\mathrm{d}\mathcal{E}}{\mathrm{dt}} = \int_\Omega &\mathbf{v} \cdot (-\nabla p + \nabla \cdot (\eta(\phi)\mathbf{D}) + \nabla \cdot \mathbf{S}_P) + \phi^\natural(-\nabla \cdot \mathbf{J}_\phi) + \mathbf{P}^\natural \cdot (-\nabla \cdot \mathbf{J}_P) \\ &+ \mathbf{P}^\natural \cdot (-\boldsymbol{\Omega} \cdot \mathbf{P} + \xi\mathbf{D} \cdot \mathbf{P}) + \frac{1}{\mathrm{Pa}}\mathbf{v} \cdot \nabla \cdot \left((\nabla\mathbf{P}^\top \cdot \nabla\mathbf{P}) + \beta(\mathbf{P} \otimes \nabla\phi)\right)\,\mathrm{d}\mathbf{x},\end{aligned}$$

where we already neglected the stress from the membrane using the definitions from eq. (3.49) and eq. (3.80) that are repetitively given by

$$\begin{aligned}\mathbf{S}_H &= \frac{1}{\mathrm{Be}}(\nabla\phi \otimes \nabla\mu - \mu\nabla\nabla\phi), \\ \mathbf{S}_{ST} &= -\frac{1}{\mathrm{Ca}}\varepsilon\nabla\phi \otimes \nabla\phi.\end{aligned}$$

Rewriting gives

$$\begin{aligned}\frac{\mathrm{d}\mathcal{E}}{\mathrm{dt}} = \int_\Omega & \mathbf{v} \cdot (\nabla \cdot (\eta(\phi)\mathbf{D}) + \nabla \cdot \mathbf{S}_P) + \phi^\natural(-\nabla \cdot \mathbf{J}_\phi) + \mathbf{P}^\natural \cdot (-\nabla \cdot \mathbf{J}_P) \\ & - \mathbf{v} \cdot \nabla \cdot \left(\frac{1}{2}\mathbf{P}^\natural \otimes \mathbf{P} - \frac{1}{2}\mathbf{P} \otimes \mathbf{P}^\natural + \frac{\xi}{2}\mathbf{P}^\natural \otimes \mathbf{P} + \frac{\xi}{2}\mathbf{P} \otimes \mathbf{P}^\natural\right) \\ & + \frac{1}{\mathrm{Pa}}\mathbf{v} \cdot \nabla \cdot \Big((\nabla \mathbf{P}^\top \cdot \nabla \mathbf{P}) + \beta(\mathbf{P} \otimes \nabla\phi)\Big)\,\mathrm{d}\mathbf{x},\end{aligned}$$

where we neglected the pressure term after integrating by parts and applied the incompressibility condition. Defining the fluxes and the remaining stress as

$$\begin{aligned}\mathbf{J}_\phi &= -\gamma \nabla \phi^\natural, \\ \nabla \cdot \mathbf{J}_P &= \frac{1}{\varkappa}\mathbf{P}^\natural, \\ \mathbf{S}_P &= -\frac{1}{\mathrm{Pa}}\Big((\nabla \mathbf{P}^\top \cdot \nabla \mathbf{P}) + \beta(\mathbf{P} \otimes \nabla\phi)\Big) + \frac{1}{2}\left(\mathbf{P}^\natural \otimes \mathbf{P} - \mathbf{P} \otimes \mathbf{P}^\natural\right) \\ &\quad + \frac{\xi}{2}\left(\mathbf{P}^\natural \otimes \mathbf{P} + \mathbf{P} \otimes \mathbf{P}^\natural\right),\end{aligned}$$

we obtain at the following energy law

$$\frac{\mathrm{d}\mathcal{E}}{\mathrm{dt}} = \int_\Omega -\eta(\phi)\mathbf{D} : \mathbf{D} - \gamma \left|\nabla \phi^\natural\right|^2 - \frac{1}{\varkappa}\left|\mathbf{P}^\natural\right|^2 \leq 0, \tag{6.10}$$

which is similarly proposed in Section 2.8 and only extended by the dissipative term for the evolution of **P**.

6.2.3. Active stress

The active stress forces the system out of equilibrium. Here, myosin motor proteins that are connected to actin filaments destroy this delicate balance as they continuously perform mechanical work from an ATP hydrolysis and add energy to the system. Within our approach, myosin is equal distributed, implicitly bounded to **P** and infinitely available. Other models consider further models describing the hydrolysis of ATP [131, 203]. Finally, the active stress that describes the phenomenologically introduced activity [206, 241] reads in non-dimensional form

$$\mathbf{S}_{active} = \frac{1}{\mathrm{Fa}}\tilde{\phi}\mathbf{P} \otimes \mathbf{P}, \tag{6.11}$$

with $\tilde{\phi} = \frac{1}{2}(\phi+1)$. In general, we can write this term without $\tilde{\phi}$ since **P** is restricted to the cell interior as a result of the double well potential. However, the inclusion of this term seems more robust. The non-dimensional parameter $\mathrm{Fa} = \eta V/\zeta L$ is similarly defined as in eq. (5.8), where ζ denotes the activity parameter. It characterizes contractile ($\zeta > 0$) and extensile stress ($\zeta < 0$). In Fig. 6.3a, we see how the contractile active stress contributes to the flow field. For equal aligned filaments, we observe a force balance and

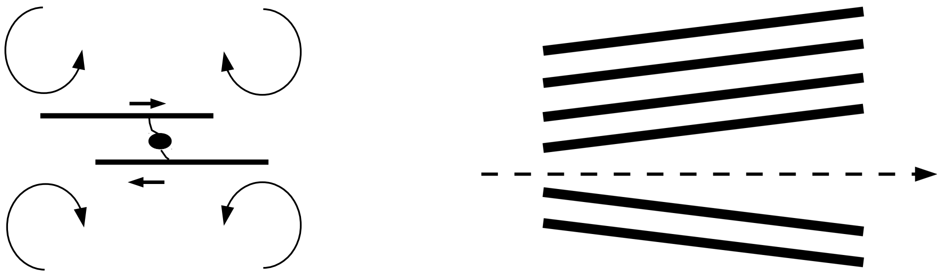

(a)

(b)

Figure 6.3. – Schematic pictures of contractile stress. (a) Contractile stress generated by myosin motor protein connected to two actin filaments. The resulting fluid flow consists of four vortices. Here, the force balance is zero and the system is not propelled. (b) Bundle of actin filaments. If the symmetry and the force balance is broken, a directed jet occurs caused by active stress that propels the system.

accordingly the system is stationary. However, if the symmetry within the alignment of the filaments is broken, the force balance vanishes and the active stress causes a directed jet that propels the system [206], see Fig. 6.3b. In this chapter, we will see how such a stationary system can become a motile non-equilibrium system by a spontaneous symmetry breaking instability [131, 242].

6.2.4. Governing equations

In the previous Sections, we have determined the unknowns such that the overall energy is decreasing in time and therefore fulfills thermodynamic consistency. In addition, we extend this model by the active stress term eq. (6.11) and consequently arrive at the following system of equations defined in $I \times \Omega$.

Flow equations

The physics of the flow are described by the Navier-Stokes equations with $\nabla \cdot \mathbf{v} = 0$ and

$$\begin{aligned}
\mathrm{Re}(\partial_t \mathbf{v} + (\mathbf{v} \cdot \nabla)\mathbf{v}) + \nabla p = {} & \nabla \cdot (\eta(\phi)\mathbf{D}) \\
& + \frac{1}{\mathrm{Be}} \nabla \cdot (\nabla\phi \otimes \nabla\mu - \mu\nabla\nabla\phi) - \frac{1}{\mathrm{Ca}} \nabla \cdot (\varepsilon \nabla\phi \otimes \nabla\phi) \\
& - \frac{1}{\mathrm{Pa}} \nabla \cdot \Big((\nabla\mathbf{P}^\top \cdot \nabla\mathbf{P}) + \beta(\mathbf{P} \otimes \nabla\phi) \Big) \\
& + \frac{1}{2} \nabla \cdot \Big(\mathbf{P}^\natural \otimes \mathbf{P} - \mathbf{P} \otimes \mathbf{P}^\natural \Big) + \frac{\xi}{2} \nabla \cdot \Big(\mathbf{P}^\natural \otimes \mathbf{P} + \mathbf{P} \otimes \mathbf{P}^\natural \Big) \\
& + \frac{1}{\mathrm{Fa}} \nabla \cdot \Big(\tilde{\phi} \mathbf{P} \otimes \mathbf{P} \Big), \qquad (6.12)
\end{aligned}$$

where the right-hand side denotes the stresses i.e the viscous stress (first line), the Helfrich and surface tension stresses arising from the coupling to the phase field (second line), the distortion stress and the stress from the aligning of $\mathbf{P}$ perpendicular to the interface (third line) and the flow alignment stress coming from the coupling between $\Omega\mathbf{P}$ and $\xi\mathbf{D}\mathbf{P}$ within the orientation field equation. We reformulate the stress from the second and third line by solving the divergence, similarly to Remark 3.2, and obtain a simpler formulation consisting of the chemical potentials $\phi^\sharp$ and $\mathbf{P}^\sharp$, defined below, see also [48, 108]. Finally, we have

$$\begin{aligned}\mathrm{Re}(\partial_t\mathbf{v} + (\mathbf{v}\cdot\nabla)\mathbf{v}) + \nabla p = \nabla\cdot\ & (\eta(\phi)\mathbf{D}) \\ & + \phi^\natural\nabla\phi \\ & + \nabla\mathbf{P}^T\cdot\mathbf{P}^\natural \\ & + \frac{1}{2}\nabla\cdot\left(\mathbf{P}^\natural\otimes\mathbf{P} - \mathbf{P}\otimes\mathbf{P}^\natural\right) + \frac{\xi}{2}\nabla\cdot\left(\mathbf{P}^\natural\otimes\mathbf{P} + \mathbf{P}\otimes\mathbf{P}^\natural\right) \\ & + \frac{1}{\mathrm{Fa}}\nabla\cdot\left(\tilde{\phi}\mathbf{P}\otimes\mathbf{P}\right). \end{aligned} \tag{6.13}$$

Phase field equation

Analog to previous sections, we consider the phase field as an implicit representation of the cell surface and consider a regularized advection equation for the phase field variable ϕ with the advected velocity given by the fluid velocity $\mathbf{v}$. The introduced diffusion term is scaled with a small mobility coefficient $\gamma > 0$. The evolution equation reads

$$\partial_t\phi + \mathbf{v}\cdot\nabla\phi = \gamma\Delta\phi^\natural, \tag{6.14}$$

with non-dimensional chemical potential

$$\phi^\natural = \frac{1}{\mathrm{Be}}\left(\Delta\mu - \frac{1}{\varepsilon^2}W_0''(\phi)\mu\right) + \frac{1}{\mathrm{Ca}}\left(-\varepsilon\Delta\phi + \frac{1}{\varepsilon}W'(\phi)\right) + \frac{1}{\mathrm{Pa}}\left(\frac{c_1}{2}|\mathbf{P}|^2 - \beta\nabla\cdot\mathbf{P}\right), \tag{6.15}$$

describing the contribution of bending, surface tension and the orientation field to the energy minimization of $\mathcal{E}_S$ with respect to ϕ. Since we apply a H^{-1}-gradient flow, ϕ is volume conserving. We further introduce the variable $\mu = \varepsilon\Delta\phi - \frac{1}{\varepsilon}W_0'(\phi)$ in order to write the higher order equation for ϕ as a system of 2nd order equations.

Orientation field equation

The orientation field equation can be derived from the polar gel theory, see e.g. [35, 168, 178, 184, 206] and most recently Prost et al. [203] for a review, and is given by

$$\partial_t\mathbf{P} + (\mathbf{v}\cdot\nabla)\mathbf{P} = -\mathbf{\Omega}\cdot\mathbf{P} + \xi\mathbf{D}\cdot\mathbf{P} - \frac{1}{\varkappa}\mathbf{P}^\natural, \tag{6.16}$$

where the left hand side is the co-moving and co-rotational derivative. The right-hand side is composed of the non-dimensional constant ξ that relates the coupling between the orientation field and the flow field and describes the alignment on $\mathbf{P}$ with the flow, where $\xi > 0$ for rod-like and $\xi < 0$ for oblate cells. Furthermore, $\varkappa = \eta_{rot}/\eta$ is a scaling factor between rotational and dynamic viscosity. The non-dimensional chemical potential reads

$$\mathbf{P}^{\natural} = \frac{1}{\mathrm{Pa}}\left(-\Delta\mathbf{P} + c_1|\mathbf{P}^2|\mathbf{P} - c_1\mathbf{P}\phi + \beta\nabla\phi\right). \tag{6.17}$$

6.2.5. Initial and boundary conditions

We consider a cell in a channel and consider Ω as a rectangular domain. We assume periodic boundary conditions on the left and right boundary for all variables. At the upper and lower boundary, we use homogeneous Neumann boundary conditions for $t > 0$ and $\mathbf{x} \in \partial\Omega$ that read

$$\nabla\mathbf{P} \cdot \mathbf{n} = \mathbf{0},\ \nabla\mu \cdot \mathbf{n} = \nabla\kappa \cdot \mathbf{n} = \nabla\phi^{\natural} \cdot \mathbf{n} = 0,$$

as well as Dirichlet boundary conditions given by

$$\mathbf{v}(t,\mathbf{x}) = \mathbf{0},\ \phi(t,\mathbf{x}) = -1.$$

As initial condition ($t = 0,\ \mathbf{x} \in \Omega$) we have $\phi(t,\mathbf{x}) = \phi^0(\mathbf{x})$ describing the initial cell shape and for $\mathbf{P}$ we apply an equal aligned filament network $\mathbf{P}(t,\mathbf{x}) = \mathbf{P}^0(\mathbf{x}) = (P_1, P_2)^\top + \boldsymbol{\delta}$, where $\boldsymbol{\delta}$ is a vector-valued random number generated from a uniform distribution on the interval $[-0.05, 0.05]$ in order to break the symmetry. For all simulations, we start with a circular cell with the radius $R = 5$, which is placed in the center of $\Omega = [0,160] \times [0,40]$. The initial condition for the orientation field is $\mathbf{P} = (1,0)^\top + \boldsymbol{\delta}$.

6.2.6. Material parameters

We consider the following material parameters, see Tab. 6.1, which are adapted from [174, 242] and the references therein. The low Reynolds number allows us to restrict the flow equation to a Stokes system, see also Remark 3.1.

6.3. Numerical approach and fully discrete finite element scheme

There have been several attempts to numerically simulate hydrodynamic active polar gels. At a microscopic scale Brownian dynamics simulation are used [193]. At larger length scales lattice Boltzmann simulations were applied in [49, 171, 172, 241, 242] and most recently in [205], where the authors described a hybrid particle-mesh method. In [176], we have presented an approach for adaptive finite elements, where the partial differential equations are treated with the parallel adaptive finite element toolbox AMDiS [252, 261]. Within this approach, we further explore an operator splitting approach, allowing us to solve the subproblems of the flow field, the orientation field and the phase-field evolution separately in an iterative process. In time, a semi-implicit discretization

Symbol	Description	Value
L	characteristic length	$10^{-6}\,\mathrm{m}$
V	characteristic velocity	$10^{-6}\,\mathrm{m/s}$
ρ	fluid density	$10^{3}\,\mathrm{kg/m^3}$
η	dynamic viscosity of the fluid	$2 \cdot 10^{3}\,\mathrm{Pa\,s}$
σ	surface tension	$0.0188\,\mathrm{N/m}$
b_N	bending rigidity	$1.26 \cdot 10^{-14}\,\mathrm{Nm}$
k	Frank constant	$2 \cdot 10^{-9}\,\mathrm{N}$, [58, 242]
ξ	shape factor	1.1, [242]
η_{rot}	rotational viscosity	$3.3 \cdot 10^{3}\,\mathrm{Pa\,s}$, [242]
ζ	activity parameter	$2 \cdot 10^{3}\,\mathrm{N/m^2}$, [259]
ε	boundary layer parameter	0.21
γ	mobility	0.025
c_1	double well parameter for $\mathbf{P}$	5
β	forcing normal direction of $\mathbf{P}$ at interface	0, 0.005, 0.05

Table 6.1. – Material parameters of the system. For the given values, we obtain the following characteristic numbers: $\mathrm{Ca} = 0.1$, $\mathrm{Be} = 0.3$, $\mathrm{Pa} = 1$, $\mathrm{Fa} = 1$ and $\mathrm{Re} = 5 \cdot 10^{-13}$.

is used, which, together with an appropriate linearization of the involved non-linear terms, leads to a set of linear systems in each time step. A further approach using finite elements focusing on strategies for time discretization and decoupling can be found in Shen and Yang [230].

The fully discrete finite element scheme follows in a straightforward manner. Fully discrete schemes for related problems such as simple two-phase flows can be found in [6, 7] and for the non-hydrodynamic Helfrich model we refer to [71, 173, 266]. Now, let $\mathcal{T}_h$ be a triangulation of the domain Ω of mesh size h. We introduce the finite element spaces

$$\begin{aligned} V_h &= \{\chi \in H^1(\Omega) | \chi_{|\mathcal{K}} \in \mathcal{P}_{l_\chi}(\mathcal{K})\}, \\ V_{0h} &= \{\theta \in H^1_0(\Omega) | \theta_{|\mathcal{K}} \in \mathcal{P}_{l_\theta}(\mathcal{K})\}, \\ W_h &= \{q \in L^2(\Omega) | q_{|\mathcal{K}} \in \mathcal{P}_{l_q}(\mathcal{K})\} \end{aligned}$$

where $\mathcal{P}_l(\mathcal{K})$ is the space for polynomials with degree equal than or less equal to l on triangle $\mathcal{K}$. We denote the space of vector test functions with dimension d by $\mathbf{V}_h = (V_h)^d$. We discretize in time as done in Section 5.3 and apply an operator splitting approach, where the upper index n denotes the time step number of the discretized time interval I. Finally, we arrive at the following scheme, where we solve in each time step:

1. The flow problem i.e. find $(\mathbf{v}^{n+1}, p^{n+1}) \in \mathbf{V}_{0h} \times W_h$ such that

   $$\begin{aligned}\langle \eta(\phi^n)\mathbf{D}^{n+1}, \nabla \boldsymbol{\nu}\rangle &= \langle p^{n+1}, \nabla \cdot \boldsymbol{\nu}\rangle + \langle {\phi^{\natural}}^{n} \nabla \phi^n + \nabla {\mathbf{P}^n}^{\top} \cdot {\mathbf{P}^{\natural}}^{n}, \boldsymbol{\nu}\rangle \\ &+ \frac{1}{\mathrm{Fa}}\langle \nabla \cdot \left(\tilde{\phi}^n \mathbf{P}^n \otimes \mathbf{P}^n\right), \boldsymbol{\nu}\rangle \\ &+ \frac{1}{2}\langle \nabla \cdot \left({\mathbf{P}^{\natural}}^{n} \otimes \mathbf{P}^n - \mathbf{P}^n \otimes {\mathbf{P}^{\natural}}^{n}\right), \boldsymbol{\nu}\rangle \\ &+ \frac{\xi}{2}\langle \nabla \cdot \left({\mathbf{P}^{\natural}}^{n} \otimes \mathbf{P}^n + \mathbf{P}^n \otimes {\mathbf{P}^{\natural}}^{n}\right), \boldsymbol{\nu}\rangle, \\ \langle \nabla \cdot \mathbf{v}^{n+1}, q\rangle &= 0,\end{aligned}$$

   $\forall (\boldsymbol{\nu}, q) \in \mathbf{V}_{0h} \times W_h$.

2. The orientation field i.e. find $({\mathbf{P}^{\natural}}^{n+1}, \mathbf{P}^{n+1}) \in \mathbf{W}_h \times \mathbf{V}_h$ such that

   $$\begin{aligned}\langle d_t \mathbf{P}^{n+1}, \mathbf{p}^{\natural}\rangle &= -\langle (\mathbf{v}^{n+1} \cdot \nabla)\mathbf{P}^{n+1}, \mathbf{p}^{\natural}\rangle - \langle \boldsymbol{\Omega}^{n+1} \cdot \mathbf{P}^{n+1}, \mathbf{p}^{\natural}\rangle + \langle \xi \mathbf{D}^{n+1} \cdot \mathbf{P}^{n+1}, \mathbf{p}^{\natural}\rangle \\ &- \langle \frac{1}{\varkappa} {\mathbf{P}^{\natural}}^{n+1}, \mathbf{p}^{\natural}\rangle, \\ \langle {\mathbf{P}^{\natural}}^{n+1}, \mathbf{p}\rangle &= \frac{1}{\mathrm{Pa}}\left(-\langle c_1 \phi^n \mathbf{P}^{n+1} + c_1 (\mathbf{P}^{n,n+1})^2 \mathbf{P}^{n,n+1}, \mathbf{p}\rangle + \langle \nabla \mathbf{P}^{n+1}, \nabla \mathbf{p}\rangle \right. \\ &\left. + \langle \beta \nabla \phi^n, \mathbf{p}\rangle\right),\end{aligned}$$

   $\forall (\mathbf{p}^{\natural}, \mathbf{p}) \in \mathbf{W}_h \times \mathbf{V}_h$. Here, we linearize $(\mathbf{P}^{n,n+1})^2 \mathbf{P}^{n,n+1} = (\mathbf{P}^n)^2 \mathbf{P}^{n+1} + 2(\mathbf{P}^n \otimes \mathbf{P}^n)\mathbf{P}^{n+1} - 2(\mathbf{P}^n)^2 \mathbf{P}^n$.

3. The phase field evolution i.e. find $({\phi^{\natural}}^{n+1}, \mu^{n+1}, \phi^{n+1}) \in V_h \times V_h \times V_{0h}$ such that

   $$\begin{aligned}\langle d_t \phi^{n+1}, \psi^{\natural}\rangle &= \langle \mathbf{v}^{n+1} \phi^{n+1}, \nabla \psi^{\natural}\rangle - \langle \gamma \nabla {\phi^{\natural}}^{n+1}, \nabla \psi^{\natural}\rangle, \\ \langle {\phi^{\natural}}^{n+1}, m\rangle &= \frac{1}{\mathrm{Be}}\left(-\langle \nabla \mu^{n+1}, \nabla m\rangle - \langle \frac{1}{\varepsilon^2} W_0''(\phi^{n,n+1}) \mu^{n,n+1}, m\rangle\right) \\ &+ \frac{1}{\mathrm{Ca}}\left(\langle \varepsilon \nabla \phi^{n+1}, \nabla m\rangle + \langle \frac{1}{\varepsilon} W'(\phi^{n,n+1}), m\rangle\right) \\ &- \frac{1}{\mathrm{Pa}}\langle \frac{c_1}{2} |\mathbf{P}^{n+1}|^2 + \beta \nabla \cdot \mathbf{P}^{n+1}, m\rangle, \\ \langle \mu^{n+1}, \psi\rangle &= -\langle \varepsilon \nabla \phi^{n+1}, \nabla \psi\rangle - \langle \frac{1}{\varepsilon} W_0'(\phi^{n,n+1}), \psi\rangle,\end{aligned}$$

   $\forall (\psi^{\natural}, m, \psi) \in V_h \times V_h \times V_{0h}$, where we again linearize the non-linear terms as done in Section 5.3.

The specified linear systems are solved using the direct solver UMFPACK [57]. We employ an adaptively refined triangular mesh $\mathcal{T}_h$ with a high resolution along the cell membrane to guarantee at least six grid points across the diffuse interface as well as a high resolution within the cell interior to appropriately resolve the orientation field. The criteria to refine or coarsen the mesh is purely geometric and related to the phase field variable ϕ. Due to the use of adaptivity, we need to interpolate the old solution defined on $\mathcal{T}_h^n$ onto the new mesh $\mathcal{T}_h^{n+1}$. To do this without violating the conservation of cell volume, we solve $\langle \phi^{n,old}, \theta \rangle = \langle \phi^{n,new}, \theta \rangle$ in every adaption step with θ and $\phi^{n,new}$ defined on $\mathcal{T}_h^{n+1}$ and $\phi^{n,old}$ on $\mathcal{T}_h^n$. We use a multi-mesh strategy [254] to virtually integrate the first term on the finest common mesh $\mathcal{T}_h^n \cup \mathcal{T}_h^{n+1}$, which guarantees a constant cell volume as long as time steps are appropriately chosen. We require the interface not to propagate over a whole element within one time step. With this restriction, all numerical tests show that $\int_\Omega \phi \, d\mathbf{x}$ is conserved.

6.4. Simulations and results

6.4.1. Motility due to contractile and extensile stress

As proposed by [242], motility can be achieved by means of a spontaneous splay deformation. This highly complex process is explained by a cartoon in Fig. 6.4 (bottom) and later on the simulation results are shown in Fig. 6.5. First, the cell elongates as a consequence of a quadrupolar straining flow, marked by the circular dashed arrows, resulting from the active stress tensor $\mathbf{S}_{active}$. The elongation stops if the surface forces characterized by Ca and Be balance the active stress. Four flow vortices within the cell can be observed. The orientation field $\mathbf{P}$ that remains rather uniform during the elongation starts to fluctuate and then induces a shear flow parallel to the orientation field, which results in a splay instability. The splayed configuration breaks the axial symmetry of the system and transforms the quadrupolar flow in a dipolar flow with two large vortices running across the cell. This has an influence on the cell shape and causes the cell to move with constant shape and at constant velocity along the symmetry axis.

In addition, we demonstrate an example for cell motility due to extensile stress, sketched by Fig. 6.4 (top) and the simulation results are given in Fig. 6.6. Here, the vortices are reverse and the cell is stretched in the x_1-direction. Together with the active stress, which now generates a flow normal to the filaments, a bend instability occurs. This is characterized by an alignment of the filaments along the curved shape of the cell, which results in a downward motion. The only modification needed to achieve this, is $1/\mathrm{Fa} = -3/2$.

During the inclination of the filaments, a delicate split happens, where one side of the filaments dominates the other one leading in different directions of the instabilities, Fig. 6.4. The dominating side and therefore the shape and the direction of both instabilities depend on the initial conditions and small disturbances due to external influences. Fig. 6.7 shows the opposite splay instability (first row) and the opposite bend instability (second row). Although the cell moves in the contrary direction the velocity profile has a similar shape as before. All these results qualitatively agree with [242]. We now turn to more quantitative comparisons and test the robustness of the instabilities.

6.4.2. Onset of motility

In this model a generic instability is used to describe a motile cell. The instability is a result of a delicate balance between active stress and elasticity of the filament network:

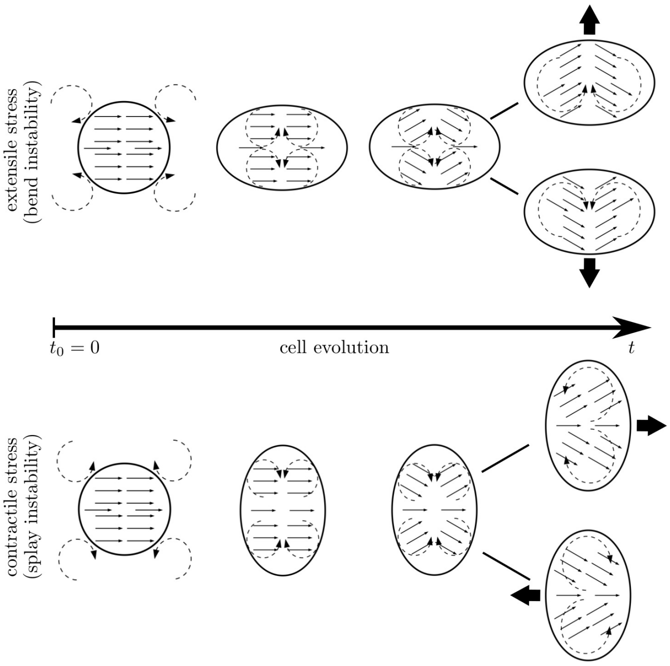

Figure 6.4. – Illustration of the formation of the bend and splay instability. The interplay between flow and elasticity together with the active stress determine the generic splay instability

the resulting fluid flow tries to incline the actin filaments and opposed the diffusion within the orientation field related to the Frank constant k, which is here carefully chosen, smooths out any perturbation. Any parameter influencing this balance can be responsible for the generation of an instability. In any case, the active stress plays a crucial role, because it intensifies the inclination of the filaments if the symmetry is already broken. Hence, motility is only possible if the strength of the myosin-actin interactions exceeds a critical value. Within our simulations we obtain a critical activity parameter $1/\mathrm{Fa}_{crit} \approx 0.75$. Below $1/\mathrm{Fa}_{crit}$ no instability occurs and the cell does not move. This is at least the case for $\beta = 0$ and in qualitative agreement with [242]. The bending capillary number Be does not influence the behavior within the considered parameter regime. However, a quantitative comparison with the results in [242], where $1/\mathrm{Fa}_{crit} \approx 0.5$ is measured, cannot be achieved as not all parameters used in [242] are known and the critical value turns out to be highly sensitive to various parameters, which will be analyzed below. Fig. 6.8 shows the upper branch of the bifurcation diagram separating a stationary state from a splayed and moving state by plotting the constant velocity of the cell. For $\beta > 0$ the transition to an immotile cell is smoothed out. We no longer have a sharp transition and observe motility also below $1/\mathrm{Fa}_{crit}$, again in agreement with [242].

The onset of the instability and the time required to reach a constant shape moving with constant velocity depends on the used parameters. As stronger the myosin-actin interactions, as faster this shape is reached. This effect is most pronounced for $\beta = 0$ and

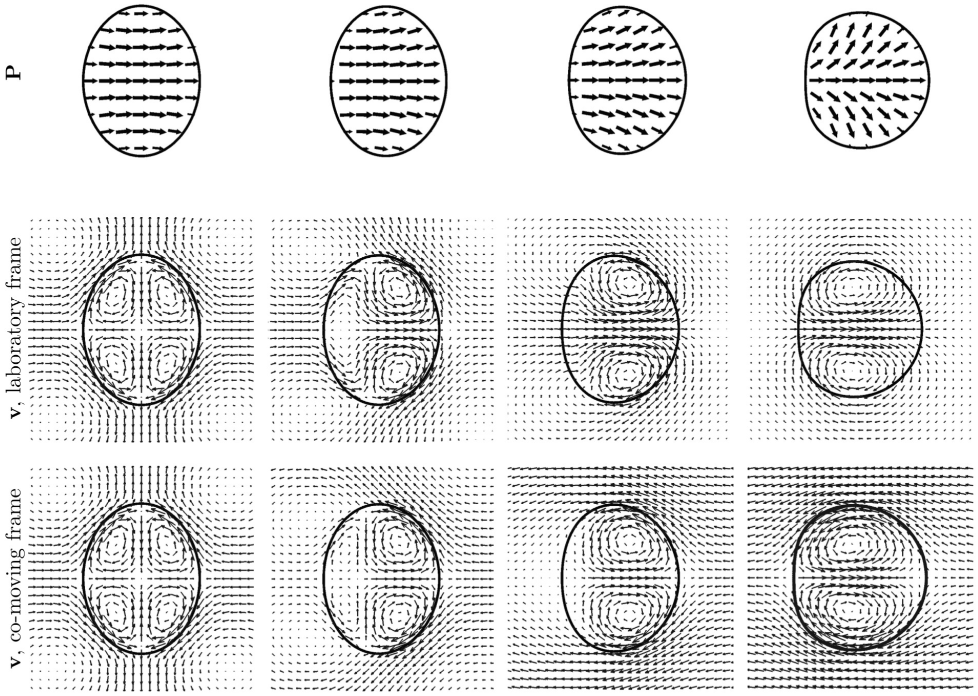

Figure 6.5. – Cell movement for contractile stress, movement to the right: first row - shape of the cell at different times evolving from left to right. Shown is the magnitude and the direction of the orientation field. second row - velocity field in a laboratory frame with different maxima: $|\mathbf{v}| = 0.1$, $|\mathbf{v}| = 0.12$, $|\mathbf{v}| = 0.19$ and $|\mathbf{v}| = 0.42$, which correspond to the cell speed v_{cell} of 0, 0.016, 0.054 and 0.125 from left to right. third row - velocity field of the co-moving frame, i.e. $(v_1 - v_{cell}, v_2)^T$. The times t shown are 100, 220, 250, 340, which correspond to seconds. The values used are from Tab. 6.1 and we changed $1/\text{Fa} = 1.125$ and take $\beta = 0$ (no explicit forcing for $\mathbf{P}$ to point outwards at the cell boundary).

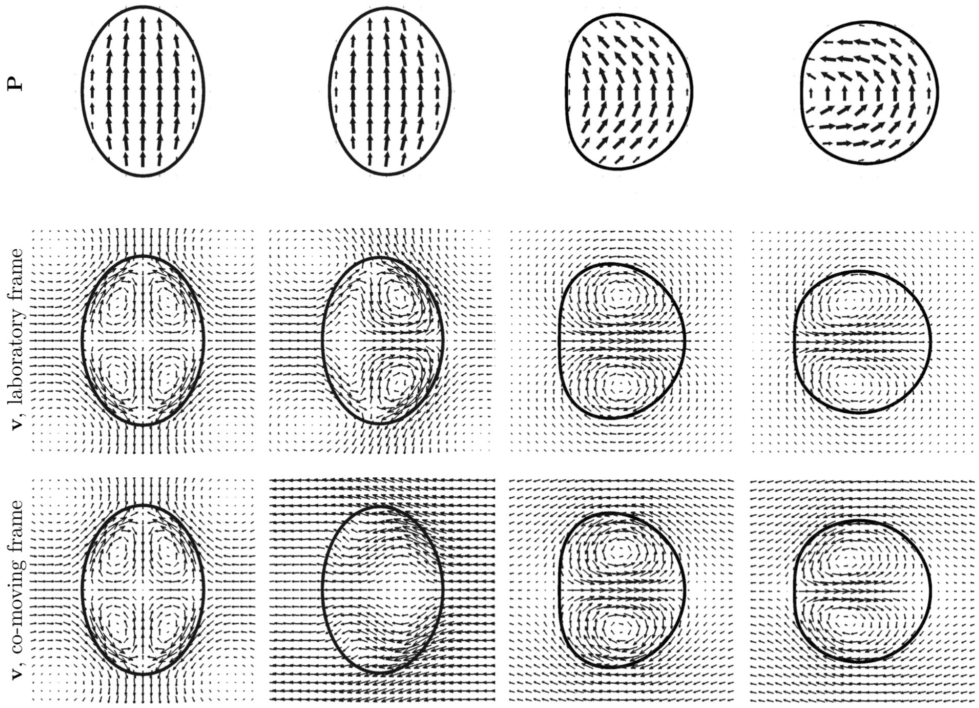

Figure 6.6. – Cell movement for extensile stress, movement downwards. first row - shape of the cell at different times evolving from left to right. Shown is the magnitude and the direction of the orientation field. second row - velocity field in a laboratory frame with different maxima: $|\mathbf{v}| = 0.117$, $|\mathbf{v}| = 0.138$, $|\mathbf{v}| = 0.266$ and $|\mathbf{v}| = 0.73$, which correspond to the cell speed v_{cell} of 0, 0.02, 0.07 and 0.16 from left to right. third row - velocity field in a co-moving frame, i.e. $(v_1 - v_{cell}, v_2)^T$. Note that bend instabilities generate a moving direction normal to the initial direction of the orientation field. The times t shown are 10, 80, 100, 170, again corresponding to seconds. The parameters are the same as in Fig. 6.5.

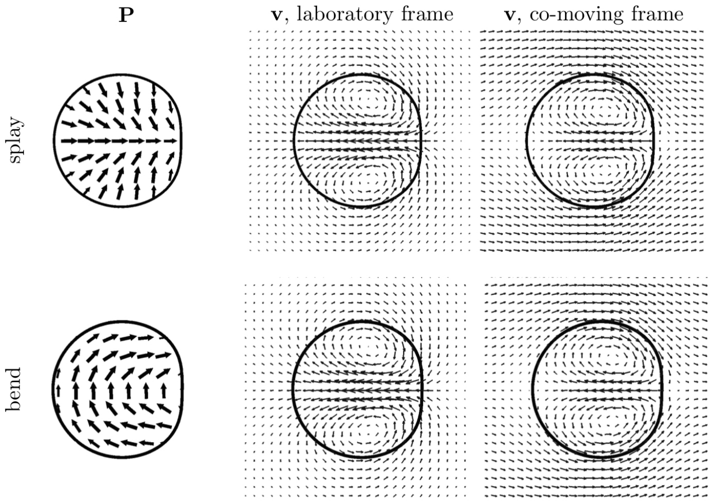

Figure 6.7. – Opposite instabilities: depending on the initial conditions as well as on the external effects the splay instability (first row) and bend instability (second row) draw a different pattern (left) and the cell moves in the opposite direction, to the left and upwards, respectively.

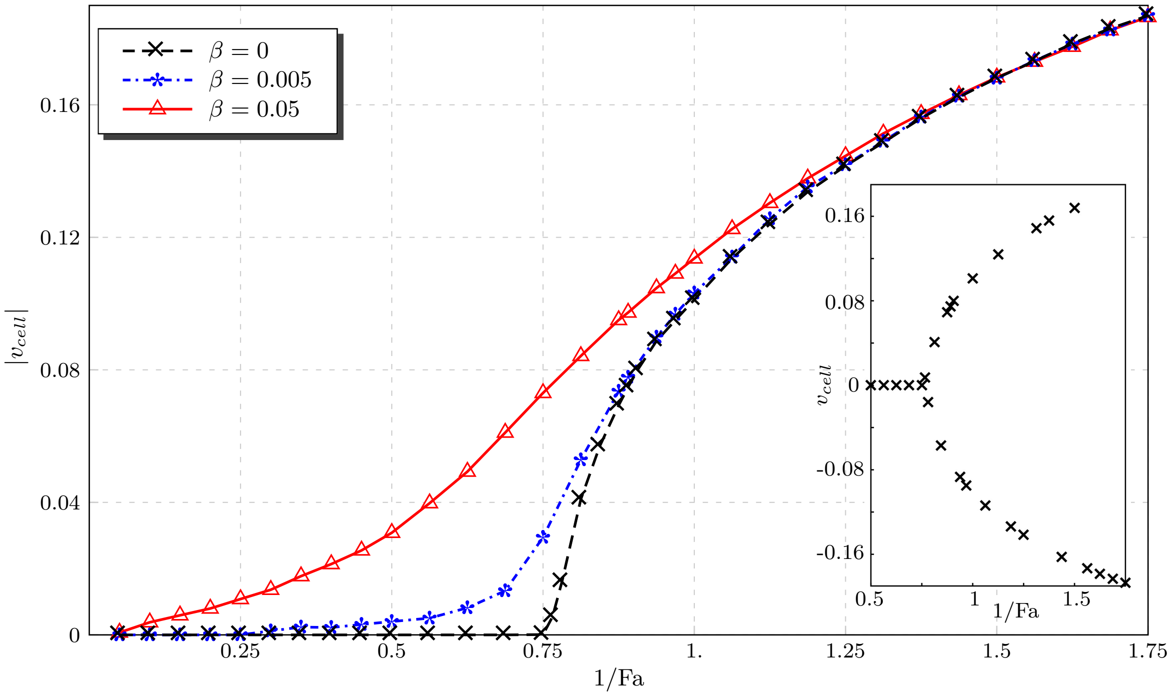

Figure 6.8. – Bifurcation diagram showing the symmetry breaking from a stationary state to a splayed and moving state for increasing 1/Fa. For $1/\mathrm{Fa} < 1/\mathrm{Fa}_{crit}$ the cell remains stationary and for $1/\mathrm{Fa} > 1/\mathrm{Fa}_{crit}$ the cell is moving, shown is the absolute value of v_{cell}. This transition is smoothed out for $\beta > 0$. The inlet shows both branches of the diagram with opposite velocities which occur only for the case $\beta = 0$.

decreases for $\beta > 0$. The time to reach a constant shape moving with constant velocity also depends on membrane properties of the cell. Here, the influence of the capillary number Ca is significant. The smaller the surface tension, the longer it takes to reach the desired shape. Again, this effect is less pronounced for $\beta > 0$.

6.4.3. Convergence tests

As already mentioned, all obtained results are very sensitive to various parameters. Due to this sensitivity on the physical parameters, we would like to consider the influence of numerical parameters on the described phenomena. We consider convergence tests. Since we are primarily interested in cell motility, we first consider a parameter regime for which our cell becomes motile and moves with a constant shape and constant velocity. We consider the case of contractile stress and thus, movement in horizontal direction. We use shape and velocity for validation and measure the following quantities:

- the x_1-coordinate of the center of mass x_{cm} as defined in eq. (5.19),
- the circularity of the cell c_{cell} as defined in eq. (5.20), and
- the mean velocity of the cell

  $$v_{cell} = \frac{\int_\Omega \tilde{\phi} v_1 \, \mathrm{d}\mathbf{x}}{\int_\Omega \tilde{\phi} \, \mathrm{d}\mathbf{x}},$$

  as an average of the x_1-component of the velocity in Ω_1, where $\mathbf{v} = (v_1, v_2)^\top$.

We used absolute values for all quantities and the following error norm: $\|e\|_2 = ((\sum_I |q_{t,ref} - q_t|^2)/(\sum_I |q_{t,ref}|^2))^{1/2}$, where q_t is the temporal evolution of quantity q. The solution on the finest grid serves as reference solution $q_{t,ref}$. Tab. 6.2 shows the relative error norms as well as the relative order of convergence (ROC) for the desired quantities if ε is reduced. We consider two cases $\beta = 0$ and $\beta = 0.05$. Together with ε, we also refine the mesh size to guarantee the same number of grid points within the diffuse interface layer for all simulations and the time step to ensure the same relation between mesh size and time step. The time interval is $I = [0, 500]$. Other parameters are obtained from Tab. 6.1. We see essentially first order convergence, the higher numbers in ROC are probably due to fortunate circumstances. Fig. 6.9 shows the shape and position for various ε, visualizing the convergence and confirming the choice of $\varepsilon = 0.21$ for the previous and further studies.

The second test considers the onset of motility. How sensitive is the obtained critical parameter $1/\mathrm{Fa}_{crit}$ on ε? The relation is shown in Fig. 6.10. A deeper analysis of the interface profile, as shown for a 1D cut of a cell in Fig. 6.11 explains this dependency as $|\mathbf{P}|$ is slightly more smeared out than ϕ. This has an influence on the active stress $\boldsymbol{\sigma}_{active}$. Its divergence is reduced at the interface for increasing ε and therefore a larger activity is needed to initiate the instability.

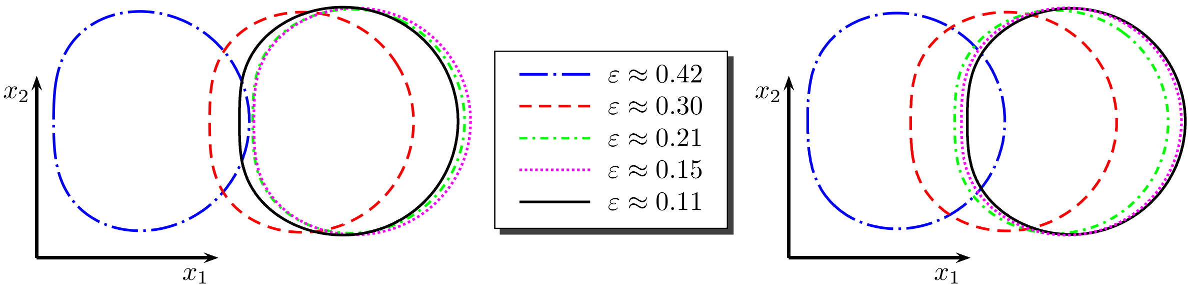

Figure 6.9. – Relative cell positions and cell shapes for different interface thicknesses ε in case of $\beta = 0$ (left) and $\beta = 0.05$ (right) at time $t = 300$. If the cell moves to the left (in case of $\beta = 0$), we reflect the cell shape with respect to the x_2 axis of the initial center of mass.

		center of mass x_{cm}		cell velocity v_{cell}		circularity c_{cell}	
	ε	$\|e\|_2$	ROC	$\|e\|_2$	ROC	$\|e\|_2$	ROC
$\beta = 0$	0.42	0.0600		0.3988		0.0398	
	0.30	0.0177	3.5298	0.1659	2.5316	0.0314	0.6823
	0.21	0.0047	3.8355	0.0787	2.1516	0.0179	1.6157
	0.15	0.0028	1.4912	0.0273	3.0575	0.0061	3.1225
$\beta = 0.05$	0.42	0.0569		0.2575		0.0430	
	0.30	0.0298	1.8715	0.1302	1.9691	0.0316	0.8921
	0.21	0.0129	2.4195	0.0511	2.6938	0.0174	1.7122
	0.15	0.0025	4.7328	0.0095	4.8514	0.0059	3.1431

Table 6.2. – Relative error norms and convergence orders for critical parameters, upper part $\beta = 0$ and lower part $\beta = 0.05$.

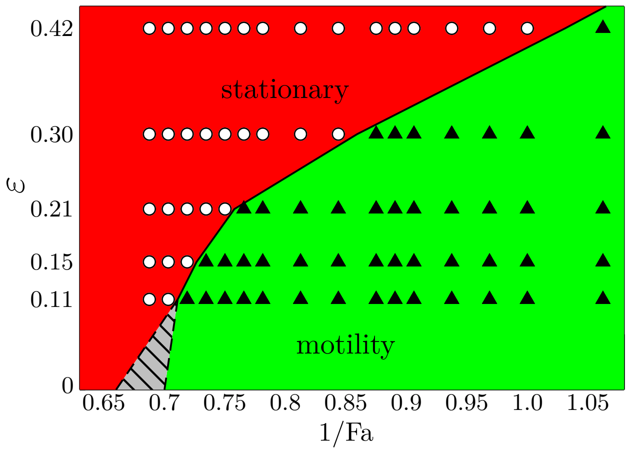

Figure 6.10. – Phase diagram distinguishing between stationary and motile state as function of 1/Fa and ε. $1/\mathrm{Fa}_{crit}$ can be considered as a function of ε with the limiting value for $\varepsilon \to 0$ presumably within the shaded region.

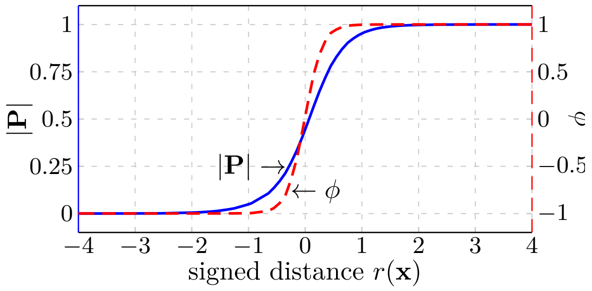

Figure 6.11. – 1D cut of the phase field function ϕ and norm of the polarization field $\mathbf{P}$ for $\varepsilon = 0.3$

6.4.4. Influence of different viscosities

Up to now we, have considered equal viscosity for the cytoplasm and the fluid outside, i.e. $\eta(\phi) = \eta$. Adopting a phase depending viscosity, where we interpolate between different viscosities η_0 and η_1 as shown in [6] the results for this approach are comparable to other more advanced approaches. In the following we only consider rescaled dimensionless viscosity ratios, see Section 3.3 and eq. (3.17). Fig. 6.12 shows the dependency of $1/\mathrm{Fa}_{crit}$ on the values of η_0 and η_1. Decreasing the viscosity, but keeping both values equal, leads to a reduction of the required activity for motility, but increasing the viscosity in the cytoplasm and keeping the viscosity in the outside fluid constant, in all cases, leads to an increase of the required activity. This can be explained by the necessity to induce a characteristic flow pattern in Ω_1 to induce the instability, which becomes harder to achieve for larger viscosities. The viscosity also has an influence on the cell velocity. The reached stationary velocity v_{cell} increases if η_0 is reduced. For more realistic parameters, with an even larger ratio of η_0/η_1 we thus expect faster moving cells. The slope of the corresponding bifurcation branch, as in Fig. 6.8, above $1/\mathrm{Fa}_{crit}$ is reduced if η_1 is increased. The sharp transition to motility for $\beta = 0$ and the smoothed out transition for $\beta > 0$ remains.

6.5. Discussion

We already emphasized, that this model describes cell motility without adhesion. Can we relate the motility mode to any freely-swimming microorganism? In order to answer this question, we first compare the induced flow field with theoretical predictions for a squirmer model [34, 154] and e.g. [191]. The surface tangential velocity for a circular squirmer in a co-moving frame in polar coordinates is given by

$$\mathbf{v}_{T,squirmer}(\alpha) = n_1(\sin\alpha + m\sin 2\alpha), \tag{6.18}$$

where n_1 determines the velocity of the cell, whereas $m = \frac{n_2}{n_1}$ defines whether the swimmer is a pusher ($m < 0$), a puller ($m > 0$) or a neutral (stealth) swimmer ($m = 0$), and α is the angle between the swimmers fixed swimming axis and the vector pointing to the

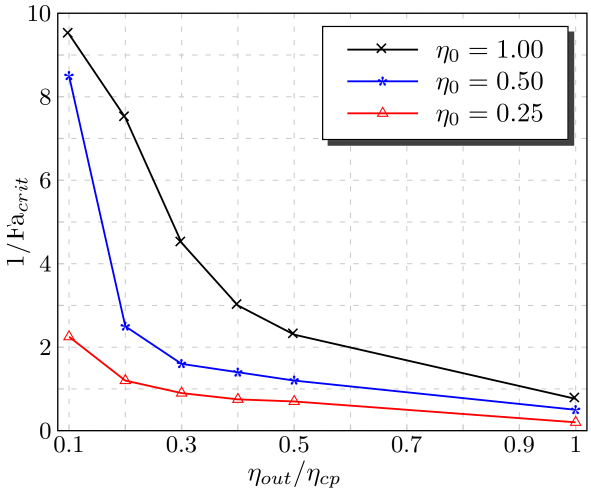

Figure 6.12. – Dependency of $1/\mathrm{Fa}_{crit}$ on viscosity ratio between outside fluid and the cytoplasm. $\eta_0 = \eta_1 = 1$ corresponds to the previously considered case.

surface. Fig. 6.13 shows the surface tangential velocity for different swimmers, where we choose $n_1 = 0.15$ as well as $m = 0$ (stealth), $m = 0.5$ (puller) and $m = -0.5$ (pusher). The profiles significantly differ with the extrema in that part of the swimmer, which is responsible for the motion. In case of a puller it is the cell front ($0 < \alpha < \pi/2$) and ($3\pi/2 < \alpha < 2\pi$), whereas as the pusher is driven by the rear, so the extrema appear for ($\pi/2 < \alpha < 3\pi/2$). For a neutral swimmer the extrema are at $\pi/2$ and $3/2\pi$.

We now compare these results with our simulations. We therefore extract the surface tangential velocity in the co-moving frame from our simulations. We use a contractile stress and consider $\mathbf{v}_T = (v_1 - v_{cell}, v_2)^\top\Big|_{\phi(x,t)=0}$ for $t > 0$ such that the stationary profile and velocity is reached. Fig. 6.14 shows the profile for various parameters $1/\mathrm{Fa}$ and $\beta = 0.05$. In comparison with the analytical results, we find puller dynamics for $1/\mathrm{Fa} \leq 0.5$, similarities to neutral swimmers for $1/\mathrm{Fa} = 0.75$ and pusher dynamics for $1/\mathrm{Fa} \geq 1$. For $\beta = 0$ we qualitatively obtain the same results for $1/\mathrm{Fa} \geq 1/\mathrm{Fa}_{crit}$ and thus only pusher dynamics. The corresponding velocity profiles from the squirmer model are obtained from a data fit, see Fig. 6.14: $n_1 = 0.086$, $m = 0.357$ (puller), $n_1 = 0.172$, $m = 0.059$ (neutral) and $n_1 = 0.291$, $m = -0.139$ (pusher), respectively. Although we compare results for nearly circular shapes, see Fig. 6.15 for the corresponding stationary profiles, with that from analytic results for circular shapes, we observe a reasonable agreement.

The analytical flow field of a circular squirmer particle can be described by a superposition of a uniform background velocity, in our case, the constant velocity of the moving cell v_{cell}, a Stokeslet, a stresslet and a source doublet. In [65] this is used to identify typical experimental flow fields. We here consider the same approach and use the velocity field of a circular cell with center of mass $\mathbf{x}_{cm} = (0,0)^\top$ in a co-moving

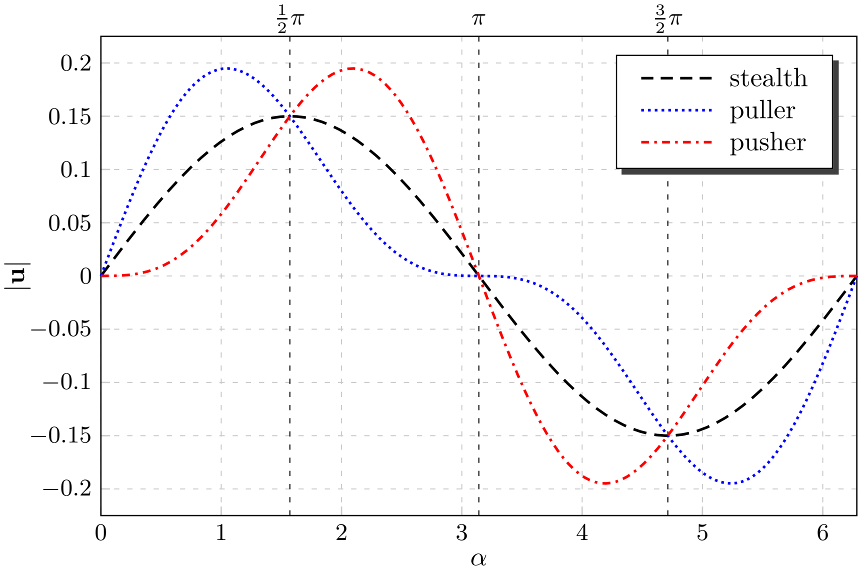

Figure 6.13. – Analytical solutions of the velocity profiles $\mathbf{v}_{T,squirmer}$ along the interface (Eq. 6.18), for different swimmer types.

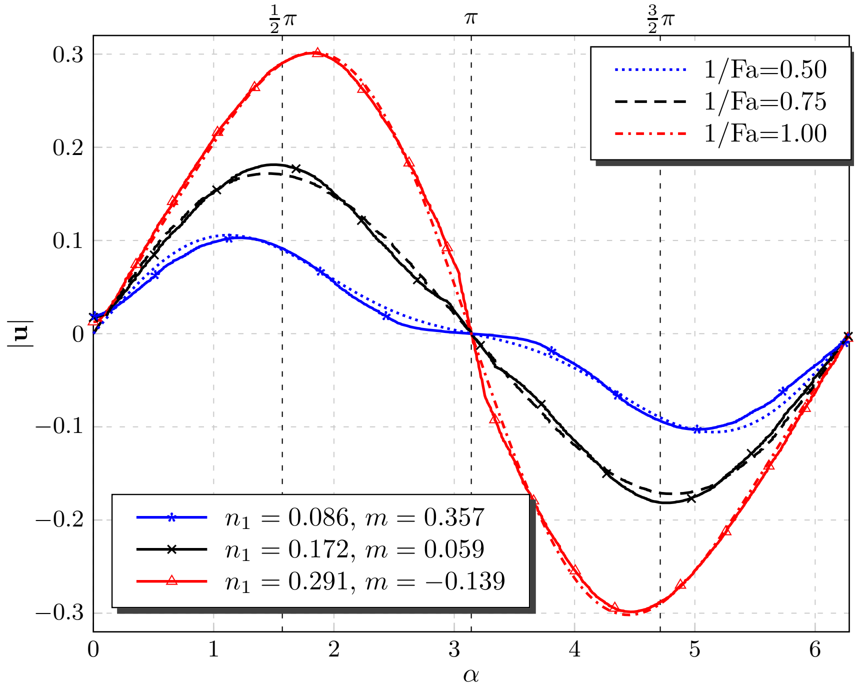

Figure 6.14. – Velocity profiles $\mathbf{v}_T$ (dashed lines) and corresponding datafit (solid lines) for various parameters 1/Fa.

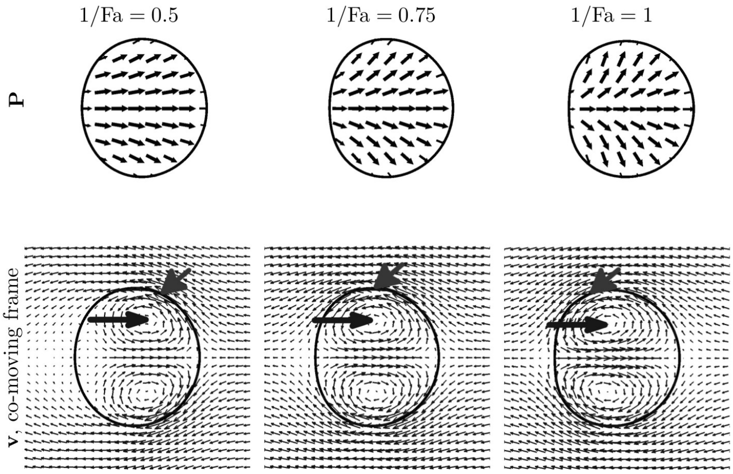

Figure 6.15. – Stationary shapes moving with constant velocity to the right for different 1/Fa: 0.5, 0.75, 1, from left to right. Polarization field (first row), velocity field in co-moving domain (second row). With increasing activity, the splay instability is enhanced, which moves the maximum of the velocity field along the interface (indicated by short angular arrow) from the front to the rear, visible also through the position of the vortices in the cell (indicated by long arrow), which are located more towards the front for puller dynamics and more towards the rear for pusher dynamics.

frame, given by

$$\mathbf{u}(\mathbf{r}) = -v_{cell}\mathbf{e}_1 - \frac{A_{st}}{r}(\mathbf{I} + \mathbf{r} \cdot \mathbf{r})\mathbf{e}_1 - \frac{A_{str}}{r^2}(1 - 3\left(\frac{x_1}{r}\right)^2)\mathbf{r} - \frac{A_{sd}}{r^3}\left(\frac{\mathbf{I}}{3} - \mathbf{r} \cdot \mathbf{r}\right)\mathbf{e}_1, \quad (6.19)$$

where $\mathbf{r} = \mathbf{x}/r$ is the polar axis, scaled with the distance $r = \sqrt{x_1^2 + x_2^2}$, $\mathbf{e}_1$ the unity vector in x_1-direction and $\mathbf{I}$ the identity matrix. We prepared our numerical solution: $\mathbf{v} = (v_1 - v_{cell}, v_2)^T$, $\mathbf{x} = (x_1 - x_{cm}, x_2 - y_{cm})^T$ and claim $|\mathbf{v} - \mathbf{u}| \to \min$ outside the circular cell shape with radius $R = 5$ to determine v_{cell}, A_{st}, A_{str} and A_{sd}. Tab. 6.3 shows the parameters obtained from the data fit. For $1/\mathrm{Fa} = 0.5$ the stresslet parameter A_{str} is negative, which indicates a puller-like velocity profile and for $1/\mathrm{Fa} = 1$ A_{str} is positive, indicating a pusher-like velocity profile. For $1/\mathrm{Fa} = 0.75$ the data fit suggests a low puller-like velocity profile. However, we should keep in mind that we compare velocity profiles of a circular and a non-circular shape. This discrepancy can be seen by analyzing the relative error $|\mathbf{v} - \mathbf{u}|/v_{cell}$ between the numerical results and the fitted analytical solution, see Fig. 6.16. The maximum of the error appears at the part of the cell, where it is compressed and does not overlap with the circular shape.

Even if a transition from puller-like to pusher-like dynamics can be observed for increasing actin-myosin interactions, the flow characteristics are much less developed than in typical squirmer models [191] and are dominated by the Stokeslet contribution. Within the analytical treatment of a circular droplet in [259] it was found that the droplet behaves like a puller. However, for the small splay considered, the corresponding flow field is not sufficient for motility and it is the quadrupole moment that characterizes the

1/Fa	v_{cell}	A_{st}	A_{str}	A_{sd}
0.50	0.0294	0.0387	-0.3541	12.5882
0.75	0.0701	0.0872	-0.1744	28.8854
1.00	0.1089	0.1460	0.3910	47.3611

Table 6.3. – Optimal parameters for background velocity v_{cell}, the Stokeslet A_{st}, the stresslet A_{str} and the source doublet A_{sd} obtained from a data fit with the numerical solution.

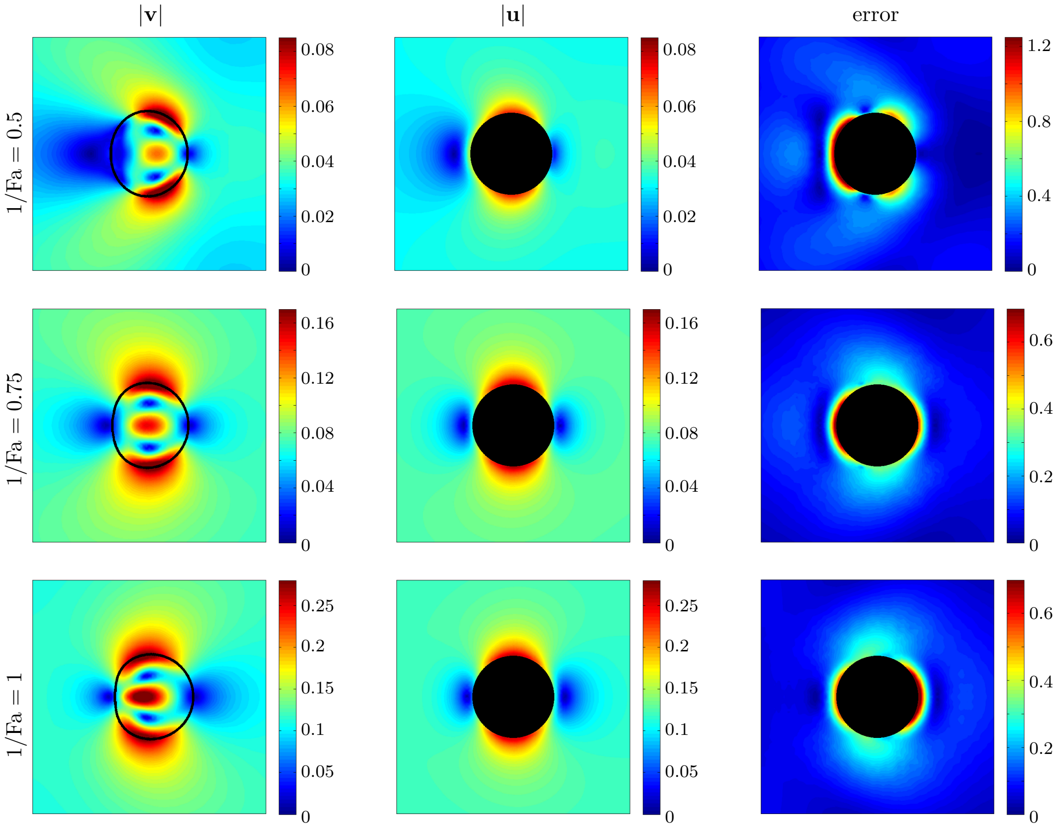

Figure 6.16. – Magnitude of the velocity profile of the numerical solution $|\mathbf{v}|$ (left), the fitted analytical solution $|\mathbf{u}|$ (middle) and the relative error (right) for $1/\text{Fa} = 0.5$ (first row), $1/\text{Fa} = 0.75$ (second row) and $1/\text{Fa} = 1$ (third row). For the analytical solution as well as the error analysis we approximated the cell shape by a circle, with radius $R = 5$ obtained from the initial condition. The data fit indicates $1/\text{Fa} = 0.5$ as puller and $1/\text{Fa} = 1$ as pusher. For $1/\text{Fa} = 0.75$ we get a puller-like velocity profile, where we expected a neutral swimmer, which of course can be a result of the approximated circular shape of the cell. (color online)

motility mechanism, resembling the motility mechanism of a squirmer. This is consistent with our findings for low 1/Fa.

In [65] the same fitting approach is used to analyze the flow topology for swimming microorganisms, such as *Cloamydomonas reinhardtii* and *Volvox carteri*. Here, the flow is also strongly dominated by the Stokeslet contribution and puller-like dynamics are only mildly developed. However, for a quantitative comparison of our results with the flow fields of such microorganisms, or that of bacteria, which typically show pusher-like dynamics, more experimental data are required. It would be interesting how predictions of the considered model in 3D compare with such measured flow fields in the future.

6.6. Conclusion

We here reviewed and extended a proposed generic model for cell motility [242], which is based on spontaneous symmetry breaking in active polar gels. It models the interaction of myosin and actin as the driving mechanism for motility and does not require adhesion. It further accounts for a more complex behavior of the cell bulk by a distinct elasticity of the filaments. The model is extended to include further membrane properties, in particular bending properties, which however turn out to be of minor relevance for motility in the considered parameter regime. Detailed numerical studies are performed and convergence studies considered to demonstrate the stability of the used algorithm, which is based on a diffuse interface description. The results clearly indicate the independence of the physical instabilities, the splay or bend instability, which are responsible for cell motility in the considered model, and possible numerical instabilities and show the robustness of the motility mode. With this confidence in the model and the developed numerical algorithm, the results are compared with model and experimental data for swimming microorganisms. Within certain parameter regimes a transition from puller-like to pusher-like dynamics can be found for increasing myosin-actin interactions, demonstrating the generic properties of the model. A quantitative comparison with swimming microorganism is not yet possible, requires 3D simulations and probably further model extension. One possible way to extend the model is a combination of the myosin-actin interactions with the treadmilling process of actin polymerization and depolymerization, described in Chapter 5. However, qualitative similarities with generated flow fields of microorganisms, such as *Volvox carteri* could already be found. The simulated flow field as well as the measured flow field is dominated by the Stokeslet contribution. In [65] it is argued that this behavior is going to have an effect on the rheology of suspensions of such microorganisms. With these properties, suspensions of our modeled cells would probably behave more like suspensions of sedimenting particles, as higher order moments are negligible in flow fields dominated by the Stokeslet contribution. However, if this assumption holds, or the weakly developed puller- or pusher-like dynamics in the considered model are already sufficient to observe typical phenomena in active fluids, e.g. as phase-separation, have to be tested. A general model for this is developed in Chapter 9.

Part II.

Dynamics of multiple cells

CHAPTER 7

A hydrodynamic model for multiple cells

In our previous work, we only considered a single cell. However, in many biological systems cells appear with various other cells. They can collide, connect or influence the flow field for other cells. Migrating cells can trace the signal of the leading cell and red blood cells in a vessel show various non-linear behavior, such as the Fåhræus–Lindqvist effect [96]. This effect describes that the macroscopic viscosity of the blood depends on the thickness of the blood vessels and therefore depends on the velocity of the blood flow, which differs from the classic Newtonian dynamics. In order to understand this phenomenon, we consider the complex microstructure of the blood, where the elasticity of the RBCs and their collision rate, which highly depend on the flow rate, affect the macroscopic properties of the blood. Moreover, actively driven cells or particles are of wide interest for many biological or soft matter physicists. So called active systems can lead to variety of non-linear phenomena, such as motility-induced phase separation, where active particles form stable clusters in absence of any attractive potential, see e.g. [114] for a review.

Up to now, there here have been various numerical approaches for multi-particle systems, especially in the sense of collective migration using particle-based methods [165, 166, 180] or Vicsek-type models [183, 253]. But all of them neglect the deformability of the particles. The deformability, in contrast, has been taken into account within a non-hydrodynamic model in [185]. Other approaches such as Level-Set methods [218], particle-based mesoscale simulation methods [100, 182], parametric finite-elements methods [25] or a combined approach that uses finite elements, immersed-boundary and lattice-Boltzmann methods [138] consider passive and not self-propelled deformable objects in fluid flow. In [41, 160, 196] the diffuse interface method has successfully been applied to multiple cells, but non of them consider fluid flow.

As a lot of those non-linear phenomena are poorly understood especially with the consideration of fluid flow, we develop a mathematical model for multiple cells based on a multi-phase approach of the diffuse interface Navier-Stokes-Helfrich model, which accounts for bending, surface tension or surface conservation and fluid flow. In Chapter 7, we describe the framework for the treatment of multiple phase field variables, where we introduce an interaction potential in order to prevent the cells from overlapping. We classify the collective motion into two groups: a passive motion, where the cells are only advected by the fluid flow and an active migration, where the cells are propelled by their own impetus resulting from cell motility or swimming mechanisms. An application for a passive motion is given in Chapter 8. Here, we simulate the flow of red and white blood cells to understand the dependency between WBC margination and the flow regime. In Chapter 9, we extend our passive model by an active polar gel theory to study binary collisions and the onset of collective migration in systems of self-propelled cells, see Chapter 6.

Within this chapter, we extend our theory for diffuse interface Navier-Stokes-Helfrich model based on a two-phase flow description for a single cell to a multi-phase flow approach that considers several cells embedded in a fluid environment. The structure of this chapter is given as follows: we introduce the notation for the multi-phase flow. We introduce the model that considers an interaction potential between different cells using a sharp interface formulation, Section 7.1.1. Then, we apply a diffuse interface approach using multiple phase field variables that leads to a thermodynamically consistent hydrodynamic model, see Section 7.1.2 and Section 7.1.3. In Section 7.2, we briefly describe the numerical treatment of all equations and point out how such highly coupled systems can be treated numerically and how its numerical costs can be limited using operator splitting approaches and problem parallelization with OPENMP. We further conduct several benchmark computations in Section 7.3 where we compare our approach with other strategies within the phase field approach and investigate its dependency on various model parameters.

The hydrodynamic approach for multiple cells, which we describe in this chapter, has recently been published in Marth et al. [177] and Ling et al. [156].

7.1. Mathematical model

7.1.1. Sharp interface formulation

We now consider multiple cells and extend the definition for cell bulk and surface as given in Section 2.1 to N cells $\bar{\Omega}_i = \Omega_i \cup \Gamma_i$ where Ω_i denotes the cell interior and Γ_i the membrane of cell i. Thus, the Helfrich energy eq. (3.5) becomes

$$E(\Gamma_i) = \int_{\Gamma_i} \frac{1}{2} b_{n,i} (H - H_{0,i})^2 \, \mathrm{ds}$$

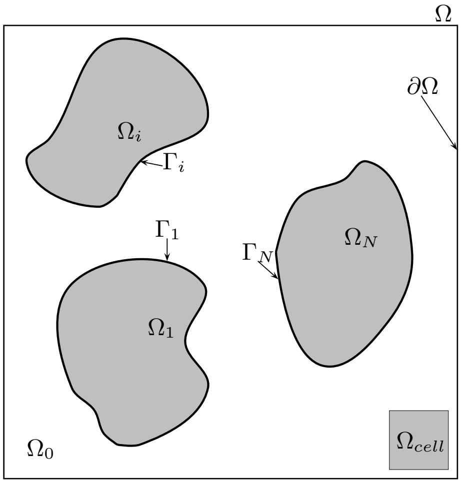

Figure 7.1. – Illustration of the two-dimensional domain Ω containing multiple cells

and accordingly assigns the different physical properties $b_{n,i}$ and $H_{0,i}$ to a specific membrane. Furthermore, the surrounding fluid is still defined as Ω_0. As before, the membrane $\Gamma_i = \bar{\Omega}_0 \cap \bar{\Omega}_i$ for $i = 1, \ldots, N$ is considered as interface between the cell and the surrounding fluid. We claim that all phases do not overlap, i.e. $\Omega_i \cap \Omega_j = \emptyset$ for $i \neq j$. Moreover, we introduce the domain $\Omega_{cell} = \cup_{i=1}^{N} \Omega_i$ containing of cell interiors and $\Gamma_{cell} = \cup_{i=1}^{N} \Gamma_i$ containing all surfaces. It is clear that $\Omega = (\Omega_{cell} \cup \Gamma_{cell}) \cup \Omega_0$, see Fig. 7.1 for an illustration. We assume each phase $\Omega_0, \ldots, \Omega_N$ to be an incompressible Newtonian fluid described by the Navier-Stokes equations as given in the eq. (2.47) -(2.48). The jump conditions across the interfaces for the velocity field is given by

$$[\mathbf{v}]_{\Gamma_i} = 0, \qquad \text{zero velocity jump,} \tag{7.1}$$

and for the stress in normal direction, we can choose between

$$[\mathbf{S} \cdot \mathbf{n}]_{\Gamma_i} = \frac{\delta E}{\delta \Gamma_i} + \lambda_{global,i} H \mathbf{n}, \qquad \text{with a global area constraint, and}$$

$$[\mathbf{S} \cdot \mathbf{n}]_{\Gamma_i} = \frac{\delta E}{\delta \Gamma_i} + \lambda_{local} H \mathbf{n} + \nabla_{\Gamma_i} \lambda_{local}, \text{with a local inextensibility constraint,}$$

with $[f]_{\Gamma_i} = f_0 - f_i$ the jump across $\Gamma_i(t)$ and $\mathbf{n}$ the outward normal pointing out of $\Omega_i(t)$. The surface gradient is $\nabla_{\Gamma_i} = \mathbf{P}_{\Gamma_i} \nabla$ with $\mathbf{P}_{\Gamma_i}$ the projection operator. Because $\lambda_{local} := \lambda_{local}(t, \mathbf{x})$ is a local variable, we do not assign λ_{local} to each cell.

In order to prevent the cells from overlapping, we model a steric interaction potential, which in the sharp interface description reads for each cell i

$$E_{i,int}(\Gamma_1, \ldots, \Gamma_N) = \sum_{\substack{j=1 \\ j \neq i}}^{N} \alpha_{ij} \int_{\Gamma_i} w_j \, \mathrm{ds},$$

where w_j is an interaction function and describes the influence of cell j to its environment.

The interaction parameter $\alpha_{ij} > 0$ determines the strength of the repulsive interaction between cell i and cell j with respect to the evolution of cell i. By setting $\alpha_{ij} < 0$, we can further describe an adhesive interaction [266]. Usually, such a contact potential is defined as

$$w_j(r_j(\mathbf{x})) = \begin{cases} \infty & \text{if } r_j(\mathbf{x}) = 0, \\ 0 & \text{otherwise.} \end{cases}$$

A much more appropriate way is to consider the short range repulsion by a Gaußian potential [266]

$$w_j(t, \mathbf{x}) = \exp\left(-\frac{r_j^2(t, \mathbf{x})}{\varepsilon^2}\right), \tag{7.2}$$

where ε is a smoothing parameter, determining the range of the interaction. Here, the signed distance function $r_j(t, \mathbf{x})$ specifies the distance between $\mathbf{x} \in \Omega$ and its nearest point on Γ_j. The calculation of $r_j(t, \mathbf{x})$ may be computationally expensive. Applying the diffuse interface approach, as discussed in the following section, will overcome this problem.

7.1.2. Diffuse interface approach

The extension to the diffuse interface is straightforward and similarly to previous sections. In addition, we introduce multiple phase field variables $\phi_1, \ldots, \phi_N$, labeling the inside and outside of each cell. The membrane Γ_i is regarded as the diffuse layer between the two phases and implicitly defined by the zero level set of ϕ_i. The phase field variables are defined as

$$\phi_i(t, \mathbf{x}) := \tanh\left(\frac{r_i(t, \mathbf{x})}{\sqrt{2}\varepsilon}\right), \tag{7.3}$$

analog to the definition for one phase field. Here, the interface thickness parameter ε is set to be constant for all phases, but the method allows us to choose different ε, for instance, to treat cells with different sizes. Moreover, the phase containing all cells, previously defined by Ω_{cell}, can thus be defined as $\phi_{cell} = 1$ with $\phi_{cell} = \max_{x \in \Omega}(\phi_1, \ldots, \phi_N)$ and its counterpart, the phase of the surrounding fluid as $\phi_0 = -\phi_{cell}$. Interaction in principle is computationally costly, as it turns the problem into a non-local one and requires the coupling of all phase field variables $\phi_1, \ldots, \phi_N$ and computations of the distance between cells. Using eq. (7.3), the signed distance function r_j can be computed within the diffuse interface region as

$$r_j = -\frac{\varepsilon}{\sqrt{2}} \ln \frac{1 + \phi_j}{1 - \phi_j}, \quad \text{for all } \mathbf{x} : |\phi_j| < 1.$$

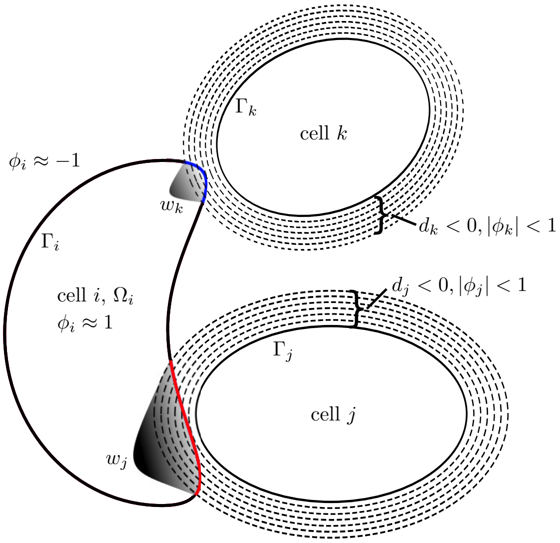

Figure 7.2. – Illustration of the interaction potential. The red and blue colored parts of Γ_i are in contact with the interfaces of cell j and cell k (dashed contours around those cells), where the signed functions r_j and r_k can be calculated and thus also the interaction functions w_j and w_k. They do not vanish in the overlapping regions.

Accordingly, we can write the short range interaction function w_j as

$$w_j = \begin{cases} \exp\left(-\frac{1}{2}(\ln\frac{1+\phi_j}{1-\phi_j})^2\right), & \text{if } |\phi_j| < 1, \\ 0, & \text{otherwise,} \end{cases}$$

and consider the interaction potential for cell i within the diffuse interface description, which reads

$$\mathcal{E}_{i,int}(\phi_1, \ldots, \phi_N) = \int_\Omega B(\phi_i) \sum_{\substack{j=1 \\ j\neq i}}^{N} \alpha_{ij} w_j \, \mathrm{d}\mathbf{x},$$

with $B(\phi_i) = \frac{1}{\varepsilon}(\phi_i^2 - 1)^2$, being nonzero only within the diffuse interface region around Γ_i. In addition, $B(\phi_i)$ serves as approximation of the surface delta function δ_Γ as $\delta_\phi := \frac{3}{4\sqrt{2}} B(\phi_i) \to \delta_\Gamma$, if $\varepsilon \to 0$. Other approaches for δ_ϕ, e.g. the Cahn-Hilliard energy eq. (2.22), may also be used. Fig. 7.2 gives a schematic illustration of the interaction terms. The algorithm considers only these cells, for which the diffuse interfaces overlap. All other cells do not contribute to the interaction. In addition, the most expensive part, computing the distance between cells, has been avoided as this information is already contained in the phase field description of the cells. The approach, thus, scales with N, the number of cells. Similar ideas to model interactions within phase field approaches have been considered in [116, 266] to model substrate adhesion for a single cell. Other approaches, such as [41, 160], consider multi-phase systems. However, all models neglect fluid flow.

Finally, we specify the non-dimensional overall energy of the system in a fluid domain containing N cells

$$\mathcal{E}(\mathbf{v},\phi_1,\dots,\phi_N) = \mathcal{E}_{kin}(\mathbf{v}) + \sum_{i=1}^{N} \mathcal{E}_{S,i}(\phi_i) + \mathcal{E}_{int}(\phi_1,\dots,\phi_N). \tag{7.4}$$

We choose the surface energy to be the Helfrich energy with surface area conservation eq. (3.33)

$$\mathcal{E}_{S,i}(\phi_i) = \frac{1}{\mathrm{Be}_i}\frac{1}{2\varepsilon}\int_\Omega \left(\varepsilon\Delta\phi_i - \frac{1}{\varepsilon}W'_{0,i}(\phi_i)\right)^2 + \frac{p_{2,i}}{2\mathrm{Be}}\left(\mathcal{E}_{CH}(\phi_i) - \mathcal{A}_{0,i}\right)^2 \mathrm{d}\mathbf{x},$$

where the volume constraint is removed since an H^{-1}-gradient flow will directly ensure the volume conservation. Furthermore, we have $W'_{0,i}(\phi_i) = (\phi_i^2 - 1)(\phi_i + H_{0,i})$, $\mathcal{A}_{0,i} = \mathcal{E}_{CH}(\phi_i(t=0,\mathbf{x}))$ and the interaction energy in non-dimensional form for all cells

$$\mathcal{E}_{int}(\phi_1,\dots,\phi_N) = \sum_{i=1}^{N}\int_\Omega B(\phi_i)\sum_{\substack{j=1\\ j\neq i}}^{N}\frac{1}{\mathrm{In}_{ij}}w_j \,\mathrm{d}\mathbf{x} \tag{7.5}$$

with $\mathrm{In}_{ij} = \frac{4\sqrt{2}}{3}\frac{\eta_0 U}{\alpha_{ij}}$ the interaction number. In the following we review the governing equations and we show that the complete system fulfills thermodynamic consistency. All further PDEs are defined in $I \times \Omega$.

Phase field equations

The evolution equation for ϕ_i reads in $I \times \Omega$

$$\partial_t\phi_i + \mathbf{v}\cdot\nabla\phi_i = \gamma\Delta\phi_i^\natural, \tag{7.6}$$

with a small positive mobility coefficient γ and the non-dimensional chemical potential

$$\phi_i^\natural := \frac{\delta\mathcal{E}(\phi_1,\dots,\phi_N)}{\delta\phi_i} = \frac{\delta\mathcal{E}_{S,i}(\phi_i)}{\delta\phi_i} + \frac{\delta\mathcal{E}_{int}(\phi_1,\dots,\phi_N)}{\delta\phi_i}, \tag{7.7}$$

where the variation of the surface energy, similar to eq. (3.62)-(3.64), is

$$\frac{\delta\mathcal{E}_{S,i}}{\delta\phi_i} = \frac{1}{\mathrm{Be}_i}\left(\Delta\mu_i - \frac{1}{\varepsilon^2}W''_{0,i}(\phi_i)\mu_i + p_{2,i}(\mathcal{E}_{CH}(\phi_i) - \mathcal{A}_{0,i})\kappa_i\right), \tag{7.8}$$

$$\mu_i = \varepsilon\Delta\phi_i - \frac{1}{\varepsilon}W'_{0,i}(\phi_i), \tag{7.9}$$

$$\kappa_i = -\varepsilon\Delta\phi_i + \frac{1}{\varepsilon}W'(\phi_i), \tag{7.10}$$

and the variation of the interaction energy is

$$\frac{\delta\mathcal{E}_{int}(\phi_1,\dots,\phi_N)}{\delta\phi_i} = B'(\phi_i)\sum_{\substack{j=1\\ j\neq i}}^{N}\frac{1}{\mathrm{In}_{ij}}w_j + w'_i\sum_{\substack{j=1\\ j\neq i}}^{N}\frac{1}{\mathrm{In}_{ji}}B(\phi_j), \tag{7.11}$$

with

$$w_i' = \begin{cases} \frac{2}{\phi_i^2-1} \ln \frac{1+\phi_i}{1-\phi_i} \exp\left(-\frac{1}{2}(\ln \frac{1+\phi_j}{1-\phi_j})^2\right), & \text{if } |\phi_j(t,\mathbf{x})| < 1, \\ 0, & \text{otherwise.} \end{cases}$$

Please note, for simplicity we only consider equal interaction numbers i.e. $\mathrm{In} = \mathrm{In}_{ij}$. Therefore, the variation eq. (7.11) becomes

$$\frac{\delta\mathcal{E}_{int}(\phi_1,\dots,\phi_N)}{\delta\phi_i} = \frac{1}{\mathrm{In}}\left(B'(\phi_i)\sum_{\substack{j=1\\j\neq i}}^{N} w_j + w_i'\sum_{\substack{j=1\\j\neq i}}^{N} B(\phi_j)\right).$$

Navier-Stokes equations

Finally, the non-dimensional Navier-Stokes equations are given by

$$\rho(\phi)\mathrm{Re}(\partial_t\mathbf{v} + \mathbf{v}\cdot\nabla\mathbf{v}) + \nabla p = \nabla\cdot(\eta(\phi)\mathbf{D}) + \sum_{i=1}^{N}\phi_i^{\natural}\nabla\phi_i, \tag{7.12}$$

$$\nabla\cdot\mathbf{v} = 0, \tag{7.13}$$

with $\rho(\phi) := \rho(\phi_1,\dots,\phi_N) = 1$ and $\eta(\phi) := \eta(\phi_1,\dots,\phi_N) = \frac{1-\phi_{cell}}{2} + \sum_{i=1}^{N}\frac{\eta_i}{\eta_0}\frac{\phi_i+1}{2}$. Different densities could be handled similarly, but are omitted here for simplicity.

Inextensibility for multiple cells

To enforce the local inextensibility constraint, we follow the first approach as described in Section 3.4.3 and [12] and extend it to multiple cells. We use the local Lagrange multiplier λ_{local} in order to enforce the inextensibility within the Navier-Stokes system. For that we consider ϕ_{cell} to merge all cells. Then, the Navier-Stokes equations become

$$\mathrm{Re}(\partial_t\mathbf{v} + \mathbf{v}\cdot\nabla\mathbf{v}) + \nabla p - \nabla\cdot(\eta(\phi)\mathbf{D}) = \sum_{i=1}^{N}\phi_i^{\natural}\nabla\phi_i + \nabla\cdot\left(\frac{|\nabla\phi_{cells}|}{2}\mathbf{P}_{\phi}\lambda_{local}\right), \tag{7.14}$$

$$\nabla\cdot\mathbf{v} = 0, \tag{7.15}$$

$$\xi\varepsilon^2\nabla\cdot(\phi_{cells}^2\nabla\lambda_{local}) + \frac{|\nabla\phi_{cells}|}{2}\mathbf{P}_{\phi} : \nabla\mathbf{v} = 0, \tag{7.16}$$

where $\xi > 0$ is a parameter independent of ε. For $\varepsilon \to 0$ we obtain $\Delta\lambda_{local} = 0$ away from Γ_{cells} and $\mathbf{P}_{\Gamma} : \nabla\mathbf{v} = \nabla_{\Gamma}\cdot\mathbf{v} = 0$ near Γ_{cells}, as shown in [12] for $n = 1$.

Initial and boundary conditions

The coupled system obeys the following initial conditions

$$\mathbf{v}(t,\mathbf{x}) = \mathbf{v}^0(\mathbf{x}),\ \phi_i(t,\mathbf{x}) = \phi_i^0(\mathbf{x}),\ i = 1,\dots,N,$$

for $t = 0$ and $\mathbf{x} \in \Omega$, which are specified in each simulation. We further have to guarantee that the ϕ_i do not overlap. In the case of solid i.e. not periodic boundaries, we consider Dirichlet boundary conditions

$$\mathbf{v}(t, \mathbf{x}) = \mathbf{0},\ \phi_i(t, \mathbf{x}) = -1,\ i = 1, \dots, N,$$

and Neumann boundary conditions

$$\nabla \mu_i \cdot \mathbf{n} = \nabla \kappa_i \cdot \mathbf{n} = \nabla \phi_i^{\natural} \cdot \mathbf{n} = \nabla \lambda_{local} \cdot \mathbf{n} = 0,\ i = 1, \dots, N,$$

which hold for $t > 0$ and $\mathbf{x} \in \partial\Omega$.

7.1.3. Thermodynamic consistency

The proposed system of equations (7.6) and (7.7) for $i = 1, \dots, N$ and eq. (7.14)-(7.16) fulfills thermodynamic consistency. To show this, we prove that the time derivative

$$\frac{\mathrm{d}\mathcal{E}}{\mathrm{dt}} = \int \mathrm{Re}\mathbf{v}\mathbf{v}_t + \sum_{i=1}^{N} \phi_i^{\natural} \partial_t \phi_i \,\mathrm{d}\mathbf{x} \tag{7.17}$$

of the overall energy eq. (7.4) is less or equal to zero. Inserting

$$\begin{aligned} \partial_t \phi_i &= -\mathbf{v} \cdot \nabla \phi_i + \gamma \Delta \phi_i^{\natural}, \\ \mathrm{Re}\partial_t \mathbf{v} &= -\mathrm{Re}(\mathbf{v} \cdot \nabla)\mathbf{v} - \nabla p + \nabla \cdot (\eta(\phi)\mathbf{D}) + \sum_{i=1}^{N} \phi_i^{\natural} \nabla \phi_i + \nabla \cdot \left(\frac{|\nabla \phi_{cells}|}{2} \mathbf{P}_{\phi} \lambda_{local} \right), \end{aligned}$$

into eq. (7.17) yields

$$\begin{aligned} \frac{\mathrm{d}\mathcal{E}}{\mathrm{dt}} = \int_{\Omega} \mathbf{v} \cdot & \Bigg(-\mathrm{Re}(\mathbf{v} \cdot \nabla)\mathbf{v} - \nabla p + \nabla \cdot (\eta(\phi)\mathbf{D}) + \sum_{i=1}^{N} \phi_i^{\natural} \nabla \phi_i \\ & + \nabla \cdot \left(\frac{|\nabla \phi_{cells}|}{2} \mathbf{P}_{\phi} \lambda_{local} \right) \Bigg) + \sum_{i=1}^{N} \phi_i^{\natural} (-\mathbf{v} \cdot \nabla \phi_i + \gamma \Delta \phi_i^{\natural}) \,\mathrm{d}\mathbf{x} \\ = & \int -\nabla \mathbf{v} : \eta(\phi)\mathbf{D} - \gamma \sum_{i=1}^{N} |\nabla \phi_i^{\natural}|^2 - \left(\nabla \mathbf{v} : \frac{|\nabla \phi_{cells}|}{2} \mathbf{P}_{\phi} \right) \lambda_{local} \,\mathrm{d}\mathbf{x} \\ = & \int -\eta(\phi)\mathbf{D} : \mathbf{D} - \gamma \sum_{i=1}^{N} |\nabla \phi_i^{\natural}|^2 - \xi \varepsilon^2 \phi_{cells}^2 |\nabla \lambda_{local}|^2 \,\mathrm{d}\mathbf{x} \leq 0, \end{aligned}$$

where we have performed the same procedure as in Section 2.8. In particular, we inserted eq. (7.16) in the last line that describes the energy law for this problem.

7.2. Numerical approach

7.2.1. Time discretization

For the time discretization, we explore an operator splitting approach and adapt the same strategy as in the previous sections. In an iterative process, we first solve the flow problem and substitute its solution into the phase-field equations, which are then solved separately with a parallel splitting method. We again split up the time interval $I = [0, T]$ as done in previous sections. For each system, a semi-implicit time discretization is used, which together with an appropriate linearization of the involved non-linear terms leads to a set of linear system in each time step:

1. the flow problem for $\mathbf{v}^{n+1}$, p^{n+1} and λ_{local}^{n+1}:

$$\begin{aligned} \mathrm{Re}\left(d_t\mathbf{v}^{n+1} + (\mathbf{v}^n \cdot \nabla)\mathbf{v}^{n+1}\right) &= -\nabla p^{n+1} + \nabla \cdot (\eta(\phi^n)\mathbf{D}^{n+1}) + \sum_{i=1}^{N} \phi^{\natural^n} \nabla \phi_i^n \\ &\quad + \nabla \cdot \left(\frac{|\nabla \phi_{cells}^n|}{2}\mathbf{P}_\phi^n \lambda_{local}^{n+1}\right), \\ \nabla \cdot \mathbf{v}^{n+1} &= 0, \\ \xi\varepsilon^2\nabla \cdot ((\phi_{cells}^n)^2 \nabla \lambda_{local}^{n+1}) &= -\frac{|\nabla \phi_{cells}^n|}{2}\mathbf{P}_\phi^n : \nabla \mathbf{v}^{n+1}, \end{aligned}$$

   where $\mathbf{P}_\phi^n = \mathbf{I} - \frac{\nabla\phi^n \otimes \nabla\phi^n}{|\nabla\phi^n|^2}$.

2. the phase field equations for ϕ_i^{n+1}, $i = 1, \ldots, N$:

$$\begin{aligned} d_t\phi_i^{n+1} &= -\mathbf{v}^{n+1} \cdot \nabla\phi_i^{n+1} + \gamma\Delta\phi_i^{\natural^{n+1}}, \\ \phi_i^{\natural^{n+1}} &= \frac{1}{\mathrm{Be}_i}\left(\Delta\mu_i^{n+1} - \frac{1}{\varepsilon^2}W_{0,i}''(\phi_i^{n,n+1})\mu_i^{n,n+1}\right) \\ &\quad + \frac{c_i}{\mathrm{Be}_i}(\mathcal{E}_{CH}(\phi_i^n) - \mathcal{A}(\phi_i^n))\left(-\varepsilon\Delta\phi_i^{n+1} + \frac{1}{\varepsilon}W'(\phi_i^{n,n+1})\right) \\ &\quad + \frac{1}{\mathrm{In}}\left(B'(\phi_i^n)\sum_{\substack{j=1 \\ j\neq i}}^{N} w_j^n + w_i'^n \sum_{\substack{j=1 \\ j\neq i}}^{N} B(\phi_j^n)\right), \\ \mu_i^{n+1} &= \varepsilon\Delta\phi_i^{n+1} - \frac{1}{\varepsilon}W_{0,i}'(\phi_i^{n,n+1}). \end{aligned}$$

   We further linearize the non-linear terms by a Taylor expansion of order one according to Section 5.3.

7.2.2. Implementation

We apply the finite element method to discretize in space, where a P^2/P^1 Taylor-Hood element is used for the flow problem. All other quantities are discretized in space using P^2 elements as done in Section 6.3. The fully discretized system of partial differential equations is implemented using the adaptive finite element toolbox AMDiS [252, 261]. We use an adaptively refined triangular mesh $\mathcal{T}_h$ with a high resolution along the cell membranes to guarantee at least six grid points across the diffuse interface. We further conduct a shared memory OPENMP parallelization, to solve the phase field evolutions via a parallel splitting method. Each linear system of equations is solved using the direct solver UMFPACK [57].

7.3. Model justification

In [12, 218] it has been shown that two inextensible objects in an extensional flow do not coalesce due to the inextensibility of the membrane, even without an interaction potential. If this would also be true in more general cases, it would allow us to use one phase field variable for all objects and drastically simplify the considered model. We therefore consider the interaction of two objects in more detail and demonstrate that the introduced model is indispensable for approaches without inextensibility and even indispensable for approaches with inextensibility as this condition is only asymptotically fulfilled for diffuse interface models.

7.3.1. Collision of two cells

We set up two elliptical objects at $(1.45, 0.88)$ and $(3.8, 0.875)$, with axis length $0.5\sqrt{2}$ in x_2-direction and 0.5 in x_1-direction, where the first object is placed a little higher in order to have comparable situations at coalescence. The computational domain is $[0, 5.25] \times [0, 1.75]$. We apply Dirichlet conditions on each boundary. To provide a collision, we adopt a space dependent volume force $\mathbf{F} = (0.5(\phi+1)\frac{1}{\mathrm{Fr}} f_1, 0)^\top$, with $f_1 = 1$, if $x_1 < 2.625$ and $f_1 = -1$ if $x_1 > 2.625$, and choose the Froude number $\mathrm{Fr}{=}10^{-5}$. We set $\mathrm{Re} = 0.01$, $\mathrm{Be}_i = 5$, mobility $\gamma = 10^{-5}$ and a viscosity ratio $\eta_i/\eta_0 = 10$. The evolution of the objects at time 0.2, 0.4, 0.6 and 2.5 is shown in Fig. 7.3. Each row considers a different modeling approach. We consider six cases: one phase field without (a) and with (b) inextensibility constraint, two phase fields without (c) and with (d) inextensibility constraint and two phase fields and an interaction potential without (e) and with (f) inextensibility constraint. The last situation describes the used model in the paper. The black lines show the zero level set and the outer interface, e.g. the $[-0.8, 0]$ level sets, are colored blue in order to visualize the effects at coalescence.

The simulations show a strong influence of the inextensibility constraint on the dynamics, the objects move more slowly. However, the strongest effect can be seen on coalescence. For one phase field variable the objects come into contact, but do not merge, as merging would cost energy, due to a violation of the tanh profile. With the inextensibility constraint, which should inhibit the objects from touching according to [12, 218], the objects come into contact only at two points. However, also in this situation the phase field is irreversibly connected. The results of [12, 218] thus cannot be generalized. However, in our approach the inextensibility condition is only asymptotically fulfilled, which seems to avoid an entire adhesion but cannot prevent the objects from touching.

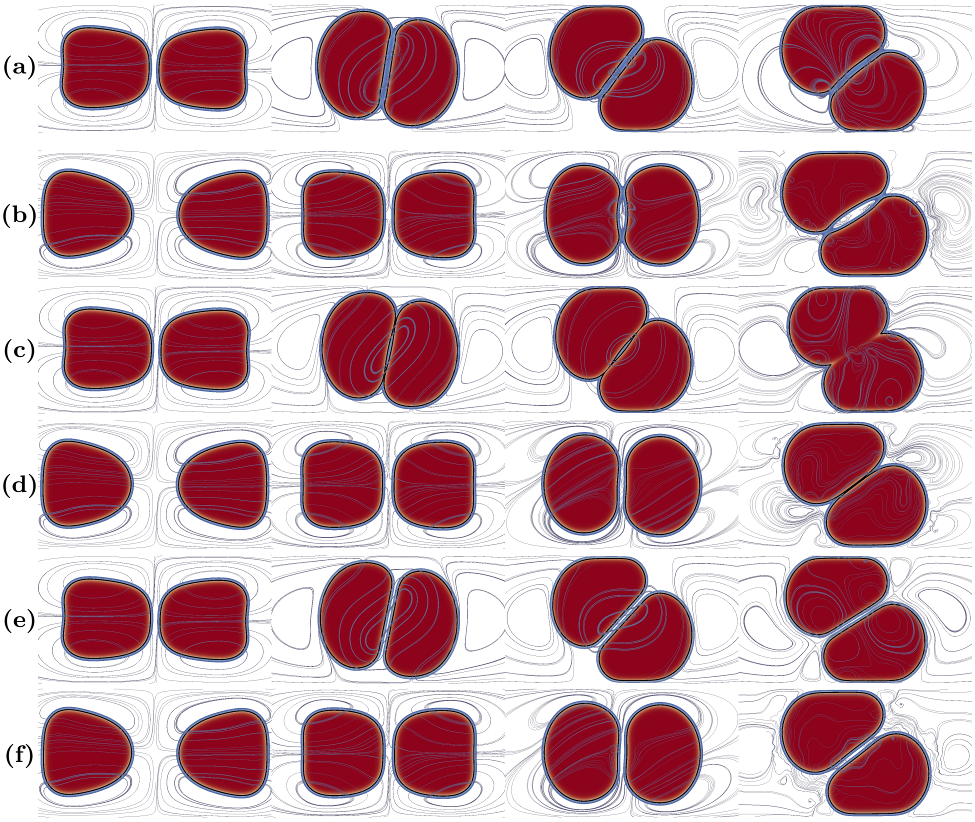

Figure 7.3. – Snapshots of the object collision for time 0.2, 0.4, 0.6 and 2.5 (from left to right). The rows indicate the used approaches: (a) one phase field, (b) one phase field with inextensibility, (c) two phase fields, (d) two phase fields with inextensibility, (e) two phase fields with interaction potential (Id= 0.01) and finally (f) two phase fields with interaction potential (Id= 0.01) and inextensibility. Shown are the streamlines of the velocity field as well as the $[-0.8, 1]$ level set of the ϕ_{cell} and the zero level set (black line)

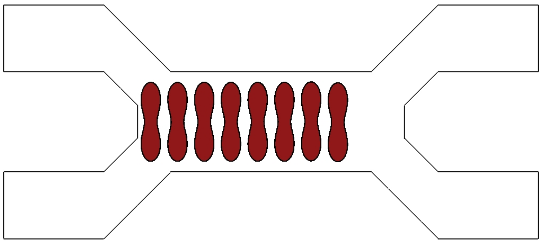

Figure 7.4. – eight RBC placed in a symmetric bifurcated vessel, initial condition

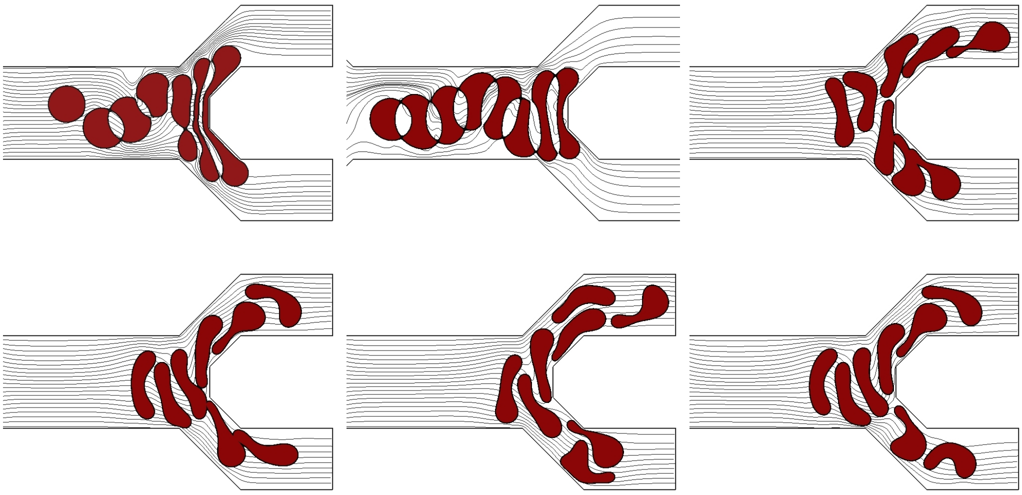

Figure 7.5. – Eight objects in a symmetric bifurcated channel (only half of the domain is shown). a) - f) are the same cases as in figure 7.3.

Overall, in our setting a single phase field is not sufficient to simulate more than one cell if contact cannot be avoided. With two phase fields but no interaction potential the situation is similar. Here, merging of objects by definition is not possible and due to the incompressibility of the fluid, overlapping objects should also not occur. However, the simulations show that objects touch each other, adhere and overlap slightly. This can be reduced by using the inextensibility constraint but not be prevented. Thus, this approach is not sufficient as well. Only with an interaction potential, contact or adhesion of objects was not observed, neither without nor with the inextensibility constraint. Only the remaining distance between the objects differs and is bigger if the inextensibility constraint is considered.

7.3.2. RBC in a bifurcated vessel

In the following, we consider a more realistic setting, where we put eight objects in a flow inside a bifurcated channel. The initial shape is a Cassini oval that is close to the discoidal shape of a RBC. We consider similar parameters as before, Re$= 1.125 \cdot 10^{-4}$, Be$_i = 2.5$, Id$= 0.01$, $\gamma = 10^{-7}$ and a viscosity ratio $\eta_i/\eta_0 = 10$. Flow is considered through the force term $\mathbf{F} = (\frac{1}{\mathrm{Fr}}, 0)^\top$, with Fr$= 2.4 \cdot 10^{-6}$ leading to a maximal velocity of magnitude 10. Figure 7.5 shows the results for the same eight cases as considered above. Also for this situation, only the cases with one phase field for each object and an interaction potential lead to acceptable results. Differences in the dynamics still can be observed for the case with and without the inextensibility constraint.

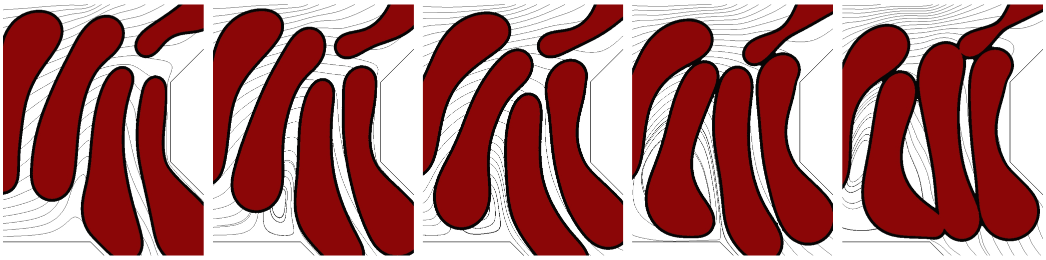

(a) In $= 0.001$ (b) In $= 0.01$ (c) In $= 0.1$ (d) In $= 1.$ (e) $1/\text{In} = 0$

Figure 7.6. – Clip from the simulation for case 5 at time 1 for different interaction strength from high interaction strength (left) to no interaction strength (right). The interaction strength should be chosen carefully as for low interaction a contact and adhesion cannot be prevented. On the other hand, a high interaction strength can compromise the simulation.

7.3.3. Variation of the interaction strength

We again start the simulation from above for case 5 and vary the strength of the interaction potential. Due to this parameter, we can adjust the distance between each vesicle during a collision. Fig. 7.6 shows that for smaller interaction strength (higher In) the distance between cells decrease unless they come directly into contact. Moreover, the choice of an interaction parameter has also direct influence to the cell's shape and position: smaller interaction strength can lead to temporary or permanent adhesion between cells and higher interaction strength can lead to a stronger deformation while a collision as the interaction potential becomes dominant in the total energy and an increasing of the Helfrich part becomes irrelevant.

7.4. Discussion and conclusion

In this chapter, we showed an approach for the treatment of multiple cells. We introduced an interaction potential that locally prevents the cells from overlapping. This approach only considers these cells for which the diffuse interfaces interfere. All other cells do not contribute to the interaction. The most expensive part, computing the distance between cells, has been avoided, as this information is already contained in the phase field description of the cells. Since our approach is given in a hydrodynamic multi-phase formulation, it offers a wide range of application.

In the previous studies, our model considers only a repulsive interaction. This approach can easily be extended to adhesion dynamics. For instance, Zhang et al. [266] modeled substrate adhesion, where they place a three-dimensional vesicle on a substrate that is implicitly defined by a signed distance function. Applications for cell-cell adhesion can be found in [160], where the authors studied collective cell migration. If an overlapping of the cell can be excluded, e.g. by a boundary condition, the adhesion interaction function is $\tilde{w}_j = -w_j$. In general, an adhesion potential should still prevent overlapping. This can be fulfilled by using a linear combination of long range adhesion

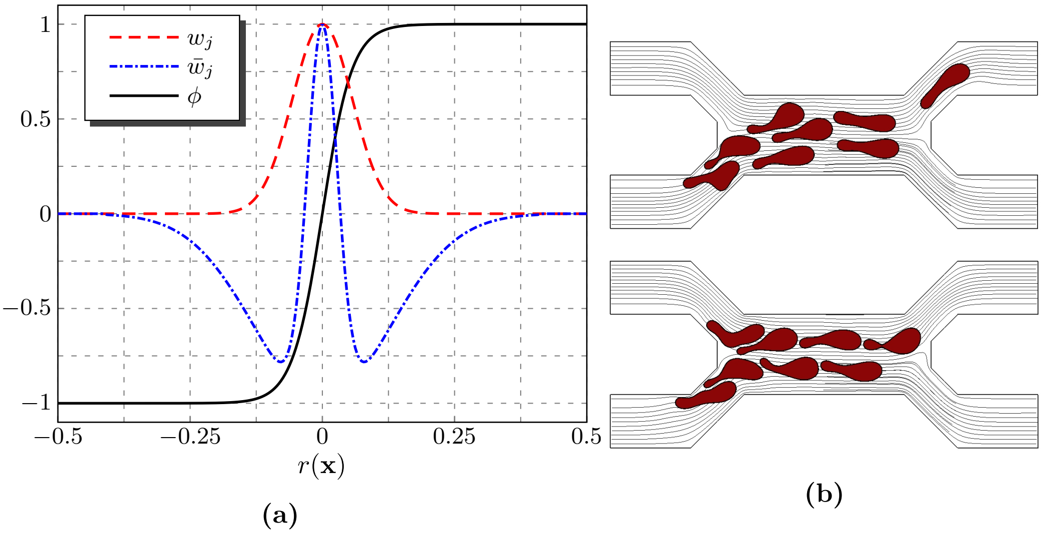

(a)

(b)

Figure 7.7. – (a) Graph of potential functions in 1D. The cell membrane is given for $r(\mathbf{x}) = 0$. Values for $r(\mathbf{x}) < 0$ can be neglected. (b) Comparison of a repulsive potential function w_j (top) and a Lennard-Jones-like potential $\bar{w}_j$ (bottom) for eight RBC in a bifurcated vessel. Because of the adhesive part the cells are much more attached and form chains of RBCs. Parameters: $\varepsilon = 0.04$; $r_1 = 1$, $r_2 = 4$, $a_1 = 0$, (w_j); $r_1 = 2$, $r_2 = 1$, $a_1 = 1$, $a_2 = 0$, $a_3 = 20$ $(\bar{w}_j)$.

and short range repulsion interaction functions, similar to a Lennard-Jones potential:

$$\bar{w}_j = \begin{cases} r_1 \exp\left(\frac{-d_j^2}{r_2 \varepsilon^2}\right) - a_1 \exp\left(\frac{-(d_j - a_2\varepsilon)^2}{a_3 \varepsilon^2}\right), & \text{if } |\phi_j(\mathbf{x})| < 1 \\ 0 & \text{otherwise.} \end{cases}$$

Here, r_1 and a_1 denote the strength of repulsion and adhesion, respectively and a_2 sets the adhesion maximum at $d_j - a_2\varepsilon$. The parameters r_2 and a_3 set the thickness of the repulsion and adhesion area, respectively. Fig. 7.7a shows the graph of a Lennard-Jones-like potential $\bar{w}_j$ compared to a normal repulsive potential w_j eq. (7.2), Moreover, Fig. 7.7b shows a comparison between $\bar{w}_j$ (bottom) and w_j (top) applied to the problem discussed in Section 7.3.2. As a result of adhesion, the RBCs are much more attached.

Chapter 8

White blood cell margination

In this chapter, we apply a multi-phase approach of the Helfrich-type model to describe white blood cell margination, a biological phenomenon that can be understood as a result of the interplay between collisions, different mechanical properties and lift forces of the red blood cells (RBCs) and white blood cells (WBCs) within the vascular system. At first, we give a short introduction of the biological problem. Then, we review existing modeling approaches before we show our model, see Chapter 7, accounting for bending and inextensibility, can be applied to this problem. In Section 8.4, the model is applied in the low Reynolds number regime. It is shown that the tendency of margination is decreased for increasing deformability and a non-monotonic dependency on hematocrit e.g. as reported before in Fedosov et al. [100]. We further study the lift force on a single RBC and a single WBC, which is the determining physical effect for WBC margination, for various Reynolds numbers. This results lead to the study of the influence of inertia to WBC margination. Finally, we observe a decreasing tendency for margination with increasing Reynolds number.

The contents of this chapter such as motivation of the problem and the observed results have already been published in Marth et al. [177]. The underlying mathematical model and its numerical treatment has already been discussed in the last chapter and can also be found in Marth et al. [177] and Ling et al. [156].

8.1. Introduction

Various experimental and simulation studies of flowing blood have shown that RBCs concentrate in the center of the blood vessel. This can be explained by a non-inertial lift force, arising from cell-wall and cell-cell hydrodynamic interactions, the high deformability of RBCs and their nonspherical shapes, see e.g. [143] for a recent review. The non-inertial lift force results in a migration of RBCs towards the center of the vessel and a RBC free layer near the wall. Differences in size, shape, and deformability are assumed to lead to different non-inertial lift forces and thus a separation of cells with different mechanical properties within the blood vessel [186]. WBCs have a near-spherical shape and are not very deformable and thus mechanically different from RBCs. The non-inertial lift force of WBCs is expected to be much lower than that on RBCs, or even zero in the limit of a rigid body approximation for WBCs [37, 113]. This suggests, that WBCs may get marginated to the RBC free layer near the wall. This effect requires the interaction of RBCs and WBCs and is of utmost importance for the functioning of the immune system, which requires the adhesion of WBCs to the vessel wall.

While for low Reynolds numbers in principle understood, detailed investigations also in this regime show a non-trivial dependence of WBC margination on various blood flow properties including hematocrit H_t, vessel geometry, and RBC aggregation [1, 128, 200], e.g. a pronounced margination within an intermediate range of $H_t \approx 0.2 - 0.3$, and reduced WBC margination for lower and higher H_t. Only recently, such behavior could be explained through simulation studies in 2D [100]. It is argued that for low H_t, WBC margination turns out to be weak due to a low concentration of RBCs and thus less interaction, while at high H_t WBC margination is attenuated due to interactions of marginated WBCs with RBCs near a wall, which significantly limit the time WBCs spend near a wall. This argumentation is confirmed by 3D simulations in an idealized blood vessel [99, 236]. The situation changes if inertial effects come into play. Now, an inertial lift force is present, which acts on all cells at intermediate Reynolds number flows [110]. Thus, also WBCs experience a lift force, even in the limit of a rigid body approximation. This contradicts the simple explanation for WBC margination given above and leads to decreasing margination for increasing Reynolds number. We vary the Reynolds number, considering values of order 10^{-4}, 10^{-2}, 1 and 10, corresponding to different regions in the cardiovascular system [104]. Reynolds numbers of order unity or higher, have been reported in large blood vessels, such as arterioles and arteries [142, 204], especially if the vessels are constricted due to diseases such as thrombosis, see e.g. [20, 250].

8.2. Previous models

Previous simulation studies that have been performed to describe WBC margination are based on strong model assumptions. The simulation approach by Freund [105] assumes an incompressible Stokes flow, where the cells are modeled with a linear elastic membrane and a global area constraint is enforced. A boundary integral formulation is used for numerical discretization. More recently, a particle-based Lagrangian approach was used [99, 100]. Here, RBCs and WBCs are described by a network model, where the cells are represented through triangulated surfaces. Penalty terms are used to ensure global volume and global area conservation as well as local area conservation for each surface element. The approach thus guarantees inextensibility for sufficiently small surface elements. Each membrane point is connected to the fluid through viscous friction. The dynamics of the fluid flow is described by the smoothed dissipative particle dynamics (SDPD) method using an approximation for the Navier-Stokes equations that is only precise if the particle density is large enough. Furthermore, the incompressibility of the fluid is not guaranteed a priori and has to be controlled. In [236] a finite element approach is used for the RBCs, which are modeled as biconcave capsules and a Lattice-Boltzmann method for the fluid flow. The models are coupled through an immersed boundary method.

8.3. Applying the diffuse interface model

We will here use a different modeling approach and first reproduce the findings of previous models. We apply our model, a Helfrich-type model from Section 3.4.2, which was extended in Chapter 7 to a multi-phase flow with cell-cell interaction. This approach accounts for bending [121] with various constraints concerning membrane inextensibility and area conservation for the RBCs. Here, the inextensibility constraint goes beyond the linear elastic membrane network model or biconcave capsule approach considered previously. Moreover, we consider a rigid body approximation or a Helfrich-type model with a weakly extensible membrane for the WBCs. The fluid flow of the blood plasma and the internal fluid of the RBCs and WBCs, according with previous studies [192], will be considered as incompressible Newtonian fluid, neglecting internal structures and the nucleous in WBCs. We account for inertial effects in the plasma as well. This approach requires only measurable parameters as input and thus in principle allows for quantitative predictions. However, we will restrict our simulations to 2D. For a much more detailed modeling approach for a WBC, we refer to [263].

The governing equations for the Helfrich-type model for multiple cells are given in Section 7.1.2. We consider $N-1$ RBCs and label the phase containing all RBCs with $\phi_{RBC} := \max_{x\in\Omega}(\phi_1, \ldots, \phi_{N-1})$. The WBC is modeled either as rigid body or again with a Helfrich-type model, where the inextensibility is at least questionable, and we thus apply global surface area conservation. To model the WBC as rigid body with a fixed spherical shape, we use the fluid particle dynamics (FPD) approach [237]. The approach uses the average fluid velocity inside

$$\mathbf{v}_{WBC}(t) = \frac{\int_\Omega \tilde{\phi}_{WBC}(t,\mathbf{x})\mathbf{v}(\mathbf{x},t)\,\mathrm{d}\mathbf{x}}{\int_\Omega \tilde{\phi}_{WBC}(t,\mathbf{x})\,\mathrm{d}\mathbf{x}},$$

where $\tilde{\phi}_{WBC}(t,\mathbf{x}) = 0.5(\phi_{WBC}(t,\mathbf{x})+1)$ and a high viscosity inside $\eta_{WBC}/\eta_0 = 50$. The motion of the WBC is given by

$$\mathbf{x}_{WBC}(t+\Delta t) = \mathbf{x}_{WBC}(t) + \tau\mathbf{v}_{WBC}(t),$$

with

$$\mathbf{x}_{WBC}(t) = \frac{\int_\Omega \tilde{\phi}_{WBC}(t,\mathbf{x})\mathbf{x}(\,\mathrm{d}\mathbf{x}}{\int_\Omega \tilde{\phi}_{WBC}(t,\mathbf{x})\,\mathrm{d}\mathbf{x}},$$

being the center of mass of the WBC and τ the simulation time step, see [237]. For the rigid body approach, the local interaction potential works as well since RBCs obtain their potential from the given phase field of the WBC. For more than one rigid body, other models with a nonlocal potential have to be applied that necessarily consider the spherical shape and a given radius of the cell.

8.4. Results and discussion

We study WBC margination for different WBC stiffnesses, different hematocrit values and different Reynolds numbers. We consider a blood vessel of thickness $20\,\mu$m and length $40\,\mu$m with periodic conditions on the in- and outflow. The relatively small length results from compromising computational efficiency and physical accuracy and has been obtained through detailed investigations on the influence of the periodicity on WBC margination. We consider RBCs with perimeter $22\,\mu$m, area $19.5\,\mu\mathrm{m}^2$, bending rigidity $b_{N,RBC} = 2 \cdot 10^{-19}\,$J, viscosity $\eta_{RBC} = 1 \cdot 10^{-3}\,$Pa s. WBCs are initially set to be circular with radius $5\,\mu$m. They have a viscosity $\eta_{WBC} = 50 \cdot 10^{-2}\,$Pa s. In order to study the influence of the stiffness of the WBCs, we consider three types: soft WBCs with $b_{N,WBC} = 2 \cdot 10^{-19}\,$J, hard WBCs with $b_{N,WBC} = 2 \cdot 10^{-18}\,$J and rigid WBCs. The interaction strength is constant between all cell types and reads $\alpha = 4.24 \cdot 10^{-7}\,$N/m. For the fluid phase, we consider the viscosity $\eta_0 = 1 \cdot 10^{-3}\,$Pa s. We consider a constant flow rate, which is realized by applying a time-dependent force term $\mathbf{F} = (\frac{1}{\mathrm{Fr}(t)}, 0)^\top$, where Fr denotes the Froude number. If the current flow rate $Q(t)$ is lower or greater than the desired flow rate Q_0, we increase the force term by multiplying it with the ratio of Q_0/Q_t. The initial force term can be estimated from its Newtonian value: $1/\mathrm{Fr}(t=0) = 12Q_0/(h_l^3\mathrm{Re})$, where h_l is the channel height. We pick $Q_0 = 15$ for all simulations, which implies an averaged velocity of $8.44 \cdot 10^{-5}\,$m/s for all simulations and thus allows us to compare the results for different settings. An overview of all used parameters is given in Tab. 8.1.

In non-dimensional units, the computational domain becomes $\Omega = [0,8] \times [0,4]$, with periodic boundary conditions in the x_1 direction. The WBC has the radius 1 and is put at (5,2). RBCs are placed randomly such that they do not overlap. The non-dimensional numbers read: Re$= 1.125 \cdot 10^{-4}$, Be$_{RBC} = 5.3$, Be$_{WBC} = 0.53$ (hard), Be$_{WBC} = 5.3$ (soft), In$= 0.1$ and $\mathrm{Fr}(t=0) = 4 \cdot 10^{-5}$. In x_2 direction we specify the Dirichlet conditions $\phi_i = -1$ for $i = 1, \ldots, N$, which ensures that all cells stay within the computational domain.

We first vary the deformability of the WBC and keep $H_t = 0.293$ constant. The results are presented in Fig. 8.1, where the lower left diagram shows the x_2- coordinate of the trajectory of the midpoint of the WBC. After an initial phase, the WBC moves

Symbol	Description	Value
L	radius of a perimeter-equivalent circular cell	$5 \cdot 10^{-6}\,\mathrm{m}$
V	characteristic velocity	$2.25 \cdot 10^{-5}\,\mathrm{m/s}$
ρ	fluid density	$10^{3}\,\mathrm{kg/m^{3}}$
η_0	dynamic viscosity of the fluid	$10^{-3}\,\mathrm{Pa\,s}$
η_{RBC}	dynamic viscosity of the RBC	$10^{-3}\,\mathrm{Pa\,s}$
η_{WBC}	dynamic viscosity of the WBC	$5 \cdot 10^{-2}\,\mathrm{Pa\,s}$
$b_{N,RBC}$	bending rigidity of the RBC	$2 \cdot 10^{-19}\,\mathrm{J}$
$b_{N,WBC}$	bending rigidity of the hard WBC	$2 \cdot 10^{-18}\,\mathrm{J}$
$b_{N,WBC}$	bending rigidity of the soft WBC	$2 \cdot 10^{-19}\,\mathrm{J}$
ε	diffuse interface thickness	0.04
γ	regularization parameter	10^{-7}
α	repulsion parameter	$8.44 \cdot 10^{-4}\,\mathrm{N/m}$

Table 8.1. – Mechanical and numerical parameters used in the simulations. Mechanical parameters correspond to the considered values in [100, 236].

towards the wall, but only the rigid WBC can attach to the wall, while the soft WBC moves away after a certain time. The lower right diagram shows the probability that the midpoint of the cell is within the upper part of the channel with height 0.1. The results nicely confirm the findings in [100], that WBC margination is high for rigid cells and decreases for softer cells.

The second test concerns the influence of H_t. We vary the number of RBCs, which lead to different values of H_t, ranging from 0.098 to 0.39. Fig. 8.2 shows the obtained results for a rigid WBC and Fig. 8.3 for a hard one.

For a rigid WBC, margination can be observed for all considered H_t. However, our simulations show a lower tendency to move to the wall for the smallest value of $H_t = 0.098$ and the largest tendency for $H_t = 0.195$ and $H_t = 0.293$. For the highest value $H_t = 0.39$, the probability slightly decreases. It seems more likely that due to the larger number of RBCs interaction between WBC and RBCs are possible also close to the wall, which moves the WBC away from the wall, see $t = 10$, $t = 22$ and $t = 30$. This results give evidence for a decreasing WBC margination for high H_t, as also observed in [100]. In the case of a hard WBC and the lowest H_t, the cell remains in the center. In contrast to Fig. 8.2, no margination occurs. Increasing H_t leads to WBC margination. However, contact with the wall cannot be achieved. We also do not see the tendency for decreasing WBC margination for $H_t = 0.39$. A further increasing $b_{N,WBC}$ or H_t is not possible due to numerical reasons.

So far only know results have been reproduced by the hydrodynmaic phase field model that can be viewed as a validation of the modeling approach. We now turn to the effect of the Reynolds number on WBC margination, Fig. 8.4. We consider $H_t = 0.293$ and a rigid WBC. Considering a constant flow rate, we obtain WBC margination for Re=$1.125 \cdot 10^{-4}$, Re=0.05 and Re=1. However, the tendency to adhere entirely decreases already for Re =1. The simulation results for Re=10 indicate no margination.

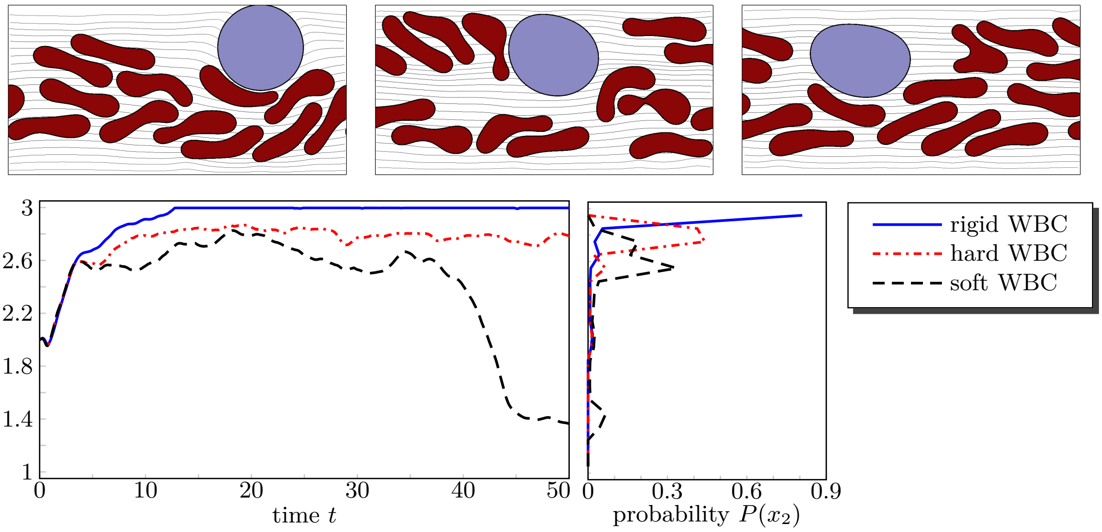

Figure 8.1. – Simulation snapshot at late time for $H_t = 0.293$ for rigid, hard and soft WBC from left to right (top), x_2 coordinate for the trajectory of the midpoint of the WBC (bottom right) and the probability that the midpoint of the WBC is inside a defined interval (bottom left). x_2 axis is split into 20 intervals of length 0.1.

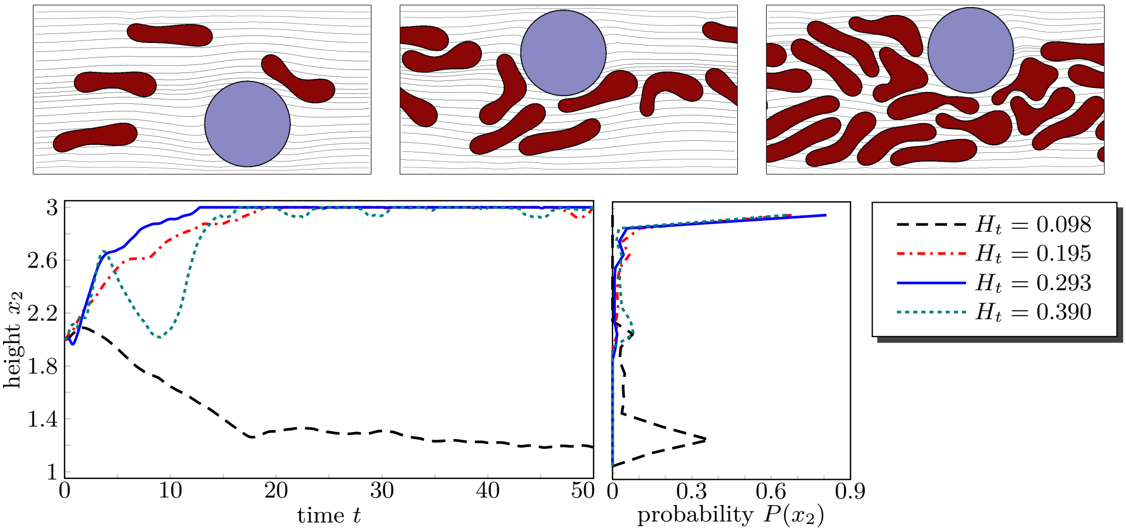

Figure 8.2. – Simulation snapshot at late time for a rigid WBC for $H_t = 0.098$, $H_t = 0.195$ and $H_t = 0.39$ from left to right ($H_t = 0.293$ is shown in figure 8.1) (top). x_2 coordinate for the trajectory of the midpoint of the WBC (bottom right) and the probability that the midpoint of the WBC is inside a defined interval (bottom left). x_2 axis is split into 20 intervals of length 0.1.

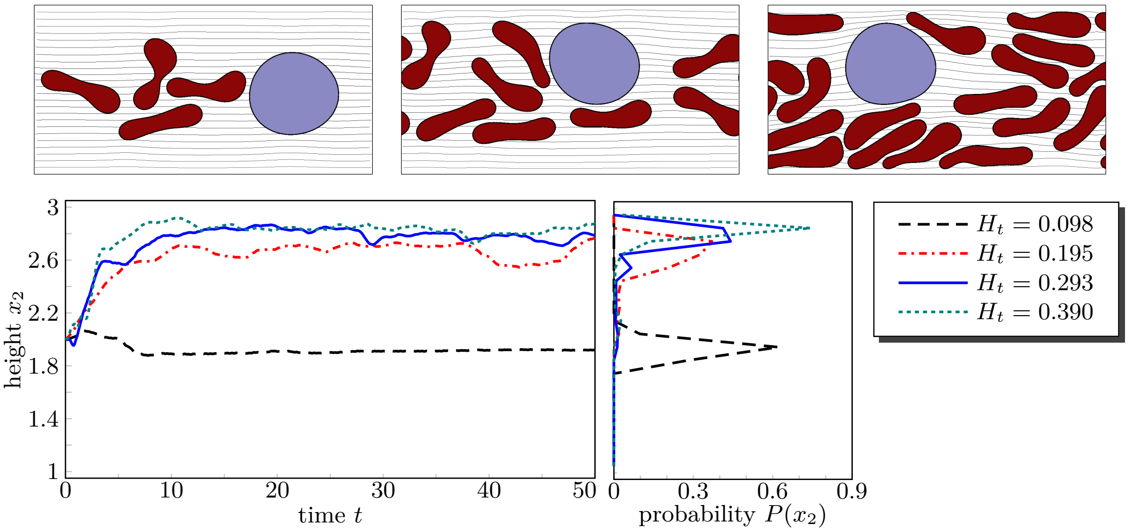

Figure 8.3. – Simulation snapshot at late time for a hard WBC for $H_t = 0.098$, $H_t = 0.195$ and $H_t = 0.39$ from left to right ($H_t = 0.293$ is shown in figure 8.1), (top). x_2 coordinate for the trajectory of the midpoint of the WBC (bottom right) and the probability that the midpoint of the WBC is inside a defined interval (bottom left). x_2 axis is split into 20 intervals of length 0.1.

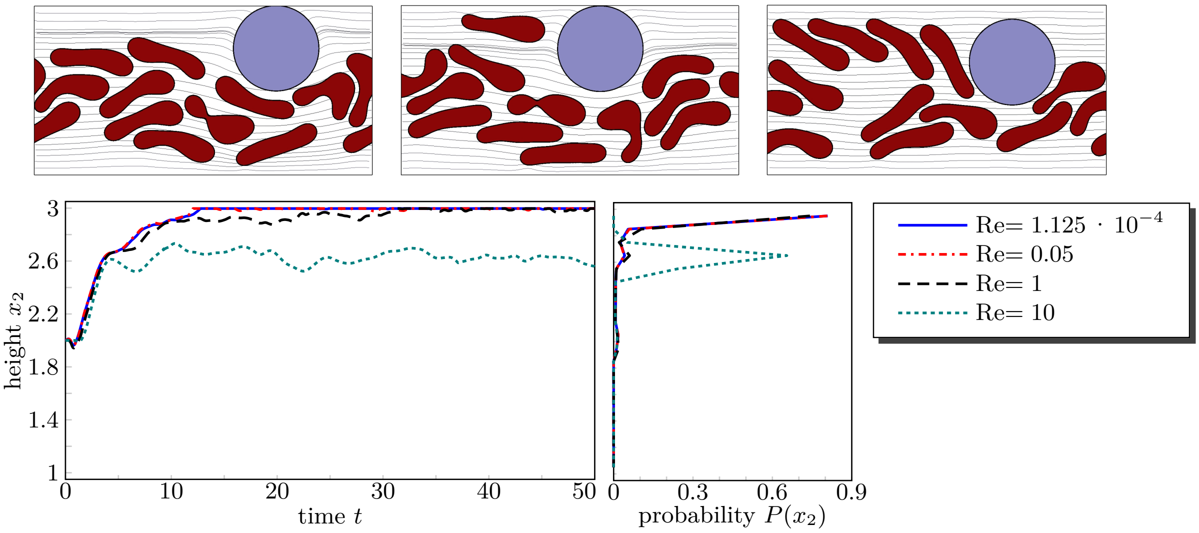

Figure 8.4. – Simulation snapshot at late time for a rigid WBC and $H_t = 0.293$ for Re=0.05, Re = 1 and Re=10 from left to right, (top). (Re = $1.125 \cdot 10^{-4}$ is shown in figure 8.1) (top). x_2 coordinate for the trajectory of the midpoint of the WBC (bottom right) and the probability that the midpoint of the WBC is inside a defined interval (bottom left). x_2 axis is split into 20 intervals of length 0.1. For Re= 0.05 a movie is provided in the online supplementary material.

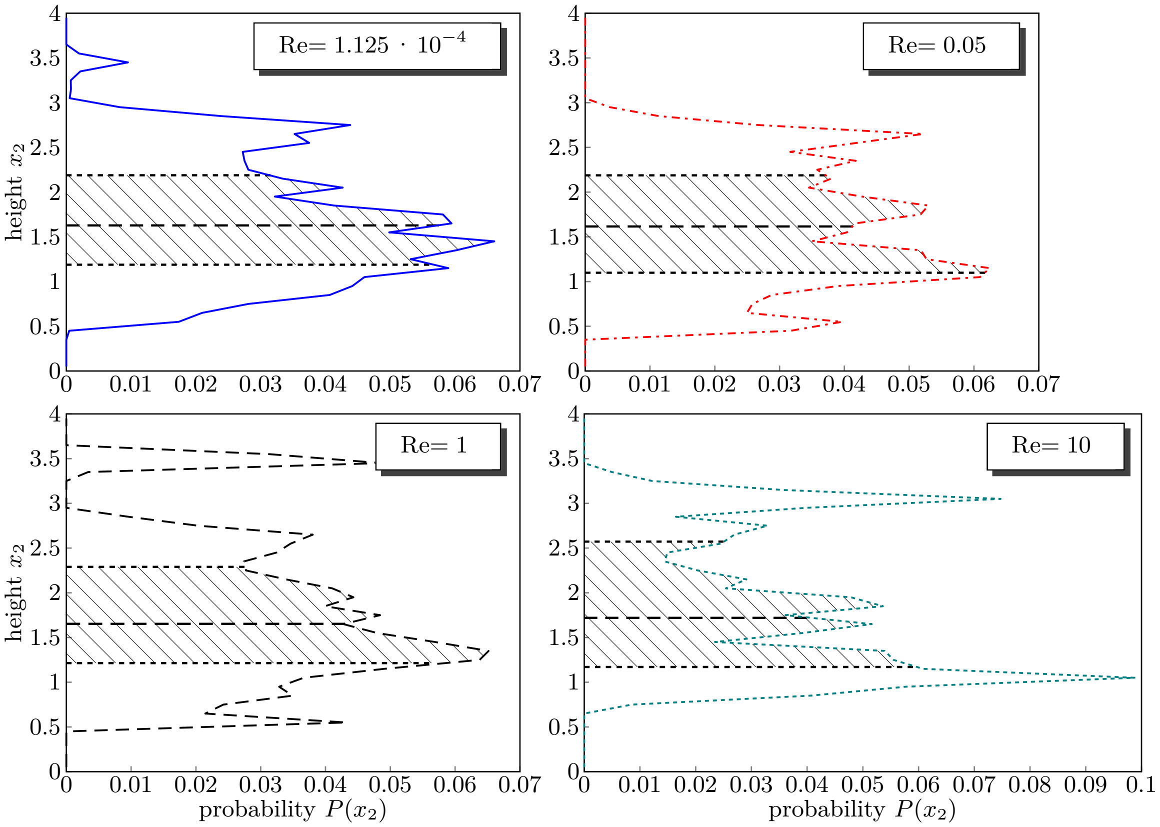

Figure 8.5. – Distribution of RBCs for different Re computed over time interval t = 10 to t = 50. The shaded region shows the interquartile range, the difference between the upper and lower quartiles together with the median.

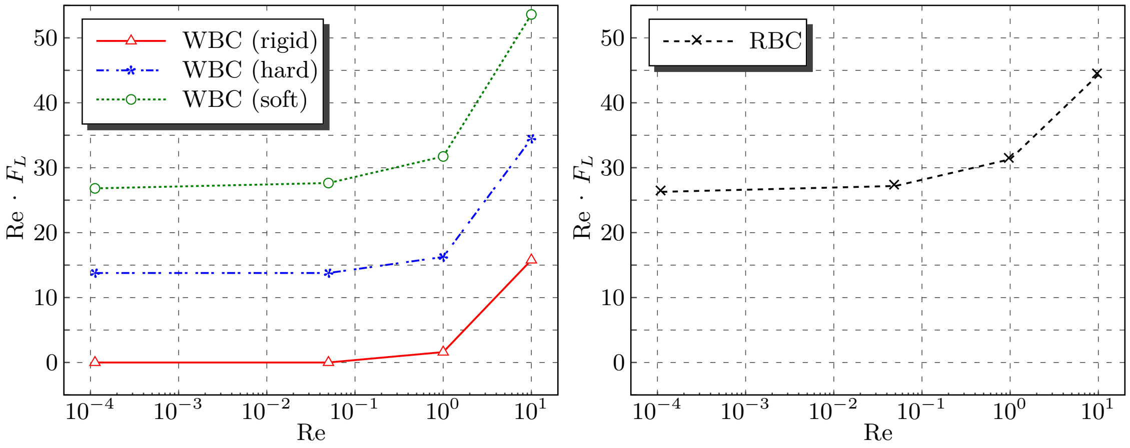

Figure 8.6. – Computed lift force for a WBC (left) and a RBC (right) as a function of Re.

Various explanations can be given. First the tendency of RBCs to aggregate in the center of the vessel might decrease with increasing Re due to the increased hydrodynamic interactions. This would increase the concentration of RBCs near the wall and thus lead to a stronger interaction with marginated WBCs, which, similar to the situation for large H_t, limits the time WBCs spend near the wall. However, this explanation cannot be justified by our numerical results. Fig. 8.5 shows the distribution of RBCs in the vessel averaged over the simulation time, which does not, or only very weakly show a dependency on Re. The median is shifted towards the lower part due to the presence of the WBC in the upper part. The peak in the distribution for $\mathrm{Re} = 1$ and $\mathrm{Re} = 10$ in the upper part close to the wall results from RBCs, which are trapped behind the WBC, see Fig. 8.4. The lower half of the vessel thus gives a clearer description of the distribution, with no clear dependency on Re. This is in agreement with the results of [138] where a qualitative similar distribution profile is observed for a suspension of soft capsules. Up to $\mathrm{Re} = 50$, the profile shows no dependency on Re but for larger Re the soft capsules are even strongly concentrated in the central region.

The second attempt considers the effect of Re on the lift force directly. The investigation of inertial forces on rigid particles dates back to [222] and its dependency on Re is today well understood for spherical objects [18, 47, 122, 179, 221]. For deformable objects this is much less investigated. [138] show that the Segre-Silberberg effect is essentially suppressed for deformable objects. We here consider the effect numerically and compute the lift force (density) as a function of Re for different cell types. We thereby follow the approach in [186] and adapt a gravitational force $\mathbf{F}_g$ acting on the cell. In the hydrodynamic phase field models eq. (7.12) and (7.14). This is realized by adding $-\frac{\phi_i+1}{2}\mathbf{F}_g$ to the right-hand side. The strength of $\mathbf{F}_g$ is varied to achieve a balance at a fixed height, which is chosen such that the lowest point of the cell is at $x_2 = 0.2$. Due to the strong deformability of the cell the usually used center of mass position of the cell is not appropriate to achieve comparable results for the same cell type. The magnitude of $\mathbf{F}_g$ thus determines the lift force (density) at position $x_2 = 0.2$. Fig. 8.6 shows the computed values for WBCs (considered as rigid, hard and soft cells) and RBCs as a function of Re. We observe an increase of the lift force (density) with increasing Re for all cell types. The increase is strongest for the soft WBC. However, also the increase of the lift force for the hard WBC is significant and explains the decrease in margination for increasing Re, as now both cell types feel a lift force and thus compete for a position away from the vessel wall. However, quantifying this effect is difficult, as the computed values for WBCs and RBCs are not directly comparable, as the actual lift force depends on cell size, viscosity and distance from the vessel wall[186], which all differ for WBCs and RBCs. The larger size of the WBCs and their higher viscosity moreover indicate a stronger increase of the lift force with Re if compared with RBCs.

8.5. Conclusion

We investigate margination of WBCs using a diffuse interface Navier-Stokes-Helfrich model. For RBCs various constraints concerning membrane inextensibility and area conservation are considered, while WBCs are modeled using a rigid body approximation or a Helfrich-type curvature model with a weakly extensible membrane. We also consider cell-cell interactions. The fluid flow of the blood plasma and the internal fluids of the cells are modeled using the incompressible Navier-Stokes equations. An idealized two-dimensional blood vessel is used as computational domain. In the low-Re regime we reproduced previous results, e.g. a decreasing tendency for margination with increasing deformability and a non-monotonic dependency on hematocrit, which quantitatively agree with results of Fedosov et al. [100]. Here, the non-inertial lift force of WBCs is much lower than that on RBCs, or even zero in the limit of a rigid body approximation. This results in margination of the WBCs to the RBC free layer near the wall. With inertial effects that can occur in small arteries and in the aorta, the simulations show a decreasing tendency for margination with increasing Re. The effect is explained by analyzing the lift force on a single WBC and a single RBC as a function of Re. We now have an additional inertial lift force that for all cell types increases if Re increases. This is also true for the hard and even the rigid WBC. These forces lead to a competition between WBCs and RBCs for a position away from the vessel wall, which suppresses margination. Due to the huge parameter space, flow confinement, deformability of the WBCs, hematocrit and inertial effects, we had to restrict our simulations to specific combinations, which show the most significant effect on WBC margination.

Chapter 9

Collective migration of cells

9.1. Introduction

Collective migration is the second principal mode of cell movement. While the study of the first mode, the single cell migration, made great progress, the processes within collective cell migration are however poorly understood. Collective cell migration is present in various physiological processes like tissue growth or cell invasion [106]. These processes reveal a rich non-linear behavior such as motility induced phase separation (MIPS) [114, 240], where clusters of cells are formed as a result of the feedback between the fact that cells accumulate where they move slowly and move more slowly, where crowded. Moreover, cell suspensions have complex rheological properties. Systems of migrating objects where an active force, arising from a motility mechanism within the microscopic constituents, constantly consumes energy are far from equilibrium and can be observed at very different scales: these can range from the actin cytoskeleton within the cell bulk [131, 203], so-called living crystals [198], motile cells and microswimmers [165, 166] to flocks and birds [244, 245].

Recently, Löber et al. [160] developed a non-hydrodynamic model that goes further than previous attempts as it considers the crucial dynamics of a single motile cell associated with cell deformations. Here, the authors used a diffuse interface model for multiple cells based on their model for single cell motility [159, 270–272].

In a hydrodynamic environment, the physics of the flow influence the dynamics of collectively migrating cells in a highly nontrivial way [240]. For instance, it has been argued that moving particles set up flow fields that influence their neighbors that can suppress motility induced phase separation (MIPS) [180]. It is supposed that collective cell migration occurs as part of the phenomenon MIPS when multiple cells form a moving cluster. However, if collective migration is suppressed, the formation of a moving cluster and finally MIPS will also be suppressed. As the influence of hydrodynamics to such complex active systems with deformable cells is poorly understood, we develop a hydrodynamic model for multi-cell dynamics. For this purpose, we extend the approach for a single migrating cell that considers the actin filaments within the cell bulk as a macroscopic orientation field determining a distinct polarization of the cell as discussed in Chapter 6 to a multi-flow approach, introduced in Chapter 7. The multi-phase approach requires one phase field for a single cell. All cells are coupled via a local interaction potential. Moreover, the approach uses one orientation field for a single cell, which ensures that the collision modeling is purely hydrodynamic as the realignment of the orientation field can only be achieved through fluid flow.

To understand how the hydrodynamics influence the collective migration of cells, we additionally consider a non-hydrodynamic model that is a simplification of [160]. Although the simplified model (model 1) neglects contractile stress and substrate adhesion, it recovers the basic dynamics of a non-hydrodynamic motion. This approach models the collision as diffusion process between two cells, which share one orientation field for the actin filaments, yielding a realignment of the orientation field and hence the direction of motion. This can be questionable from a biological point of view. We therefore extend model 1 to multiple orientation field variables (model 1B). All models are introduced in Section 9.2. In Section 9.5.1, we perform several benchmark computations for a binary collision to study if the developed models are capable of describing elastic and inelastic collisions and to predict how bigger systems of collectively migrating cells evolve. Finally, in Section 9.5.2, we study the onset of collective motion depending on various parameters for an initially disordered crowd. We show that within the non-hydrodynamic system the elasticity of the actin network in the bulk allows us to determine the length of the transient phase within the ordering process. Here, the onset of collective motion is attenuated for a high elasticity of the active polar gel. Moreover, the simulations of the hydrodynamic model do not indicate a suppression of collective motion due to fluid flow.

The considered model and some of the results are submitted for publication, see Marth and Voigt [175].

9.2. Mathematical models for multiple active cells

In the following section, we specify the mathematical models, that are based on the models from Chapters 6 and 7. All given equations are defined in $I \times \Omega$. In the following, we consider N cells. A variable is associated to a specific cell by the index i, with $i = 1, \dots, N$. Appropriate initial and boundary conditions can be obtained from further sections. Moreover, we denote the phase containing all cells as $\phi_{cell} = \max_{x \in \Omega}(\phi_1, \dots, \phi_N)$.

9.2.1. Non-hydrodynamic model with one orientation field - Model 1

The Non-Hydrodynamic model considers the elastic Frank energy eq. (6.4) and the surface energy accounting for bending and surface tension eq. (3.78). Together with our approach for multiple cells that includes multiple phase field variables and an interaction energy eq. (7.5), the overall energy reads

$$\begin{aligned}
\mathcal{E}(\phi_1,\dots,\phi_N,\mathbf{P}) &= \mathcal{E}_P(\mathbf{P},\phi_{cell}) + \sum_{i=1}^{N}\mathcal{E}_{S,i}(\phi_i) + \mathcal{E}_{int}(\phi_1,\dots,\phi_N)\\
&= \frac{1}{\mathrm{Pa}}\int_\Omega \frac{1}{2}(\nabla\mathbf{P})^2 + \frac{c_1}{4}|\mathbf{P}|^2(-2\phi_{cell}+|\mathbf{P}|^2) + \beta\mathbf{P}\cdot\nabla\phi_{cell}\,\mathrm{d}\mathbf{x}\\
&\quad+\sum_{i=1}^{N}\int_\Omega \frac{1}{\mathrm{Be}_i}\frac{1}{2\varepsilon}\left(\varepsilon\Delta\phi_i - \frac{1}{\varepsilon}W'_{0,i}(\phi_i)\right)^2 + \frac{1}{\mathrm{Ca}_i}\left(\frac{\varepsilon}{2}|\nabla\phi_i|^2 + \frac{1}{\varepsilon}W(\phi_i)\right)\mathrm{d}\mathbf{x}\\
&\quad+\frac{1}{\mathrm{In}}\sum_{i=1}^{N}\int_\Omega B(\phi_i)\sum_{\substack{j=1\\ j\neq i}}^{N} w_j\,\mathrm{d}\mathbf{x}. \qquad (9.1)
\end{aligned}$$

Within an energy variation approach the following equations can be derived for the phase field ϕ_i:

$$\partial_t\phi_i = -\nabla\cdot(v_0\phi_i\mathbf{P}) + \gamma\Delta\phi_i^\natural, \qquad (9.2)$$

$$\begin{aligned}
\phi_i^\natural &= \frac{1}{\mathrm{Be}_i}\left(\Delta\mu_i - \frac{1}{\varepsilon^2}W''_{0,i}(\phi_i)\mu_i\right) + \frac{1}{\mathrm{Ca}_i}\left(-\varepsilon\Delta\phi_i + \frac{1}{\varepsilon}W'(\phi_i)\right)\\
&\quad+\frac{1}{\mathrm{Pa}}\left(\frac{c_1}{2}|\mathbf{P}|^2 - \beta\nabla\cdot\mathbf{P}\right) + \frac{1}{\mathrm{In}}\left(B'(\phi_i)\sum_{\substack{j=1\\ j\neq i}}^{N} w_j + w'_i\sum_{\substack{j=1\\ j\neq i}}^{N} B(\phi_j)\right). \qquad (9.3)
\end{aligned}$$

For the orientation field $\mathbf{P}$, we obtain the following system

$$\partial_t\mathbf{P} + (v_0\mathbf{P}\cdot\nabla)\mathbf{P} = -\frac{1}{\varkappa}\mathbf{P}^\natural, \qquad (9.4)$$

$$\mathbf{P}^\natural = \frac{1}{\mathrm{Pa}}\left(-c_1\phi_{cell}\mathbf{P} + c_1\mathbf{P}^2\mathbf{P} - \Delta\mathbf{P} + \beta\nabla\phi_{cell}\right), \qquad (9.5)$$

which is similar to eq. (6.16) and eq. (6.17), but without flow coupling. For a further description of all parameters, we refer to Section 6.2.4.

9.2.2. Non-hydrodynamic model with multiple orientation fields - Model 1B

However, a single orientation field $\mathbf{P}$ for all cells might not be appropriate as the actin filaments of the cells usually do not interact. To account for this, we assign a specific orientation field $\mathbf{P}_i$ to each cell ϕ_i. Accordingly, the overall energy for model 1B reads as

$$
\begin{aligned}
\mathcal{E}(\phi_1,\dots,\phi_N,\mathbf{P}_1,\dots,\mathbf{P}_N) &= \sum_{i=1}^{n}\mathcal{E}_P(\mathbf{P}_i,\phi_i) + \sum_{i=1}^{N}\mathcal{E}_{S,i}(\phi_i) + \mathcal{E}_{int}(\phi_1,\dots,\phi_N), \qquad (9.6)\\
&= \sum_{i=1}^{n}\frac{1}{\mathrm{Pa}_i}\int_\Omega \frac{1}{2}(\nabla\mathbf{P}_i)^2 + \frac{c_1}{4}|\mathbf{P}_i|^2(-2\phi_i + |\mathbf{P}_i|^2) + \beta_i\mathbf{P}_i\cdot\nabla\phi_i\,\mathrm{d}\mathbf{x}\\
&\quad + \sum_{i=1}^{N}\int_\Omega \frac{1}{\mathrm{Be}_i}\frac{1}{2\varepsilon}\left(\varepsilon\Delta\phi_i - \frac{1}{\varepsilon}W'_{0,i}(\phi_i)\right)^2 + \frac{1}{\mathrm{Ca}_i}\left(\frac{\varepsilon}{2}|\nabla\phi_i|^2 + \frac{1}{\varepsilon}W(\phi_i)\right)\mathrm{d}\mathbf{x}\\
&\quad + \frac{1}{\mathrm{In}}\sum_{i=1}^{N}\int_\Omega B(\phi_i)\sum_{\substack{j=1\\ j\neq i}}^{N} w_j\,\mathrm{d}\mathbf{x}, \qquad (9.7)
\end{aligned}
$$

which now prevents any diffusion between the orientation fields of each cell. The evolution equations for ϕ_i are given by

$$
\begin{aligned}
\partial_t\phi_i &= -\nabla\cdot(v_0\phi_i\mathbf{P}_i) + \gamma\Delta\phi^\natural_{i,B}, \qquad (9.8)\\
\phi^\natural_{i,B} &= \frac{1}{\mathrm{Be}_i}\left(\Delta\mu_i - \frac{1}{\varepsilon^2}W''_{0,i}(\phi_i)\mu_i\right) + \frac{1}{\mathrm{Ca}_i}\left(-\varepsilon\Delta\phi_i + \frac{1}{\varepsilon}W'(\phi_i)\right)\\
&\quad + \frac{1}{\mathrm{Pa}_i}\left(\frac{c_{1,i}}{2}|\mathbf{P}_i|^2 - \beta_i\nabla\cdot\mathbf{P}_i\right) + \frac{1}{\mathrm{In}}\left(B'(\phi_i)\sum_{\substack{j=1\\ j\neq i}}^{N} w_j + w'_i\sum_{\substack{j=1\\ j\neq i}}^{N} B(\phi_j)\right). \qquad (9.9)
\end{aligned}
$$

Moreover, we consider multiple equations for $\mathbf{P}_i$ that read

$$
\begin{aligned}
\partial_t\mathbf{P}_i + (v_0\mathbf{P}_i\cdot\nabla)\mathbf{P}_i &= -\frac{1}{\varkappa}\mathbf{P}^\natural_i, \qquad (9.10)\\
\mathbf{P}^\natural_i &= \frac{1}{\mathrm{Pa}}\left(-c_1\phi_i\mathbf{P}_i + c_1\mathbf{P}_i^2\mathbf{P}_i - \Delta\mathbf{P}_i + \beta\nabla\phi_i\right). \qquad (9.11)
\end{aligned}
$$

9.2.3. Hydrodynamic model with multiple orientation fields - Model 2

The hydrodynamic model is based on the active polar gel approach from Chapter 6 that is extended to multiple phase field variables. Here, we combine model 1B with fluid flow such that the overall energy reads

$$
\mathcal{E}(\mathbf{v},\phi_1,\dots,\phi_N,\mathbf{P}_1,\dots,\mathbf{P}_N) = \int \frac{\mathrm{Re}}{2}|\mathbf{v}|^2\,\mathrm{d}\mathbf{x} + \mathcal{E}(\phi_1,\dots,\phi_N,\mathbf{P}_1,\dots,\mathbf{P}_N), \qquad (9.12)
$$

which is an extension of eq. (9.7) with the kinetic energy of the fluid. Within the Navier-Stokes equation each orientation field induces a specific stress:

$$
\begin{aligned}
\mathrm{Re}(\partial_t \mathbf{v} + (\mathbf{v} \cdot \nabla)\mathbf{v}) + \nabla p = {}& -\theta \mathbf{v} + \nabla \cdot (\eta(\phi_{cell})\mathbf{D}) + \sum_{i=1}^{n} \phi^{\natural}_{i,B} \nabla \phi_i + \sum_{i=1}^{n} \nabla \cdot \mathbf{S}_{i,P} \\
& + \frac{1}{\mathrm{Fa}_{poly}} \sum_{i=1}^{n} \mathbf{P}_i + \frac{1}{\mathrm{Fa}_{con}} \sum_{i=1}^{n} \nabla \cdot (\mathbf{P}_i \otimes \mathbf{P}_i), && (9.13) \\
\nabla \cdot \mathbf{S}_{i,P} = {}& \nabla \cdot \left(\frac{1}{2}(\mathbf{P}^{\natural}_i \otimes \mathbf{P}_i - \mathbf{P}_i \otimes \mathbf{P}^{\natural}_i) + \frac{\xi}{2}(\mathbf{P}^{\natural}_i \otimes \mathbf{P}_i + \mathbf{P}_i \otimes \mathbf{P}^{\natural}_i) \right) \\
& + \nabla \mathbf{P}^T_i \cdot \mathbf{P}^{\natural}_i, && (9.14) \\
\nabla \cdot \mathbf{v} = {}& 0. && (9.15)
\end{aligned}
$$

The phase field equations are regularized with the chemical potential obtained from eq. (9.9) and read

$$
\partial_t \phi_i + \mathbf{v} \cdot \nabla \phi_i = \gamma \Delta \phi^{\natural}_{i,B}. \tag{9.16}
$$

$$
\tag{9.17}
$$

Finally, the orientation field equations are given by

$$
\begin{aligned}
\partial_t \mathbf{P}_i + (\mathbf{v} \cdot \nabla)\mathbf{P}_i + \mathbf{\Omega} \cdot \mathbf{P}_i &= \xi \mathbf{D} \cdot \mathbf{P}_i - \frac{1}{\varkappa} \mathbf{P}^{\natural}_i, && (9.18) \\
\mathbf{P}^{\natural}_i &= \frac{1}{\mathrm{Pa}} \left(-c_1 \phi_i \mathbf{P}_i + c_1 \mathbf{P}^2_i \mathbf{P}_i - \Delta \mathbf{P}_i + \beta \nabla \phi_i \right). && (9.19)
\end{aligned}
$$

9.3. Parameters

All models are given in a very general formulation accounting for several physical properties. Re denotes the Reynolds number, Ca the capillary number, Be the bending capillary number, Pa the elasticity number of the actin solution and In the interaction number. For simplicity, we simplify our models by choosing

$$
\phi^{\natural}_i = \frac{1}{\mathrm{Ca}_i} \left(-\varepsilon \Delta \phi_i + \frac{1}{\varepsilon} W'(\phi_i) \right) + \frac{1}{\mathrm{In}} \left(B'(\phi_i) \sum_{\substack{j=1 \\ j \neq i}}^{N} w_j + w'_i \sum_{\substack{j=1 \\ j \neq i}}^{N} B(\phi_j) \right), \tag{9.20}
$$

which is a Cahn-Hilliard potential accounting for surface tension and interaction. We furthermore restrict the coupling between Navier-Stokes equation and orientation field equation to the polymerization force: $\mathrm{Fa}_{poly} > 0$. The contractile stress $1/\mathrm{Fa}_{con} = 0$ and the orientation stress $\mathbf{S}_P = \mathbf{0}$ are neglected. Other parameters are given in Tab. 9.1 for models 1/1B and in Tab. 9.2 for model 2. Tab. 9.3 incorporates the parameters for the orientation field equation(s).

Symbol	Description	Value
ε	diffuse interface thickness	0.2
γ	mobility	1
Ca	capillary number	0.0281
In	interaction number	0.1125
v_0	activity	2.25

Table 9.1. – List of numerical and physical parameters for the defaults case for the non-hydrodynamic models 1/1B

Symbol	Description	Value
ε	diffuse interface thickness	0.2
γ	mobility	$3 \cdot 10^{-3}$
Re	Reynolds number	10^{-3}
Ca	Capillary number	0.025
In	interaction number	0.1
Fa_{con}	contractile stress number	$1/\mathrm{Fa}_{con} = 0$
v_0	activity	4
$\mathrm{Fa}_{poly}=1/v_0$	polymerization stress number	0.25
θ	friction parameter	1
ρ/ρ_i	density ratio in phase i	1
η/η_i	viscosity ratio in phase i	1

Table 9.2. – List of numerical and physical parameters for hydrodynamic model 2

Symbol	Description	Value
Pa	polarity elasticity number	0.1
$\varkappa$	scaling factor between rotational and dynamic viscosity	1
c_1	double well parameter for $\mathbf{P}$	10
β	forcing normal direction of $\mathbf{P}$ on the interface, polymerization rate	0.5
ξ	shape factor (for hydrodynamic model)	0

Table 9.3. – The parameters for orientation field are the same for all models.

9.4. Numerical approach and implementation

Similar to the previous chapters, the numerical scheme is straightforward. We use a semi-implicit time discretization and an operator splitting approach that allows us to decouple all subproblems. We further conduct a shared memory OPENMP problem parallelization to solve the phase field equations and the orientation field equations in models 1B/2 via a parallel splitting method. Each linear system of equations is solved using the direct solver UMFPACK [57]. We discretize in space using finite elements, similar to further sections. Since the computational mesh has to be fine along the interface, adaptive mesh refinement is heavily used within diffuse interface models. It allows us to increase the numerical efficiency of the method while the numerical error does not rise. Usually, the mesh is coarser outside the interface. Using a single mesh for all variables is not appropriate in this case as it would lead to redundant grid points for one variable where another variable needs a fine grid. This yields a quadratic complexity of the problem depending on the number of cells. The multi-mesh strategy overcomes these numerical problems [254] and assigns a single mesh to a single phase field or orientation field. This allows us to carry out an independent adaptive mesh refinement for each variable. Furthermore, it provides an adequate treatment of coupling terms that live on different meshes as it interpolates between these meshes without loss of information [156, 254].

9.5. Simulations and results

We first study binary collisions of cells. These simulations are useful to understand the interactions between the two cells and are therefore often used as a benchmark problem to predict how bigger systems evolve. Then, we perform simulations to study the onset of collective cell migration. In both cases, we choose a quadratic two-dimensional computational domain with size $[0, 50]^2$ and apply periodic boundary conditions in each direction.

9.5.1. Binary collisions

For our computational setting, we set up two circular cells with radius $R = 4$ and with the initial direction of $\mathbf{P}$ such that the cells collide with incidence angle $\alpha_{in} = 45°$. We observe the trajectories of the cell's center of mass and denote a collision elastic if the emergent angle $\alpha_{out} \approx \alpha_{in}$ and inelastic if $\alpha_{out} < \alpha_{in}$, see e.q. Fig. 9.3 for an elastic (top) and inelastic collision (bottom). We first analyze model 1 and vary one of the parameters set by default to $v_0 = 2.25$, $\mathrm{Ca} = 0.056$, $\mathrm{Pa} = 0.1$ and $\beta = 0.5$. As Ca and γ have the same physical meaning, we pick $\gamma = 1$ and vary Ca. Fig. 9.1 shows the trajectories for the cell collisions. It turns out that all parameters except v_0 heavily influence the collision. To be more precise, the higher the surface tension (decreasing Ca), the lower the elasticity within $\mathbf{P}$ (increasing Pa) and the less pronounced the splay (decreasing polymerization rate β) (Fig. 9.3), the more inelastic is the collision. Interestingly, v_0 does not influence the collision. Various explanations can be given. For small v_0 the cells stay longer in contact and for higher v_0 the cells are more deformed. Both phenomena increase the tendency of the orientation field to realign.

For model 1B, we do not observe any elastic collision, see Fig. 9.2. This can especially be observed for $\beta = 0$. However, for increasing β the collision becomes slightly more elastic. As the diffusion between different $\mathbf{P}_i$ is prevented, we observe a different collision mechanism that results from the deformation of the cells and the coupling between $\mathbf{P}_i$ and ϕ_i [185].

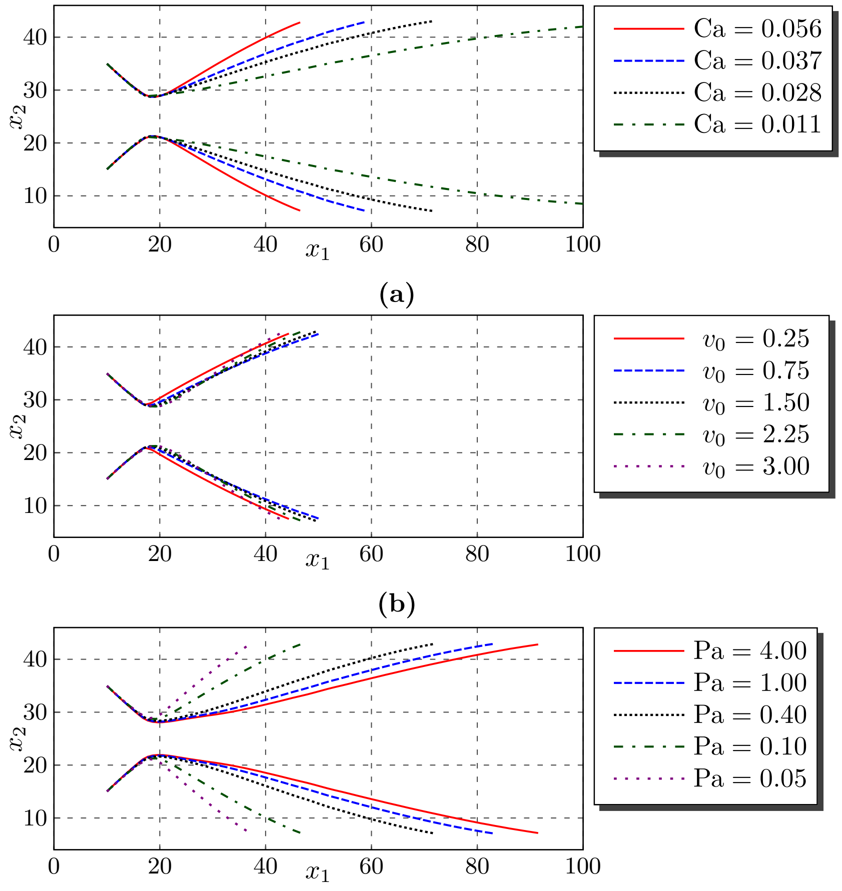

(a)

(b)

(c)

Figure 9.1. – Cell trajectories of a binary collision for non-hydrodynamic model 1 with single orientation field for $v_0 = 2.25$, Ca = 0.056, Pa = 0.1 and $\beta = 0.5$ for varying (a) Ca, (b) v_0 and (c) Pa. Further parameters are obtained from Tab. 9.1.

Now, we consider the hydrodynamic model 2. We vary one of the parameters set by default to $v_0 = 4$, Ca = 0.025, Pa = 0.1, $\beta = 0.5$ and Re = 10^{-3}. Model 2 shows only slight dependencies on v_0, β and Ca, see Fig. 9.4, as the orientation field and accordingly the collision is mostly influenced by fluid flow. We observe that the advection of the cells causes two vortices above and under the cell in the direction of motion. During a collision, the vortices close to the neighboring cell vanish and the cell is rotated away

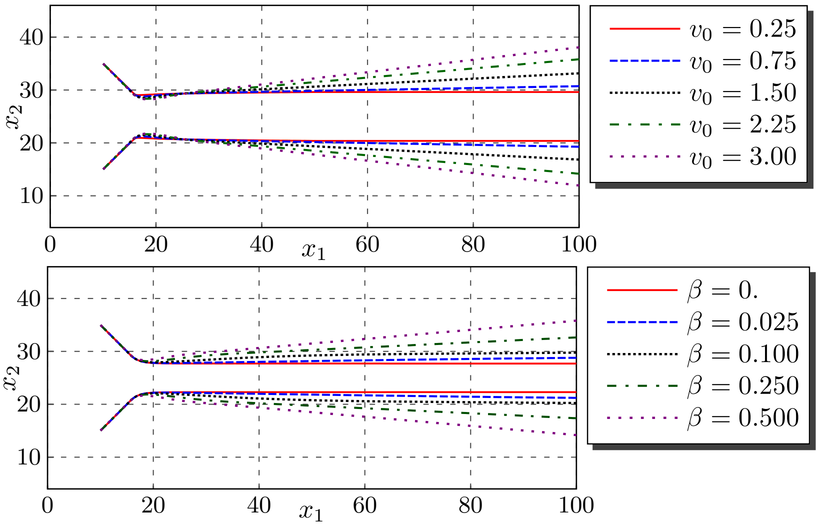

Figure 9.2. – Cell trajectories of a binary collision for non-hydrodynamic model 1B with multiple $\mathbf{P}_i$ for varying (a) v_0 and (b) β. Other parameters are similar to Fig. 9.3. All collisions are strongly inelastic. As the diffusion between different $\mathbf{P}_i$ is prevented, a different effect determines the collision for $\beta > 0$.

from the other cell, see Fig. 9.5b. However, for varying Pa, the trajectories differ much more within the observed parameter range, see Fig. 9.4c. We observe slight to strong inelastic collisions for decreasing diffusion rates. Up to now, all collisions for model 2 are inelastic. For Re = 10, as shown in Fig. 9.5a, we obtain a nearly elastic collision, which can be a result of the decreased viscous drag. Moreover, we observe that the cells are much more stretched for higher Re.

9.5.2. Collective motion

We now investigate how bigger systems of cells evolve within the different models. To show this, we position 23 cells in the domain with randomly chosen initial orientations. However, the initial direction of the cells are kept constant for different simulations. Here, we study how certain parameters determine the onset of collective motion and how hydrodynamics influence this process. It is assumed that the onset of collective motion is even more suppressed if the binary collisions become more elastic. To characterize the collective motion, we introduce an order parameter

$$\omega(t) = \frac{1}{N} \left| \sum_{i=1}^{N} \bar{\mathbf{v}}_i(t) \right|,$$

the measure the translational direction of all cells. Here, N denotes the number of cells and $\bar{\mathbf{v}}_i$ is the unity velocity vector of the i-th cell. The parameters ω is 1 if all cells move in the same direction and 0 if no correlation exists. The unity velocity vector can be

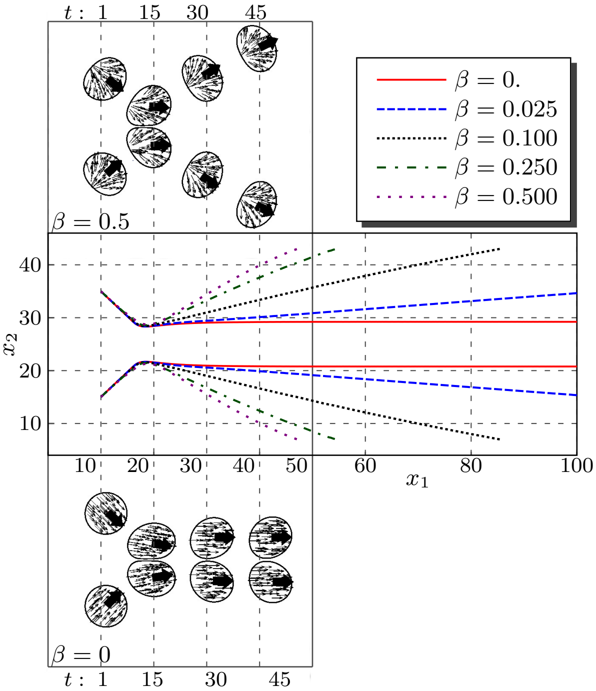

Figure 9.3. – Cell trajectories of a binary collision for non-hydrodynamic model 1 with single orientation field for $v_0 = 2.25$, $\mathrm{Ca} = 0.056$, $\mathrm{Pa} = 0.1$ and varying β. Cell evolution for $\beta = 0.5$ (top) and $\beta = 0$ (bottom). Shown are the cell shapes, the orientation field $\mathbf{P}$ (small arrows) and the main direction (big arrow) of four states at various times. For increasing β the collision becomes more elastic as a result of the increasing splay in the orientation field.

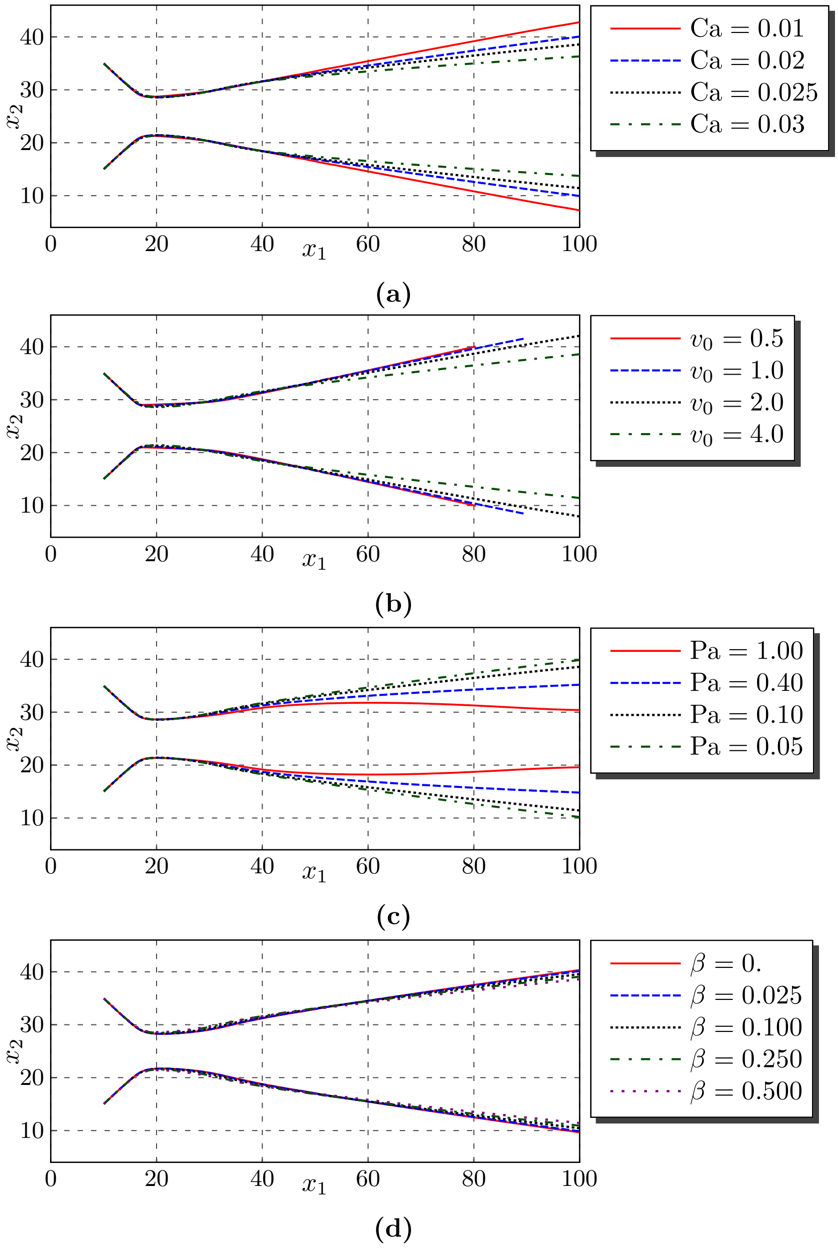

(a)

(b)

(c)

(d)

Figure 9.4. – (a) Cell trajectories for hydrodynamic model 2 for $v_0 = 4$, Ca $= 0.025$, Pa $= 0.1$, $\beta = 0.5$ for one varying (a) Ca, (b) v_0, (c) Pa and (d) β. Further parameters are obtained from Tab. 9.2. All collisions are mostly inelastic.

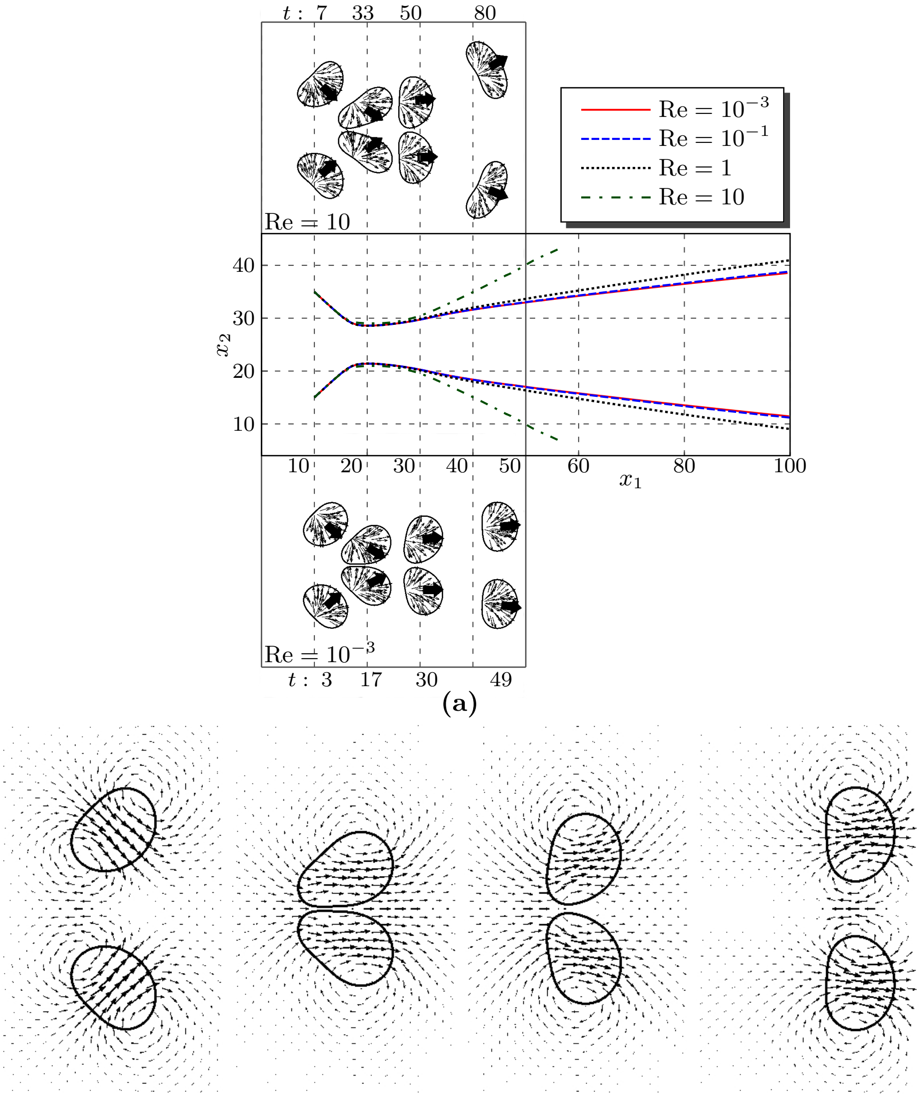

(a)

(b)

Figure 9.5. – (a) Cell trajectories for hydrodynamic model 2 with multiple orientation fields for $v_0 = 4$, $\mathrm{Ca} = 0.025$, $\mathrm{Pa} = 0.1$, $\beta = 0.5$ and varying Re. Cell evolution for $\mathrm{Re} = 10$ (top) and $\mathrm{Re} = 10^{-3}$ (bottom). Shown are the cell shapes, the union of all orientation fields $\mathbf{P}_{cell}$ (small arrows) and the main direction (big arrow) of four states at various times. Model 2 provides an elastic collision for high Re. (b) Clips of the cell evolution and velocity field for corresponding case as shown in (a)(bottom). We observe two vortices above and under the cell in the direction of motion. During a collision the vortices close to the neighbouring cell vanish and the cell is rotated away from the other cell.

obtained from the orientation field (model 1/1B) and velocity field (model 2):

$$\bar{\mathbf{v}}_i = \frac{\int_\Omega \tilde{\phi}_i \mathbf{P}\ \mathrm{d}\mathbf{x}}{\int_\Omega \tilde{\phi}\, \mathrm{d}\mathbf{x}} \qquad \text{model 1,}$$

$$\bar{\mathbf{v}}_i = \frac{\int_\Omega \mathbf{P}_i\ \mathrm{d}\mathbf{x}}{\int_\Omega \tilde{\phi}\, \mathrm{d}\mathbf{x}} \qquad \text{model 1B,}$$

$$\bar{\mathbf{v}}_i = \frac{\int_\Omega \tilde{\phi}_i \mathbf{v}\ \mathrm{d}\mathbf{x}}{\int_\Omega \tilde{\phi}\, \mathrm{d}\mathbf{x}} \qquad \text{model 2.}$$

First, we adopt model 1 with the parameters given in Tab. 9.1 and Tab. 9.3 and vary the polymerization rate β. As shown in Fig. 9.6, for $\beta = 0$, Pa $= 0.1$, we observe collective motion after a transient of $t = 80$ whereas for $\beta = 0.5$, Pa $= 0.1$ collective motion is suppressed. Accordingly, β and is crucial for the onset of collective motion. Moreover, the elasticity influences collective motion as well. For increasing elasticity of the cells (decreasing Pa), we notice a longer transient phase from undirected motion to directed motion. The results of model 1B, see Fig. 9.7a, show a collective motion for $\beta > 0$, where the used parameters are the same as in the last simulation. For both models, we observe that the onset of collective motion is suppressed if the results of the binary collision indicate an elastic collision and supported if the collision is mostly inelastic. However, this is not true for model 1B for $\beta = 0$. Accordingly, the alignment parameter ω stays constant as an external influence to the orientation field is missing and the realignment is prevented.

Finally, Fig. 9.7b shows the evolution of ω for the hydrodynamic model 2 where we vary Re and the viscosity ratio. The parameters are obtained from Tab. 9.2 and Tab. 9.3. In general, we observe a collective migration in all cases. The difference between Re $= 1$ and Re $= 10^{-3}$ is negligible. If we decrease the viscosity of the surrounding fluid by factor 10, the influence from neighboring cells is reduced and therefore the onset of collective motion is supported. However, it can not be justified by our results that hydrodynamics suppress collective motion.

9.6. Conclusion

In this chapter, we developed a hydrodynamic model for collective migration accounting for deformable cells. We therefore coupled a multi-phase model, which considers bending and surface tension along the cell membrane, to an active polar get theory that describes the orientation of the actin filaments in the cell bulk. Within our approach, which is formulated in a diffuse interface approach, we assign a single orientation field to a single cell (model 2). This guarantees that the collision mechanism is purely hydrodynamic. To compare this model, we further developed a non-hydrodynamic model based on a simplification of [160] using one orientation field for all cells (model 1) and a further non-hydrodynamic approach using multiple orientation fields (model 1B). For all models, we performed several benchmark computations for a binary collision to study the underlying collision modeling and its dependence on various parameters. We found

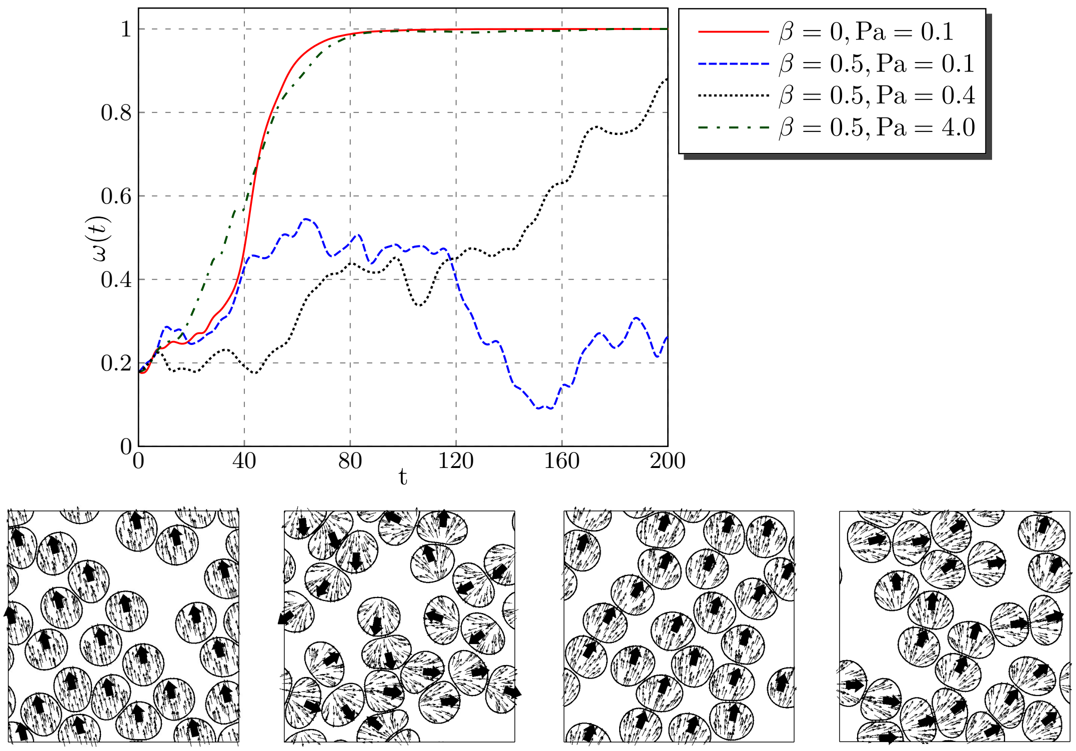

Figure 9.6. – The diagram shows the temporal evolution of ω for the non-hydrodynamic model 1. All simulations start with the same initial direction. For increasing elasticity (decreasing Pa) and increasing β (higher polymerization rate) the onset of collective motion is suppressed. The bottom line shows the simulation snapshot for t=200, where the small arrows are the direction of $\mathbf{P}$ and the big arrow indicate the averaged direction $\bar{\mathbf{v}}_i$.

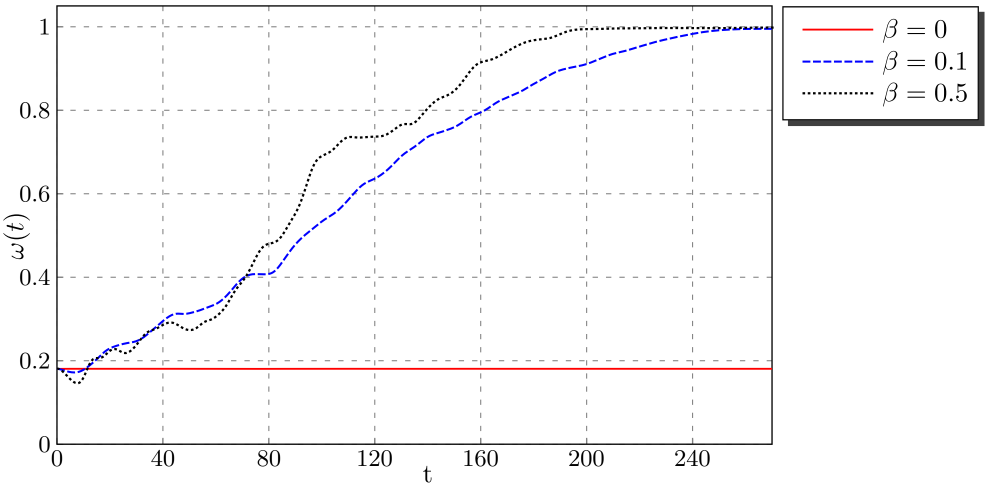

(a)

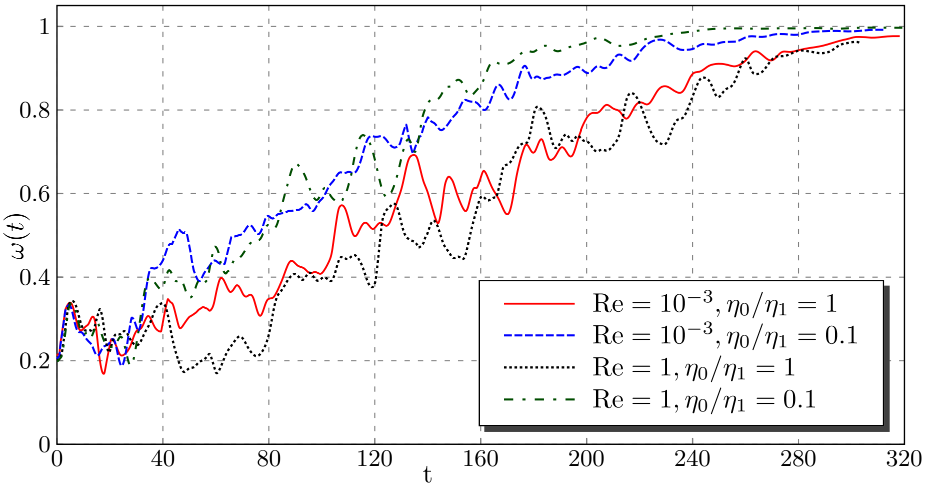

(b)

Figure 9.7. – (a) Temporal evolution of ω for various β for model 1B. We observe a collective motion for $\beta > 0$. For $\beta = 0$, the alignment parameter ω stays constant as no external influence can realign the orientation. (b) Temporal evolution of ω for model 2 for $\mathrm{Re} = 10^{-3}$ and $\mathrm{Re} = 1$ with varying viscosity ratios. For all cases, we observe a collective migration. A reduction of the viscosity of the surrounding fluid by factor 10 decreases the transient phase and supports the onset of collective motion.

out that, in general, multiple orientation fields within models 1B/2 suppress elastic collisions. However, this is not true for higher Re in the hydrodynamic case. We further investigated the collective motion of cells. For model 1, we observed that the transient phase increases if the cells are more elastic. Moreover, we showed that hydrodynamics do not completely suppress the onset of collective motion, within the considered parameters space of model 2. However, if hydrodynamics suppress or support collective motion is difficult to verify as this model is not easily to compare to non-hydrodynamic models. Nevertheless, our model 2 is a promising approach for the study of the dynamics of multiple deformable cells in hydrodynamic suspensions.

Chapter 10

Conclusions and outlook

In this thesis, we have studied different mathematical models that describe the morphology of a generalized biological cell considered as a thermodynamic system. Applications are given for cell motility, blood flow and collective cell migration. Our basic model uses a diffuse interface approach for a Helfrich-type membrane model. Here, the cell membrane is considered as a closed lipid bilayer that underlies bending and inextensibility. A further approach incorporates surface tension. We considered streaming effects in the cytoplasm and the surrounding of the cell that are described by the Navier-Stokes equations, which together with the membrane evolution yield a two-phase flow problem. It was shown how such a two-phase flow problem can be reformulated within the diffuse interface method in order to use the effectiveness and the robust physical basis of phase field simulations. We used an energy variation approach to derive the diffuse interface Navier-Stokes-Helfrich model that served as basis for further studies.

In the first part of this thesis, we studied models for cell motility. Within a first model, we combined the diffuse interface Navier-Stokes-Helfrich model with a biochemical network model given by reaction-diffusion equations for membrane-bound and cytoplasmic GTPases. Within the biochemical network model, the required polarization is achieved by a Turing-type instability as a result of different association and disassociation rates between membrane and cytoplasm. In contrast to previous models, the Turing instability is also formed in case of equal diffusion rates along the membrane. The diffuse interface approach, hereby, circumvents the numerical subtleties in solving differential equations on evolving domains with different dimensionalities. Within the first model, we assume that the actin polymerization is related to the concentration of the active membrane-bound GTPase enforcing membrane protrusion in the normal direction.

In a second model, we extended the diffuse interface Navier-Stokes-Helfrich model with an active polar gel theory. We reviewed an existing model and showed how this model can be derived by an energy variation approach. Here, the polymerization of the cell is achieved through an orientation field that moreover describes the alignment of the actin filament solution within the cell bulk. Besides actin polymerization, contractile stress within the actin meshwork caused by myosin motors is a fundamental part during cell motility. Within the model, the active stress can cause a generic splay instability that is responsible for cell motion even in the case without adhesion.

For both models, the motility mechanism arises from a delicate balance of the used parameters. Accordingly, we performed detailed numerical and convergence studies to demonstrate the stability of the used algorithm and to confirm the independence of the instability from the numerical approach. In the first model, we analyzed the interplay between protrusion, membrane and fluid forces and their effect on the cell shape. It turned out that, in particular, bending properties are of minor relevance for motility in the considered parameter regime. Moreover, we could reproduce characteristic cell motions according to external signals, so-called chemoattractants. Furthermore, we compared the second model with experimental data for swimming microorganisms. Within certain parameter regimes, a transition from puller-like to pusher-like dynamics can be found for increasing myosin-actin interactions, demonstrating the generic properties of the model. A quantitative comparison with swimming microorganism is not yet possible, requires 3D simulations and probably further model extension.

Within the used models, we considered the bulk of the cell as a single phase. However, it would be meaningful to consider an additional phase for the viscoelastic or fully elastic nucleus in order to study its influence to the shape of the cell. Moreover, the coupling to the active polar gel approach would allow us to investigate how the actin cytoskeleton determines the movement of the nucleus to the back of the cell during the onset of motility [134, 203, 243]. Finally, the application of the active polar gel theory is not only restricted to cell motility, it rather offers extensive opportunities for modeling approaches for cellular processes [203].

Although, both models incorporate several simplifications, we are able to qualitatively recover the basic shapes and important aspects of motile cells. Both approaches can also be extended to incorporate additional phenomena. The simulation results are obtained not for a specific cell type, but within a realistic parameter range spanning a large class of cells and their environment. We therefore expect the model and the numerical approach to be useful for quantitative simulations of specific cells.

In the second part of this thesis, we considered multiple cells that are of wide interest as their collective behavior shows a rich non-linear behavior. We extended the diffuse interface Navier-Stokes-Helfrich model to a multi-phase flow for several cells. Here, each cell is described by a single phase field that is combined to other cells by a local interaction potential. This approach is not restricted to a specific surface energy and has a wide applicability for multi-phase problems. Here, the most expensive part, i.e. computing the distance between cells, has been avoided as this information is already contained in the phase field description of the cells. We applied a Gaußian potential

cell types (Chapter)	effective physical property bending stiffness	 surface tension	 cell bulk	 active force
cell motility (5)	yes	yes	viscous	polymerization related to biochemical network
cell motility (6)	yes	yes	act. polar gel	contractile stress from polar field
RBC (8)	yes	inext.	viscous	-
WBC hard/soft (8)	yes	yes	viscous	-
active cells (9)	yes	yes	act. polar gel	polymerization, contractile stress from polar field

Table 10.1. – Effective physical properties considered in our models

in our model. However, the computed distance allows us to construct more complex potentials within the interface region. We applied this model in order to describe WBC margination. We reproduced previous findings in the low Reynolds number regime that have been achieved by particle methods and we moreover studied regimes with higher Re numbers where we found out that inertial effects suppress margination.

Finally, we combined the multi-cell approach with the active polar gel theory. We conducted several benchmark computations and compared this model to similar but non-hydrodynamic approaches. As the collision modeling between the cell is hydrodynamic, we do not observe elastic collisions within low Reynolds number regimes. Moreover, we studied the onset of collective migration. Within the considered parameters space, we showed that hydrodynamics do not suppress the onset of collective motion. However, as our approach combines active motion, deformable cells and hydrodynamics, it may help to give a better understanding of the processes determining collective cell migration.

In this thesis, we accounted for different physical properties of the cell depending on the considered cell or the spacial and temporal scale of the biological phenomenon. In Tab. 10.1, we summarize the accounted effective physical properties within our models. So far, the cell bulk was considered as a viscous fluid or active polar gel. For further studies, however, an appropriate model might account for viscolelasticity and membrane elasticity that are outlined in following. In addition to the viscous stress, a viscoelastic approach incorporates an elastic stress tensor: so let $\mathbf{u}(t, \mathbf{x})$ be a displacement field, then the elastic stress tensor is given by

$$\begin{aligned} \mathbf{S}_{el} &= \frac{E}{3}(\nabla \mathbf{u} + \nabla \mathbf{u}^\top) && \text{in } \Omega_1, \\ \mathbf{S}_{el} &= 0 && \text{in } \Omega_0, \\ \partial_t \mathbf{u} + \mathbf{v} \cdot \nabla \mathbf{u} &= \mathbf{v} && \text{in } \Omega_1, \end{aligned}$$

see also [33, 187, 265, 269]. Membrane elasticity, caused by the actin cortex attached to the membrane, can be described by the following functional [30, 220]

$$E_{el}(\Gamma) = \frac{E_{2D}}{1-\nu^2}\int_\Gamma (1-\nu)\mathbf{e}_{2D} : \mathbf{e}_{2D} + \nu \mathrm{tr}(\mathbf{e}_{2D})\,\mathrm{ds},$$

and the jump condition $[\mathbf{S}\cdot\mathbf{n}]_\Gamma = \frac{\delta E_S}{\delta\Gamma} + \frac{\delta E_{el}}{\delta\Gamma}$, where E_S is a surface energy.

Several numerical methods have been developed to solve free moving boundary problems. Each of those methods exhibits advantages and disadvantages. The applied diffuse interface or phase field method allows to combine the numerical method and the physical model. Accordingly, the resulting systems can be derived from physical laws and fulfill thermodynamical consistency. Topological changes may be treated without any problems and can be used for the description of e.g. endocytosis, see [163]. We have seen that further equations can easily be coupled to describe more and more complex phenomena. Moreover, it is simple to extend the method from 2D to 3D simulations and to calculate surface parameters such as curvature and normal vector. Furthermore, the method can easily be implemented with standard finite elements and therefore can serve as a first or a reference solution. On the other hand, we should be aware of the disadvantages or challenges of the diffuse interface method. Introducing a diffuse interface adds a further error to the approach. This error is mostly much smaller than the modeling error. However, to verify the approximation, an asymptotic analysis has to be performed which is not trivial. Finally, the considered method is computationally expensive. Considering many cells, especially in 3D, the method lags behind fast particle methods. To offset the distance, further numerical studies have to be performed.

In this thesis, we numerically solved our models using the finite element toolbox AMDiS. The numerical treatment was straightforward. We performed a linearization and operator splitting approach for the highly coupled and nonlinear system, which, however, led to small time steps. A deeper investigation of stabilization and time discretization techniques, as it was done for Navier-Stokes-Cahn-Hilliard fluids in [5], for both explicit and implicit coupling, might be meaningful. We further applied some features of the toolbox AMDiS to decrease the computational costs. In time, we performed an OPENMP problem parallelization that nearly reached an ideal speedup. In space, we used adaptive mesh refinement and multi-mesh strategies. To solve occurring linear systems of equation, we used the direct solver UMFPACK. However, for the treatment of larger systems, that occur especially in 3D, an iterative solver has to be used that requires the development of suitable preconditioners for the conserved Helfrich flow or for the implicit coupled Helfrich-Navier-Stokes system.

In this thesis, we have seen that the diffuse interface method is a powerful tool to describe and numerically solve highly complex phenomena. We studied hydrodynamic free boundary problems that result from a mathematical description of cells, their membrane and their surrounding. We produced qualitative results for the evolution of cells. Moreover, such hydrodynamic diffuse interface models signify the need for further mathematical analysis and quantitative comparison to experimental data that also requires intensive 3D simulations.

Bibliography

[1] K. B. Abbitt and G. B. Nash. Rheological properties of the blood influencing selectin-mediated adhesion of flowing leukocytes. *Am. J. Physiol.-Heart C*, 285: H229–H240, 2003.

[2] H. Abels. On a diffuse interface model for two-phase flows of viscous, incompressible fluids with matched densities. *Arch. Rational Mech. Anal.*, 194(2):463–506, 2009.

[3] H. Abels, H. Garcke, and G. Grün. Thermodynamically consistent, frame indifferent diffuse interface models for incompressible two-phase flows with different densities. *Math. Mod. Meth. Appl. S.*, 22(03):1150013, 2012.

[4] M. Abercrombie. The croonian lecture, 1978: the crawling movement of metazoan cells. *P. Roy. Soc. Lond. B Bio.*, 207(1167):129–147, 1980.

[5] S. Aland. Time integration for diffuse interface models for two-phase flow. *J. Comput. Phys.*, 262C:58–71, 2014.

[6] S. Aland and A. Voigt. Benchmark computations of diffuse interface models for two-dimensional bubble dynamics. *J. Num. Meth. Fluids*, 69:747–761, 2012.

[7] S. Aland, J. Lowengrub, and A. Voigt. Two-phase flow in complex geometries: A diffuse domain approach. *CMES-Comp. Model. Eng.*, 57(1):77, 2010.

[8] S. Aland, J. Lowengrub, and A. Voigt. A continuum model of colloid-stabilized interfaces. *Phys. Fluids*, 23(6):062103, 2011.

[9] S. Aland, J. Lowengrub, and A. Voigt. Particles at fluid-fluid interfaces: A new navier-stokes-cahn-hilliard surface-phase-field-crystal model. *Phys. Rev. E*, 86(4): 046321, 2012.

[10] S. Aland, S. Boden, A. Hahn, F. Klingbeil, M. Weismann, and S. Weller. Quantitative comparison of taylor flow simulations based on sharp-interface and diffuse-interface models. *Int. J. Numer. Methods Fluids*, 73(4):344–361, 2013.

[11] S. Aland, C. Lehrenfeld, H. Marschall, C. Meyer, and S. Weller. Accuracy of two-phase flow simulations: The taylor flow benchmark. *Proc. Appl. Math. Mech.*, 13: 595–598, 2013.

[12] S. Aland, S. Egerer, J. Lowengrub, and A. Voigt. Diffuse interface models of locally inextensible vesicles in a viscous fluid. *J. Comput. Phys.*, 277:32–47, 2014.

[13] N. D. Alikakos, P. Bates, and X. Chen. Convergence of the cahn-hilliard equation to the hele-shaw model. *Arch. Rational Mech. Anal.*, 128(2):165–205, 1994.

[14] J. Allain and M. Ben Amar. Biphasic vesicle: instability induced by adsorption of proteins. *Phys. A*, 337:531–545, 2004.

[15] W. Alt and M. Dembo. *A contraction-disassembly model for intracellular actin gels.* Springer, 1983.

[16] S. J. Altschuler, S. B. Angenent, Y. Wang, and L. F. Wu. On the spontaneous emergence of cell polarity. *Nature*, 454:886–889, 2008.

[17] D. Anderson, G. B. McFadden, and A. Wheeler. Diffuse-interface methods in fluid mechanics. *Annu. Rev. Fluid Mech.*, 30(1):139–165, 1998.

[18] E. S. Asmolov. The inertial lift on a spherical particle in plane poiseuille flow at large reynolds number. *J. Fluid Mech.*, 381:63–87, 1999.

[19] O. Axelsson and M. Neytcheva. Operator splittings for solving nonlinear, coupled multiphysics problems with an application to the numerical solution of an interface problem. *Inst. Inf. Tech.*, 9:2011, 2011.

[20] D. L. Bark and D. N. Ku. Wall shear over high degree stenoses pertinent to atherothrombosis. *J. Biomech.*, 43:2970–2977, 2010.

[21] E. Barnhart, K.-C. Lee, K. Keren, A. Mogilner, and J. Theriot. An adhesion-dependent switch between mechanisms that determine mitile cell shape. *PLoS Biol.*, 9:e1001059, 2011.

[22] J. W. Barrett, H. Garcke, and R. Nürnberg. A parametric finite element method for fourth order geometric evolution equations. *J. Comput. Phys.*, 222(1):441–467, 2007.

[23] J. W. Barrett, H. Garcke, and R. Nürnberg. Parametric approximation of willmore flow and related geometric evolution equations. *SIAM J. Sci. Comput.*, 31(1):225–253, 2008.

[24] J. W. Barrett, H. Garcke, and R. Nürnberg. Numerical approximation of gradient flows for closed curves in rd. *IMA J. Numer. Anal.*, 30(1):4–60, 2010.

[25] J. W. Barrett, H. Garcke, and R. Nürnberg. Numerical computations of the dynamics of fluidic membranes and vesicles. *Phys. Rev. E*, 92:052704, Nov 2015.

[26] J. Beaucourt, F. Rioual, T. Seon, T. Biben, and C. Misbah. Steady to unsteady dynamics of a vesicle in a flow. *Phys. Rev. E*, 69:011906, 2004.

[27] G. Bellettini and L. Mugnai. On the approximation of the elastica functional in radial symmetry. *Calc. Var. Partial Differ. Equ.*, 24(1):1–20, 2005.

[28] M. Beneš, K. Mikula, T. Oberhuber, and D. Ševčovič. Comparison study for level set and direct lagrangian methods for computing willmore flow of closed planar curves. *Comput. Vis. Sci.*, 12(6):307–317, 2009.

[29] A. Bershadsky, M. Kozlov, and B. Geiger. Adhesion-mediated mechanosensitivity: a time to experiment, and a time to theorize. *Curr. Opin. Cell Biol.*, 18(5):472–481, 2006.

[30] H. Berthoumieux, J.-L. Maître, C.-P. Heisenberg, E. K. Paluch, F. Jülicher, and G. Salbreux. Active elastic thin shell theory for cellular deformations. *New J. Phys.*, 16(6):065005, 2014.

[31] T. Biben and C. Misbah. Tumbling of vesicles under shear flow within an advected-field approach. *Phys. Rev. E*, 67:031908, 2003.

[32] T. Biben, K. Kassner, and C. Misbah. Phase-field approach to three-dimensional vesicle dynamics. *Phys. Rev. E*, 72:041921, 2005.

[33] R. B. Bird, R. Armstrong, and O. Hassager. *Dynamics of polymeric liquids. Vol. 1: Fluid mechanics.* John Wiley and Sons Inc., New York, NY, 1987.

[34] J. R. Blake. A spherical envelope approach to ciliary propulsion. *J. Fluid Mech.*, 46:199–208, 1971.

[35] H. R. Brand, H. Pleiner, and F. Ziebert. Macroscopic dynamics of polar nematic liquid crystals. *Phys. Rev. E*, 74:021713, 2006.

[36] Y. Brenier. The least action principle and the related concept of generalized flows for incompressible perfect fluids. *J. Amer. Math. Soc.*, 2(2):225–255, 1989.

[37] F. P. Bretherton. The motion of rigid particles in a shear flow at low reynolds number. *J. Fluid Mech.*, 14:284–304, 1962.

[38] G. Caginalp and X. Chen. *Phase field equations in the singular limit of sharp interface problems.* Springer, 1992.

[39] J. W. Cahn and J. E. Hilliard. Free energy of a nonuniform system. i. interfacial free energy. *J. Chem. Phys.*, 28(2):258–267, 1958.

[40] J. W. Cahn, C. M. Elliott, and A. Novick-Cohen. The cahn–hilliard equation with a concentration dependent mobility: motion by minus the laplacian of the mean curvature. *European J. Appl. Math.*, 7(03):287–301, 1996.

[41] B. A. Camley, Y. Zhang, Y. Zhao, B. Li, E. Ben-Jacob, H. Levine, and W.-J. Rappel. Polarity mechanisms such as contact inhibition of locomotion regulate persistent rotational motion of mammalian cells on micropatterns. *PNAS*, 111 (41):14770–14775, 2014.

[42] F. Campelo and A. Hernández-Machado. Dynamic model and stationary shapes of fluid vesicles. *Eur. Phys. J. E Soft Matter*, 20(1):37–45, 2006.

[43] F. Campelo and A. Hernández-Machado. Model for curvature-driven pearling instability in membranes. *Phys. Rev. Lett.*, 99(8):088101, 2007.

[44] F. Campelo and A. Hernández-Machado. Shape instabilities in vesicles: A phase-field model. *Eur. Phys. J. Spec. Top.*, 143:101–108, 2007.

[45] F. Campelo and A. Hernandez-Machado. Polymer-induced tubulation in lipid vesicles. *Phys. Rev. Lett.*, 100(15):158103, 2008.

[46] P. B. Canham. The minimum energy of bending as a possible explanation of the biconcave shape of the human red blood cell. *J. Theor. Biol.*, 26(1):61–81, 1970.

[47] D. D. Carlo, E. J. Humphry, H. Stone, and M. Toner. Particle segregation and dynamics in confined flows. *Phys. Rev. Lett.*, 102:094503, 2009.

[48] M. E. Cates. Complex fluids: The physics of emulsions. *Lecture Notes for Soft Interfaces*, 2012.

[49] M. E. Cates, O. Henrich, D. Marenduzzo, and K. Stratford. Lattice boltzmann simulations of liquid crystalline fluids: active gels and blue phases. *Soft Matter*, 5: 3791–3800, 2009.

[50] P. Cermelli, E. Fried, and M. E. Gurtin. Transport relations for surface integrals arising in the formulation of balance laws for evolving fluid interfaces. *J. Fluid Mech.*, 544:339–351, 2005.

[51] N. Cogan and R. D. Guy. Multiphase flow models of biogels from crawling cells to bacterial biofilms. *HFSP J.*, 4(1):11–25, 2010.

[52] P. Colli and P. Laurencot. A phase-field approximation of the willmore flow with volume constraint. *Interface Free Bound.*, 13(3):341–351, 2011.

[53] P. Colli and P. Laurencot. A phase-field approximation of the willmore flow with volume and area constraints. *SIAM J. Math. Anal.*, 44(6):3734–3754, 2012.

[54] C. Cowan. The cahn-hilliard equation as a gradient flow. Master's thesis, Simon Fraser University, 2005. Thesis (M.Sc.) - Department of Mathematics - Simon Fraser University.

[55] G. Danuser, J. Allard, and A. Mogilner. Mathematical modeling of eukaryotic cell migration: insights beyond experiments. *Annu. Rev. Cell Dev. Biol.*, 29:501, 2013.

[56] S. Das and Q. Du. Adhesion of vesicles to curved substrates. *Phys. Rev. E*, 77, 2008.

[57] T. A. Davis. Algorithm 832: Umfpack v4. 3—an unsymmetric-pattern multifrontal method. *ACM T. Math. Software*, 30(2):196–199, 2004.

[58] P.-G. de Gennes and J. Prost. *The physics of liquid crystals.* Clarendon Press, Oxford, 2nd edition, 1993.

[59] S. R. De Groot and P. Mazur. *Non-equilibrium thermodynamics.* Courier Corporation, 2013.

[60] K. Deckelnick, G. Dziuk, and C. M. Elliott. Computation of geometric partial differential equations and mean curvature flow. *Acta Numer.*, 14:139–232, 2005.

[61] M. Dembo and F. Harlow. Cell motion, contractile networks, and the physics of interpenetrating reactive flow. *Biophys. J.*, 50(1):109, 1986.

[62] P. DiMilla, K. Barbee, and D. Lauffenburger. Mathematical model for the effects of adhesion and mechanics on cell migration speed. *Biophys. J.*, 60(1):15, 1991.

[63] K. Doubrovinski and K. Kruse. Cell motility resulting from spontaneous polymerization waves. *Phys. Rev. Lett.*, 107:258103, 2011.

[64] V. Doyeux, Y. Guyot, V. Chabannes, C. Prud'Homme, and M. Ismail. Simulation of two-fluid flows using a finite element/level set method. application to bubbles and vesicle dynamics. *J. Comput. Appl. Math.*, 246:251–259, 2013.

[65] K. Drescher, R. E. Goldstein, N. Michel, M. Polin, and I. Tuval. Direct measurement of the flow field around swimming microorganisms. *Phys. Rev. Lett.*, 105: 168101, 2010.

[66] M. Droske and M. Rumpf. A level set formulation for willmore flow. *Interface Free Bound.*, 6(3):361–378, 2004.

[67] Q. Du. Phase field calculus, curvature-dependent energies, and vesicle membranes. *Philos. Mag.*, 91(1):165–181, 2011.

[68] Q. Du and M. Li. Analysis of a stochastic implicit interface model for an immersed elastic surface in a fluctuating fluid. *Arch. Rational Mech. Anal.*, 199(1):329–352, 2011.

[69] Q. Du and X. Wang. Convergence of numerical approximations to a phase field bending elasticity model of membrane deformations. *Inter. J. Numer. Anal Model*, 4:441–459, 2007.

[70] Q. Du and J. Zhang. Adaptive finite element method for a phase field bending elasticity model of vesicle membrane deformations. *SIAM J. Sci. Comput.*, 30: 1634–1657, 2008.

[71] Q. Du and L. Zhu. Analysis of a mixed finite element method for a phase field bending elasticity model of vesicle membrane deformation. *J. Comput. Math.*, 24 (3):265–280, 2006.

[72] Q. Du, C. Liu, and X. Wang. A phase field approach in the numerical study of the elastic bending energy for vesicle membranes. *J. Comput. Phys.*, 198(2):450–468, 2004.

[73] Q. Du, C. Liu, R. Ryham, and X. Wang. Modeling the spontaneous curvature effects in static cell membrane deformations by a phase field formulation. *Comm. Pure Applied Anal.*, 4:537–548, 2005.

[74] Q. Du, C. Liu, R. Ryham, and X. Wang. A phase field formulation of the willmore problem. *Nonlinearity*, 18:1249–1267, 2005.

[75] Q. Du, C. Liu, and X. Wang. Simulating the deformation of vesicle membranes under elastic bending energy in three dimensions. *J. Comput. Phys.*, 212:757–777, 2006.

[76] Q. Du, M. Li, and C. Liu. Analysis of a phase field navier-stokes vesicle-fluid interaction model. *Discrete Contin. Dyn. Syst. Ser. B*, 8:539–556, 2007.

[77] Q. Du, C. Liu, R. Ryham, and X. Wang. Energetic variational approaches in modeling vesicle and fluid interactions. *Phys. D*, 238:923–930, 2009.

[78] G. Dziuk and C. M. Elliott. Finite elements on evolving surfaces. *IMA J. Numer. Anal.*, 27(2):262–292, 2007.

[79] G. Dziuk and C. M. Elliott. Eulerian finite element method for parabolic pdes on implicit surfaces. *Interface Free Bound.*, 10(119-138):464, 2008.

[80] G. Dziuk and C. M. Elliott. An eulerian approach to transport and diffusion on evolving implicit surfaces. *Comput. Vis. Sci.*, 13(1):17–28, 2010.

[81] G. Dziuk and C. M. Elliott. Finite element methods for surface pdes. *Acta Numer.*, 22:289–396, 2013.

[82] G. Dziuk, E. Kuwert, and R. Schatzle. Evolution of elastic curves in \rn: Existence and computation. *SIAM J. Math. Anal.*, 33(5):1228–1245, 2002.

[83] C. M. Elliott and B. Stinner. Analysis of a diffuse interface approach to an advection diffusion equation on a moving surface. *Math. Mod. Meth. Appl. S.*, 19(05): 787–802, 2009.

[84] C. M. Elliott and B. Stinner. Modeling and computation of two phase geometric biomembranes using surface finite elements. *J. Comput. Phys.*, 229(18):6585–6612, 2010.

[85] C. M. Elliott and B. Stinner. A surface phase field model for two-phase biological membranes. *SIAM J. Appl. Math.*, 70(8):2904–2928, 2010.

[86] C. M. Elliott, B. Stinner, V. Styles, and R. Welford. Numerical computation of advection and diffusion on evolving diffuse interfaces. *IMA J. Numer. Anal.*, 31 (3):786–812, 2011.

[87] C. M. Elliott, B. Stinner, and C. Venkataraman. Modelling cell motility and chemotaxis with evolving surface finite elements. *J. R. Soc. Interface*, 9(76):3027–3044, 2012.

[88] H. Elliott, R. S. Fischer, K. A. Myers, R. A. Desai, L. Gao, C. S. Chen, R. S. Adelstein, C. M. Waterman, and G. Danuser. Myosin ii controls cellular branching morphogenesis and migration in three dimensions by minimizing cell-surface curvature. *Nat. Cell Biol.*, 17(2):137–147, 2015.

[89] H. Emmerich. *The Diffuse Interface Approach in Material Science.* Springer-Verlag Berlin Heidelberg, 2003.

[90] M. Enculescu, A. Gholami, and M. Falcke. Dynamic regimes and bifurcations in a model of actin-based motility. *Phys. Rev. E*, 78:031915, 2008.

[91] M. Enculescu, M. Sabouri-Ghorni, G. Danuser, and M. Falcke. Modeling of protrution phenotypes driven by the actin-membrane interaction. *Biophys. J.*, 98: 1571–1581, 2010.

[92] S. Esedoglu, A. Rätz, and M. Röger. Colliding interfaces in old and new diffuse-interface approximations of willmore-flow. *Comm. Math. Sci.*, 12:125–147, 2014.

[93] E. Evans and W. Rawicz. Entropy-driven tension and bending elasticity in condensed-fluid membranes. *Phys. Rev. Lett.*, 64:2094–2097, 1990.

[94] E. A. Evans. Bending resistance and chemically induced moments in membrane bilayers. *Biophys. J.*, 14(12):923, 1974.

[95] L. C. Evans, H. M. Soner, and P. E. Souganidis. Phase transitions and generalized motion by mean curvature. *Comm. Pure Appl. Math.*, 45(9):1097–1123, 1992.

[96] R. Fåhræus and T. Lindqvist. The viscosity of the blood in narrow capillary tubes. *Am. J. Physiol.-Leg. C*, 96(3):562–568, 1931.

[97] M. H. Farshbaf-Shaker and H. Garcke. Thermodynamically consistent higher order phase field navier-stokes models with applications to biological membranes. *Discrete Contin. Dyn. Syst. Ser. S*, 4(2):371–389, 2011.

[98] A. Farutin, T. Biben, and C. Misbah. 3d numerical simulations of vesicle and inextensible capsule dynamics. *J. Comput. Phys.*, 275:539–568, 2014.

[99] D. A. Fedosov and G. Gompper. White blood cell margination in microcirculation. *Soft Matter*, 10:2961–2970, 2014.

[100] D. A. Fedosov, J. Fornleitner, and G. Gompper. Margination of white blood cells in microcapillary flow. *Phys. Rev. Lett.*, 108:028104, 2012.

[101] J. J. Feng. Theoretical aspects of liquid crystals and liquid crystalline polymers. In *Encyclopedia of Chemical Processing*, pages 2955–2964. CRC Press, 2006.

[102] T. M. Fischer, M. Stöhr-Liesen, and H. Schmid-Schönbein. The red-cell as a fluid droplet: tank tread-like motion of the human erythocyte-membrane in shear flow. *Science*, 202:894–896, 1978.

[103] B. Flaherty, J. McGarry, and P. McHugh. Mathematical models of cell motility. *Cell Biochem. Biophys.*, 49(1):14–28, 2007.

[104] L. Formaggiam, A. Quarteroni, and A. Veneziani. *Cardiovascular Mathematics: Modeling and simulation of the circulatory system.* Springer, 2000.

[105] J. B. Freund. Leukocyte margination in a model microvessel. *Phys. Fluids*, 19(2): 023301, 2007.

[106] P. Friedl and D. Gilmour. Collective cell migration in morphogenesis, regeneration and cancer. *Nat. Rev. Mol. Cell Biol.*, 10(7):445–457, 2009.

[107] P. Friedl and K. Wolf. Tumour-cell invasion and migration: diversity and escape mechanisms. *Nat. Rev. Cancer*, 3(5):362–374, 2003.

[108] S. Fürthauer, M. Neef, S. W. Grill, K. Kruse, and F. Jülicher. The taylor-couette motor: spontaneous flows of active polar fluids between two coaxial cylinders. *New J. Phys.*, 14(2):023001, 2012.

[109] J. Geiser. Iterative operator-splitting methods with higher-order time integration methods and applications for parabolic partial differential equations. *J. Comput. Appl. Math.*, 217(1):227–242, 2008.

[110] T. M. Geislinger and T. Franke. Hydrodynamic lift of vesicles and red blood cells in flow - from Fåhraeus & Lindqvist to microfluidic cell sorting. *Adv. Colloid Interface Sci.*, 208:161–176, 2014.

[111] G. Ghigliotti, T. Biben, and C. Misbah. Rheology of a dilute two-dimensional suspension of vesicles. *J. Fluid Mech.*, 653:489–518, 2010.

[112] L. Giomi and A. DeSimone. Spontaneous division and motility in active nematic droplets. *Phys. Rev. Lett.*, 112:147802, 2014.

[113] H. L. Goldsmith and S. G. Mason. Axial migration of particles in poiseuille flow. *Nature*, 190:1095–1096, 1961.

[114] G. Gonnella, D. Marenduzzo, A. Suma, and A. Tiribocchi. Motility-induced phase separation and coarsening in active matter. *C. R. Phys.*, 2015.

[115] A. B. Goryachev and A. V. Pokhilko. Dynamics of cdc42 network embodies a turing-type mechanism of yeast cell polarity. *FEBS Lett.*, 582:1437–1443, 2008.

[116] R. Gu, X. Wang, and M. Gunzburger. Simulating vesicle-substrate adhesion using two phase field functions. *J. Comput. Phys.*, 275:626–641, 2014.

[117] J. Happel and H. Brenner. *Low Reynolds number hydrodynamics: with special applications to particulate media*, volume 1. Springer Science & Business Media, 2012.

[118] F. Haußer, S. Li, J. Lowengrub, W. Marth, A. Rätz, and A. Voigt. Thermodynamically consistent models for two-component vesicles. *Int. J. Biomath. Biostat.*, 2(1):19–48, 2013.

[119] R. J. Hawkins, R. Poincloux, O. Bénichou, M. Piel, P. Chavrier, and R. Voituriez. Spontaneous contractility-mediated cortical flow generates cell migration in three-dimensional environments. *Biophys. J.*, 101(5):1041–1045, 2011.

[120] A. Heintz. A numerical method for simulation dynamics of incompressible lipid membranes in viscous fluid. *J. Comput. Appl. Math.*, 289:87–100, 2015.

[121] W. Helfrich. Elastic properties of lipid bilayers: theory and possible experiments. *Z. Naturforsch.*, 28:693–703, 1973.

[122] B. P. Ho and L. G. Leal. Inertial migration of rigid spheres in two-dimensional unidirectional flows. *J. Fluid Mech.*, 65:365–400, 1974.

[123] P. Hohenberg and B. Halperin. Theory of dynamic critical phenomena. *Rev. Mod. Phys.*, 49:435–479, 1977.

[124] W. R. Holmes and L. Edelstein-Keshet. A comparison of computational models for eukaryotic cell shape and motility. *PLoS Comput. Biol*, 8(12):e1002793, 2012.

[125] S. M. Hosseini and J. J. Feng. How malaria parasites reduce the deformability of infected red blood cells. *Biophys. J.*, 103(1):1–10, 2012.

[126] W.-F. Hu, Y. Kim, and M.-C. Lai. An immersed boundary method for simulating the dynamics of three-dimensional axisymmetric vesicles in navier–stokes flows. *J. Comput. Phys.*, 257:670–686, 2014.

[127] D. Jacqmin. Calculation of two-phase navier–stokes flows using phase-field modeling. *J. Comput. Phys.*, 155(1):96 – 127, 1999.

[128] A. Jain and L. L. Munn. Determinants of leukocyte margination in rectangular microchannels. *PLoS One*, 4(9):e7104, 2009.

[129] D. Jamet and C. Misbah. Towards a thermodynamically consistent picture of the phase-field model of vesicles: Local membrane incompressibility. *Phys. Rev. E*, 76 (5):051907, 2007.

[130] A. Jilkine and L. Edelstein-Keshet. A comparison of mathematical models for polarization of single eukaryotic cells in response to guided cues. *PLoS Comput. Biol.*, 7, 2011.

[131] J.-F. Joanny and J. Prost. Active gels as a description of the actin-myosin cytoskeleton. *HFSP J.*, 3(2):94–104, 2009.

[132] F. Jülicher, A. Ajdari, and J. Prost. Modeling molecular motors. *Rev. Modern Phys.*, 69(4):1269, 1997.

[133] K. Keren, Z. Pincus, G. M. Allen, E. L. Barnhart, G. Marriott, A. Mogilner, and J. A. Theriot. Mechanism of shape determination in motile cells. *Nature*, 453 (7194):475–480, 2008.

[134] S. B. Khatau, R. J. Bloom, S. Bajpai, D. Razafsky, S. Zang, A. Giri, P.-H. Wu, J. Marchand, A. Celedon, C. M. Hale, et al. The distinct roles of the nucleus and nucleus-cytoskeleton connections in three-dimensional cell migration. *Sci. Rep.*, 2, 2012.

[135] Y. Kim and M.-C. Lai. Simulating the dynamics of inextensible vesicles by the penalty immersed boundary method. *J. Comput. Phys.*, 229:4840–4853, 2010.

[136] Y. Kim and M.-C. Lai. Numerical study of viscosity and inertial effects on tank-treading and tumbling motions of vesicles under shear flow. *Phys. Rev. E*, 86: 066321, Dec 2012.

[137] M. Kraus, W. Wintz, U. Seifert, and R. Lipowsky. Fluid vesicle in shear flow. *Phys. Rev. Lett.*, 77:3685–3688, 1996.

[138] T. Krüger, B. Kaoui, and J. Harting. Interplay of inertia and deformability on rheological properties of a suspension of capsules. *J. Fluid Mech.*, 751:725–745, 2014.

[139] K. Kruse and F. Jülicher. Actively contracting bundles of polar filaments. *Phys. Rev. Lett.*, 85:1778–1781, 2000.

[140] K. Kruse, J.-F. Joanny, F. Jülicher, J. Prost, and K. Sekimoto. Asters, vortices, and rotating spirals in active gels of polar filaments. *Phys. Rev. Lett.*, 92:078101, 2004.

[141] K. Kruse, J.-F. Joanny, F. Jülicher, J. Prost, and K. Sekimoto. Generic theory of active polar gels: a paradigm for cytoskeletal dynamics. *Eur. Phys. J. E Soft Matter*, 16(1):5–16, 2005.

[142] D. Ku. Blood flow in ateries. *Annu. Rev. Fluid Mech.*, 29:399–434, 1997.

[143] A. Kumar and M. D. Graham. Margination and segregation in confined flows of blood and other multicomponent suspensions. *Soft Matter*, 8:10536–10548, 2012.

[144] A. Laadhari, P. Saramito, and C. Misbah. Vesicle tumbling inhibited by inertia. *Phys. Fluids*, 24:031901, 2012.

[145] A. Laadhari, P. Saramito, and C. Misbah. Computing the dynamics of biomembranes by combining conservative level set and adaptive finite element methods. *J. Comput. Phys.*, 263:328–352, 2014.

[146] L. D. Landau. *On the theory of phase transitions.* Collected Papers of L.D. Landau. Gordon and Breach, New York, 1937.

[147] C. Landsberg, F. Stenger, A. Deutsch, M. Gelinsky, A. Roesen-Wolff, and A. Voigt. Chemotaxis of mesenchymal stem cells within 3d biomimetic scaffolds-a modeling approach. *J. Biomech.*, 44:359–364, 2011.

[148] F. Lautenschläger, S. Paschke, S. Schinkinger, A. Bruel, M. Beil, and J. Guck. The regulatory role of cell mechanics for migration of differentiating myeloid cells. *PNAS*, 106(37):15696–15701, 2009.

[149] G. R. Lázaro, K. A. Melzak, J. L. Toca-Herrera, I. Pagonabarraga, and A. Hernández-Machado. Elastic energies and morphologies of the first stages of the discoechinocyte transition. *Soft Matter*, 9(28):6430–6441, 2013.

[150] G. R. Lázaro, A. Hernández-Machado, and I. Pagonabarraga. Rheology of red blood cells under flow in highly confined microchannels: I. effect of elasticity. *Soft Matter*, 10(37):7195–7206, 2014.

[151] G. R. Lázaro, I. Pagonabarraga, and A. Hernández-Machado. Phase-field theories for mathematical modeling of biological membranes. *Chem. Phys. Lipids*, 185: 46–60, 2015.

[152] H. Levine and W.-J. Rappel. Membrane-bound turing patterns. *Phys. Rev. E*, 72: 061912, 2005.

[153] X. Li, J. Lowengrub, A. Raetz, and A. Voigt. Solving pde's in complex geometries: A diffuse domain approach. *Comm. Math. Sci.*, 7:81–107, 2009.

[154] M. J. Lighthill. Hydromechanics of aquatic animal propulsion. *Annu. Rev. Fluid Mech.*, 1(1):413–446, 1969.

[155] F.-H. Lin and C. Liu. Nonparabolic dissipative systems modeling the flow of liquid crystals. *Comm. Pure Appl. Math.*, 48(5):501–537, 1995.

[156] S. Ling, W. Marth, S. Praetorius, and A. Voigt. An adaptive finite element multimesh approach for interacting deformable objects in flow. *Comp. Meth. Appl. Math.*, 2016.

[157] C. Liu and J. Shen. A phase field model for the mixture of two incompressible fluids and its approximation by a fourier-spectral method. *Phys. D*, 179(3):211–228, 2003.

[158] Y. Liu, T. Takahashi, and M. Tucsnak. Strong solutions for a phase field navier–stokes vesicle–fluid interaction model. *J. Math. Fluid Mech.*, 14(1):177–195, 2012.

[159] J. Löber, F. Ziebert, and I. S. Aranson. Modeling crawling cell movement on soft engineered substrates. *Soft Matter*, 10:1365–1373, 2014.

[160] J. Löber, F. Ziebert, and I. S. Aranson. Collisions of deformable cells lead to collective migration. *Sci. Rep.*, 5, 2015.

[161] J. Lowengrub and L. Truskinovsky. Quasi–incompressible cahn–hilliard fluids and topological transitions. *P. Roy. Soc. Lond. A Math. P.*, 454(1978):2617–2654, 1998.

[162] J. Lowengrub, J. Xu, and A. Voigt. Surface phase separation and flow in a simple model of multicomponent drops and vesicles. *Fluid Dyn. Mat. Proc.*, 3:13–28, 2007.

[163] J. Lowengrub, J. Allard, and S. Aland. Numerical simulation of endocytosis: Viscous flow driven by membranes with non-uniformly distributed curvature-inducing molecules. *Journal of Computational Physics*, 309:112–128, 2016.

[164] J. S. Lowengrub, A. Rätz, and A. Voigt. Phase-field modeling of the dynamics of multicomponent vesicles: Spinodal decomposition, coarsening, budding, and fission. *Phys. Rev. E*, 79:031926, 2009.

[165] E. Lushi and C. S. Peskin. Modeling and simulation of active suspensions containing large numbers of interacting micro-swimmers. *Comp. Struct.*, 122:239–248, 2013.

[166] E. Lushi, H. Wioland, and R. E. Goldstein. Fluid flows created by swimming bacteria drive self-organization in confined suspensions. *PNAS*, page 201405698, 2014.

[167] E. Maitre, C. Misbah, P. Peyla, and A. Raoult. Comparison between advected-field and level-set methods in the study of vesicle dynamics. *Phys. D*, 241(13):1146 – 1157, 2012.

[168] M. C. Marchetti, J.-F. Joanny, S. Ramaswamy, T. B. Liverpool, J. Prost, M. Rao, and R. A. Simha. Hydrodynamics of soft active matter. *Rev. Mod. Phys.*, 85(3): 1143–1189, 2013.

[169] A. F. Marée, V. A. Grieneisen, and L. Edelstein-Keshet. How cells integrate complex stimuli: the effect of feedback from phosphoinositides and cell shape on cell polarization and motility. *PLoS Comput. Biol.*, 8(3):e1002402, 2012.

[170] A. F. M. Maree, A. Jilkine, A. Dawes, V. A. Grieneisen, and L. Edelstein-Keshet. Polarization and movement of keratocytes: A multiscale modelling approach. *Bull. Math. Bio.*, 68:1169–1211, 2006.

[171] D. Marenduzzo, E. Orlandini, M. E. Cates, and J. M. Yeomans. Steady-state hydrodynamic instabilities of active liquid crystals: Hybrid lattice boltzmann simulations. *Phys. Rev. E*, 76:031921, Sep 2007.

[172] D. Marenduzzo, E. Orlandini, and J. M. Yeomans. Hydrodynamics and rheology of active liquid crystals: A numerical investigation. *Phys. Rev. Lett.*, 98:118102, Mar 2007.

[173] W. Marth. Mathematische modellierung und simulation von biomembranen mit phasenfeldmodellen. Master's thesis, Technische Universität Dresden, 2012. Diplomarbeit - Institut für Wissenschaftliches Rechnen - TU Dresden.

[174] W. Marth and A. Voigt. Signaling networks and cell motility: A computational approach using a phase field description. *J. Math. Biol.*, July:1–22, 2013.

[175] W. Marth and A. Voigt. Collective cell migration - a hydrodynamic phase field approach. *Journal of The Royal Society Interface Focus (submitted)*, 2016.

[176] W. Marth, S. Praetorius, and A. Voigt. A mechanism for cell motility by active polar gels. *J. R. Soc. Interface*, 12(107):20150161, 2015.

[177] W. Marth, S. Aland, and A. Voigt. Margination of white blood cells: a computational approach by a hydrodynamic phase field model. *J. Fluid Mech.*, 790: 389–406, 3 2016.

[178] P. C. Martin, O. Parodi, and P. S. Pershan. Unified hydrodynamic theory for crystals, liquid crystals, and normal fluids. *Phys. Rev. A*, 6:2401–2420, 1972.

[179] J.-P. Matas, J. F. Morris, and E. Guazzelli. Inertial migration of rigid spherical particles in Poiseuille flow. *J. Fluid Mech.*, 515:171–195, 2004.

[180] R. Matas-Navarro, R. Golestanian, T. B. Liverpool, and S. M. Fielding. Hydrodynamic suppression of phase separation in active suspensions. *Phys. Rev. E*, 90 (3):032304, 2014.

[181] H. McMahon and J. Gallop. Membrane curvature and mechanisms of dynamic cell membrane remodelling. *Nature*, 438:590–596, 2005.

[182] J. L. McWhirter, H. Noguchi, and G. Gompper. Flow-induced clustering and alignment of vesicles and red blood cells in microcapillaries. *PNAS*, 106(15):6039–6043, 2009.

[183] E. Méhes and T. Vicsek. Collective motion of cells: from experiments to models. *Integr. Biol.*, 6(9):831–854, 2014.

[184] A. Menzel. Tuned, driven and active soft matter. *Phys. Rep.*, 554:1, 2015.

[185] A. M. Menzel and T. Ohta. Soft deformable self-propelled particles. *Europhys. Lett.*, 99(5):58001, 2012.

[186] S. Meßlinger, B. Schmidt, H. Noguchi, and G. Gompper. Dynamical regimes and hydrodynamic lift of viscous vesicles under shear. *Phys. Rev. E*, 80:011901, 2009.

[187] A. Mietke. *Theoretical and Experimental Analysis of Cell Deformations by Hydrodynamic Forces in Microfluidic Channels.* PhD thesis, Technische Universität Dresden, 2014.

[188] L. Modica. The gradient theory of phase transitions and the minimal interface criterion. *Arch. Rational Mech. Anal.*, 98:123–142, 1987.

[189] A. Mogilner and K. Keren. The shape of motile cells. *Curr. Biol.*, 19(17):R762–R771, 2009.

[190] A. Mogilner and G. Oster. Cell motility driven by actin polymerization. *Biophys. J.*, 71(6):3030, 1996.

[191] J. J. Molina, Y. Nakayama, and R. Yamamoto. Hydrodynamic interactions of self-propelled swimmers. *Soft Matter*, 9:4923–4936, 2013.

[192] N. A. N'Dri, W. Shyy, and R. Tran-Son-Tay. Computational modeling of cell adhesion and movement using a continuum-kinetics approach. *Biophys. J.*, 85: 2273–2286, 2003.

[193] F. Nedelec and D. Foethke. Collective langevin dynamics of flexible cytoskeletal fibers. *New J. Phys.*, 9(11):427, 2007.

[194] M. P. Neilson, D. M. Veltman, P. J. van Haastert, S. D. Webb, J. A. Mackenzie, and R. H. Insall. Chemotaxis: a feedback-based computational model robustly predicts multiple aspects of real cell behaviour. *PLoS Biol.*, 9(5):1072, 2011.

[195] H. Noguchi, G. Gompper, L. Schmid, A. Wixforth, and T. Franke. Dynamics of fluid vesicles in flow through structured microchannels. *Europhys. Lett.*, 89(2): 28002, 2010.

[196] M. Nonomura and Y. Xu. Study on multicellular systems using a phase field model. *PLoS One*, 7(4):e33501, 2012.

[197] L. Onsager. Reciprocal relations in irreversible processes. i. *Phys. Rev. D*, 37(4): 405, 1931.

[198] J. Palacci, S. Sacanna, A. P. Steinberg, D. J. Pine, and P. M. Chaikin. Living crystals of light-activated colloidal surfers. *Science*, 339(6122):936–940, 2013.

[199] T. Papanastasiou, G. Georgiou, and A. N. Alexandrou. *Viscous fluid flow*. CRC Press, 1999.

[200] M. J. Pearson and H. H. Lipowsky. Influence of erythrocyte aggregation on leukocyte margination in postcapillary venules of rat mesentery. *Am. J. Physiol.-Heart C*, 279:H1460–H1471, 2000.

[201] R. L. Pego. Front migration in the nonlinear cahn-hilliard equation. *P. Roy. Soc. Lond. A Math. P.*, 422(1863):261–278, 1989.

[202] R. Poincloux, O. Collin, F. Lizárraga, M. Romao, M. Debray, M. Piel, and P. Chavrier. Contractility of the cell rear drives invasion of breast tumor cells in 3d matrigel. *PNAS*, 108(5):1943–1948, 2011.

[203] J. Prost, F. Jülicher, and J. Joanny. Active gel physics. *Nat. Phys.*, 11(2):111–117, 2015.

[204] J. W. Prothero and A. C. Burton. The physica of blood flow in capillaires. *Biophys. J.*, 2:199–212, 1962.

[205] R. Ramaswamy, G. Bourantas, F. Jülicher, and I. F. Sbalzarini. A hybrid particle-mesh method for incompressible active polar viscous gels. *J. Comput. Phys.*, 291: 334–361, 2015.

[206] S. Ramaswamy. The mechanics and statistics of active matter. *Annu. Rev. Condens. Matter Phys.*, 1(1):323–345, 2010.

[207] A. Rätz. Turing-type instabilities in bulk–surface reaction–diffusion systems. *J. Comput. Appl. Math.*, 289:142–152, 2015.

[208] A. Rätz and M. Röger. Turing instabilities in a mathematical model for signaling networks. *J. Math. Bio.*, 65:1215–1244, 2012.

[209] A. Rätz and M. Röger. Symmetry breaking in a bulk–surface reaction–diffusion model for signalling networks. *Nonlinearity*, 27(8):1805, 2014.

[210] A. Rätz and A. Voigt. Pde's on surfaces - a diffuse interface approach. *Comm. Math. Sci.*, 4:575–590, 2006.

[211] A. Rätz and A. Voigt. A diffuse-interface approximation for surface diffusion including adatoms. *Nonlinearity*, 20(1):177, 2007.

[212] M. Röger and R. Schätzle. On a modified conjecture of de giorgi. *Math. Z.*, 254 (4):675–714, 2006.

[213] B. Rubinstein, K. Jacobson, and A. Mogilner. Multiscale two-dimensional modeling of a motile simple-shaped cell. *Multiscale Model. Sim.*, 3(2):413–439, 2005.

[214] B. Rubinstein, M. F. Fournier, K. Jacobson, A. B. Verkhovsky, and A. Mogilner. Actin-myosin viscoelastic flow in the keratocyte lamellipod. *Biophys. J.*, 97(7): 1853–1863, 2009.

[215] J. Rubinstein, P. Sternberg, and J. B. Keller. Fast reaction, slow diffusion, and curve shortening. *SIAM J. Appl. Math.*, 49(1):116–133, 1989.

[216] R. E. Rusu. An algorithm for the elastic flow of surfaces. *Interface Free Bound.*, 7(3):229–239, 2005.

[217] R. Ryham, F. S. Cohen, and R. Eisenberg. A dynamic model of open vesicles in fluids. *Comm. Math. Sci.*, 10:1273–1285, 2012.

[218] D. Salac and M. J. Miksis. A level set projection model of lipid vesicles in general flows. *J. Comput. Phys.*, 230:8192–8215, 2011.

[219] D. Salac and M. J. Miksis. Reynolds number effects on lipid vesicles. *J. Fluid Mech.*, 711:122–146, 2012.

[220] G. Salbreux, G. Charras, and E. Paluch. Actin cortex mechanics and cellular morphogenesis. *Trends Cell Biol.*, 22(10):536–545, 2012.

[221] J. Schonberg and E. Hinch. Inertial migration of a sphere in p oiseuille flow. *J. Fluid Mech.*, 203:517–524, 1989.

[222] G. Segre and A. Silberberg. Radial particle displacements in p oiseuille flows of suspensions. *Nature*, 189:209–210, 1961.

[223] U. Seifert. Adhesion of vesicles in two dimensions. *Phys. Rev. A*, 43(12):6803, 1991.

[224] U. Seifert. Configurations of fluid membranes and vesicles. *Adv. in Physics*, 46: 13–137, 1997.

[225] U. Seifert and R. Lipowsky. Adhesion of vesicles. *Phys. Rev. A*, 42:4768–4771, 1990.

[226] U. Seifert and R. Lipowsky. Morphology of vesicles. *Handb. Biol. Phys.*, 1:403–464, 1995.

[227] U. Seifert, K. Berndl, and R. Lipowsky. Shape transformations of vesicles: Phase diagram for spontaneous-curvature and bilayer-coupling models. *Phys. Rev. A*, 44 (2):1182, 1991.

[228] D. Shao, W.-J. Rappel, and H. Levine. Computational model for cell morphodynamics. *Phys. Rev. Lett.*, 105:108104, 2010.

[229] D. Shao, H. Levine, and W.-J. Rappel. Coupling actin flow, adhesion, and morphology in a computational cell motility model. *PNAS*, 109:6851–6856, 2012.

[230] J. Shen and X. Yang. Decoupled energy stable schemes for phase-field models of two-phase complex fluids. *SIAM J. Sci. Comput.*, 36(1):B122–B145, 2014.

[231] R. Simson, E. Wallraff, J. Faix, J. Niewohner, G. Gerisch, and E. Sackmann. Membrane bending modulus and adhesion energy of wild-type and mutant cells of dictyostelium lacking talin or cortexillins. *Biophys. J.*, 74:514–522, 1998.

[232] I. Singer-Loginova and H. Singer. The phase field technique for modeling multiphase materials. *Rep. Prog. Phys.*, 71(10):106501, 2008.

[233] J. S. Sohn, Y.-H. Tseng, S. Li, A. Voigt, and J. S. Lowengrub. Dynamics of multicomponent vesicles in a viscous fluid. *J. Comput. Phys.*, 229:119–144, 2010.

[234] I. Steinbach. Phase-field models in materials science. *Modell. Simul. Mater. Sci. Eng.*, 17(7):073001, 2009.

[235] H. Strey and M. Peterson. Measurment of erythrocyte-membrane elasticity by flicker eigenmode decomposition. *Biophys. J.*, 69:478–488, 1995.

[236] N. Takeishi, Y. Imai, K. Nakaaki, T. Yamaguchi, and T. Ishikawa. Leukocyte margination at arteriole shear rate. *Physiol. Rep.*, 2:e12037, 2014.

[237] H. Tanaka and T. Araki. Simulation method of colloidal suspensions with hydrodynamic interactions: Fluid particle dynamics. *Phys. Rev. Lett.*, 85:1338–1341, 2000.

[238] K. E. Teigen, X. Li, J. Lowengrub, F. Wang, and A. Voigt. A diffuse-interface approach for modeling transport, diffusion and adsorption/desorption of material quantities on a deformable interface. *Comm. Math. Sci.*, 7:1009–1037, 2009.

[239] K. E. Teigen, P. Song, J. Lowengrub, and A. Voigt. A diffuse-interface method for two-phase flows with soluble surfactants. *J. Comput. Phys.*, 230(2):375–393, 2011.

[240] A. Tiribocchi, R. Wittkowski, D. Marenduzzo, and M. E. Cates. Active model h: Scalar active matter in a momentum-conserving fluid. *Phys. Rev. Lett.*, 115(18): 188302, 2015.

[241] E. Tjhung, M. E. Cates, and D. Marenduzzo. Nonequilibrium steady states in polar active fluids. *Soft Matter*, 7(16):7453, 2011.

[242] E. Tjhung, D. Marenduzzo, and M. E. Cates. Spontaneous symmetry breaking in active droplets provides a generic route to motility. *PNAS*, 109(31):12381–12386, 2012.

[243] E. Tjhung, A. Tiribocchi, D. Marenduzzo, and M. Cates. A minimal physical model captures the shapes of crawling cells. *Nat. Comm.*, 6, 2015.

[244] J. Toner and Y. Tu. Long-range order in a two-dimensional dynamical XY model: How birds fly together. *Phys. Rev. Lett.*, 75:4326–4329, 1995.

[245] J. Toner and Y. Tu. Flocks, herds, and schools: A quantitative theory of flocking. *Phys. Rev. E*, 58:4828–4858, 1998.

[246] B. Vanderlei, J. J. Feng, and L. Edelstein-Keshet. A computational model of cell polarization and motility coupling mechanics and biochemistry. *Multiscale Model. Sim.*, 9:1420–1443, 2011.

[247] S. Veerapaneni, D. Gueyffier, D. Zorin, and G. Biros. A boundary integral method for simulating the dynamics of inextensible vesicles suspended in a viscous fluid in 2d. *J. Comput. Phys.*, 228:2334–2353, 2009.

[248] S. K. Veerapaneni, A. Rahimian, G. Biros, and D. Zorin. A fast algorithm for simulating vesicle flows in three dimensions. *J. Comput. Phys.*, 230(14):5610 – 5634, 2011.

[249] A. Veksler and N. S. Gov. Phase transitions of the coupled membrane-cytoskeleton modify cellular shape. *Biophys. J.*, 93:3798–3810, 2007.

[250] P. Vennemann, R. Lindken, and J. Westerweel. In vivo whole-field blood velocity measurement techniques. *Exp. Fluids*, 42:495–511, 2007.

[251] A. B. Verkhovsky, O. Y. Chaga, S. Schaub, T. M. Svitkina, J.-J. Meister, and G. G. Borisy. Orientational order of the lamellipodial actin network as demonstrated in living motile cells. *Mol. Biol. Cell*, 14(11):4667–4675, 2003.

[252] S. Vey and A. Voigt. Amdis: adaptive multidimensional simulations. *Comput. Vis. Sci.*, 10:57–67, 2007.

[253] T. Vicsek, A. Czirók, E. Ben-Jacob, I. Cohen, and O. Shochet. Novel type of phase transition in a system of self-driven particles. *Phys. Rev. Lett.*, 75(6):1226, 1995.

[254] A. Voigt and T. Witkowski. A multi-mesh finite element method for lagrange elements of arbitrary degree. *J. Comput. Sci.*, 3(5):420–428, 2012.

[255] X. Wang. Asymptotic analysis of phase field formulations of bending elasticity models. *SIAM J. Math. Anal.*, 39(5):1367–1401, 2008.

[256] X. Wang and Q. Du. Modelling and simulations of multi-component lipid membranes and open membranes via diffuse interface approaches. *J. Math. Bio.*, 56: 347–371, 2008.

[257] R. Wedlich-Soldner, S. Altschuler, L. Wu, and R. Li. Spontaneous cell polarization through actomyosin-based delivery of the cdc42 gtpase. *Science*, 299:1231–1235, 2003.

[258] R. Wedlich-Soldner, S. Wai, T. Schmidt, and R. Li. Robust cell polarity is a dynamic state established by coupling transport and gtpase signaling. *J. Cell Bio.*, 166:889–900, 2004.

[259] C. A. Whitfield, D. Marenduzzo, R. Voituriez, and R. J. Hawkins. Active polar fluid flow in finite droplets. *Eur. Phys. J. E*, 37(2):1–15, 2014.

[260] T. J. Willmore and T. J. Willmore. *Riemannian geometry.* Oxford University Press, 1996.

[261] T. Witkowski, S. Ling, S. Praetorius, and A. Voigt. Software concepts and numerical algorithms for a scalable adaptive parallel finite element method. *Adv. Comput. Math.*, 2015.

[262] T. Wu and J. J. Feng. Simulation of malaria-infected red blood cells in microfluidic channels: Passage and blockage. *Biomicrofluidics*, 7(4):044115, 2013.

[263] T. Wu and J. J. Feng. Modeling the mechanosensitivity of neutrophils passing through a narrow channel. *Biophys. J.*, 109(11):2235–2245, 2015.

[264] P. Yue, J. J. Feng, C. Liu, and J. Shen. A diffuse-interface method for simulating two-phase flows of complex fluids. *J. Fluid Mech.*, 515:293–317, 2004.

[265] P. Yue, C. Zhou, J. J. Feng, C. F. Ollivier-Gooch, and H. H. Hu. Phase-field simulations of interfacial dynamics in viscoelastic fluids using finite elements with adaptive meshing. *J. Comput. Phys.*, 219(1):47–67, 2006.

[266] J. Zhang, S. Das, and Q. Du. A phase field model for vesicle-substrate adhesion. *J. Comput. Phys.*, 228:7837–7849, 2009.

[267] H. Zhao and E. S. G. Shaqfeh. The dynamics of a vesicle in simple shear flow. *J. Fluid Mech.*, 674:578–604, 2011.

[268] D. V. Zhelev, D. Needham, and R. Hochmuth. A novel micropipet method for measuring the bending modulus for vesicle membranes. *Biophys. J.*, 67:720–727, 1994.

[269] C. Zhou, P. Yue, J. J. Feng, C. F. Ollivier-Gooch, and H. H. Hu. 3d phase-field simulations of interfacial dynamics in newtonian and viscoelastic fluids. *J. Comput. Phys.*, 229(2):498–511, 2010.

[270] F. Ziebert and I. S. Aranson. Effects of adhesion dynamics and substrate compliance on the shape and motility of crawling cells. *PLoS One*, 8:e64511, 2013.

[271] F. Ziebert, S. Swaminathan, and I. S. Aranson. Model for self-polarization and motility of keratocyte fragments. *J. R. Soc. Interface*, page rsif20110433, 2011.

[272] F. Ziebert, S. Swaminathan, and I. S. Aranson. Model for self-polarization and motility of keratocyte fragments. *J. R. Soc. Interface*, 9:1084–1092, 2012.

Selbstständigkeitserklärung

Die eingereichte Dissertation zum Thema

Hydrodynamic Diffuse Interface Models for Cell Morphology and Motility

wurde am Institut für Wissenschaftliches Rechnen der Technischen Universität Dresden unter Betreuung durch Prof. Dr. rer. nat. Axel Voigt angefertigt. Hiermit versichere ich, dass ich die vorliegende Arbeit ohne unzulässige Hilfe Dritter und ohne Benutzung anderer als der angegebenen Hilfsmittel angefertigt habe; die aus fremden Quellen direkt oder indirekt übernommenen Gedanken sind als solche kenntlich gemacht. Die Arbeit wurde bisher weder im Inland noch im Ausland in gleicher oder ähnlicher Form einer anderen Prüfungsbehörde vorgelegt.

Dresden, den 24. März 2016

Dipl.-Math. Wieland Marth